Novel Shear Force Scanning Modes Enabled with Digital Implementations of Robust Nano-Precision Controllers and Estimators

Kaiqiang Zhang

Mechanical Engineering Department

University of Bristol

A dissertation submitted to the University of Bristol in accordance with the requirement of the degree of Doctor of Philosophy in the Faculty of Engineering.

Word Count: 60,000 (approx)

01 September 2018

Abstract

The research primarily focuses on the development of novel instrument and control (I&C) for a Transverse Dynamic Force Microscope (TDFM) system, which is a special Probe Microscope enabling the specimens morphology on nanometre scale. The TDFM genuinely allows accurate specimen morphology in non-contact manner, whereas typical Atomic Force Microscopes (AFMs) image the specimen topography via physical contact and therefore may cause damage to delicate specimens.

The novel I&C design realises a digital control solution using field programmable gate array (FPGA) boards, which have high computational power running at fast implementation rates (e.g. 4 MHz). This novel system integrates a previous TDFM mechanical design with a novel cantilever-specimen separation sensing mechanism, an online reconfigurable digital control programme, etc.. An offline optimisation method is developed to enhance the robustness of the digital control programmes to perform dynamic scans of various samples.

The novel cantilever-specimen separation sensing mechanism exploits the cantilever oscillation amplitude in relation to the cantilever-specimen distance. The sensing method improves the sensing range up to $\sim$6 nm in contrary to the previous range of $\sim$2 nm.

The nonlinear dynamics of the vertical positioning systems for the cantilever, which have not been sufficiently studied before, are investigated. Robust H_∞ control algorithms are designed for two nonlinear vertical positioning systems. Two developed closed-loop systems are implemented and practically achieve robust cantilever positioning performance at 1 nm accuracy.

Significantly, the thesis provides the first interaction force reconstruction method for real-time scanning in practice. The force reconstruction algorithm is developed employing a sliding mode observer using FPGA. The digital design and implementation are presented. Practical assessments show that the force reconstruction can identify the variation of the low interaction-force at sub-nN level in real-time. Therefore, the mechanical properties, including viscosity and elasticity, of the scanned specimen surface can be reconstructed.

The developed TDFM system integrates these novel features collectively and enables three functional modes, i.e. contact mode, non-contact mode, and force-scan mode, at 1 nm precision avoiding physically cantilever-specimen contacts. The contact and non-contact modes are two specimen scanning modes that allow imaging nano-structure of delicate specimens. Specifically, the non-contact mode is focused and considered more powerful in the thesis. The completely novel force-scan mode reconstructs the cantilever-specimen interaction force allowing to analyse the specimen surface properties for various practical purposes, e.g. physics, chemistry, medicine.

Acknowledgement

"格物致知" is an ancient Chinese aphorism from about 400 BC. It appears in a classic book called "大學", literally translated to "university" in English, teaches the methodology to gain wisdom. The aphorism explains that the avenue to gain knowledge is to investigate, research, and learn from the world in practice with critical thinking. The PhD research experience gives me a period of time to explore new knowledge on the specific topic, and also deeply plants the sense of "格物致知" in my mind. However, as I always know, an entire life time is too short to learn the world, and the true wisdom.

This study presents the development of the instrument and control for a sensitive nano-precision system. The research experience on the complicated high-precision system is transferable to and valuable for system control on relatively large scale. The project requires various practical skills, e.g. system integration, software framework design, system identification, control design, estimator implementation, system diagnostics, maintenance, etc..

The accomplishment relies on the help from the University of Bristol. Specifically, the Faculty of Engineering funded the postgraduate research scholarship of the PhD and the laboratory expense to stay at the centre of Nano Science and Quantum Information (NSQI). Also, the NSQI provided the laboratory support during the whole period.

The author has to present the best respects to the dear supervisor Dr. Guido Herrmann, a patient and supportive mentor. The project is benefited from his active supports, deep theoretical background, and practical engineering experience. My co-supervisors, Prof. Mervyn Miles (a fellow of the Royal Society) and Dr. Massimo Antognozzi, provided the opportunity to work on the high-precision system, invented by them. Specifically, Dr. Antognozzi generously shared the key experience that he gained in about two decades.

Thanks the other collaborators, including Dr. Toshiaki Hatano, Prof. Christopher Edwards, Prof. Stuart Burgess, etc., who have helped getting started and contributed to the project. I do appreciate the help from Dr. Peter Dunton and Mr. Mark Fitzgerald. I would recognise Prof. Jing Na for sharing his understanding on control and estimation algorithms. I am honoured and grateful to obtain supportive advices from Prof. Alan Champneys, the PhD reviewer.

Personally, I gratefully appreciate for the all-through-the-way support from my parents, Shijie Zhang and Dong Wang. Thanks to the ever-growing family of friends in the ACT-Lab 'the Cave/Farm', and my dear companions who have been standing together on the journey, particularly Dr Yuan Li, Dr Yuzhou Liu, Dr Bin Zhu, Yuanfei Ge, and Dr Andrea Iannelli.

For my dream destination, the universe.

To the beloved ones, who love me.

Declaration

I declare that the work in this dissertation was carried out in accordance with the requirements of the University's *Regulations and Code of Practice for Research Degree Programmes* and that it has not been submitted for any other academic award. Except where indicated by specific reference in the text, the work is the candidate's own work. Work done in collaboration with, or with the assistance of, others, is indicated as such.

Any views expressed in this dissertation are those of the author and in no way represent those of the University of Bristol.

The dissertation has not been presented to any other university for examination either in the United Kingdom or overseas.

SIGNED: _____

DATE: _____

Contents

List of Figures

Nomenclature

I&C	Instrument & Control
AFM	Atomic Force Microscope
EM	Electron Microscope
SEM	Scanning Electron Microscope
SFM	Shear Force Microscope
TEM	Transmission Electron Microscope
TDFM	Transverse Dynamic Force Microscope
LMFM	Lateral Molecule Force Microscope
DNA	Deoxyribonucleic acid
A/D	Analog-to-Digital
D/A	Digital-to-Analog
DSP	Digital Signal Processor
FPAA	Field Programmable Analogue Array
FPGA	Field Programmable Gate Array
DMA	Direct memory access
RAM	Random-access memory
PI	Proportional–integral
PD	Proportional–derivative
PID	Proportional–integral–derivative
ILC	Iterative Learning Control
RC	Repetitive Control
GUI	Graphic user interface
N.A.	Numerical aperture
fxp	fixed-point representation
$I16$	16 bit-Integer
Relative height	The distance from cantilever to the sample-substrate in the TDFM
Absolute height	The distance from cantilever to the sample-holder in the TDFM

CRH	Constant relative height
CAH	Constant absolute height
ω	Angular velocity in radians per second
j	Unit imaginary number
$H(s)$	Arbitrary transfer function represented in s domain
$H(z)$	Arbitrary transfer function represented in z domain
$\mathcal{L}$	Laplace transformation operation
TDF-I	Transposed direct form I
TDF-II	Transposed direct form II
IIR	Infinite impulse response
E	Young's modulus of the cantilever
ρ	Density of the cantilever
I	Second moment of area
γ	Viscous coefficient of cantilever damping
L	Cantilever length
A_s	Cross-section area of the cantilever
f	Cantilever-sample interaction shear-force
u	Excitation of the cantilever
y_c	Cantilever oscillation
SAGE	Self-assembled cage-like particles
HEPES	A zwitterionic organic chemical buffering agent (4-(2-hydroxyethyl)-1-piperazineethanesulfonic acid)

Chapter 1

Introduction

1.1 Overview

This thesis tackles the research on the development of a sensing mechanism, an instrument & control (I&C) solution, and a real-time estimation approach at nano-metre resolution for a specific probe microscope, the Transverse Dynamic Force Microscope (TDFM) (Antognozzi et al. 2008), developed at the University of Bristol. This research is based on a sensing mechanism that can measure the interaction shear-force between an oscillating vertically oriented cantilever (or probe) and the sample-substrate in a noncontact manner. In principle, it permits to develop devices allowing topography and surface-property investigations of delicate specimens at nano-precision, avoiding contact or damage (Betzig et al. 1992, Antognozzi 2000, Harniman 2013). Previous research has contributed to understanding fundamental physics (Antognozzi et al. 2016), chemical reaction observation (Harniman et al. 2017), and biological mechanism investigation (Fletcher et al. 2013).

The topography-scanning feature is realised with the so-called Shear Force Microscope (SFM), a kind of Atomic Force Microscope (AFM), that translates the measured atomic force interaction into the topographic information of the sample-substrate (Binnig et al. 1986). Specifically, at Bristol, the principle of the shear-force interaction has been studied by Antognozzi since 2000 (Antognozzi 2000). In 2008, a new optical sensing mechanism is proposed to improve the shear-force sensitivity to pN level (Antognozzi et al. 2000). Recently, a prototype Transverse Dynamic Force Microscope (TDFM) based on this novel sensing mechanism was developed by Harniman (2013) allowing to image delicate specimens at high precision (Harniman et al. 2012, Fletcher et al. 2013) in liquid environments. This TDFM, a kind of SFM or alternatively named as the Lateral Molecular Force Microscope (LMFM), has also been used as a sensitive force sensor to measure optical momentum or antibiotic reaction (Antognozzi et al. 2016, Antognozzi 2017).

This previous research on the TDFM successfully demonstrates the topography-scanning and force-sensing capability at high precision. In comparison with typical AFMs, the TDFM (Harniman 2013) has

shown the advantage of observing the nano-structure of specimens, while avoiding damage to delicate specimens. However, so far, the TDFM had a limited imaging depth of field and a constrained performance due to the design of the cantilever-specimen separation sensing mechanism. Additionally, the scanning precision of the TDFM system could not be guaranteed. This is because the applied proportional-integral (PI) controller is ad-hoc tuned during scans and the creep effect of the piezo-actuators is disregarded. When the TDFM was employed for interaction force sensing measurement in previous work, the cantilever oscillation had to be recorded in experiments and the interaction shear-force was subsequently computed from the oscillation data offline (Antognozzi et al. 2001, 2016).

Therefore, this work aims to overcome the limitations and improve the performance of the TDFM employing control engineering approaches. A completely new digital control solution is introduced to the previous TDFM mechanical set-up, for realising a multi-mode shear-force scanning device – an upgraded TDFM. Extensive knowledge and work on the system is needed to complete the I&C design procedure, including design requirements analysis, control solution development, control system integration, dynamics study, and application of suitable control schemes. The embedded digital control solution is based on Field Programmable Gate Array (FPGA) hardware, which permits implementing digital control circuit designs reliably running at extremely high implementation frequency. The novel integrated TDFM system realises multi shear force scanning modes of the TDFM at 1 nm precision.

In addition, significant practical research is carried out to achieve specimen imaging applications. Significantly, the vertical cantilever positioning system is strongly influenced by the nonlinear atomic-force interaction and the presence of environmental perturbations. Hence, the vertical positioning system dynamics are studied in a step wise manner in order to achieve good control performance at high precision. The fixed-point arithmetic based control programmes have to be parametrically optimised and to be robust against the varying signal range in dynamic scans. Thus, an offline optimisation tool is developed for digital FPGA programming designs to guarantee the design quality before being deployed on FPGA boards. Excessive practical experience has been obtained; successful scans rely on various experimental factors, e.g. an optimised optical sensitivity, the tip geometry, etc., combined with diligent practical operation.

The author expects that the research experience can benefit the development of other systems at high precision or on larger scales. Importantly, the experience of designing the FPGA control programmes contributes to the development of control applications using the FPGA technology, which has gained great attention in research and industry. The proposed digital control programme design provides a solution that allows to online reconfigure the controller without the need to reload the control programming onto FPGA boards. The developed offline FPGA programming optimisation tool improves the programming efficiency for the fixed-point arithmetic based control programmes before practical deployment. The control algorithm development procedure gives a solution to control complex nonlinear systems with significant noise and disturbances. Also, the reconstruction of an unknown system input, i.e. the interaction

shear-force at a high frequency of 200 kHz and at high precision 0.1 nN, is a practical application of data fusion to obtain signals that cannot or too expensive to be measured.

Specifically, the research in this thesis aims to improve the TDFM system in the following three respects.

1.2 Motivation: Distance Measurement at Nano-precision in a Noncontact Manner

The previous TDFM (or called the LMFM) is able to sense the shear-force interaction between the cantilever and the sample-substrate a range of about 2 nm (Harniman 2013) in a liquid environment. This limited sensing range is mainly a consequence of the sensing component design that will be introduced in the literature review, Chapter 2.

Two operation modes have been developed for the previous set-up: a shear-force feedback mode and an optical feedback mode (Harniman 2013, Harniman et al. 2012). In the shear-force feedback mode, an ad-hoc tuned PID (mostly PI) controller is used to control the vertical position of the cantilever to retain a constant cantilever oscillation amplitude or phase, i.e. a constant shear-force interaction is kept between the cantilever and the sample-substrate. The height of the sample-substrate is computed from the control signal of the piezo-actuator in feedback control. The shear-force feedback loop fails, as soon as the system measurement exceeds the sensing range caused by rapid change of specimen topography or disturbances. In other words, the limited shear-force interaction sensing range constraints the working range of the TDFM in shear-force feedback mode. Thus, the TDFM in this mode has only been applied to specimens of less than 3 nm height, specifically DNA samples (Harniman 2013, Harniman et al. 2012). The previous optical feedback mode also employs a PI controller (Harniman 2013) to retain a constant optical measurement, indicating the distance from the cantilever to the sample-holder surface. Meanwhile, the specimen, in the 2 nm sensing range under the cantilever, is imaged by the measured cantilever oscillation phase, i.e. the shear-force interaction (Harniman 2013, Harniman et al. 2012, Fletcher et al. 2013). In this mode, the TDFM only has a 2 nm imaging depth of field and there is no direct measurement for the specimen where the sensing range is exceeded.

In theory, a TDFM allows a shear-force interaction range of about 6 nm (Israelachvili & Pashley 1983) or up to about 8 nm (Antognozzi 2000) in a liquid environment. Motivated to break the limitations to the topography analysis performance, a novel sensing mechanism is required for the accessibility to the whole theoretical $\sim$6 nm interaction range. Subsequently, it is expected and will be seen that the depth of imaging field will be enlarged and the limitation of the specimen height is released in the novel TDFM design (see applications and discussions in Chapter 6).

1.3 Motivation: Practical Development for Real-time Microscopy Imaging

The previous TDFM (Harniman 2013) employs an ad-hoc tuned PI-controller to control the cantilever vertical position in two operation modes. The control gains have to be ad-hoc tuned with respect to any change of the experimental conditions (e.g. cantilever, specimen, scan medium, etc.) in each scan. This online controller adjustment design needs rich operational expertise, toughening the use of the TDFM. As a result, the specimen-imaging performance strongly relies on the operational proficiency, and the control performance cannot be guaranteed during a dynamic scanning procedure.

In addition, the utilisation of the PI control scheme limits the vertical positioning performance, subsequently the imaging quality, of the TDFM. Hence, the previous TDFM set-up in the shear-force feedback mode (Harniman 2013) fails to scan relatively high specimens taking a limited 2 nm control range into account. It has been found out that a simple frequency shaping control scheme, specifically a lag-controller with even up to 6 nm working range, provides a poor imaging performance scanning 50 nm high specimens in a similar working mode (see the first noncontact mode scanning result in Chapter 6).

Another design issue of the shear-force feedback mode in the previous set-up (Harniman 2013) is taking the feedback control signal of the piezo-actuator as the sample-substrate topographic measurement. In the set-up, a second piezo-actuator, which vertically translates the cantilever into the vicinity of the sample substrate, works in open-loop. The design ignores the creep effect of both piezo-actuators, i.e. this brings inaccuracy into the topographic measurement.

Therefore, the other motivation of this research is to resolve these design issues to improve the potential specimen imaging capability of the TDFM. This requires to facilitate a new embedded system control solution realising multiple real-time microscopy functions. In the control system, the compatibility to advanced control algorithms has to be considered within the system design. Sufficient investigations on the system dynamics at high precision are necessary for designing suitable control algorithms for the TDFM. Specifically, the principles of the specimen-morphology modes need to be upgraded for an enhanced imaging performance.

1.4 Motivation: Online Atomic Force Reconstruction

An important application of AFMs is to measure and investigate the atomic forces, and subsequently study the specimen-surface properties (Antognozzi et al. 2001, Labernadie et al. 2014, Rigato et al. 2015, Ding et al. 2015, Antognozzi et al. 2016). The reconstruction of the atomic-forces or mechanical properties for specimen surfaces is critical for biology and physics research, for instance, understanding the structure of cells (Labernadie et al. 2014), cell mechanics (Rigato et al. 2015), diagnosis of early cancer (Ding et al. 2015), observation of molecular structures (Antognozzi et al. 2001), investigate optomechanics

(Antognozzi et al. 2016), etc. However, all the state-of-the-art research needs to record the AFM measurements and then to offline process the data, in order to reconstruct the atomic-forces and mechanical properties (e.g. viscosity or elasticity) over the scanned specimens surface. There is no practical AFM system achieving the atomic-force reconstruction in real-time.

Recent research on the TDFM (Nguyen et al. 2015, 2016) shows a potential technique allowing to reconstruct the interaction force at a single sample-substrate position. This method develops an unknown input observer to estimate the interaction shear-force with limited known system states. The mechanical property, the elasticity and viscosity, over the specimens surface can be subsequently reconstructed. The realisation of this real-time shear-force reconstruction method potentially benefits the TDFM with real-time atomic force sensing capability. This function intuitively provides the ability of interaction force scans and mechanical property mapping for various specimens in a noncontact way.

Thus, another main motivation is to facilitate the real-time interaction force reconstruction function for the TDFM system. Shear-force and mechanical properties mapping scans are completely novel scanning features of the TDFM. Particularly, the main challenge is to implement the theoretical design in practice with careful design and appropriate development.

1.5 Thesis Outline

Motivated by these objectives, this research has been carried out in a directed step-wise manner while the comprehension on the system increases through a trial-and-error design process. In lieu of presenting this whole step-wise procedure, the content is constructed to describe the electro-mechanical design (Chapter 3), the dynamics study and the control algorithms development (Chapter 4), the real-time atomic-force reconstruction technique (Chapter 5), and the scanning applications (Chapter 6) in four chapters respectively. The practically learnt experience are given as remarks within each chapter, so that the practitioners in different related fields have the access to each topic with ease.

This introduction **Chapter 1** gives a brief overview of the objectives, novelty, and motivations of this research and the topics dealt with in each chapter. Related publications of the author are listed to present the research contributions.

Chapter 2 provides a literature review. Firstly, the background of the working principles and the advantages of AFMs, especially the TDFM, is discussed. Then, a survey introduces the control solutions and estimation algorithms used in different AFM applications, i.e. this is expected to benefit the system development. The last part introduces various challenges for a control system at nano-precision required within this research.

The **Chapter 3** presents the integrated system design of the TDFM. At first, it describes the set-up and the essential operations to enable the fundamental shear-force sensing mechanism. The electronics

and mechanical design integrates with the FPGA-based control system realising the high-precision vertical position control and atomic-force reconstruction. Based on the digital control solution design, control programmes are developed according to practical design requirements. Specifically, a design methodology is proposed to allow online reconfiguring different control programmes on the same FPGA implementation. Employing a developed offline programme optimisation tool, the digital FPGA programmes for sensing and control can guarantee an enhanced performance and robustness for dynamic scans.

In **Chapter 4**, the sensing curves of two kinds of cantilever vertical positioning systems, which represent the distances from the cantilever to the sample-holder or to the sample-substrate, are investigated. Then, the dynamics of the two positioning systems are identified in the frequency domain and the control algorithms are subsequently developed respectively. Control performance of two positioning systems is verified in practice and confirmed to achieve 1 nm positioning accuracy. This demonstrates that the control systems are well developed for various scanning functions of the TDFM. Comparative studies of different control methods for two positioning systems are provided, so as the advances of the proposed robust control designs are addressed.

The next **Chapter 5** puts the attention on facilitating the real-time interaction-force reconstruction. A practically oriented modelling method is introduced to develop a numerical model of the cantilever oscillation when it is influenced by the shear-force. Based on the model, a sliding mode observer is developed to estimate (i.e. reconstruct) the interaction shear-force. A parameter estimator is then suggested to estimate the elasticity and viscosity over the specimen surface. Simulation and experimental assessments show that the successful implementation of the real-time interaction-force measurement, subsequently realising online elasticity, viscosity, elastic force, and the viscous force sensing function. It will be proven in the **Chapter 6** that the interaction shear-force can be successfully reconstructed during a dynamic specimen morphology scan.

Chapter 6 presents the three scanning modes of the developed TDFM system (see details in the chapter). Two scanning modes, contact mode and noncontact mode, are developed from the two scanning modes of the previous TDFM respectively. Experimental scanning results shows that the developed TDFM system has an improved morphology capability in comparison to the previous TDFM (Harniman 2013). The novel force-scan mode successfully achieves the force strength mapping and subsequently the mechanical characteristics (elasticity and viscosity) mapping of a scanned area in practice.

At last, the conclusions and discussions are given in **Chapter 7** together with several suggestions of potential future work.

1.6 Publications

The main contributions of this research are addressed by the following publications:

- *"A real-time transverse dynamic force estimation approach in fixed-point arithmetic"*, Zhang, K., G. Herrmann, M. Antognozzi, et al., Prepared for journal submission.
- *"A Multi-mode Transverse Dynamic Force Microscope - Design, Identification and Control"*, Zhang, K., G. Herrmann, M. Antognozzi, et al., Under journal revision.
- *"Enhancing fixed-point control robustness for experimental non-contact scans with the Transverse Dynamic Force Microscope"*, Zhang, K., T. Hatano, G. Herrmann, et al., *American Control Conference (ACC) 2018, IEEE.*
- *"A specimen-tracking controller for the Transverse Dynamic Force Microscope in non-contact mode"*, Hatano, T., K. Zhang, SG. Khan, et al., *American Control Conference (ACC) 2016, IEEE*, 2016: 7384-7389.

There are other publications strongly connected with the research project in an order of relevance to the research topic:

- *"Cantilever modelling, calibration and shear force reconstruction with a super-twisting observer for a vertically oriented probe microscope"*, Zhang, K., T. Hatano, TN. Tien, et al., Submitted for journal publication.
- *"Real-Time sliding mode observer scheme for shear force estimation in a Transverse Dynamic Force Microscope"*, Tien, TN., S. Khan, T. Hatano, K. Zhang, et al., *Asian Journal of Control*, 2017, vol. 19, pp. 1-12.
- *"Estimation of the shear force in transverse dynamic force microscopy using a sliding mode observer"*, Tien, TN., T. Hatano, S. Khan, K. Zhang, et al., *AIP Advances*, 2015, vol. 5(9), 097157.
- *"Improving transient performance of adaptive control via a modified reference model and novel adaptation"*, Na, J., G. Herrmann, K. Zhang, *International Journal of Robust and Nonlinear Control*, 2017, vol. 27(8), pp.1351–1372.
- *"Optimisation of a nano-positioning stage for a Transverse Dynamic Force Microscope"*, De Silva, G., S. Burgess, T. Hatano, S. Khan, K. Zhang, et al., *Precision Engineering*,Precision Engineering, 2017, vol. 50, pp. 183-197.
- *"An optimized nano-positioning stage for Bristol's Transverse Dynamic Force Microscope"*, De Silva, G., S. Burgess, T. Hatano, S. Khan, K. Zhang, et al., *7th IFAC Symposium on Mechatronic Systems & 15th Mechatronics Forum International Conference*, 2016, pp. 120-126.

Chapter 2

Literature Review

2.1 Introduction

This chapter comprises three sections on different aspects to understand the importance, the related state-of-the-art of AFM development, and challenges for developing the Transverse Dynamic Force Microscope (TDFM). The first part presents the advantages, basic principles, and current limitations of force microscopes and subsequently TDFMs. The next section reviews the system integration solutions, including novel control and estimation algorithms, for various Atomic Force Microscope (AFM) systems. Moreover, the practical issues of implementing and operating the TDFM, as a special AFM, are discussed in the last section of this chapter. This is to clarify significant challenges of this research.

2.2 An Introduction into the Transverse Dynamic Force Microscope

The section introduces the TDFM as a special subset of a force and probe microscope. Hence, a short history of microscopes and AFMs will provide a basis and justification to the research on TDFMs and their control. AFMs are special and very different to other microscopy systems. They can scan the topography of almost any material under various environmental conditions on nanometre scale. In contrast, different kinds of Electron Microscopes (EMs) are only capable to image conductive/specially-treated samples in limited environments to avoid undesirable scattering of electrons. Hence, an explanation of the advantages and disadvantages of AFMs is then introduced to present and explain the working principles and the development of the TDFM/Shear Force Microscope (SFM). The special working principle of SFM allows a true non-contact scan mode to improve the imaging accuracy and to avoid possible damage to the samples. The next parts of this section specifically focus on the development of TDFM and recent relevant research at the University of Bristol to further clarify the contribution of this thesis.

2.2.1 A Brief History of Microscopy Systems and Atomic Force Microscopy

Research of improving microscopes' resolving power has been appreciated by the public and was awarded several Nobel prizes since 1925 (Nobel Media 2018). Previous optical microscopes have contributed to life science, materials science, manufacturing, and assembly (e.g. the optical microscopes from Carl Zeiss AG (2018)). This followed the first microscopy application, the observation of 'the fly' by Galileo Galilei in 1609 (Uluç et al. 2009). However, an optical microscope using visible light illumination reaches at best a resolution of 200 nm (Flegler et al. 1993). This resolution is insufficient for virus observation that requires a resolution of 20-60 nm or better (Flegler et al. 1993).

In 1932, Knoll & Ruska (1932) invented the Electron Microscope (EM) starting a new era of specimen observation at nanometre resolution. This particular kind of EM (Knoll & Ruska 1932) is also known as the Transmission Electron Microscope (TEM). It exploits high-speed electrons passing through very thin (40-150 nm thick) sections of specimens or small particles on thin membranes in a high-vacuum environment. The transmitted electrons are then projected to and observed on a fluorescent screen. Recent research by Creemer et al. (2008) and De Jonge & Ross (2011) has removed the need of the vacuum environment for the TEMs. However, these TEM instruments still require harsh experimental conditions, such as high working temperature at about $500°C$ (Creemer et al. 2008) or extremely thin sample solutions (De Jonge & Ross 2011). In 1938, the invention of the Scanning Electron Microscope (SEM) by Von Ardenne (1938) made it possible to image the surface of conductive specimens instead of imaging sections of specimens. In SEMs, the surface imaging function achieves a resolution of 3-6 nm by scanning the sample-surface with a focused beam of high-speed electrons following a raster trajectory (Flegler et al. 1993). The imaging principle of sensing the electron interaction with the sample surface depends on a complex preparation of the biological specimens (Flegler et al. 1993). For instance, most of bio-specimens in SEM have to be coated with conductive material (mostly gold) resulting in the death of living specimens (Flegler et al. 1993). Moreover, an environmental SEM permits to image untreated biological specimens, but the instrument is still insufficiently robust to provide consistent imaging performances (Donald 2003). Uniquely, the Cryo-electron microscope images the specimen at sub-nanometre resolution in 3D by composing a cluster of TEM images of thin sections of the frozen specimens (Gebel Berg 2015). It is still an unresolved issue to use an EM for on-line observation of living biological specimens due to the restrictive experimental conditions.

In contrast, the invention of the AFM, by Binnig et al. (1986), has allowed nanometre/Angstrom resolution overcoming the mentioned issues of severe environmental/specimens conditions in the use of EMs. In 1981, Binnig and Rohrer invented the Scanning Tunneling Microscope imaging conductive or semi-conductive material surfaces at sub-nanometre scale at IBM (the International Business Machines Co.) (Binnig et al. 1982, Binnig & Rohrer 2000). On leave from IBM, Binnig started to work on imaging the sample surface through other means than STMs (Rugar & Hansma 1990). Measuring atomic force has the advantage to allow topography scanning of samples regardless their material. The concept

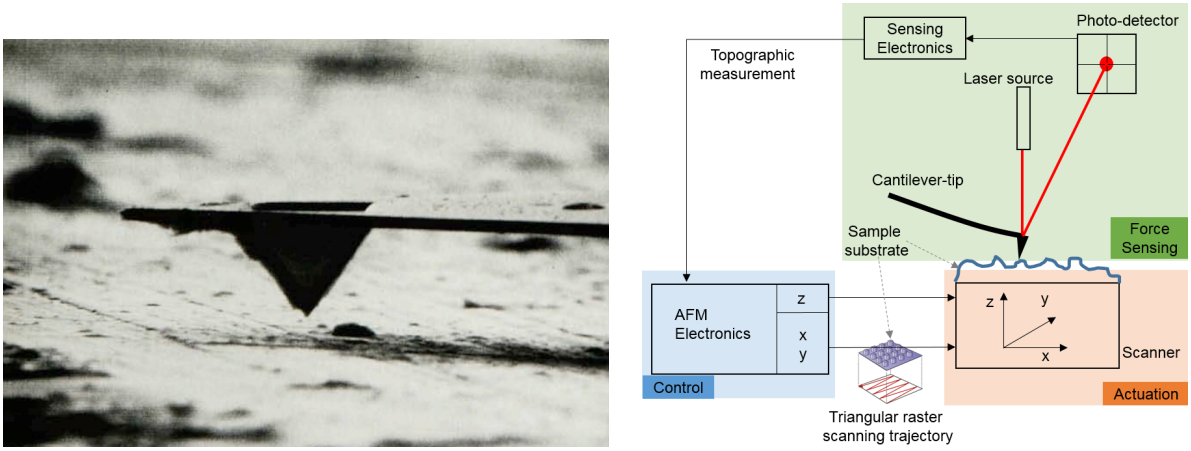

(a) (b)

FIGURE 2.1: Basic principles of AFMs: a) a photo of a cantilever above a sample-surface where the silicon nitride cantilever-tip was manufactured by Park Scientific Instruments for contact mode AFMs (Rugar & Hansma 1990); (b) the schematic of a standard AFM system structure, which feedbacks the operation in z (vertical) direction for topographical compensation while scanning along a raster trajectory in the x&y directions (within the horizontal plane).

of force measurement was developed by employing a cantilever as a spring, which was soft enough to approximate the spring constant between atoms (Rugar & Hansma 1990). In 1986, the first prototype of an AFM was developed by Binnig et al. (1986), extensively expanding opportunities for research on nanoscale. Avoiding the principal difficulties of using EMs, AFMs have been widely used in different fundamental research fields (including: material science (Kim et al. 2015), biological studies (Ando et al. 2013), medical development (Balasubramanian et al. 2014), etc.) with the later adaptation to various environments (vacuum (Meyer & Amer 1988), ambient (Chen et al. 2004), or liquid solution (Kiselyova et al. 2003)).

Over the last three decades of development, the basic structure (Figure 2.1b) of an AFM always consists of an atomic force interaction measurement component, a nano-positioning actuation component, and the control unit with respect to the design requirements (Giessibl 2003). In AFM, the force sensor is often a horizontal cantilever (see the photo of Figure 2.1a), which has a small tip at the free side to vertically interact with the sample-substrate (see Figure 2.1b and 2.2). The deflection of the cantilever changes with respect to the interaction force between the tip and the sample-substrate and can be translated into the tip-specimen separation information. Employing appropriate control schemes, the actuation component changes the vertical position of the cantilever-tip in z direction to keep a constant interaction with the sample-substrate. At the same time, the positioning component is controlled to follow a designed pattern (typically a raster trajectory in the x-y plane) horizontally changing the force measuring position over the sample-substrate, i.e. the topographic data of the sample-substrate is collected as shown in Figure 2.1b.

In order to improve the resolution of AFMs, the cantilever-tip system has been further developed

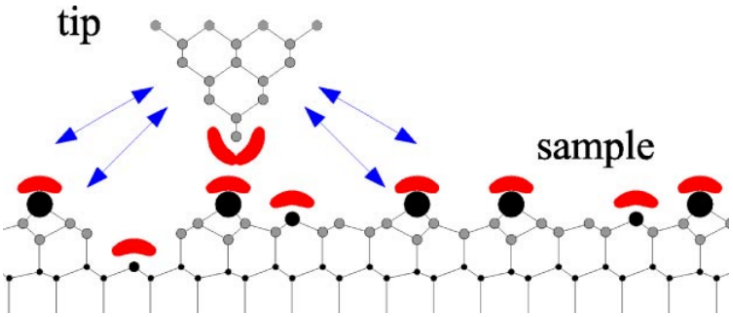

FIGURE 2.2: Schematic of an AFM cantilever-tip closed to a sample surface: short-range forces act when the tip and sample (red) orbits overlap, and long range forces (blue) always affect the tip-sample interaction (Giessibl 2003).

to increase the sensitivity to low atomic forces. The cantilever material has changed over time: gold at the time of invention (Binnig et al. 1986) and then silicon based materials for ease and feasibility of manufacture (Albrecht et al. 1990). Ideally, the force measurement is a result of the interaction between the single atom at the very tip of the cantilever and the sample surface as Figure 2.2 shows. Hence, advanced tip fabricating methods have received significant research attention: the micro-manufactured tip can be produced with a curvature of less than 1 nm^{-1} (Marcus et al. 1990); a nano-tube is grown from the free end of a cantilever for high resolution AFMs (Hafner et al. 1999). In addition to use the cantilever for morphology studies, the tip can be modified to change an AFM into a bio-sensor. For instance, polyanilines are attached at the cantilever-tip to turn the AFM into a minimal pheromone detector (Steffens et al. 2014).

Motivated to improve the imaging quality, control engineers have tried to tackle various practical issues when operating AFMs. There are two common operation modes in a typical AFM with horizontal cantilever: the contact mode and the dynamic mode. In contact mode, the cantilever-tip is driven along the sample-substrate surface by imposing some pressure in the vertical direction on the cantilever. Physically, the cantilever-tip used in this mode touches the sample-substrate, probably causing inaccuracy due to the downward forces and the subsequent vertical forces, perpendicular to the horizontal cantilever (Ortega-Esteban et al. 2012). A feasible solution is to operate an AFM in the dynamic mode, which is often realised as the tapping mode. In this mode, the horizontal cantilever works under a vertical excitation, i.e. creating a repeated tapping on the sample, ideally with a fixed distance to the sample. The cantilever-tip oscillation information, e.g. amplitude or frequency, is affected by the force between the sharp tip and the sample surface. The change of the cantilever oscillation is regarded as the inter-distance measurement for feedback control. However, the tip-sample interaction may be challenged by the changing sample topography when the cantilever has a soft spring constant, i.e. a high atomic force sensitivity. In detail, the contact to the sample during a tapping mode scan can be lost if the topography changes sharply. This causes the issue of the so-called jump effect (Lee et al. 2002). To resolve these issues, various control algorithms have been developed in different AFM systems for accurate imaging performance, like the research of Wu et al. (2009) and Shiraishi & Fujimoto (2012).

Despite these advances, high-speed AFM system development has drawn great attention because the scans using a raster scanning method, in particular in commercial AFMs, can often take several seconds or minutes. The research on AFMs has been fuelled by the high performance nano-positioning devices and sensitive force measurement mechanisms with high bandwidth (Ando et al. 2013). Alternatively, a new concept of non-raster scanning was suggested by Marinello et al. (2009) to image the sample-substrate along a free path instead of the common raster pattern. Different non-raster scanning schemes were developed including: Lissajous pattern based scanning trajectories (Tuma et al. 2012), local specimen contour tracing methods (Andersson 2007, Zhang et al. 2015), etc.

2.2.2 Shear Force Microscope

The shear force microscope (SFM) is a special kind of force microscopes invented by Betzig et al. (1992). The innovative concept is to use a vertically oriented probe (used instead of the horizontal cantilever in typical AFMs) measuring the shear force between the probe (or cantilever) and the sample-substrate (Figure 2.3). In an SFM, the probe is horizontally excited usually with a sinusoidal excitation signal. The probe tip is brought above the sample-substrate, in the proximity of the sample. The shear-force interaction varies as the probe-sample separation changes. As a result, the varying shear force changes the quality factor of the probe with respect to the distance between sample and probe. Hence, the amplitude and the phase of the probe oscillation are consequently changed. The shear-force interaction is measured by sensing the cantilever oscillation using a position sensitive detector (Betzig et al. 1992). The advantage of the SFM is that it can use small excitation levels and much softer cantilevers which has allowed high-resolution scans. For instance, the SFM is able to scan nano-spheres with the smallest diameter of 19 nm (Betzig et al. 1992).

Early work has shown that the shear-force interaction is caused by a mixture of various forces, like electrostatic forces, visosity forces, etc. (Davy et al. 1998). That fact is an important basis of the work here, as it allows to create deeper understanding of the material of the sample surface. This will be later discussed in Chapter 5. James et al. (2001) is possibly the first to use the term of Transverse Dynamic Force Microscope as an alternative to SFM. Particularly, the term 'transverse' indicates the force measurement along the direction perpendicular to the vertical probe and parallel to the sample-substrate surface, while the term 'dynamic force' indicates the dynamic combination of various atomic forces (James et al. 2001). At about the same time, the research of Antognozzi et al. (2001) proposes that the interaction force at the excited probe is limited to a confined water film. This confined water film exists over the sample-substrate in liquid/ambient environments. This is reconfirmed by Ewing (2006) where a thin confined water layer is discovered existing over insulating materials. In an ambient environment, the investigation of Carrasco et al. (2012) proves the extremely thin layers of water molecules exist over the metal surfaces (Carrasco et al. 2012, 2013). The discovery of the confined water film additionally shows that the probe of an SFM in fact interacts with the ordered layers of water molecules as described by Antognozzi et al. (2001) (Figure 2.3c).

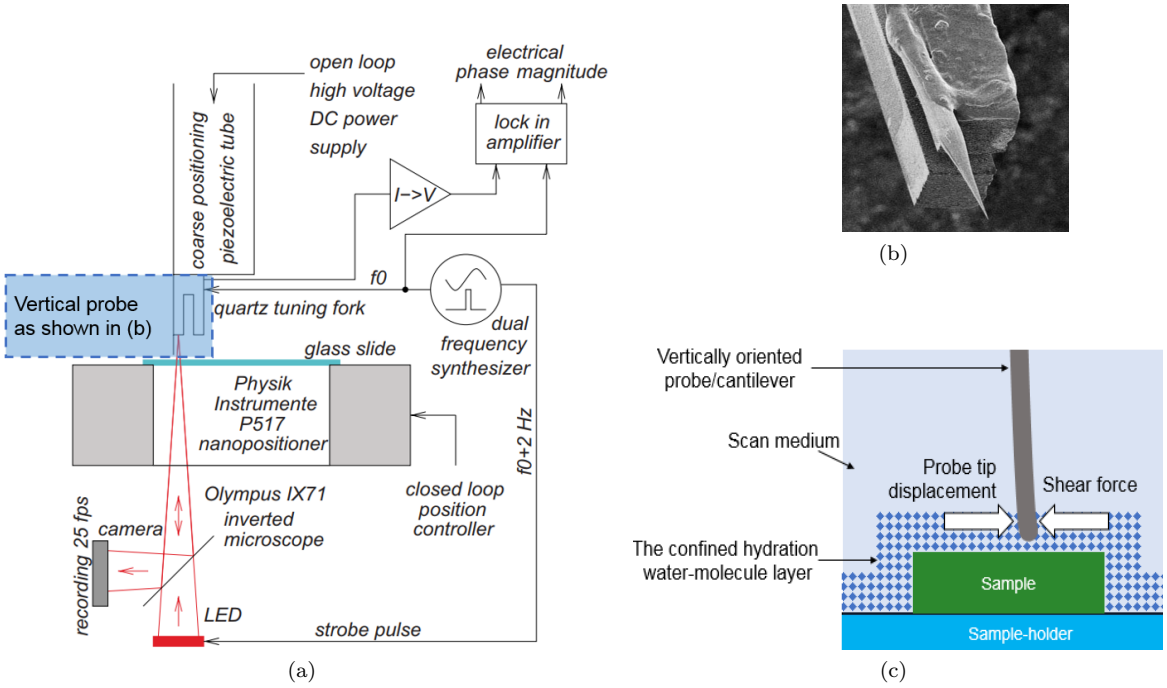

FIGURE 2.3: Working principle of an SFM: a) a typical set-up of an SFM with tuning fork in (Sandoz et al. 2008); b) an SEM image of a tuning fork loaded with an SFM probe (Sandoz et al. 2008); c) a schematic of a probe in a SFM interacting with the confined water layer.

In principle, therefore, SFMs can benefit from the use of the thin confined hydration water layer. If the probe-sample separation is properly controlled, the probe can remain in the water layer and avoid touching the actual specimens, hence, the damage to the sample-substrate is mitigated in scans. This advantage is exploited in this thesis to create a novel non-contact scanning mode. In contrast, in a typical AFM, the vertical interaction between the cantilever-tip and the specimen might lead to possible damage of delicate specimens (in either the contact mode (Thormann et al. 2010) or the tapping mode (Vahdat & Carpick 2013)). An example of scanning delicate specimens will be given in Chapter 6. Another significant advantage of SFMs is a result of using the vertically oriented probe/cantilever. Similar to typical AFMs, the probes in SFM have to be sufficiently soft to guarantee high sensitivity to low atomic forces. In SFM scans, the excited probe/cantilever has high stiffness in the vertical direction, while the stiffness can be low to sense the small shear force in the horizontal direction. Thus, the SFMs genuinely avoids the 'jump-effect' (Lee et al. 2002), which is, in typical AFMs, a consequence of the required low-cantilever-stiffness in the vertical direction and the attractive atomic forces between the horizontal cantilever and specimens, e.g. the van der Waals forces.

The sensing bandwidth of the shear force in SFMs is mainly determined by two factors: the probe/ cantilever oscillation frequency and the sensing mechanism detecting the cantilever's dynamic deflection. The first SFM measured the oscillation of an optical fibre, i.e. the probe, which has to retain a constant shear force interaction between the fibre and the sample. Laser light is vertically transmitted through the optical fibre and creates a light field at the tip of the fibre, when the aperture of the fibre-tip and

the laser wavelength are carefully chosen. The light is then magnified and then projected onto a position sensitive detector. The SFM achieves a shear-force sensing bandwidth of about 10 kHz, limited by the fibre excitation frequency at 123 kHz and the employed lock-in amplifier. Moreover, this sensing mechanism strongly relies on the near-field optics, depending on the aperture of the optical fibre and the laser wavelength. Hence, as reported by Grober et al. (1994), the needed large aperture of the optical fibre results in a large tip geometry, and subsequently a limited imaging resolution of 12 nm in the horizontal plane. To eliminate this limitation, the tuning fork is first introduced to the SFM developed by Karrai & Grober (1995). In this SFM, the probe is attached to one prong of the tuning fork, of which both prongs are piezo-electrically coupled. The dynamic deflection of the probe changes the piezoelectric potential between the two prongs, i.e. the varying potential is a measure of the shear interaction. Significantly, the sensing mechanism allows the free choice of the cantilevers' material in SFM, i.e. this eliminates the limitation of using optical fibres as the sensing probe. The sensing mechanism is then widely used in SFMs for surface topography scans (e.g. DNA imaging (Ruiter et al. 1997), the viscosity and elasticity of the hypothetical third body filling the tip-sample gap (Karrai & Tiemann 2000, Antognozzi et al. 2001) using complex off-line computation methods). In the work of Mühlschlegel et al. (2006), the probe is designed to be attached to one prong of a tuning fork by a preload pressure, i.e. the imaging quality was significantly improved by avoiding the uncertainty caused by cautious gluing of the probe on the tuning folk. However, the sensing mechanism using a tuning fork has to oscillate the cantilever at the harmonic frequency of the tuning fork, i.e. the potential sensing bandwidth of the SFMs is limited to the excitation frequency often slower than 33 kHz in recent research (La Rosa et al. 2005, Mühlschlegel et al. 2006, Sandoz et al. 2008, Park et al. 2014). To be free from the tuning fork, a split photodiode is used to detect a laser beam reflected on the probe surface to detect the probe deflection (James et al. 2001). In 2004, Iwata et al. (2004) suggested to focus a wide laser beam on the tip of a vertical probe excited at its resonance of 20 kHz, i.e. the shadow of the probe tip is detected for shear force measurement. Recently, the shear force interaction between a nanowire and the sample achieves a sensing bandwidth of 10 kHz by measuring the reflection of a focused laser beam with a diameter of 300 nm (De Lépinay et al. 2017). Specifically, a 200 nm wide nanowire is used as the probe in the application.

Cantilever-sample separation distance control, also named as shear force feedback control, in SFM systems has been relevantly designed according to the sensing mechanism. The measurement of the interaction shear-force are often detected by an lock-in amplifier in SFMs (Karrai & Tiemann 2000, James et al. 2001, Sandoz et al. 2008). Hence, Phase-locked-loop (PLL) based control is commonly chosen, such as the research of Mühlschlegel et al. (2006) and Sandoz et al. (2008). Also, the control scheme, the standard feedback control implemented by customised filters, has been applied to amplitude modulation (Iwata et al. 2004) or phase modulation (Ruiter et al. 1998). So far, the articles in the SFM research community mainly focused on methods to measure the cantilever tip oscillation, i.e. as an indirect measurement of the interaction shear-force. There has been no known research on the dynamics of the shear-force interaction dynamics in the vertical direction and only few control applications (Antognozzi

et al. 2003) in the field of SFM systems until the work described in this thesis.

2.2.3 Transverse Dynamic Force Microscope Research at Bristol

The initial research on shear force microscopes at the University of Bristol has been conducted by the research team of Miles and Antognozzi using an alternative sensing scheme (Antognozzi et al. 2000). In the beginning, their sensing scheme uses a cylindrical probe to interact with the sample-substrate. A laser is horizontally projected on the probe surface and the reflection is then detected by a photo-detector to obtain the probe oscillation signal. This sensing mechanism avoids the limitation of using a tuning fork and is used in the SFM scans by James et al. (2001), where the term of Transverse Dynamic Force Microscope (TDFM) is employed for the first time to distinguish the new microscope and its sensing system. Following this work, significant research results have been obtained for the new TDFMs in Bristol (such as the research of Humphris et al. (2002) or Antognozzi et al. (2002)). For instance, using this TDFM set-up, it was possible to etch a solid magnesium-aluminum-hydroxide-silicate surface through a charging process creating nano-patterns (Valdrè et al. 2012). In this work, the organised nano-patterns can guide DNA deposition along predetermined directions without the need of a chemical etching process.

The force sensor of Bristol's TDFMs was a cylindrical probe initially. At the beginning, the TDFM research focused on the principles of the probe oscillation and scanning applications (Antognozzi et al. 2000, Humphris et al. 2002). In 2002, it illustrated the TDFM's capability to analyse the stiffness of the particle surface at a single molecule level (Humphris et al. 2002). In the same year, the TDFM was first applied to imaging of DNAs by Antognozzi et al. (2002), indicating the great potential of the TDFM in the field of biology due to the nature of true non-contact imaging at high resolution. In 2003, the imaging quality of the TDFM was significantly improved by introducing a quality factor control scheme (Antognozzi et al. 2003). Then, many studies used the TDFM to comprehend the surface properties and the activating-mechanism of DNAs (Valdrè* et al. 2004, Antognozzi et al. 2006, Amrute-Nayak et al. 2008). However, at that time, the probe in TDFMs had to be wide enough to allow laser reflection and together with the circular cross-section the spring constant of the cantilever was limited to high values. This created a definite lower bound of the sensitivity to forces. For a precise measurement of the probe deflection, the laser beam had to be well aligned to focus on the very end of the probe, which was very difficult to achieve due to the vertically mounted orientation of the probe.

In 2008, Antognozzi developed a novel evanescent field based sensing mechanism with an extremely high sensitivity of 0.17 pN/nm in the TDFM as shown in Figure 2.4 (Antognozzi et al. 2008). A laser is projected to a high numerical aperture (N.A.) lens to create a total internal reflection at a transparent sample-holder slide. As a result, an evanescent field is generated above the sample-holder surface. The probe is manufactured to be a cantilever being excited by a dither piezo-actuator. The cantilever reflects some of this light from the evanescent field and the emitted light is projected to a photo-detector. The cantilever oscillation produces a change of the reflected evanescent field, which is sensed by the

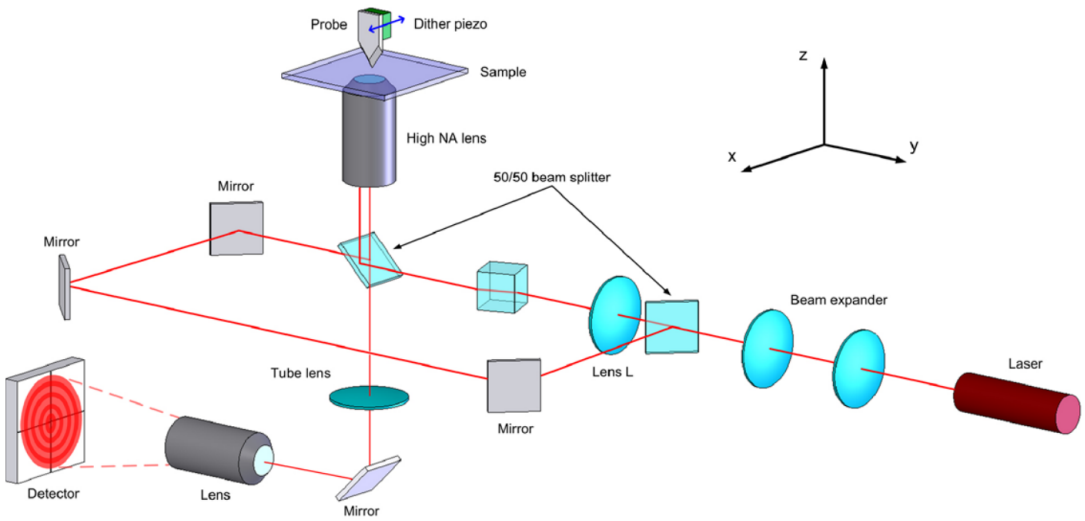

FIGURE 2.4: The schematic presents the TDFM set-up, as invented by Antognozzi et al. (2008).

photodetector. Therefore, the shear-force interaction can be evaluated by the cantilever oscillation using PLL devices or lock-in amplifiers.

In the new sensing set-up, the force sensor was selected as a vertically oriented cantilever with non-symmetric rectangular cross-section, creating a lower spring constant and reducing some of the issues of the laborious alignment of the laser path towards the probe-tip. This gave the advantage of an improved sensitivity since a cantilever can be manufactured with less stiffness than any other force microscopy probes (Vicary et al. 2011). Particularly, Vicary et al. (2011) succeeded to micro-manufacture ultra-soft Si_3N_4 cantilevers achieving a spring constant of $\sim 10^{-5}$ N/m for TDFMs. Consequently, the cantilever can be tailored to different applications requiring specific mechanical properties, such as spring constant or resonant frequency. Also, the thermal excitations and axis rotation along the x/y direction in the horizontal plane can be determined by the geometry of the cantilever's cross section. The sensing mechanism also benefits the imaging quality in liquid environment. The new evanescent field mechanism works well for thin or transparent specimens, while the previous laser reflection mechanism may be difficult for specimens in liquid medium that causes unexpected diffraction in the liquid droplets.

The novel force sensing mechanism developed at Bristol is built up by an ultra-soft cantilever within an evanescent field detecting the cantilever motion. The great advantage is an improved sensitivity to the shear interaction at pN level with customisable cantilevers in contrary with other SFMs. The shear force interaction within the confined water layer was first studied for the new TDFM in a liquid environment (Ulcinas et al. 2011). Later, the TDFM has been applied to various research problems in the biology field. For instance, the TDFM was used to study the molecular motor protein kinesin-l to understand a biomolecular motors' mechanical characterization (Scholz et al. 2011). The TDFM helps to detect the protein conformation at the bacterium surface by measuring the growth of the cell surface (Agnew et al. 2011). Specifically, the cantilever is horizontally translated to touch one side of the cell, and the change of the contact position is taken as the difference of the cell dimension. In 2012, two methods for DNA scans

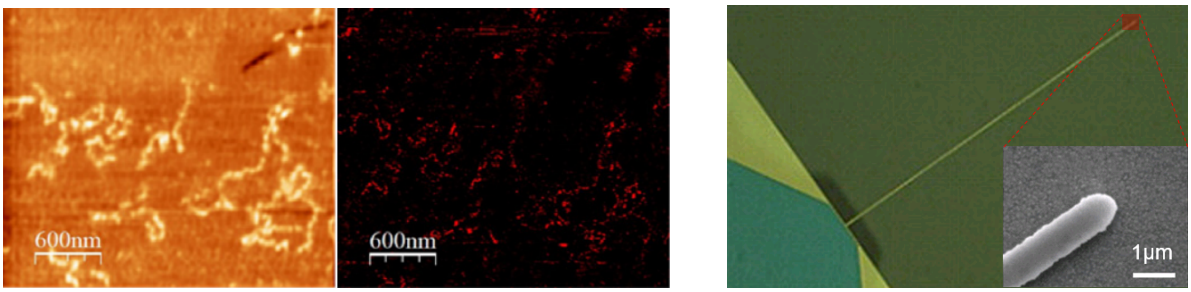

(a) (b)

FIGURE 2.5: Demonstration of scanning results and a cantilever in the novel TDFM: a) DNA scans using the two scanning modes suggested by Harniman et al. (2012) using the TDFM; b) The geometry of a micro-fabricated cantilever, where the photo of the cantilever was zoomed in by an SEM, for the TDFM systems (Vicary et al. 2011).

in the TDFM were achieved by Harniman et al. (2012) (see Figure 2.5a): 1) the TDFM uses a phase-locked loop for a constant height over the sample-substrate surface (left); 2) an optical feedback method kept the cantilever at a constant height away from the sample-holder and the top surface of the DNA is imaged by the phase signal measured by a lock-in amplifier (right). The first scan mode is a typical non-contact scanning method, called the 'force feedback' mode using the measurement of the shear force interaction, in TDFMs. However, the specimen height for the non-contact mode had to be practically limited to approximately 3 nm, because the employed phase-measurement sensing mechanism results in a sensing range of $\sim$2 nm. In contrast, the optical-feedback scan mode regards the cantilever-sample interaction, i.e. the phase, as a topographic measurement. For this second method, the feedback-loop uses the evanescent field strength as a measure of height to the specimen holder and it is therefore independent from the shear-force interaction. The measured signal for scanning in this case was the phase which is again only available within a $\sim$2 nm imaging range above the top of the specimen in water environment. Thus, the cantilever tip has to remain within that range and has to be carefully positioned at an appropriate height above the sample-substrate in scans. The other constraint is that the specimen height has to be a priori-knowledge before scans to avoid collision between the cantilever and the specimens.

So far at Bristol or elsewhere, the dynamics of the vertically positioning system for the cantilever have been insufficiently investigated and characterised in terms of positioning control and real-time estimation of the shear-forces. For that reason, the control schemes of the TDFMs so far have been used only with conventional proportional-integral control algorithms for the relevant applications (Antognozzi et al. 2008, Harniman et al. 2012, Fletcher et al. 2013).

A significant impact was the imaging of nano-patterns on nano-sphere particles which were made up from self-assembled proteins (Fletcher et al. 2013). The hollow particles were so fragile that the observation of the nano-patterns is impossible for conventional AFMs. More results will be seen in Chapter 6 demonstrating the improved imaging capability of this research. In the work of Tang et al.

(2013), to understand the mechanisms of molecular uptake into micro-droplets, the cantilever in the TFDM was used to measure the varying charge ratios of different single micro-droplets. However, the utilisation of the previous evanescent field based detection mechanism limits the applications of the new TDFM set-up. In detail, the sample-holder needs to be transparent to generate the evanescent field. Additionally, the specimens for topographic imaging have to be sufficiently small on a few hundred nanometres scale to avoid significant influence of the specimens on the evanescent field. In the following, the investigated TDFM research considers a novel set-up using the evanescent field sensing mechanism for scans, study of specimen topography, and real-time shear-force analysis.

2.2.4 Recent Research on TDFM

In the last five years, the TDFM with optical feedback mode was developed to achieve high-speed scans at Bristol. Particularly, the TDFM achieved to track metal nucleation in real-time for the first time (Harniman et al. 2017). Differently from previous set-ups, the TDFM used a high-speed horizontal stage for a fast scanning speed in order to record the continuous change of the imaging surface. The TDFM was in optical feedback mode to scan at a constant vertical position above the sample-holder slide. As the metal nucleus appeared and grew on the sample-holder, the topography of the nucleus was gradually bulged up at the scanning height. The used high-speed stage with a resonance at 4 kHz was driven by periodically forward and backward motion in a fast-scan axis in open-loop without any control scheme applied.

As discussed by Harniman et al. (2012), the scanning speed of the TDFM is physically limited by the horizontal positioning stage. The ultra-soft cantilevers, which can be tailored to have a very high resonance up to but not limited to 1.66 MHz (NuNano Ltd. 2018), no longer constrain the scanning speed in the TDFM. Motivated to improve the scanning speed, a research team led by Herrmann at Bristol optimised the TDFM nano-positioning stage pushing the mechanical resonance to over 6 kHz (De Silva et al. 2017). The novel positioning stage used laser-interferometers as the horizontal displacement sensors achieving a closed loop-control frequency of 1.73 kHz. This novel design guarantees accurate nano-positioning, i.e. reliable TDFM imaging, in contrast to previous scans using the positioning stage in open-loop (Harniman et al. 2017). Research has been ongoing to use the high-precision stage for practical scans.

Simpson et al. (2015) have used the evanescent field based TDFMs to measure the optical force density of an evanescent field and to adjust the optical force applied to particles caused by the evanescent field. Later, Antognozzi et al. (2016) achieved to measure the momentum of light in an evanescent wave by using the cantilever in the TDFM. These have shown that the TDFM is a precise tool to measure direction-resolved optical momentum and forces on sub-wavelength scales. Also, the TDFM was experimentally applied to antimicrobial resistance research (Antognozzi 2017) as a consequence of the work by Vicary et al. (2011). In this work, the cantilever with an anti-microbial drug attached to its tip was placed at

the side-wall of a living bacteria cell. Hence, the reaction of the bacteria cell to the antimicrobial drug was detected by the variation of the interaction force between the cantilever and the cell side surface.

The advances in the TDFMs only permitted to analyse the interaction force by processing the measured cantilever deflection offline. Thus, a principal research (Nguyen et al. 2015) proposed an estimation scheme to obtain the shear-force in real-time based on the cantilever modelling methods proposed by Antognozzi (2000). Nguyen et al. (2016) within Herrmann's team at Bristol presented an algorithm to estimate the shear force interaction using a sliding mode observer. The force estimation performance was assessed in a separate PC with practical cantilever oscillation data at single surface points. In contrast, Chapter 5 will present a force estimation (or reconstruction) method with completely real-time capability. Also, its implementation for full imaging scans will be introduced in Chapter 5. It will be seen that the developed feature allows the TDFM to obtain important additional material information of the whole scanning regions of specimens (see the results in Chapter 5 and 6) in real-time at high speed. Therefore, the developed TDFM is expected to gain further impact in the field of physics, material, biology, and so on. For instance, the reconstructed real-time interaction force measurement can be used for designing a direct force-feedback control for scans in contrast to current phase feedback control techniques (Harniman 2013, Harniman et al. 2012). Significantly, the viscosity and the elasticity over the scanned sample surface can be reconstructed by using the real-time force measurement, i.e. it is possible to investigate the sample surface properties to understand the molecule mechanism/optical momentum in real-time. Knowledge of the material properties in biological specimen can be vital to relevant studies, e.g. viral infections (Guerra et al. 2017), mechanical property investigation of soft material (Payam et al. 2015), early diagnosis of cancers (Ding et al. 2015). Hence, this PhD research produces an important basis for the necessary practical techniques for these purposes.

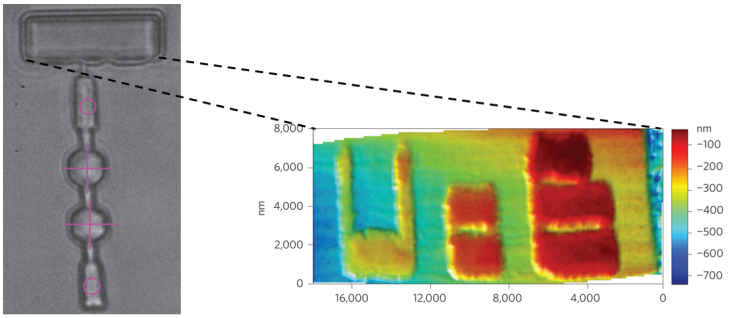

FIGURE 2.6: A TDFM-like microscope that is controlled by optical tweezers in 3D in vacuum (Phillips et al. 2014). The particle-assembled probe (left) is controlled at two (crossed) positions and the vibration of the probe is measured by detecting the motions at circled positions. A calibration sample (scanned data in 3D on the right) was scanned in vacuum as the left (SEM image) shows.

Recently, a special TDFM-like microscope was developed to work in a vacuum environment using optical tweezers as shown in Figure 2.6 (Phillips et al. 2014). A probe was constructed by two microparticles manipulated by optical tweezers, which trap particles using densely focused laser beams. A low force was applied by the optical tweezers on the probe to contact the sample surface. The probe deflection

caused by the contact force is detected by the relative displacement of the micro-particles. Unlike all SFMs, only Brownian motion drives the probe to move along each scanning line.

2.3 Control solutions and Estimation Schemes in AFMs

This section presents the signal processing and control system integration solutions, control schemes, and estimation algorithms in the AFMs. The review discusses the advantages and the limitations of the state-of-the-art techniques in AFM community. This will clarify the uniqueness of the control and estimation approaches presented in this thesis.

2.3.1 System Integration Solutions

The sensing mechanism of the cantilever/probe deflection is fundamental for the interaction force measurement of TDFMs/AFMs (Giessibl 2003). The deflection of the cantilever is often directly used as the force measure in the contact mode (e.g. the AFM research of Schitter, Stark & Stemmer (2004)). However, in the dynamic mode AFMs, the rapidly changing deflection is not a true reflection of the interaction force so that the interaction force is usually an indirectly measured signal (Giessibl 2003), including: tapping mode AFMs (Sulchek et al. 2000, Kodera et al. 2006), Bristol's TDFMs (Antognozzi et al. 2000, James et al. 2001), etc. The interaction has to be measured by the alteration of cantilever/probe oscillation, i.e. change of the amplitude, phase, or frequency due to the interaction. The common solution is to employ a lock-in amplifier or a PLL unit to calculate the amplitude or the phase shift in comparison to a reference signal (Giessibl 2003, Kodera et al. 2006, Stark et al. 1999). In a tapping mode AFM, the frequency of the cantilever oscillation is measured by using an electronic differentiator or a phase shifter to process the cantilever oscillation signal (Sulchek et al. 2000). Albrecht et al. (1991) suggested that the cantilever deflection frequency can be measured by digital frequency counters, gated timers, or other analogue demodulator circuits.

The sample in general is placed on an x-y-z scanner (Sandoz et al. 2008, Ando et al. 2013) or on an x-y planar stage (Antognozzi et al. 2000). The horizontal in-plane motion is often presented by two measurements, the displacement along the x-axis and y-axis, indicating the coordinate position to locate the force measurement in the horizontal plane (Figure 2.7). The electromechanical designs for the displacement measurements can be realised in various ways: laser displacement sensors (Guo et al. 2015), laser interferometry (Eves 2009), integrated piezo-resistance (Sun et al. 2008), linear variable differential transformer (Sebastian & Salapaka 2005), giant magneto-resistivity (Tuma et al. 2014), and most commonly capacitance sensors (Kim & Gweon 2012). Regardless the sensing mechanism of this relative motion, the positioning signals are always directly measured signals from the sensors in contrast to usually indirect measurements of atomic interaction forces.

The dynamic mode AFMs and all TDFMs generally use a form of actuation to excite the cantilever/probe for force interaction. The most straightforward mechanical design is to attach a piezo-actuator to the cantilever to provide demanded excitation (Antognozzi et al. 2008, Ando et al. 2013). In early TDFMs, the vertical probe/cantilever is generally attached to a prong of a quartz tuning fork, such as the research of Sandoz et al. (2008). A clear disadvantage of these actuation schemes is that the actuators require a relatively large set-up space compared with the small cantilevers. Thus, a complex fabrication procedure was developed to integrate a piezo-actuator and the oscillation sensor on a small cantilever (Shibata et al. 2004). A research of Pedrak et al. (2003) demonstrated an alternative solution of micro-fabricating a thermal bimorph actuator on the cantilever achieving a thermally-driven oscillation at 716 kHz. Lee et al. (2000) used a planar coil that was fabricated for the cantilever, i.e. the cantilever was electro-magnetically actuated by creating a coil current through an external magnetic field. On the other hand, there is no need of any particular mechanical component to actuate the cantilever in contact mode AFMs. (Note that contact mode AFMs do not require the cantilever to be excited.)

The mechanical actuation components of AFMs sometimes use a single positioning unit to control the relative motion along three axis as shown in Figure 2.7. The vertical z-axis presents the atomic force measurement direction along the force sensor toward the sample, and the x/y-axis positioning permits force sensing at various points of the sample-substrate. In this layout, the positioning unit carries either the force sensor (e.g. the set-ups of El Rifai & Youcef-Toumi (2007) and Ruiter et al. (1998)) or the sample holder (e.g. the systems developed by Schitter, Stark & Stemmer (2004) and Sandoz et al. (2008)) providing relative displacement. The positioning unit is often implemented by a piezo-tube (El Rifai & Youcef-Toumi 2007) or a specially designed 3-axis scanner (Schitter et al. 2007). In contrast to many other probe microscopes, the TDFM with the evanescent field based sensing mechanism has to implement the 3D positioning feature by two separate components (Antognozzi et al. 2008, Harniman 2013): a z-axis actuating unit and an x-y planar positioning unit. The cantilever, i.e. the force sensor, is attached to the z-axis actuating unit to realise feedback control of the cantilever-sample interaction. The x-y positioning unit carries the sample-holder to create raster or non-raster trajectories for sample topography scanning. This two-positioning-unit layout of the TDFM permits to test different sensor/actuation schemes for the vertical z-axis or horizontal in-x-y-plane positioning.

In this thesis, the research is only concerned with the control and estimation algorithms for the positioning in the z-axis and the cantilever sensing of the TDFM set-up, which is based on the evanescent field sensing mechanism. The cantilever is excited by piezo-actuators for shear-force sensing and the cantilever deflection sensing set-up is similar to Figure 2.4. The z-axis actuation uses two piezo-actuators allowing coarse and fine positioning in the vertical direction. For enabling scanning, it is vital to obtain at first a robust sensing mechanism and positioning performance in the z-direction. Hence, there has been less interest in the control of the horizontal positioning system. Thus, the motion in the x/y-directions is realised by a commercial horizontal positioning stage, which integrates capacitive sensors, piezo-actuators, and built-in controllers through a commercial positioning stage. One future research will involve a fast,

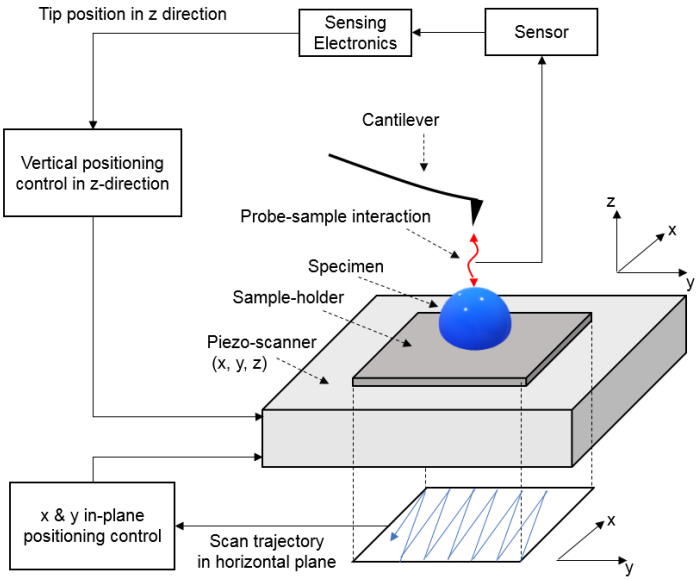

FIGURE 2.7: A typical three axis control strategy of AFMs: In detail, the cantilever is used to sense the interaction with sample-substrate. The measured interaction is taken as the topographic data in vertical direction along z-axis. The sample-substrate is carried by the piezo-scanner that moves along a raster scanning trajectory along the x&y axis in the horizontal plane.

high precision stage (De Silva et al. 2017), in order to further enhance the TDFM scanning performance.

The control hardware to realise the control solutions crucially determines the performance of an AFM. Both analogue and digital regimes have been widely used as control hardware in AFMs. The first AFM was controlled by two pure analogue circuits: one feedback circuit is used to control a scanner providing horizontal relative motion between the cantilever-tip and the sample; the other is designed to keep a constant tunnel current between the cantilever-tip and a scanning tunnel tip (Binnig et al. 1986). Before 2000, analogue circuits have been commonly employed to utilise control of AFMs (Grober et al. 1994, Ruiter et al. 1997). In recent years, novel Field Programmable Analog Array (FPAA) technology was applied to AFMs (Schitter & Phan 2008, Yong et al. 2013). The FPAA based control solution implements the controllers as combinations of analogue filters without the need to consider the sampling frequency, which is a vital design requirement in digital control solutions. The FPAA based control solution has no issue with control signal inaccuracy caused by the quantisation error, which would happen during analogue-to-digital (A/D) conversion and must be considered in digital control designs. However, the FPAA based control solution is limited by the type and number of available analogue filters. In contrast, the control hardware based on programmable digital circuits, e.g. Digital Signal Processor (DSP) or Field Programmable Gate Array (FPGA), allows to realise various complex control algorithms while having to deal with quantization and sampling rate constraints.

The development of integrated circuit technology has popularised digital control solutions to implement controllers of AFMs. In 1991, a digital control solution was developed for the stable positioning control of the tip-sample separation in open-loop and later published by Wong & Welland (1993), whereas

AFMs with analogue control strategy had an issue of signal drifting. The digital hardware solution has also provided casual users a friendly programmable environment for the control programme implementation in AFMs (for example the AFM developed by Baselt et al. (1993)). Most importantly, digital control solutions used microprocessors (Lee et al. 2002) and DSP slices (Ando et al. 2001, 2002) enabling convenient modification of the control programmes on off-the-shelf prototyping hardware. Hence, advanced controllers can be tailored to different design requirements without altering the control hardware. In recent time, the FPGA technology has been considered as the most powerful digital control hardware for AFM development (Huang 2013, Jerez et al. 2014, Soltani Bozchalooi 2015). The FPGA based control solution allows to customise the control programmes running at a few Megahertz rate, i.e. advanced control algorithms are implementable at high bandwidths. The other significant advantage of FPGA based control solutions is the ability to dynamically reconfigure the control parameters. Thus, it allows ad-hoc tuning of a controller to improve the control performance or immediately stopping the control to ensure the instrument safety. Hence, an FPGA based control solution was selected for the work in this project.

2.3.2 Control Algorithm Developments

Motivated to improve the scanning quality and speed of AFMs, control engineers (e.g. Schitter et al. (2001), Schitter, Stemmer & Allgöwer (2004), Abramovitch et al. (2009), Ando (2012)) developed various algorithms for the x-y in-plane positioning and the z-axis sensing and positioning. The following focuses on the state-of-the-art control schemes applied to the z-axis sensing and positioning, i.e. the atomic force interaction. The advantages and disadvantages of the existing control algorithms in the AFM domain are considered with respect to practical issues of the TDFM control.

The common control schemes of AFMs are proportional–integral (PI)/proportional–derivative (PD)/ proportional–integral–derivative (PID) feedback control (e.g. the work of Ando et al. (2001) and Harniman et al. (2012)). It is known that PID control is a mature, easy, and intuitive controller even for z-axis control in varying environmental conditions and changing cantilever mechanical properties in AFMs. PI/PD/PID control performance is often visually evaluated and manually optimised by the operator during scans. Motivated to improve the convenience to use AFMs, automated PID tuning algorithms were developed for optimal PID control performance using an trial-and-error method (Kohl et al. 2016) or simple frequency shaping method (Abramovitch et al. 2009) (as demonstrated in Figure 2.8).

It is noted that the performance of a PID controller is algorithmically limited by its simple frequency-shape. Therefore, a special PID control method was proposed by Ren & Fang (2013) providing the ability to shape the closed-loop response in different frequency ranges. In detail, the z-axis plant dynamics were split into various frequency ranges by low-pass/bandpass/high-pass filters and each controlled by a specific a PID controller. Hence, the z-axis control performance can be optimised by tuning each PID controllers. There are some other algorithms, particularly fuzzy control (Payam et al. 2011) or chaos control (Arjmand

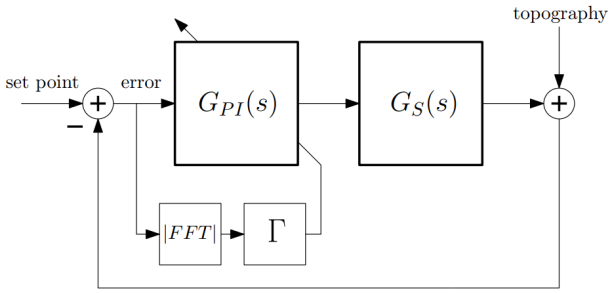

FIGURE 2.8: Block diagram of a semi-automatic tuned PID feedback control scheme (Kohl et al. 2016).

et al. 2008), developed for simple feedback control structure. These control algorithms (Payam et al. 2011, Arjmand et al. 2008) were only assessed in simulations and had low control performance with settling time longer than 0.01 s.

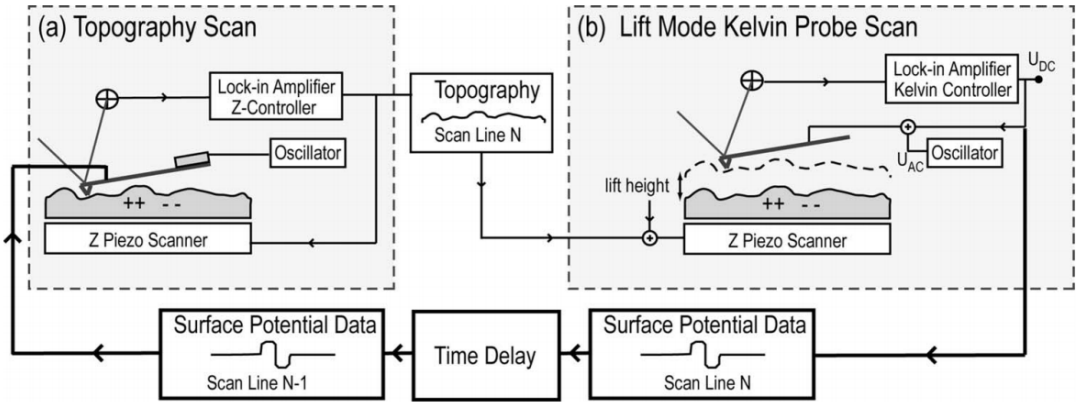

FIGURE 2.9: Schematic of a topography feedforward control for an AFM (Ziegler et al. 2008).

To minimise electrostatic forces during scanning, the sample topographic data of a raster scanning line in the forward direction was applied as the composition signal to the scan in the backward direction (Figure 2.9 (Ziegler et al. 2008)). Similarly, repetitive control (RC) can estimate the scanning sample topography according to previous raster-scanned lines (Necipoğlu et al. 2010), i.e. the z-axis controller used a feedforward compensation signal obtained from the sample profile measurement. However, this pure RC feedforward scheme only uses historical data without counting in any current sample topographic information. In order to react to current control errors, the RC feedforward control can be extended in cooperation with a PI feedback controller for enhanced performance (Necipoglu et al. 2011). Iterative learning control (ILC) is an alternative to compensate for similar sample topography resulting in a reduced control error/interaction forces in scans. For instance (Tien et al. 2005), an ILC provides the feedforward compensation signal for a PI feedback control, however, with a long convergence time (60 steps for each sample-substrate) of the ILC. An improved ILC working with a PI feedback controller was suggested by Tien et al. (2005), which has a fast ILC converging time at a bandwidth of 1 kHz. Another method to provide the feedforward signal is the utilisation of surface observers. For example (Fujimoto & Oshima 2008), the z-axis control signal used the PI feedback control signal and the sample topography

compensation signal that was computed by a surface observer.

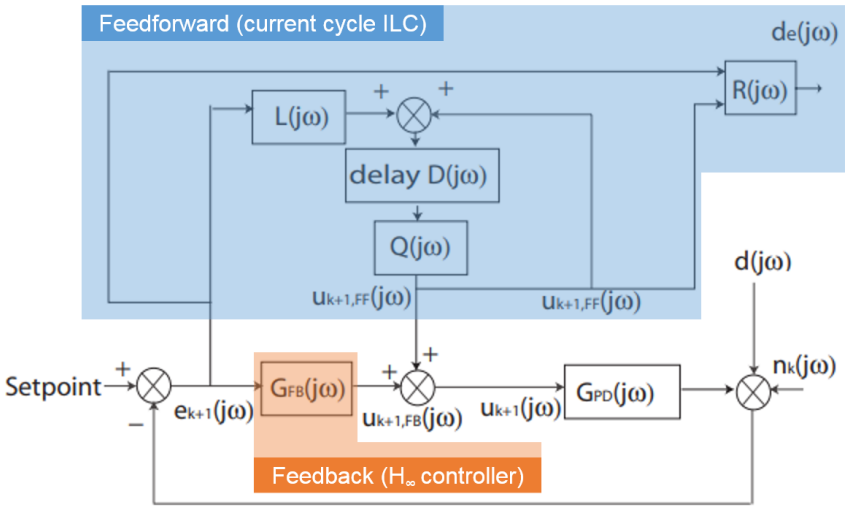

FIGURE 2.10: Block diagram of a feedforward and feedback control scheme for an AFM (Wu et al. 2009).

Advanced control algorithms, e.g. H_∞ or adaptive control, also have been applied to AFMs (Schitter et al. 2001, 2003, El Rifai & Youcef-Toumi 2007, Zhang et al. 2010) to enhance control performance in AFMs, i.e. to allow for higher robustness and faster scanning speed. In 2001, Schitter et al. (2001) suggested to employ model based control designs, particularly H_∞, because it was designed for the complete dynamics of the AFM in contrast to an ad-hoc tuned PID control algorithm. The H_∞ feedback control results in a high control bandwidth with the great advantage of robustness against cantilever model uncertainties (Schitter et al. 2001). Later, dual H_∞ control was developed by Schitter et al. (2003) which consisted of a H_∞ feedforward signal compensating the historical scanned data and a H_∞ feedback signal reacting to current control errors. Moreover, a current cycle ILC decoupling the effect of high speed x/z-axis correlation was developed as Figure 2.10 shows (Wu et al. 2009). The current cycle ILC in cooperation with an H_∞ feedback controller achieved 64 Hz scanning rate, which was 8 times of the scanning speed employing a typical PI feedback control in the same set-up. Also, adaptive control algorithms were developed for AFMs to gain the robustness to model uncertainty and system disturbances (El Rifai & Youcef-Toumi 2007, Zhang et al. 2010). However, the work of Zhang et al. (2010) was only assessed in simulation and the experimental results of El Rifai & Youcef-Toumi (2007) only performed a long settling time of 0.02 s.

2.3.3 Force Reconstruction Algorithms and Applications

Particularly, in TDFM research, the modelling methodology of probes/cantilevers has been proposed by Antognozzi (2000) to enable the offline reconstruction of the shear force. Work of Herrmann's team at the University of Bristol (Nguyen et al. 2015, 2016) proposed a two-inputs-single-output model of the cantilever: one of the inputs is the known cantilever excitation, the other input is the unknown interaction

shear force at the tip of the cantilever, and the output is the measurable cantilever oscillation motion in the complex scan medium.

The interaction force reconstruction in typical AFMs is often carried out by offline processing the cantilever oscillation or deflection (Payam et al. 2015, Labernadie et al. 2014, Ding et al. 2015). Most of the research reconstructs the atomic-forces in the way, which processes recorded cantilever deflection/oscillation data via statistical computation methods. Especially, Sahin et al. (2007) suggested a complex offline signal processing method to reconstruct the interaction force in tapping mode AFMs. The force reconstruction takes about 250 μs using a discrete Fourier transformation analysis to detect the torsion motion of a 'T-shape' cantilever. The Fourier transformation analysis was applied to the average of at least 12 periods of the cantilever oscillation for an accurate computation, i.e. the measurement mechanism has a bandwidth (reaching 4 kHz at best in (Sahin et al. 2007, Sahin & Erina 2008)) no larger than the 1/12 of the exciting cantilever harmonic frequency. This method fundamentally relies on the specially designed 'T-shape' torsion harmonic cantilever. Considering the complexity of the method, it was implemented on a PC (Sahin et al. 2007) and it would not be easily possible to implement this at a higher sampling rate. Hence, an alternative observer based approach will be presented in this thesis allowing real-time detection without further averaging for cantilever resonances well above 200 kHz.

Various observers have been applied to AFM systems previously. For example, an observer (Besançon et al. 2008) was used to determine the probe loss areas in images and the unknown forces affecting the dynamics of a cantilever (De et al. 2006). A linear observer is developed by Sebastian et al. (2003) to estimate the tapping-mode cantilever's transient states (particularly the position, velocity). Assuming the tip-sample interaction only happens for a very short time in each cantilever oscillation period, the cantilever-deflection estimation error is then used to interrogate the presence of sample. Shiraishi & Fujimoto (2012) proposed a linear observer to improve the topography measurement of a standard AFM avoiding height measurement distortions due to resonances. This permitted to analyse frequencies below 10 kHz, requiring only a sampling frequency of 20 kHz. In a simulated work of Fang et al. (2002), a sliding mode-like observer was developed for unknown input estimation problems related to traditional AFMs. However, this work had to be realised by exploiting measurements of both position and velocity. It is evident that practically it is not always possible to have the velocity of the cantilever tip available. The probe/sample interaction force was estimated by the precise measurements of the first eigenmode motion and the cantilever deflection based on a two degree of freedom model of a tapping mode AFM.

These mentioned algorithms are not feasible for the shear-force reconstruction in the TDFM due to the differences of the set-up. In detail, a TDFM probe continuously interacts with the specimen at each imaging position during specimen scans. Differently, a tapping mode AFM only contacts or approximates the specimen top at a short time in each oscillation period. The other significant challenge is the TDFM system is expected to excite the cantilevers at the scale of hundreds kilo-Hertz, which is higher than for the existing experimental observers in other AFMs. Also, another potential solution is to design an

H_∞ robust estimator (Stoustrup & H Niemann 2002). Unfortunately, an H_∞ estimator would be often formulated as a high-order transfer function which might be an issue for implementation in practice.

Subsequently, in order to implement the shear-force reconstruction, the potential algorithms have to be investigated in an unknown input observer framework. The structure of the model, capturing the dynamics between the unknown force and the tip of the cantilever, suggests the use of a sliding-mode observer (Davila et al. 2005). It is well known that sliding mode observers exhibit a high degree of accuracy and are capable of simultaneously estimating both the state variables and unknown inputs with finite-time guarantees (Davila et al. 2005, Fridman et al. 2008, Tan & Edwards 2010). This is quite different from the characteristics of high gain observers (Khalil & Praly 2014). As suggested by Nguyen et al. (2016), a sliding mode observer successfully used a separate PC to estimate the unknown shear force input by processing collected practical data for single points only (Nguyen et al. 2016). Subsequently, this also allowed the components of the shear force to be estimated, i.e. the elastic and viscous forces, which also creates a scanning point specific understanding of the material properties of the investigated specimen, i.e. elasticity and viscosity. However, prior to this thesis, the robust implementation of the estimation algorithm, which allows obtaining real-time scanned images of the shear force and material properties of large areas of specimen, is still absent in the TDFM research. Also, the robust implementation will be realised using FPGAs at a Mega-Hertz sampling rate in practice.

2.4 Discussion of Major Practical Implementation Issues

In this section, practical and implementation issues of AFMs are introduced in detail to prepare for similar issues with the TDFM. It will be seen (in Chapter 4) that the control of the TDFM is so challenging that the design has to tackle various noises, different plant nonlinearities, implementation constraints of digital control. Additionally, the operation of the TDFM as a specimen morphology analysis tool is a non-trivial procedure, which needs to be learnt in practice.

2.4.1 Environmental and Instrumental Noise

AFM systems, including TDFMs, have to be well designed and controlled against various mechanical perturbations, such as vibrations due to working machinery, acoustic noise affecting the microscope even through air, or ground vibrations of the earth. The sensitivity required for the measurement of the mechanical deflection of a cantilever/probe has to be extremely high to detect the atomic interaction force (Harke et al. 2012). An intuitive solution is to take the AFM measurements at nights or weekends when the mechanical noise from the street is minimal (Gołek et al. 2014). To protect AFMs from building/earth vibrations, a common solution (e.g. the work of Zhao et al. (2000), Trache & Lim (2010), Kuo & Chen (2012)) is to assemble the highly sensitive components on a vibration isolation table. Recently, new active vibration isolation tables (Wallace 2015, Savage 2008) demonstrated an improved AFM scanning quality

in contrast to the performance on conventional passive vibration suppression tables (Newport Co. 2018, Wallace 2015). Advanced control designs have been developed in AFM systems to resist the mechanical disturbances. In 2002, Schitter & Stemmer (2002) suggested a method to subtract recorded mechanical perturbations from the AFM images, i.e. the effect due to mechanical vibrations are cancelled in the AFM images. An alternative set-up was implemented by Sparks & Manalis (2006) to suppress the effect caused by mechanical disturbances. In this implementation, the topographic data is measured using an additional filtered laser interferometer, which is less affected by mechanical vibrations than the cantilever is. A complex AFM head with an active vibration suppression control successfully compensated for the mechanical vibration in harsh experiments (Ito et al. 2017).

One electrical noise source in AFMs/TDFMs is from the urban electricity supply directly. Therefore, it is suggested that AFMs are used at night time for clean electricity (Gołek et al. 2014). The devices in an AFM also have to be well connected to avoid electrical ground loops (Chang et al. 2012). In a typical digital control design of an AFM (Schitter, Stemmer & Allgöwer 2004), the cantilever-tip sample interaction is often achieved via control using piezo-actuation. The control signal from a digital controller is converted by a digital-to-analogue (D/A) converter and amplified to drive the piezo-actuators. Hence, the devices (e.g. piezo-positioning stages, signal converters, or amplifiers) in AFMs also generate noises caused by their electronics specifications. The existing electronic noise perturbs the cantilever-tip sample interaction, resulting in the inaccuracy of the AFM measurement. For instance, significant noise caused by the piezo-positioning stage is observed in the closed-loop response of a tuning-fork based TDFM (Atia & Davis 1997). In general, stable low-noise amplifiers are required in AFMs to guarantee an appropriate electrical noise level (Brook et al. 2002, Putman et al. 1992). Even the cantilever deflection sensing mechanism integrated with piezoresistors (Hansen & Boisen 1999, Thaysen et al. 2000, Rasmussen et al. 2001) or with capacitance sensors (Joyce & Houston 1991) cause some inherent electrical noise, including the white Johnson noise and flicker noise.

Thermal fluctuation is a fundamental factor causing inaccuracy in AFMs (Butt & Jaschke 1995). In detail, thermal fluctuation can cause the measurable deflection/vibrations of the cantilever, i.e. the precision of the force detection is limited. However, thermal noise can be used for cantilever calibration (Hutter & Bechhoefer 1993) or the spring constant measurement (Levy & Maaloum 2001). Research (Schäffer 2005), studying the AFM inaccuracy caused by thermal noise, demonstrated that an influence on high order vibration modes in both ambient and liquid environment. In practice, a high Q-factor is desirable for improved measurement sensitivity. Hence, the Q-factor is controlled to be high enough for a low tip-sample interaction force (Ashby 2007). However, the AFM application on imaging soft materials found that the thermal noise can be amplified when the cantilever is controlled to gain a larger Q-factor. In brief, careful selection of the AFM cantilever is a common solution for suppressing thermal noise; this has been also investigated for TDFMs by Vicary et al. (2011). Alternatively, an external dissipative magnetic field is controlled to decouple the thermal noise by attaching a ferrite particle on the cantilever (Liang et al. 2000). However, this technique to compensate for the thermal noise has not been applied

on AFM scans in practice.

The sensing mechanism to detect the cantilever deflection causes different types of inaccuracy in the measurement and the control of AFMs. Common diode laser reflection based sensing mechanism has major noise sources (Fukuma & Jarvis 2006), including mode hopping noise which is caused by mirror vibrations in the optical path or environmental temperature fluctuations (Ojima et al. 1986). The laser interferometer based sensing mechanism is a conventional method to measure displacement at the highest precision (Fukuma et al. 2005). However, the inaccuracy of the laser interferometry is caused by many environmental factors, like air movement (Schönenberger & Alvarado 1989), temperature (Zygo Co. 2008), or humidity (Zygo Co. 2008). The cantilever integrated with piezoresistors also suffers inaccuracy caused by electronic noise (e.g. the Johnson noise and the amplifier noise (Itoh & Suga 1993)) as discussed before.

Brownian motion of the molecules causes cantilever vibrations, i.e. the inaccuracy of measurement, over all frequencies (Sader 1998). In AFMs, the inaccuracy caused by the Brownian motion of the molecules in environment is unavoidable due to the existence of the phenomenon in air/liquid at an ambient temperature. Additionally, the samples, which are not firmly attached at the sample-holder, are always in Brownian motion (Ando et al. 2002, Suzuki et al. 2010). A solution is suggested to use high-speed AFM to capture the uncertainty caused by the samples' Brownian motion while scanning in AFMs (Ando et al. 2002, Suzuki et al. 2010). For instance, the arbitrary motion of the particles have been observed in a high speed AFMs with a temporal frame-recording time of about 30 ms (Yamashita et al. 2007). However, the inaccuracy caused by the Brownian motion of the samples is unavoidable in typical AFMs, which are not fast enough to capture the Brownian motion.

2.4.2 High Nonlinearity

The interaction force between the cantilever and the specimens is a collective of the atomic interaction forces and the local material properties, such as elasticity, hardness, Hamaker constant, adhesion and surface charge densities (Butt et al. 2005). The atomic interaction force, the van der Waals force, has been discovered to be highly nonlinear varying with the relative distance toward the sample-substrate (Ashby et al. 2000). After the invention of AFM, the attractive force between an excited tungsten tip and a silicon surface was found to be exponentially decreasing as the distance increases (Martin et al. 1987). The work concluded that the tip-cantilever oscillation amplitude increases as the distance increases following a relationship similar to a logarithmic function. In 2005, Butt et al. (2005) presented a detailed report on the techniques and applications of the force measurement using horizontal cantilever based AFMs. The interaction including all atomic effects was modelled as a combination of a contact region and a non-contact region. The force-distance curve in AFMs is nonlinear in both the regions and the connection of two force-distance curves can be discontinuous (Figure 2.11). Consequently, the cantilever

deflection measurement depending on the tip-sample distance has a strong nonlinearity along the vertical direction.

Differently, in a TDFM, the work of James et al. (2001) demonstrated that the interaction shear force was overall an almost continuous nonlinear function of the separation between the probe and the sample-substrate. The probe oscillation amplitude was a logarithmic function of the probe-sample distance in a 20 nm range (James et al. 2001). For the precise control of AFMs/TDFMs, it is clearly a challenge to design appropriate control algorithms to account for the strong nonlinearity in the vertical z-axis direction. Even though the force-distance curve is possibly challenging in TDFMs, the TDFM does not have to deal with all the adhesive forces. Specifically, as introduced in Section 2.2.2, the horizontally excited probe/cantilever avoids to be exposed by the adhesive force in the vertical direction.

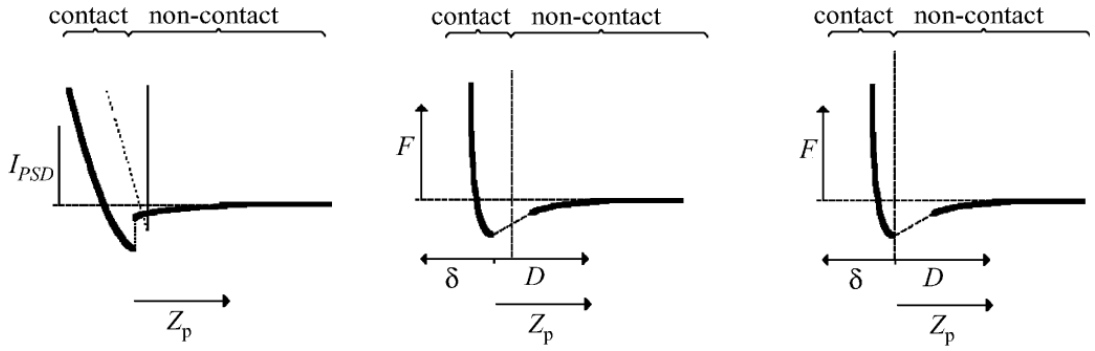

FIGURE 2.11: The cantilever-deflection and the atomic force v.s. the tip-sample inter-distance (Butt et al. 2005). Here, the samples are assumed to be deformable materials with attraction and adhesion forces. The right figure shows the usual misinterpretation, in which zero distance is placed to the end of the jump-in. The difference between the middle figure and the right figure is caused by adhesion forces.

For AFM in general, but for TDFM in particular, Antognozzi et al. (2001) found that the molecular structures of the confined liquid layers covering the sample-substrate surface result in the discontinuity of the force-distance (in the vertical direction) curve (Butt et al. 2005). For instance, the molecular layers of a confined water film, which covers the sample-substrates in ambient and water environments, was studied in water using a TDFM (Antognozzi et al. 2001). The elastic force and viscous force between the oscillating probe and the confined water layer has a strong nonlinear force-distance curve on nanometre scale in Figure 2.12. It is clear that the interaction shear force increases as the distance between the vertical probe and the sample-substrate decreases. Note also the inconsistent force-distance relationship in Figure 2.12. This is also confirmed by the shear-force reconstruction results as presented in Chapter 5. The irregular Brownian motion of the sample also caused a force-distance nonlinearity on molecular scale. For instance, the research of Scholz et al. (2005) reported that the Brownian motion of a single myosin molecule had a reducing strength in a discontinuous manner as the molecule surface is approached along the z-axis.

In AFMs, the geometry of the cantilever's tip might be another main reason of nonlinearities between the cantilever-tip and the sample, as shown in Figure 2.13. The roughness of the contact surface deter-

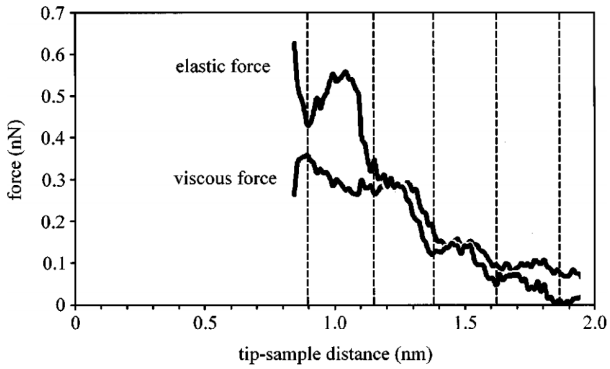

FIGURE 2.12: For a TDFM, the interaction elastic/viscous forces between the cantilever and the sample-substrate vary in a nonlinear and discontinuous manner as a result of the confined water-layer's lattice-structure (Antognozzi et al. 2001)

mines the adhesion force between the cantilever-tip and the sample-substrate (Butt et al. 2005). Hao et al. (1991) demonstrated that the tip geometry significantly determined the measurement force curve in relation to the cantilever deflection. Similarly, the tip geometry of the vertically oriented cantilever affects the force sensitivity and the tip-sample contact area in the TDFM (Harniman 2013). Also, as confirmed in this work, the tip geometry will strongly affect the scanning quality (see remark in Chapter 6). The fabrication to make the tip geometry uniform was investigated by Harniman (2013) and a sharpened tip improved sensitivity. However, the high cost of this process may make this approach practically difficult. In brief, the vertical positioning system dynamics of AFMs/TDFMs are varying due to diverse tip geometries (Butt et al. 2005, Harniman 2013).

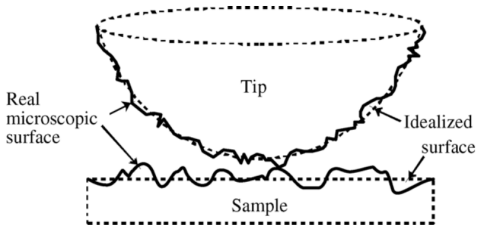

FIGURE 2.13: Nonlinearity caused by the tip geometry in AFMs (Butt et al. 2005).

The force measurement may have an inherent nonlinearity from the sensing mechanism of the cantilever deflection: For instance, the work of Martin et al. (1987) applied laser interferometry to precisely sense the deflection of the horizontal cantilever. Here, an accurate interaction force measurement had to be taken in a short period of 1 s due to the thermal drift of the laser interferometer. In the context of the TDFM, the evanescent field based sensing mechanism (Antognozzi et al. 2008) provided the highest sensitivity to the vertically oriented cantilever deflection. The captured light-strength has a nonlinear relationship with the distance between the cantilever and the sample-holder in the z-axis, due to the nonlinearity of the evanescent field strength. Also, the nonlinearity of the evanescent field strength changes with respect to the environmental conditions, such as a change of the sample-holder thickness/transparency or a switch between ambient/water environments. Hence, it is critical to consider

the nonlinearity of the sensing mechanism in high precision control designs of Bristol's TDFM.

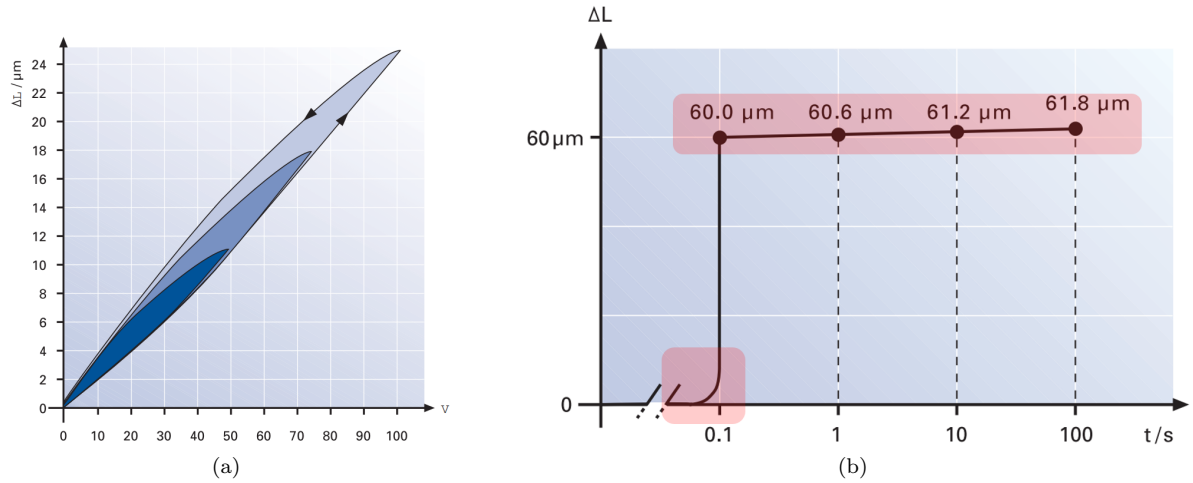

FIGURE 2.14: Nonlinearity of piezo-actuation (Physik Instrumente (PI) GmbH & Co. 2008): a) the hysteresis effect of a piezo-actuator; b) the nonlinear effect (also called creep effect) of a piezo-actuator, as displacement does not precisely follow the change of input voltage.

Piezo-actuators are mostly used to provide actuation for the displacement control of the force sensor for constant force interaction in AFMs as introduced in Section 2.3.1 or for the TDFM (Harniman 2013). However, the hysteresis effects (Figure 2.14a) and the nonlinearity (Figure 2.14b) of the piezo-actuation (Physik Instrumente (PI) GmbH & Co. 2008) results in nonlinear dynamics of the vertical plant (Fu 1995). Since the z-axis control requires precise positioning over the sample-substrate, the nonlinear dynamics caused by piezo-actuators are often compensated by advanced control algorithms (Zou et al. 2004). In some specimen imaging applications (e.g. the AFM of Sparks & Manalis (2006) or the TDFM of Harniman (2013)), the piezo-actuation signal is recorded to capture the cantilever position in the z-direction, i.e. to provide the specimen topographic data directly. Specifically, in the TDFM applications (Harniman et al. 2012, Harniman 2013), the nonlinearity of the piezo-actuators are not considered, i.e. this introduces imaging inaccuracy in the so-called force-feedback (i.e. a cantilever oscillating phase feedback mode in fact) scan mode. Hence, Chapter 6 will introduce an modified scan mode to avoid this issue.

2.4.3 Digital Control Implementation Constraints

Since the early 90s, digital hardware based control has been adopted to realise control of AFMs, e.g. the AFM developed by Wong & Welland (1993). The significant advantage is the great flexibility to implement a complex control programme at comparably low hardware cost, whilst analogue hardware is limited to implement filters-based transfer functions (Wong & Welland 1993, Baselt et al. 1993, Ando et al. 2001, Heyde et al. 2001, Zahl et al. 2003, Schitter et al. 2003, Kos & Hurley 2007, Huang 2013, Jerez et al. 2014, Soltani Bozchalooi 2015). For a successful control implementation, an embedded control programme has to carefully consider the following practical issues.

The hardware to implement the digital control programme often runs on an integrated circuit board. In practice, there is a limited amount of available processors on a DSP board (Schitter et al. 2003) or a limited number of programmable binary gates on an FPGA board (Huang 2013). The onboard clock also limits the clock cycle period, which is the minimal running time to execute the fundamental functions of the digital circuit. Hence, at each clock period, the capacity to execute a numerical calculation on a digital control board is physically constrained by the hardware. A practical solution is to run the control programme at a slower speed, i.e. the control board has an extra time for complex calculation. For instance, the DSP board has a minimal clock period of 10 μs in the AFM set up of Baselt et al. (1993). The DSP board was slowed down to a running period of 15 μs allowing the realisation of a control programme. In the context of FPGA based control, similar calculating procedures can be realised by one programme on board, i.e. the physical resource is saved by letting the same hardware handles different signals at the cost of extra data storage and signal flow (Soltani Bozchalooi 2015, Monmasson & Cirstea 2007). However, this requires a significantly dedicated design of the FPGA programme. The increase of the programme complexity and the repetitive call of the the same programme part will always use a few extra clock cycles. It is clear that the control realisation has to balance the programme complexity and the limited computational capacity considering the hardware running period to satisfy the digital control requirements.

The numerical accuracy of a digital controller is often ignorable in DSP based control solutions because the numerical operations are executed in floating point format on DSP boards. It is noticeable that the z-axis dynamics are often simply controlled by PI or PID algorithms in DSP control based AFMs (Wong & Welland 1993, Baselt et al. 1993, Heyde et al. 2001, Ando et al. 2001, Zahl et al. 2003, Kos & Hurley 2007). In contrast, the control programmes on FPGA are likely to be realised by fixed-point arithmetic (Monmasson & Cirstea 2007) for a higher running speed at lower hardware resource and energy consumption. A variable or a numerical operation is able to be presented in a fixed-point representation as $fxp(word, fraction)$, where $fraction$ indicates the number of digits to present the fractional part of the arithmetic and the $word$ denotes the number of binary digits to express the variable or the operation. Hence, a fixed-point arithmetic has a limited numerical precision defined by $fraction$. The $word$ and $fraction$ parameters together determine the numerical range of a variable or a mathematical operation

on an FPGA board. Clearly, a complex control algorithm, e.g. a model predictive controller (Jerez et al. 2013), requires a significant cost of hardware resource due to high algorithmic complexity. At the same time, there is always a design requirement to guarantee an adequate calculation accuracy, which needs sufficient binary gates set as the *fraction* digits. For example, the paper of Jerez et al. (2013) reported the numerical precision of a control algorithm was limited by the fixed-point arithmetic configurations. Thus, the control programme design has to consider the trade-off between the complexity of the control algorithm and the relative numerical precision of the programme facing a limited hardware resource.

The A/D and D/A converters also significantly affects the digital control performance of AFMs (Ando et al. 2001, Heyde et al. 2001, Zahl et al. 2003, Schitter et al. 2003, Hatano et al. 2016). The AFMs controlled by DSP boards have had a control bandwidth no more than 70 kHz, also due to the A/D conversion rate slower than 200 kHz (Ando et al. 2001, Heyde et al. 2001, Zahl et al. 2003, Schitter et al. 2003). In the FPGA controlled AFMs, the running speed of digital control programmes also needs to consider the speed limitation of the A/D converters. For instance, the feedback control cycle time of the TDFM set-up (Hatano et al. 2016) was limited to and had an inherent delay of 1.33 μs, which was in this case not a limiting factor but had to be carefully considered in the overall practical controller design. The performance of A/D and D/A converters not only affects the bandwidth but also the precision of the controller. In detail, a measurement represented as a bounded analogue signal is converted to a digital signal with a fixed resolution by an A/D converter. A significant quantization error occurring during the conversion intuitively results in a highly inaccurate control signal. The accuracy to recover the digital control signal in relation to an analogue signal needs to be decided according to the sub-nanometre precision control requirement (usually needed in in AFM control). As described by Wong & Welland (1993), the A/D converters often constrain the AFM performance more than the DSP boards and the D/A converters do. It can be concluded that an adequate digital control programme design has to consider the performance of A/D and D/A conversion of the hardware.

2.4.4 Proficiency Requirements for Instrumentation

Operating an AFM (TDFM) requires a relatively high proficiency in the working principles of AFM, instrument maintenance, basics of tuning PID control, etc. (Veeco Instruments Inc. 2004). There is even more pronounced evidence in the literature (Antognozzi et al. 2000, Vicary et al. 2011), indicating that TDFM operation requires professional skills given as below. It will be seen that work conducted here has contributed to the advancement of the use and robustness of the TDFM system, while some of the problems listed below are still to be resolved in future work.

The beginning of the set-up procedure is to locate the force sensor, which are often extremely small cantilever-tips (Giessibl 2003) in commercial AFMs or tiny cantilevers (Antognozzi et al. 2008) in TDFMs. After correctly locating the sensor with a high-magnification camera, the optical path has to be well aligned to maximise the sensitivity to the cantilever deflection (Veeco Instruments Inc. 2004, Antognozzi

et al. 2000). With the enabled cantilever-deflection detection, the next critical step is to enhance the signal-to-noise ratio by adjusting the optical path and then to position the cantilever-tip carefully at a few tens of nanometres above the sample-holder surface (Vicary et al. 2011).

In addition to the required proficiency of preparing the sample-substrates, the force sensor (cantilever) needs to be at an appropriate position towards the sample (Giessibl 2003). In detail, the AFMs operated in contact mode have to be ad-hoc operated to achieve a small contact force with the sample-subtract. The TDFMs that only work in a non-contact mode require to place the oscillating cantilever within the vicinity of the sample-substrate (Harniman 2013). Insufficient cantilever-sample contact may cause the failure of imaging or the lack of contrast. However, a too large contact force would wear the cantilever-tips in typical AFMs or the cantilevers in TDFMs or even damage the cantilevers.

The basic comprehension of control theory is a vital skill for successfully operating AFM scans. In the commercial AFMs (e.g. the D3100AFM (Veeco Instruments Inc. 2004)) and the early TDFMs (Harniman et al. 2012, Harniman 2013, Harniman et al. 2017), the operator needs to ad-hoc tune the PID control parameters during the scanning, i.e. this online tuning procedure may cause aggressive actuation and damage the cantilevers. Hence, control engineers developed automatic/semi-automatic PID tuning algorithms for AFMs (Kohl et al. 2016, Abramovitch et al. 2009). Otherwise, a good controller has to be a priori-designed using a good model of the vertical positioning system dynamics in the z-direction, like the control design of Schitter et al. (2001).

Location of the target samples in a large sample-substrate is another significant difficulty, which often requires several hours for proficient AFM operators (Roy et al. 2013, Caplan et al. 2011). Additionally, it is noticeable that successful scans require experimental proficiency to deal with the scanning samples as addressed by Requicha et al. (1998). It is impossible to guarantee that the obtained scanning data is as expected even when operating a well prepared AFM system (Requicha et al. 1998). Hence, quantitative research for unknown samples or unknown atomic behaviours is still non-trivial and not readily validated.

2.5 Summary

The TDFM, as a special AFM, genuinely permits the specimen topography analysis at nanometre precision with few requirements on the environmental conditions. Most importantly, the non-contact sensing mechanism of the TDFM avoids physical contact with specimens during scans, i.e the damage to delicate specimens is prevented. After reviewing previous TDFM research and current AFM systems, various AFM control techniques are found useful to improve the TDFM's scanning capability and enrich its functionality. Hence, driven by the research motivations, this work has to tackle several practical challenges including environmental noises, high system nonlinearity, digital control implementation difficulties, and significant requirements of operation proficiency.

Chapter 3

System Design & Optimisation of the Transverse Dynamics Force Microscope

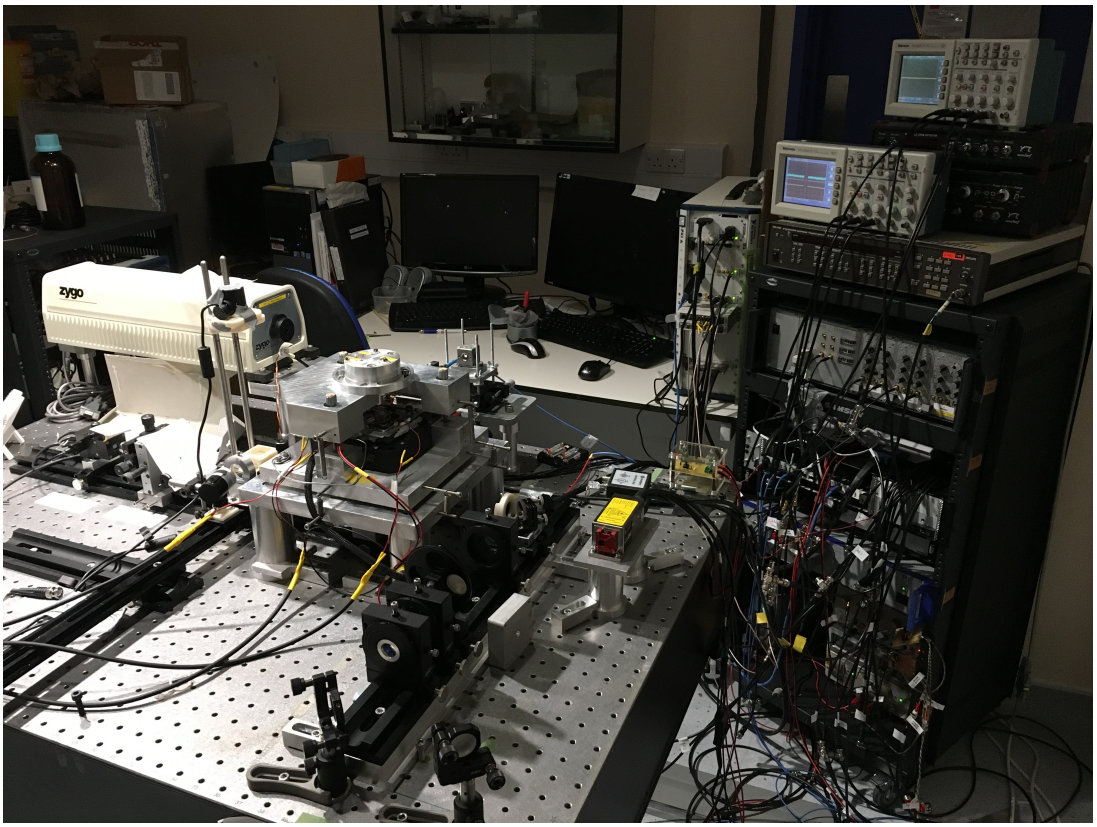

FIGURE 3.1: The developed TDFM system as placed in the Nano-Science and Quantum Information Centre at the University of Bristol.

3.1 Introduction

This chapter focuses on the electronic design of the I&C system for the TDFM as shown in Figure 3.1. The realisation of the sensing component, the core of the system, is described at the beginning. The next section introduces the system integration design: the electronic design to obtain the z-axis measurements and the electromechanical design to implement the vertical z-axis positioning system. Then, the structural and numerical design of the control programmes are designed to validate the system control. Subsequently, the digital control programme design is detailed. This includes an a-priori optimisation approach that is designed to avoid any numerical overflow of the control programme, including the z-axis high-precision controllers, in practice.

The I&C development mainly focuses on the digital control programme implementation, the control framework design, and the system integration of the TDFM. Hence, the system is equipped with various functional features: a graphic user interface (GUI), a raster-scanning trajectory planner, a heady-duty data buffering mechanism, and so on.

Importantly, a novel cantilever-specimen separation sensing mechanism is developed for the TDFM by evaluating the cantilever oscillation amplitude. The proposed sensing mechanism has a sensing range of $\sim$6 nm in water environment (proven in Chapter 4), in which the previous signal phase based sensing mechanism only allows a $\sim$2 nm sensing range (Harniman 2013). The improved sensing range will be applied to the vertical positioning control systems of the cantilever in Chapter 4, resulting in an improved specimen imaging performance as Chapter 6 shows.

The research also contributes a practical design methodology to implement fixed-point-arithmetic based digital control on FPGA hardware. As a result, the developed novel digital control programme allows online reconfiguring advanced control algorithms in the TDFM digital control system, whereas only an ad-hoc tuned PID control was used in the previous set-up (Harniman et al. 2012, Harniman 2013, Harniman et al. 2017). Additionally, an offline optimisation is proposed to verify FPGA control programmes before compiling and loading on FPGA boards. This tool can benefit the digital programme design in general FPGA based control systems, not only the TDFM.

Supporting publications:

- *"Enhancing fixed-point control robustness for experimental non-contact scans with the Transverse Dynamic Force Microscope"*, Zhang, K., T. Hatano, G. Herrmann, et al., *American Control Conference (ACC) 2018, IEEE.*

- *"A specimen-tracking controller for the Transverse Dynamic Force Microscope in non-contact mode"*, Hatano, T., K. Zhang, SG. Khan, et al., *American Control Conference (ACC) 2016, IEEE*, 2016: 7384-7389.

3.2 TDFM Optical Sensing Component

The sensing component is designed to detect the oscillating cantilever immersed in an evanescent field. For the operation of the TDFM, it is necessary to measure the oscillatory motion of the tip of the cantilever (see Section 2.2.2 in Chapter 2). According to the discussions in Section 2.2.2, the TDFM optical sensing component need to be able to detect the cantilever oscillation at a high excitation frequency, motivated to achieve a high sensing bandwidth.

Therefore, at first, the selection of the cantilevers is made in consideration of the design requirements: a sufficient force sensitivity at a high sensing bandwidth. Also, a set-up to visualise the extremely small cantilevers is introduced to assist the cantilever localisation for the system adjustment. Then, the optical sensing mechanism is described which enables two vertical position measurements of the cantilever, i.e. this in principle permits two height-feedback control modes for scanning. As the evanescent field generation is a non-trivial laborious procedure, procedural explanations are provided to help with the adjustment of the complex optical path. Then, a low-frequency gain calibration method is discussed as an essential preparation before any experiment.

3.2.1 Cantilever Selecting, Mounting, and Localising

Cantilever selection

The vertically oriented cantilever needs to be well chosen to implement the shear-force sensing mechanism in the TDFM. There are mainly two design requirements while selecting the cantilevers. One design requirement aims to realise dynamic force sensing at a high bandwidth. Hence, the selected cantilevers need to have relatively high resonances in both ambient and wet environments. This contrasts the typical SFMs, such as those of La Rosa et al. (2005), Mühlschlegel et al. (2006), Sandoz et al. (2008), Park et al. (2014) that excite vertical probes around 33 kHz. The other important design criterion is that the cantilever has to be sufficiently soft to guarantee sub-nano Newton sensitivity along the interacting y-axis.

At Bristol, cantilevers have been provided by NuNano Ltd. (2018). The candidate cantilevers type A and type B (as shown in Table 3.1) are chosen from the NUVOC-Standard200 series, a series of non-coated ultra-soft tip-less silicon nitride probes.

Table 3.1: Specifications of the candidate cantilevers.

	Length	Width	Thickness	Spring constant	First resonance in air
Cantilever A	18 μm	1 μm	200 nm	0.07 N/m	820 kHz
Cantilever B	28 μm	2 μm	200 nm	0.04 N/m	340 kHz

The vertically oriented cantilevers are made of silicon nitride (Si_3N_4) without coating. Practically, there are often several cantilevers micro-fabricated at the lower-end of a Si_3N_4 chip in order to reduce

the cost of material and production effort (Figure 3.2a). The vertically-oriented-cantilever chip is approximately 2.3 mm × 1.3 mm in size. It is noticeable that the selected cantilevers only have a high sensitivity in the y-direction of the horizontal plane (Figure 3.2b) because of their asymmetry along the x and y axis. Hence, the cantilever distortion in the x-direction (e.g. caused by shear forces) is negligible (see Figure 3.2b). This results in a focused directional shear-force sensitivity, in contrast of a cylindrical probe, which has equal sensitivity to shear forces in both x & y direction (Figure 3.2c).

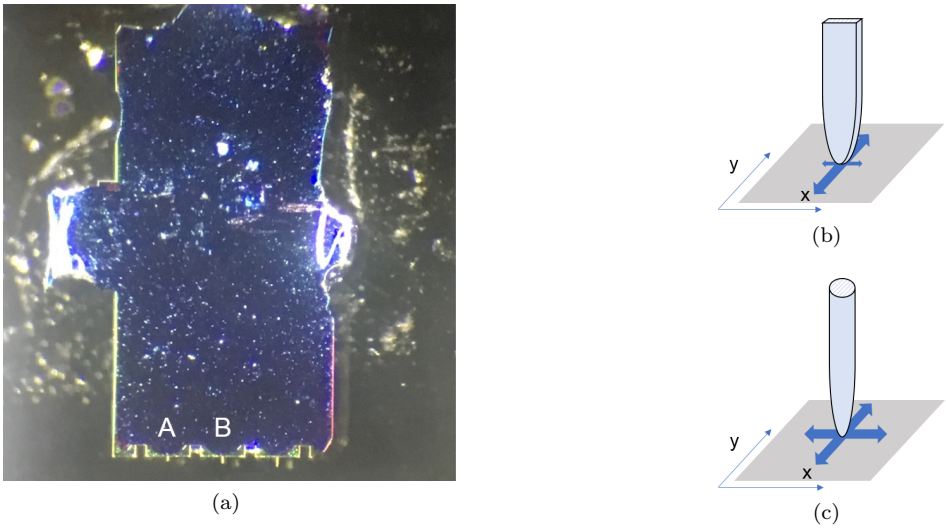

FIGURE 3.2: A photo of a chip with cantilevers, a schematic of the cantilever in TDFM, and a schematic of a cylindrical probe in typical SFM: a) a photo (150× zoom-in by an optical microscope from Carl Zeiss AG (2018)) of a Si_3N_4 chip that has three cantilevers (two A type cantilevers and one B type cantilever) at its lower-edge; b) a schematic of the cantilever which has extremely high sensitivity only in the y-axis direction in TDFM; c) a schematic of a cylindrical probe that has equal sensitivity in the horizontal plane due to its symmetry along the vertical z-axis (in many typical SFMs).

The vertically oriented cantilever chip has to be carefully attached to a chip holder. Practically, the chip and the chip-holder are glued to each other by a very thin layer of wax. An appropriate amount of wax is first placed and melted at the lower-end of the chip-holder. Then, the chip is gently pressed on the melted wax until the wax is cooled down. The amount of wax has to be sufficient for creating a consistent attachment between the chip and the holder. On the other hand, the thickness of the adhesive wax requires to be thin enough to avoid extra damping and dynamics caused by the wax layer.

The TDFM only has a limited area in the horizontal plane, which is feasible to use the sensing mechanism for cantilever-deflection detection, similar to most AFM systems (Veeco Instruments Inc. 2004, La Rosa et al. 2005, Mühlschlegel et al. 2006, Schitter & Phan 2008, Sandoz et al. 2008, Ando 2012, Park et al. 2014). Hence, after the cantilever chip attachment, the next operation is to bring the cantilever in a vertical position into a limited horizontal area, a small vicinity of the sample-holder slide. Similar to a commercial D3100 AFM from Veeco Instruments Inc. (2004), a far-field camera is used to zoom into a limited horizontal area above the sample-holder slide to localise the small cantilever that is invisible to naked eyes. To observe the vertically oriented cantilever via this camera, an LED light

is placed over the sample-holder slide near the camera-focused area (see Figure 3.3). As a result, the far-field camera can observe the cantilever's shadow that indicates the cantilever's horizontal position above the sample-holder slide as shown on the right of Figure 3.3. Because the far-field camera is focused on the sample-holder slide, the cantilever's shadow gets sharper as the cantilever approaches the target space. This cantilever-localisation is a purely manual procedure that requires to adjust the chip-holder 3D position carefully to avoid crushing the fragile cantilevers onto the sample-holder slide.

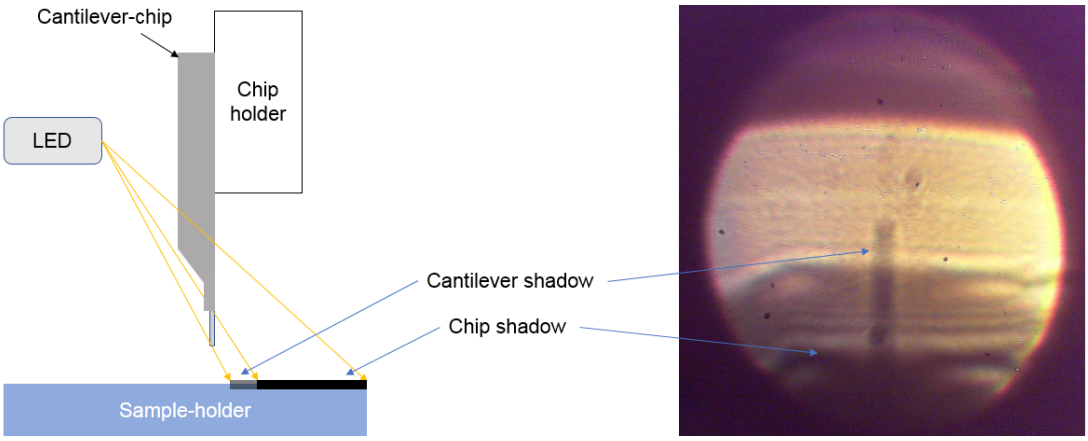

FIGURE 3.3: The set-up to localise the cantilever in an appropriate space and to manually pre-calibrate the optical sensing mechanism in the TDFM. The right shows the shadow of the lower-edge of a localised chip observed by the far-filed camera.

3.2.2 Optical Sensing Mechanism

The optical sensing mechanism is designed as shown in Figure 3.4 which has greater adjustable flexibility to maximise the optical sensitivity than the set-up introduced in Figure 2.4. The laser source generates the 660 nm wavelength laser at a maximum output power of 170 mW (Coherent Inc. 2018). Hence, the laser power is strong enough to guarantee the strength of the evanescent field, which influences the sensitivity to detect the cantilever deflection. Then, the laser is collimated and expanded by a pair of Galilean beam expanders. Subsequently, the diameter of the laser is increased to 1 mm to allow later the laser collimation. Here, the selection of a Galilean style beam expander is chosen for a higher optical stability in lieu of the Keplerian style. Additionally, a set of natural density filters is deployed before the long focal lens, focusing the expanded laser on the high numerical aperture (N.A.) lens, a Nikon Apochromat TIRF (Total Internal Reflection Fluorescence) 100x (NIKON Co. 2015). The filter-set allows full-power, half-power, or quarter-power of the expanded laser into the later optical path for the convenience to optimise the sensing component. For instance, the half-powered laser provides an appropriate image brightness for far-field camera visualisation when the light reflection angle requires to be optimised for maximising the optical sensitivity. The light reflection angle within the high numerical aperture lens is important to create total internal reflection for the laser within the lens-oil composition medium.

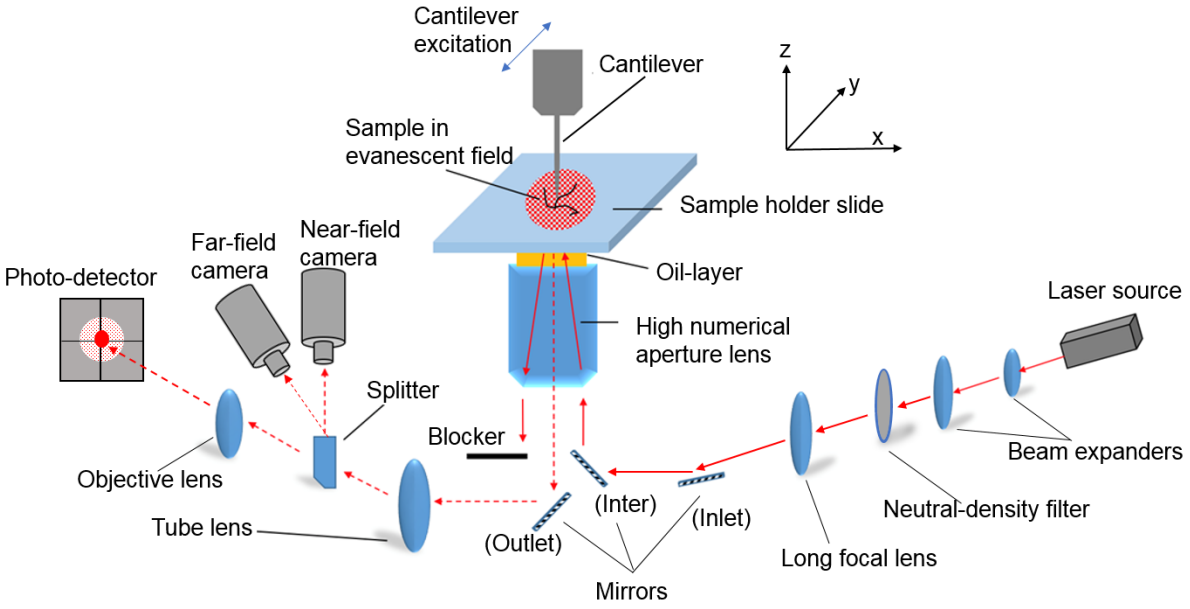

FIGURE 3.4: Schematic of the optical path to implement the evanescent field based sensing mechanism in the TDFM. The evanescent field is generated at the sample-holder surface, where the source laser is adequately conditioned to be totally reflected. Consequently, the photo-detector detects the focused light that is scattered and reflected by the cantilever in the light field. The cantilever is excited in y direction and its vertical position along the z-axis is feedback-controlled. The sample is translated in a raster pattern, which moves in x and y directions providing the fast and the slow scan axes respectively.

To generate an evanescent field, the expanded laser is then focused at the back focal plane of the high numerical aperture (N.A.) lens by a long focal lens with a focal length of 300 mm. The top surface of the sample-holder slide has to be placed on the back focal plane where a total internal reflection is created. The total reflection just appears on the sample-holder surface on which a light field is generated with a few hundred nano-meter depth and approximately 20 μm diameter. This light field is the so-called evanescent field necessary for the sensing mechanism of the TDFM. The evanescent field is scattered and reflected by any object in that field of suitable size, including samples, unknown-particles, rough surface of the sample-holder slide, and cantilevers. Hence, the excited cantilever in the evanescent field results in the motion of the light reflected from the cantilever. In addition, the strength of the evanescent field exponentially decreases away from the light-field centre. Hence, the strength of the light reflection caused by the cantilever increases, when the cantilever is closer to the sample-holder surface. The light reflected from objects in the scattered evanescent field is directed down through the high N.A. lens for measurement (see Figure 3.5).

Importantly, the optical sensitivity of the evanescent field has to be carefully optimised. Here, an inlet mirror is introduced to adjust the radial distance and the angle of the inlet laser directed through the high N.A. lens, i.e. the optical path can be adjusted to change the position of the evanescent field independent from the refractive index of the scanning medium. An intermediate lens (abbreviated as inter-lens, see Figure 3.4) is placed under the high N.A. lens to direct the laser into the high N.A. lens and to avoid blocking the light path. To ensure the evanescent field explicitly occurs at the sample-holder

surface, three high-precision adjustment screws (from Newport Co. (2015)) are used to adjust the height and the orientation of a focusing plate carrying the sample-holder slide. An oil layer is dropped between the high N.A. lens and the sample-holder slide. This oil-layer has the same refractive index as the high N.A. lens introducing a continuous optical medium, therefore the potential interference caused by an ambient gap between the lens and the sample-holder slide is eliminated. The amount of oil needs to be just enough to bridge the lens and the sample-holder to avoid flowing and subsequently interfering the laser path.

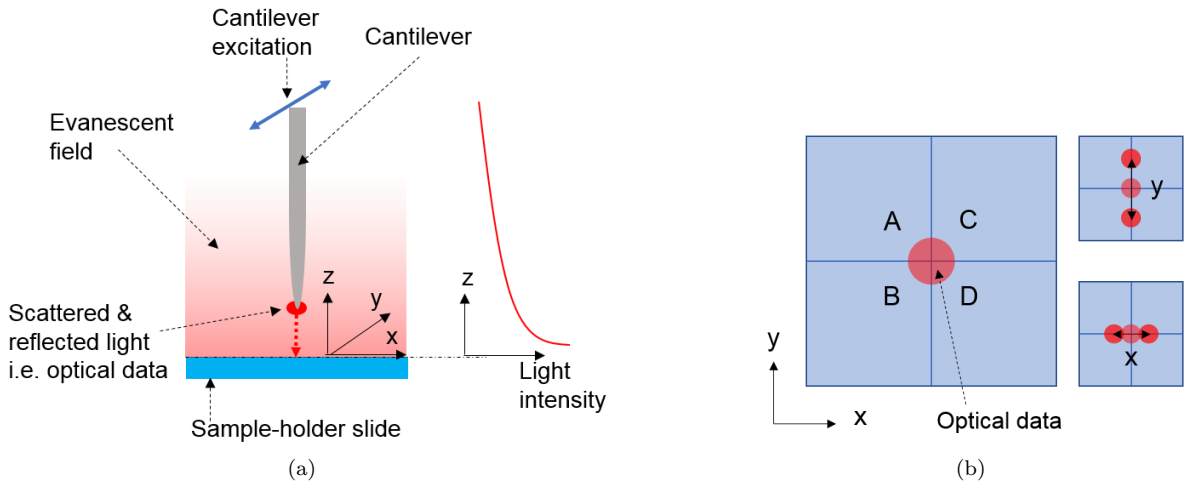

FIGURE 3.5: The schematic of the photo-detector detecting the optical measurements of the light reflected from the cantilever: a) a schematic presents the optical measurements, including the light intensity and the motion of the cantilever reflection in the evanescent field; b) a schematic of the working principle of the position-sensitive photo-detector that senses the light reflected from the cantilever (see Equation 3.1).

The exit laser from the high N.A. lens contains the light reflected from the cantilever and the totally reflected reference beam (Figure 3.4). A moveable plate is introduced to block the reference beam, avoiding the saturation of the optical sensor, i.e. the photo-detector. Then, a 45° outlet mirror is fixed beneath the high N.A. lens to direct the reflected light away for measurement. The light from the outlet mirror is collimated by a tube lens with a 200 mm focal length. The collimated light is split up into three parts by an optical splitter. One part is captured by the far-field camera for localising the cantilever. One part is taken by a near-field camera for evanescent field adjustment and fine cantilever-positioning. Both the cameras are positioned to focus on the sample-holder slide surface. The major part is directed through a 100× objective lens onto the photo-detector. The photo-detector (Hamamatsu Photonics K.K. 2018) is an integrated 4-segment silicon photodiode. The photo-detector has the sensing bandwidth of 1 MHz; and it is sensitive to 660 nm wavelength, as generated by the laser source, for maximal sensitivity. The light reflected from the cantilever is focused as a laser spot, which causes a voltage on the position-sensitive

(a) (b) (c)

FIGURE 3.6: An optimised evanescent field observed in the far-field and near-field cameras: a) the scattered evanescent field is often observed and optimised with half-powered source laser in the near-field camera image, and gold particles are distributed on the sample-holder slide; b) the near-field camera observes the cantilever scattering and reflecting the evanescent field light and showing the shadow of the cantilever; c) the same scattered evanescent field and the cantilever-chip's shadow are seen zoomed out in the far-field camera image. In b) and c), the evanescent field is generated by the half-powered laser source and the cantilever shadow is created by the LED.

photo-detector as shown in Figure 3.5. The voltages on 4 segments measures three signals by:

$$\begin{aligned} V_{Light\ intensity} &= V_A + V_B + V_C + V_D \\ V_x &= \frac{(V_A + V_B) - (V_C + V_D)}{V_{Light\ intensity}} \\ V_y &= \frac{(V_A + V_C) - (V_B + V_D)}{V_{Light\ intensity}} \end{aligned} \tag{3.1}$$

where V_A, V_B, V_C, and V_D denote the voltages for the 4 different segments in Figure 3.5b. $V_{Light\ intensity}$ is the measurement of the cantilever's reflection strength. V_x and V_y is the position of the cantilever in the evanescent field in x and y direction respectively. In summary, two signals are used in this work:

- $V_{Light\ intensity}$ measures the distance from the cantilever towards the sample-holder slide. $V_{Light\ intensity}$ exponentially increases as the distance decreases.
- V_y is measured as the cantilever oscillation in the y-direction that the cantilever is excited along. The cantilever oscillation varies with the relative distance between the cantilever and the sample-substrate, e.g. the amplitude drops when the cantilever approaches the sample-surface.

The generation of the evanescent field relies on the complex optical path. This optical path has to be manually tuned and aligned at a considerable time cost. When there is a change of the scanning medium or a drift of any critical optical component, adjustment or re-tuning process is necessary to guarantee the high-system performance.

Remark 1 Here, a manual adjustment procedure is provided for guidance. This is to create an evanescent field in ambient conditions:

- *Step 1)* Direct the source laser towards the centre of the beam expander, while making sure that the laser is perpendicular to the expander.

- *Step 2)* Allow half-power of the laser to pass the focal lens and to be at the centre of the inlet mirror.
- *Step 3)* Adjust the focusing plate to make the sample-holder slide perpendicular to the vertical z-axis.
- *Step 4)* Tilt the inlet mirror, and then translate the inlet and inter mirrors until the inlet laser passes through the high N.A. lens and the sample-holder slide. The laser path through out the sample-holder slide needs to be parallel to the z-axis. The cross section of the laser path in the x&y plane is expected to be a circular spot as small as possible.
- *Step 5)* Simultaneously translate the inlet and the inter mirrors. The outlet laser is expected to appear on the far-field camera. Stop the translation as soon as the outlet disappears from the camera. This means the laser is totally internally reflected.
- *Step 6)* Move the inlet and inter mirrors slightly back along the rails until the outlet laser appears in the near field camera image. At this time, the inlet laser is just about to be totally internally reflected. Use the reference beam blocker to block out the major reference laser for the next adjustment step.
- *Step 7)* Carefully adjust the height of the sample-holder slide and the outlet laser in the near-field camera. For instance, Figure 3.6a shows the sample-substrate with a well focused evanescent field. The evanescent field in the case of Figure 3.6a is scattered by gold particles and the rough surface of a grade 1 glass sample-holder slide, which is about 0.13-0.16 mm thick. Any particles on the sample-holder are expected to be sharply focused as tiny spots in the near-field camera image. Also the surface roughness of the sample-holder slide causes scattering of the evanescent field as a bright circular area in the near-field camera.

○

After the evanescent field is well focused in the ambient environment, the sample-solution or the scan medium can be dropped on the sample-holder slide. Often the sample solution requires five minutes to wait until the particles in the droplet are steadily settled on the sample-holder slide for scans. The evanescent field has to be adjusted to obtain the best optical sensitivity every time after the sample-holder slide is changed or the sample-solution/scan-medium is dropped.

3.2.3 Sensitivity Calibration and Optimisation

After preparing the evanescent field, the cantilever needs to be carefully positioned into the evanescent field before calibration. One requirement is that the cantilever is to be perpendicular to the x-y horizontal plane, i.e. the actuation to position the cantilever is purely in the z-direction. Because there is often a

limited driving range of the z-axis actuator, the cantilever has to be placed at an appropriate distance away from the sample-holder. Hence, the cantilever is suggested to be manually positioned at the upper edge of the evanescent field where the cantilever just slightly scatters/reflects the light field as shown in Figure 3.6b and 3.6c.

The optical sensitivity is then to be calibrated by using the method introduced in Antognozzi (2000). During calibration, the laser is fully powered to maximise the evanescent field strength. The cantilever is still without any excitation and positioned at a fixed point in the horizontal plane above the sample-holder. Then, the cantilever is vertically translated to gently touch the sample-holder surface. As the cantilever is attached to the sample-holder, the cantilever and its reflection moves with the motion of the sample-holder slide. For calibration, the sample-holder is driven by a sinusoidal signal at low-frequency with a constant known amplitude along the y-axis. The cantilever attached to the sample-holder consequently causes a sine-wave optical measurement in voltage at the same frequency as shown in Figure 3.7. The sensitivity constant $S_{y,calib}$ at the set-point in y-direction is computed by

$$S_{y,calib} = \frac{Amp_{y,resp}}{Amp_{y,motion}} \tag{3.2}$$

where $Amp_{y,motion}$ indicates the amplitude of the sample-holder translation along a sine wave in y-axis. The $Amp_{y,resp}$ is the amplitude of the sine wave response of the optical measurement, the detected cantilever deflection by the sensing mechanism.

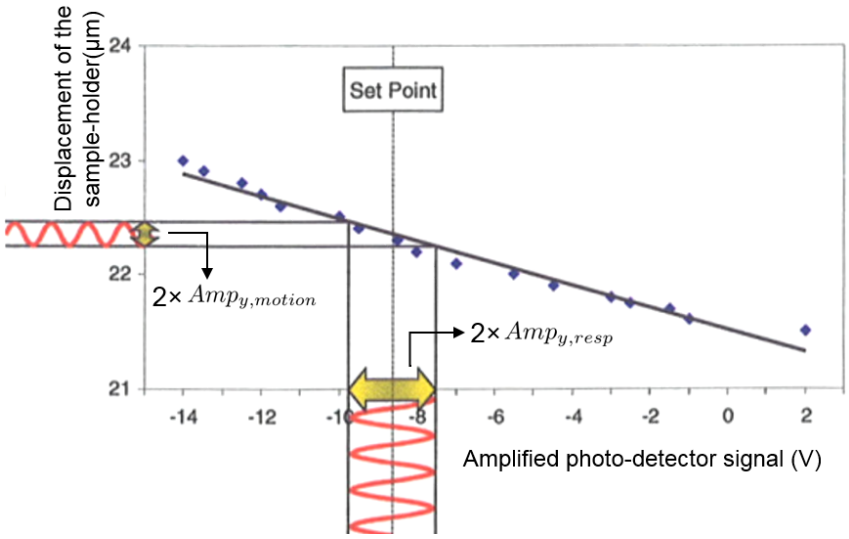

FIGURE 3.7: The schematic presents the method for calibrating the optical sensitivity to measure the cantilever deflection in the TDFM. The amplitude of the measured cantilever deflection signal $Amp_{y,resp}$ is divided by the known cantilever motion amplitude $Amp_{y,motion}$ to obtain the low-frequency sensitivity $S_{y,calib}$.

In practice, the sample-holder is usually driven by a sine-wave with a 0.1 μm amplitude along the y-axis at 1 Hz. The optical measurement from the photo-detector is 25 times amplified to obtain the $Amp_{y,resp}$ for computing $S_{y,calib}$ in the calibration procedure. The measurement is low-pass filtered at

a cut-off frequency at 1 MHz, i.e. the sensing bandwidth of the photo-detector, to reduce electro-noise. In order to achieve 1 nm/pixel resolution in horizontal plane, the sensitivity constant $S_{y,calib}$ has to be approximately 6 mV/nm at least (see an optimised evanescent field with a cantilever type A in Figure 3.8b). For a 2 nm/pixel scan, the $S_{y,calib}$ has to be about 4 mV/nm to ensure a sufficient signal-to-noise ration in scans. Practically, the evanescent field is affected by various conditions, e.g. the thickness of the sample-holder slide, the scan medium, the actual geometry of the cantilever's tip, etc. It is found that the calibration procedure is a necessary check before any experiments in the TDFM. Additionally, the calibration of $S_{y,calib}$ helps to compute the actual cantilever deflection for modelling the cantilever dynamics, which is is a basic requirement for the design of the shear force estimator in Chapter 5.

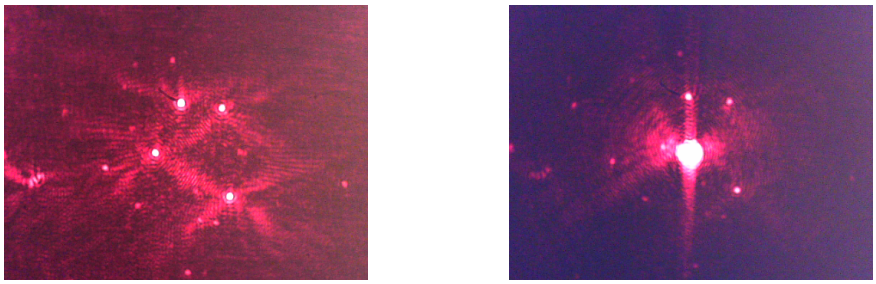

(a) (b)

FIGURE 3.8: An optimised evanescent field is generated by the full power laser source and is observed by the near-field camera: a) the optimised evanescent field with samples in water environment; b) the optimised evanescent field with a cantilever and samples in water environment.

Remark 2 Depending on specific experimental conditions, sometimes it needs significant diligence to reach sufficient optical sensitivity. Some hints are learnt from practice as the suggestion to maximise the optical sensitivity $S_{y,calib}$:

- *Hint 1)* The evanescent field has to be well adjusted when the total internal reflection just appears, i.e. the strength of the evanescent field is maximised.
- *Hint 2)* The sample-holder slide needs to be perpendicular to the vertical z-axis as much as possible, otherwise the evanescent field will be away from the central focal axis too much to be captured by the photo-detector.
- *Hint 3)* The cantilever is best to be placed at the centre of the evanescent field in both x and y directions, because the centre has a maximal strength and subsequently maximum optical sensitivity.
- *Hint 4)* It is possible to adjust the blocker (see Figure 3.4) to allow for a small portion of the reference beam together with the light reflected from the cantilever. This will increase the strength of the light reflected by the cantilever and subsequently improve the optical sensitivity. However, the portion has to be well controlled to avoid influencing the cantilever-deflection measurement.

- *Hint 5)* The photo-detector is suggested to be positioned to image the focal plane of the objective lens, i.e. the light reflected from the evanescent field is well focused as a very tiny spot on the photo-detector. This maximises the optical sensitivity to the cantilever deflection.

○

3.3 Novel Mechatronics Design

The new system design mainly focuses on facilitating the vertical positioning of the cantilever in the z-axis. The first part introduces the electronic design of the sensing system measuring two cantilever position signals: the distance from the cantilever towards the sample-holder slide, and the distance between the oscillating cantilever and the sample-substrate. Particularly, a novel electronic design is developed for sensing the cantilever-sample inter-distance by averaging the cantilever oscillation amplitude. The novel design avoids the use of lock-in amplifiers or PLL devices, i.e. the sensing component of the TDFM is simplified and the sensing range of the shear-force-interaction is significantly increased. The actuation and digital control components are designed to implement real-time feedback control for the TDFM scans. The new digital control solution allows to implement high-order controllers, i.e. advanced control algorithms can be applied to the cantilever positioning control compared with the previous PID control scheme. In addition to the positioning system in the z-axis, the horizontal x-y positioning component is presented as the last part of the second section.

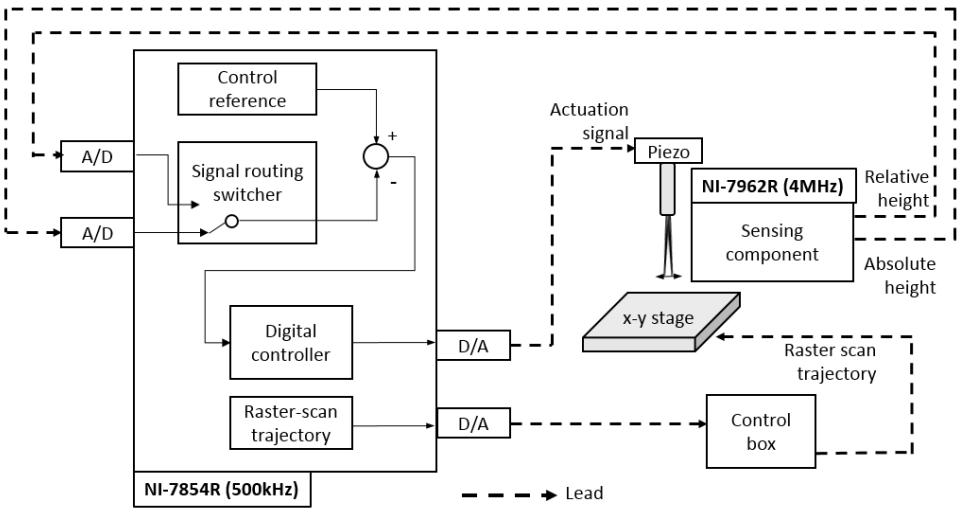

FIGURE 3.9: The concept design of the TDFM control system. The cantilever vertical positioning system is controlled using either the absolute/relative height measurement by a feedback loop. The topographic data is simultaneously generated by recording the other height measurement. A commercial x/y horizontal stage is controlled by a control box given raster scan trajectory from the NI-7854R FPGA board.

This work applied an FPGA based real-time control solution in order to achieve high sensing and control bandwidth (see the concept design in Figure 3.9). FPGA based solutions are powerful and still

novel in the AFM control area (Kuiper et al. 2013, Soltani Bozchalooi 2015). FPGA based design easily permits prototyping different digital circuit designs and promises reliability to run a control program at high sampling frequency. Here, an NI-7962R and an NI-7854R both integrating DSP-slices and FGPAs onboard are chosen from National Instruments (NI) Co. (2015). To programme the real-time control, the coding environment is the NI LabVIEW (2011 version) with an NI FPGA module. Practical programming design issues are resolved by the developed solutions.

Note that the electronics are deployed on two FPGA boards, because the hardware resource on each board is limited and they have each special capabilities. The NI-7962R allows to run the sensing electronics at a high frequency of 4 MHz, i.e. high sensing bandwidth. The NI-7854R, a lower cost cost equipment than the NI-7962R, is fully loaded by the control programmes running at a relatively low 500 Hz sampling rate. In this way, the electronic design maximises the deployment efficiency of both FPGA boards achieving an optimal functionality of the system and retaining a relatively low cost.

3.3.1 Signal Measurement

The electronic components for sensing employ a customised pre-amplifier (SA500 provided by Wolfgang Oeffner, Germany) to amplify the signals from the photo-detector (Figure 3.10). The light intensity $V_{Light\ intensity}$ is 20 times amplified and low-pass filtered with a 1 MHz cut-off frequency. The amplified signal is directly used as a measure of the absolute height that presents the distance from the cantilever away from the sample-holder slide.

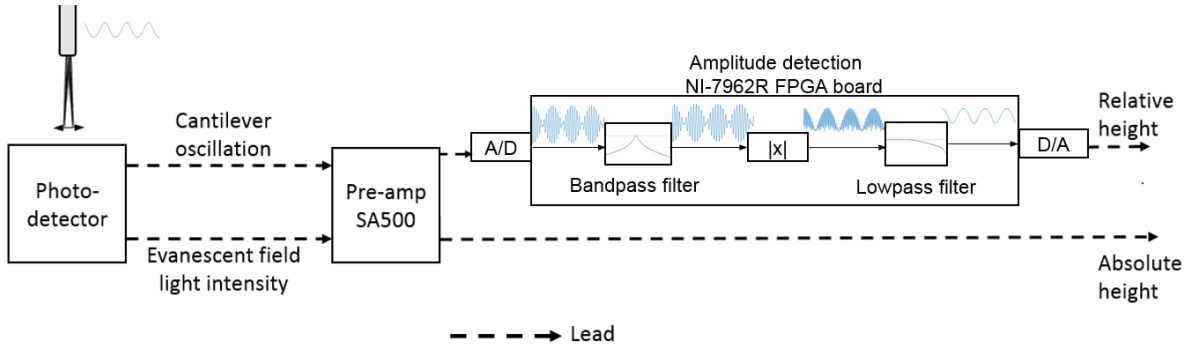

FIGURE 3.10: The concept design of the sensing component measuring two cantilever vertical positions.

As shown in Figure 3.10, the cantilever oscillation signal V_y is amplified by a gain of 500 and bandpass-filtered by using a bandwidth region from 1 kHz to 1 MHz in experiments. The bandpass filtered signal is led to an NI-5781 baseband transceiver to be processed by an NI-7962R FPGA board with an analog input range of ± 1 V. On the NI-7962R board, the digitized signal is filtered by a bandpass filter to focus on the region around the excitation frequency of the selected cantilevers in each experiment, i.e. the influence of low frequency disturbances and high frequency electro-magnetic noise is partially eliminated. Then, a low-pass filter is applied to the absolute value of the bandpass filtered signal. Hence, the averaged

(low-pass filtered) absolute value of the oscillation signal, i.e. a measure of the signal amplitude, is sent to an analogue output channel with a range of ±1 V. This cantilever oscillation amplitude signal is regarded as the relative height, i.e. a measurement of the distance between the oscillating cantilever and the sample-substrate. In practice, the type A cantilever is excited at its first resonance 200 kHz in water and is only used in the wet environment created by purified water. The bandpass region is designed with an 180-220 kHz bandpass region and the low-pass filter has a cut-off frequency at 60 kHz. The type B cantilever oscillates at 350 kHz, which is its first resonance in ambient condition and around another resonance in the wet environment. Hence, in the design, the bandpass region is chosen from 330 kHz to 370 kHz and the low-pass filtering cut-off frequency is 100 kHz. The NI-7962R is configured to run at 4 MHz clock frequency to guarantee fast enough data acquisition speed and high signal processing bandwidth.

As a result, the sensing solution is presented as shown in Figure 3.10. There are two cantilever vertical position measurements provided by the sensing components (see Figure 3.11):

- **Relative height**: the distance from the cantilever to the sample-substrate (which is related to the amplitude of the cantilever oscillation).
- **Absolute height**: an increase in distance of the cantilever to the sample-holder causes the total light intensity of the tuned evanescent field to decrease.

Note that the absolute height is a direct measurement of the light strength reflected from the evanescent field. The relative height measurement is an indirect measurement of the cantilever-sample interaction. Hence, the sensitivity of both height measurements depends on the quality of the evanescent field, the geometry of the cantilever-tip, and the scan medium. Particularly, the cantilever-sample interaction is also affected by the oscillation frequency and the excitation amplitude of the cantilever. As a result, the relative height measurement is additionally conditioned by the cantilever excitation signal and the cantilever's mechanical characteristics also varying with the scan medium.

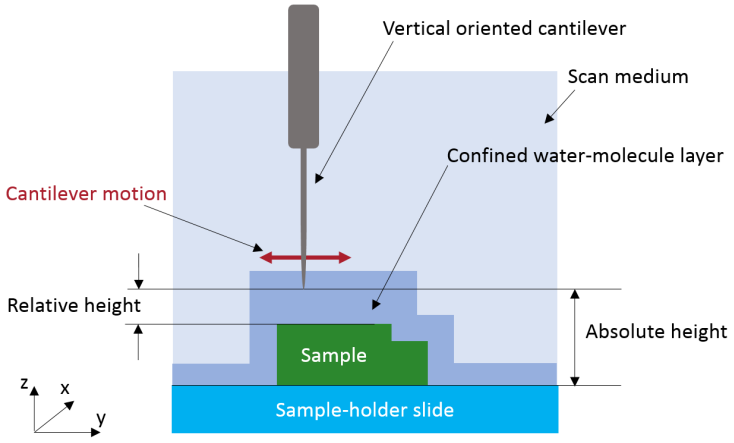

FIGURE 3.11: Absolute height and relative height measurements of the cantilever in the TDFM.

3.3.2 Actuation and Digital Feedback Control Solution

The vertical axis positioning system consists of the introduced optical sensing system, the cantilever, two vertical, and one horizontal piezo actuator. In detail, a TDFM-head is designed to accommodate the cantilever chip and piezo actuators as an adjustable unit, which is manually operated to localise the cantilever as introduced in Section 3.2.1. As shown in Figure 3.12, the chip holder is attached to the dither piezo-actuator (PL088.31, Physik Instrumente (PI) GmbH & Co. (2015)) at the end of the TDFM head. The dither actuator is driven by an external signal generator (with a frequency range from 0.1 Hz to 20 MHz) to horizontally excite the cantilever in the y-axis direction. The coarse piezo-actuator (P-885.51, PI) has a nominal translation of 125 nm/V, providing the cantilever a large constant translation to position it into the evanescent field. Such a positioning action is not easy to carry out via closed-loop control as the sensitivity of the cantilever detection is highly nonlinear and also strongly distance limited. The fine piezo-actuator (PL055.30, PI) is to drive the cantilever in the vertical direction (z-axis) for feedback control when scanning the specimen. The fine actuator has a nominal actuation of 22 nm/V subsequently enabling precise control performance.

The TDFM head is sat on a TDFM base that holds the horizontal stage carrying the sample-holder slide at the planar centre. Both the TDFM head and the base are manufactured at high weight, hence, the influence of the piezo-actuation components on the system dynamics is minimised. The piezo-actuation component is designed to be at the planar centre of the mass of both the TDFM head and the base. Therefore, the cantilever-chip is always positioned at the planar centre of the mass.

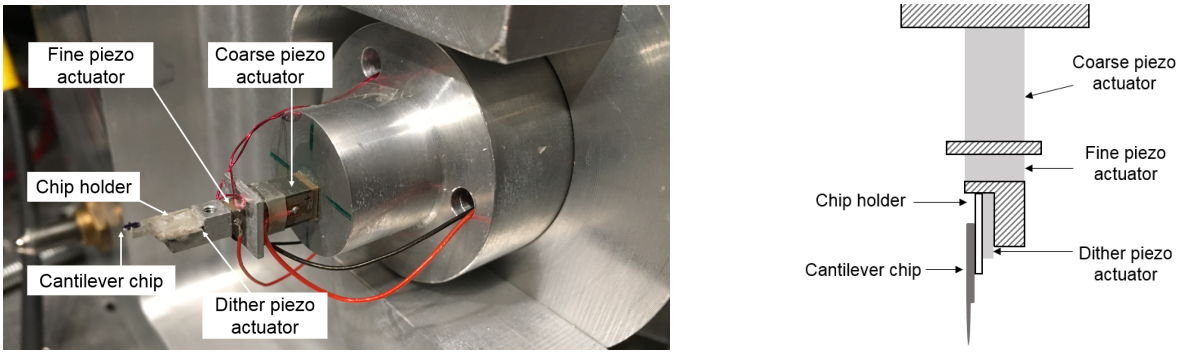

(a) (b)

FIGURE 3.12: A photo a) and the mechanical set-up b) of the TDFM head which consists of the chip holder to attach with the vertically oriented cantilever chip, a dither piezo-plate to excite the cantilever horizontally, a coarse piezo-actuator to vertically position the cantilever in the sensing range, and a fine piezo-actuator to facilitate the closed-loop vertically positioning.

The real-time control of the vertical axis positioning system is designed as shown in Figure 3.9) on an NI-7854R FPGA board (NI). The digital control loop runs at the frequency of 500 kHz considering the maximum A/D channel sampling rate of 750 kHz. The A/D and D/A channels have the same input/output range of ± 10 V and the input/output digital variables are presented by signed $I16$-variables (16-bit integers) by default. For a uniform the representation of variables, the absolute height and relative

height measurements are both presented by signed $I16$-variables on the NI-7854R, the host-PC, and in the following content.

For the vertical cantilever positioning system, a negative feedback control loop is constructed by taking the control error of a height measurement and using a digital controller. In the design, the reference signal is given by a digital signal generator programme (modified from the default signal generator block in the NI FPGA module) on the FPGA board. The digital controller is designed as customisable digital filters, i.e. various controller designs can be implemented and tested in this work. The control signal (in signed $I16$ representation) is converted by an D/A channel and directly drives the fine piezo-actuator. Hence, the vertical axis control has an actuation range of 440 nm with a resolution of about 0.067 nm per integer representation. Here, a signal routing function can switch to feedback either of the two heights to be controlled for retaining a constant height. Meanwhile, the other height signal is recorded as the topographic data. In principle, the vertical axis control solution permits two scanning modes:

- constant relative height (CRH) scan: The absolute height is recorded as the topographic data while keeping a constant relative height to the sample-substrate.
- constant absolute height (CAH) scan: The cantilever is kept at a constant distance to the sample-holder slide. The top part (within the relative height sensing range below the scanning height) of the specimen is imaged.

The horizontal x/y-axis control employs a nano-precision x-y stage (P.734, PI) with a digital control box (E-710, PI). A trajectory planner is designed to provide the trajectory reference signals in the x and y directions from the NI-7854R. The raster trajectory has to be customisable to adjust the size of a scan task, the scanning speed, and the imaging resolution.

In the trajectory planner, two digital integrators with customisable step-sizes are programmed for x-axis and y-axis separately. The step-sizes are calculated on the host-PC while configuring the raster scans in terms of frame-size, imaging resolution, and scanning speed. Here the x-axis, which is horizontally perpendicular to the cantilever excitation direction, is set as fast axis along raster patterns. Thus, the fast scanning motion has little influence to height measurements. There are two common AFM raster scanning trajectories as shown in Figure 3.13. One trajectory retains a constant slow axis position and drives the cantilever along the fast axis in forward and back-ward direction (Figure 3.13a). The other trajectory moves the cantilever along a sawtooth trajectory as shown in Figure 3.13b. Using both scan trajectories, the sample-substrate topographic data collected in forward direction and in back-ward directions are called trace data/image and retrace data/image respectively. A successful scan has high similarity between the trace and retrace data (see scanning results in Chapter 6). Both the scan trajectories are implemented, whereas the sawtooth trajectory is not used in practice. This is because the first trajectory keeps a constant displacement along y axis in each scanning line, i.e. the influence on cantilever excitation in y-direction is less than using the sawtooth trajectory. The planned trajectory

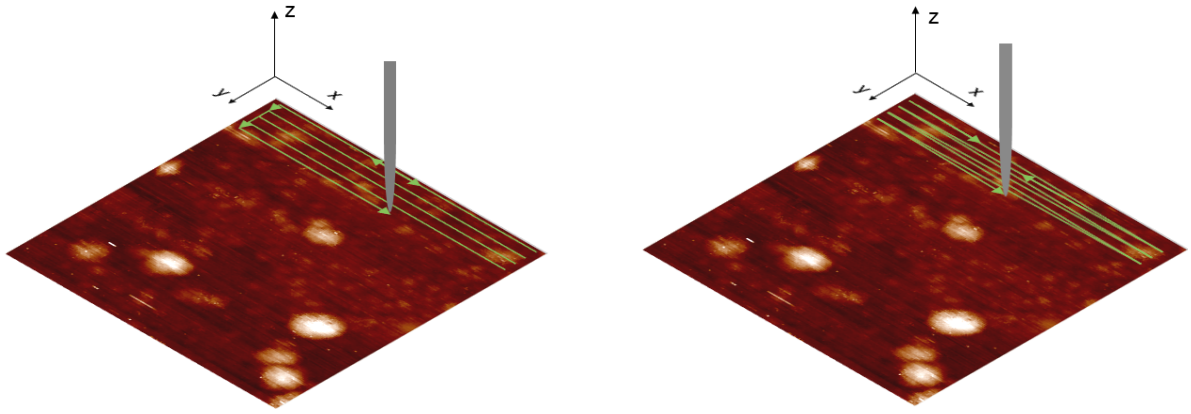

(a) (b)

FIGURE 3.13: Two typical raster scanning trajectories in AFMs are programmed in this work, whereas only the design in a) is adopted for less interference on the vertical axis measurement caused by the raster scanning displacement in the y-direction. The topographic data are collected as the trace image and the retrace image when the cantilever is driven forward and back-ward in the fast scanning x-axis respectively.

signals have a range of ±10 V from two AI channels of NI-7854R. Then, these signals are amplified with a gain of 0.1 by an analogue circuit in order to reduce the noise from the FPGA board. As a result, a 1 nm resolution can be achieved with a noise level at about 0.015 nm. Another two AI channels are used to provide constant displacement with a range of 10 μm for a large enough area to allocate specific specimens.

3.4 Control Programmes and Offline Optimisation Tool

This section presents practical programming strategies to implement the integrated control of the TDFM. As the FPGA boards run at very high implementation rates, an efficient data streaming structure is necessary for real-time data monitoring and processing via the host-PC. In FPGA design, it is straightforward to implement a control programme whilst it is a travail to guarantee the robustness of the programme during dynamic scans. Hence, a practical programming solution is suggested for quick FPGA programming implementation. Additionally, an offline FPGA programme optimisation tool is developed to enhance the robustness of the FPGA functional components.

3.4.1 Data Streaming Scheme

The communication between the host-PC and the FPGAs (NI-7962R, NI-7854R) is set up using a direct memory access (DMA) approach, which is a first-in-first-out bus mechanism. In detail, the host-PC commands the FPGAs to configure the FPGA boards, the scan trajectory, and feedback control for vertical positioning system. Also, the host-PC receives a huge amount of data from the FPGA boards

FIGURE 3.14: The graphic user interface of the TDFM in a scanning task.

to real-time image the scans and monitor the TDFM system status (e.g. cantilever oscillation signal, vertical positioning control performance, etc.) using three DMAs. As the PC has a limited memory and computational capability, the programmed control software only permits to monitor one fast DMA channel from NI-7962R at a sampling frequency of 4 MHz. The PC uses the other two DMA channels to capture data from NI-7854R at a 500 kHz sampling frequency: one DMA is to process the control signal, the control error and two height measurements; one DMA is used to receive x/y coordinate values of the imaging position in the horizontal plane.

The real-time topography imaging feature requires more computational resource of the host-PC compared with the data monitoring features, which are commonly used for online checking the control performance of each positioning systems. Hence, a two layer buffer structure is programmed on the host-PC in order to process the large amount of real-time data. The fast buffer immediately loads the data from the DMA to the random-access memory (RAM) of the PC to avoid overflow of the DMA. The data monitoring feature shows the data from the first buffer directly on the graphic user interface (GUI) of the TDFM system. The second buffer processes the topographic data and the corresponding x/y position from the fast buffer for data processing and real-time imaging at a slower speed (see the GUI as shown in Figure 3.14). Note that the data from separate DMAs are not naturally synchronised due to the time difference of initialising DMAs. Here, a digital trigger is programmed on the NI-7854R to assist the host-PC to recognise the start/pause/end time point of a scan. Using this approach, the synchronisation between the topographic data and the x/y position data is achieved for image processing in scans.

3.4.2 Practical Issues in Digital Control using the FPGA Boards

The FPGAs (NI-7962R, NI-7854R) allow both integer and fixed-point presentations in FPGA programming. Fixed-point arithmetic is adopted as an efficient way to implement controllers in FPGA-control implementation (Monmasson & Cirstea 2007) with the advantage of low computational resource

requirement and applicability to fast execution. The numeric range and the precision of the fixed-point-arithmetic are customisable, but are fixed at the time of implementation. The calculation range and the precision of the fixed-point-arithmetic is limited by the length of the assigned binary bits. An overflow occurs when the (ideal) calculation result exceeds the assigned length of the fixed-point arithmetic, i.e. the actual FPGA results can easily "saturate" at the maximal/minimal values. The overflow can cause non-linearity and unpredictable/unstable control. It is possible to avoid overflow and to improve the fixed-point arithmetic accuracy by using more digits to represent variables and to execute the calculations. However, the FPGA computational source is physically fixed.

Moreover, careful FPGA resource distribution is a significant practical issue for fixed-point arithmetic based digital control. In practice, the commercial method to implement high order transfer functions is to employ loops for the repetitive fixed-point-arithmetic parts in a transfer function (see implementations in Section 3.4.3). However, a transfer function block implemented by using loops has to run at a slower overall sampling frequency to obtain the filtering results. For example, the loop design of a 6th order digital filter reduces over 60% of the fixed-point arithmetic operations when compared to an intuitive Transposed-Direct-Form-II implementation. However, the Transposed-Direct-Form-II implementation permits the programme to execute at a higher sampling rate than the commercial loop-format programming structure.

Also, it is impossible to run a complex calculation, like a digital filtering process, in just one single on-board clock cycle time. For example, it takes about one on-board clock cycle to execute one 32-bit multiplication. Hence, filter operations always require several cycles. A feasible solution to practically implement a feedback controller is to divide the program into different parts. By running each part in parallel, the overall program performs as a digital controller and requires fewer clock cycles, i.e. it allows for higher sampling frequency of the digital control. However, the parallel programming scheme introduces more latches/shift-registers or requires more hardware resources to transport data between different clock cycles. Hence, the programming structure needs to be carefully designed considering the sampling frequency and the time delay of the digital feedback controller.

The ranges of the A/D and D/A channels on FPGA boards constrain control accuracy and practical implementation. For instance in this work, the A/D input channels of the NI-7854R have an input range of ± 10 V which is presented as signed 16-bits integer numbers, i.e. the resolution of an input/output port is constrained at ($10 \text{ V} \div 2^{15} \approx$) 0.305 mV. The input representation accuracy affects the calculation results of the digital transfer function programme, and consequently influences the digital control output accuracy. Moreover, the maximum control output relates to the digital control gain on-board. Hence, the actual A/D and D/A signal ranges have to be balanced with respect to the digital control function on the FPGA boards. The other issue is that A/D and D/A channels are limited by their maximal hardware-constrained sampling frequency. For instance, the NI-7854R FPGA for control implementation can run at most at a clock frequency of 40 MHz but the A/D sampling frequency is at most only 750

kHz. Only if all the above mentioned aspects are taken into account can the FPGA program be uploaded and run successfully on the FPGA boards.

3.4.3 Digital Filtering in Fixed-Point Arithmetic

A single-input-single-output controller can be implemented by a filter H, equivalently presented by a transfer function without time delay in the Laplace $\mathcal{L}$ domain as

$$H(s) = \frac{b_{n,con}s^n + b_{n-1,con}s^{n-1} + .. + b_{1,con}s + b_{0,con}}{a_{n,con}s^n + a_{n-1,con}s^{n-1} + .. + a_{1,con}s + a_{0,con}} \tag{3.3}$$

Here, $a_{N,con}$ and $b_{N,con}$ are real number coefficients for the denominator and the numerator of $H(s)$ in $\mathcal{L}$ domain where $N = n, n-1, .., 1, 0$ and n is the order of $H(s)$. A filter $H(s)$ is adopted to be implemented as an infinite impulse response (IIR) filter in a digital design. To do so, the $H(s)$ has to be discretised and transformed into $H(z)$ as:

$$H(z) = \frac{b_n + b_{n-1}z^{-1} + .. + b_1 z^{-n+1} + b_0 z^{-n}}{1 + a_{n-1}z^{-1} + .. + a_1 z^{-n+1} + a_0 z^{-n}} \tag{3.4}$$

where $b_{N=n,n-1,..,1,0}$ and $a_{N=n,n-1,..,1,0}$ are real numbers as the coefficients of $H(z)$.

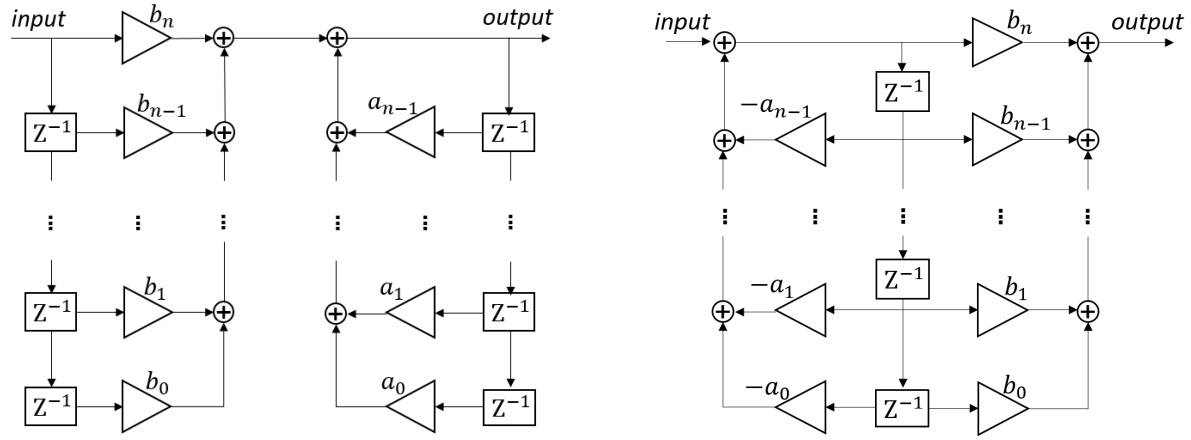

(a) Transposed Direct Form I

(b) Transposed Direct Form II

FIGURE 3.15: Transposed Direct Form I and Transposed Directed Form II implementations of digital IIR filters in digital circuit design.

A digital IIR filter $H(z)$ is commonly implemented in two formats: Transposed-Direct-Form-I (TDF-I) in Figure 3.15a and Transposed-Direct-Form-II (TDF-II) in Figure 3.15b. Both implementation formats employs multiplication, addition, and z^{-1} delay operations on the FPGA boards. In FPGA digital circuit design, the z^{-1} delays are preferred to be implemented by using shift-registers, which shift the fixed-point variables from the last clock cycle to be computed at the current cycle at minimal hardware resource cost. Additionally, the input variable, output variable, the multiplication operations, and the addition operations are implemented in fixed-point arithmetic. It is clear that the TDF-I format requires

more digital hardware resource to programme more z^{-1} delays than the TDF-II format implementation needs. Hence, the TDF-II implementation is adopted for digital filter implementation at high-sampling frequency in this work for the sake of reducing hardware resource cost. Particularly, the lowpass filter and the band-pass filter are directly implemented as two 2nd order transfer-functions in the TDF-II format running at 4 MHz on the NI-7962R.

On the NI-7854R, the digital controller may be implemented by a high-order transfer function, which the FPGA programme also requires to be compatible with. The overall 500 kHz clock frequency theoretically allows the execution of an up-to 6th order digital filter. In order to reduce the hardware resource usage, the digital filter programme in TDF-II form is transformed and implemented in a cascaded biquad form using loops as shown in Figure 3.16. Note that the subtraction and multiplication of the coefficients operations are also implemented by fixed-point arithmetic in the programme. Overall, the digital control programme employs two 6th order digital filters in series running in parallel, i.e. advanced control design like H_∞ controller can be implemented.

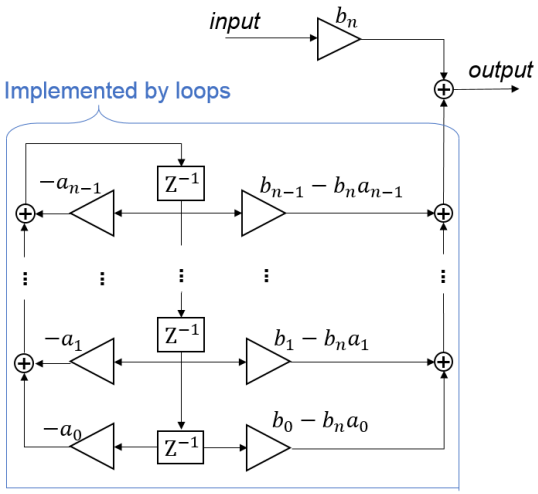

FIGURE 3.16: The transposed direct form II implementation of a digital filter is transformed and implemented in cascaded biquad form, i.e. the digital filter can be implemented using loops to save computational hardware resource.

Importantly for the FPGA digital filter design, the TDF-II implementation and the cascaded biquad TDF-II implementation have limited accuracy and computational range with respect to the fixed-point arithmetic configurations. The coefficients at higher order of a filter $H(z)$ have stronger influence on the accuracy and the computational range of the implementation due to more computational contribution on the final filtering output.

This thesis suggests employing a bank of digital filters in series with a pre-chosen constant fixed-point-arithmetic range instead of verifying each arithmetic element carefully, since the amount of validation tests exponentially increases with respect to the order of the filter. Particularly, in the relative height sensing electronics and the digital feedback control programme, every fixed-point arithmetic is configured as signed $fxp(32, 16)$ (i.e. 32 bits word length overall with 16 fractional bits). For each filter component,

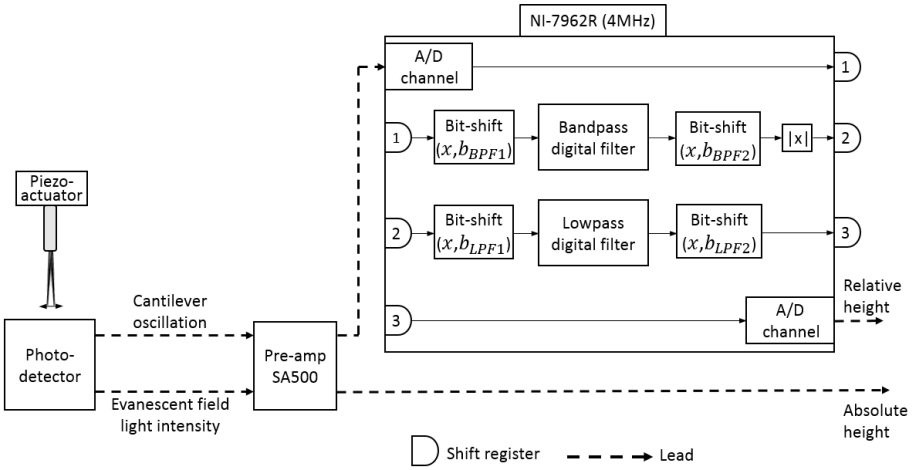

(a) The electronic design of the cantilever vertical position sensing component.

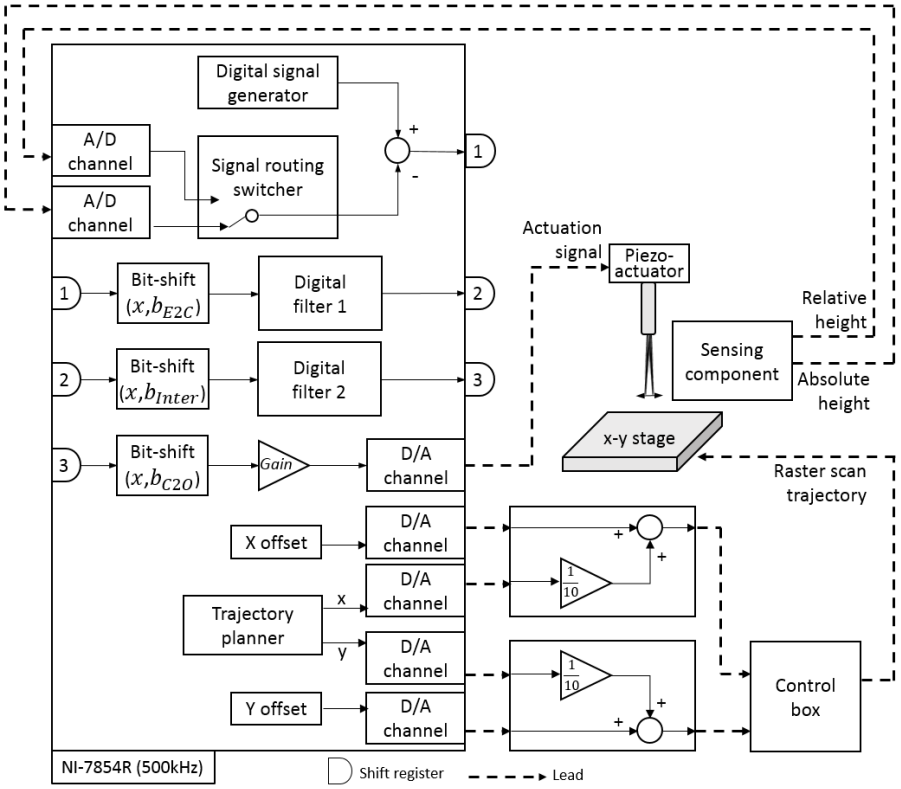

(b) The electronic design of the integrated TDFM scanning system.

FIGURE 3.17: The electronic design of the TDFM system.

a specific relative fixed-point value representation is used to avoid overflow and to improve calculation accuracy, and extra gains are introduced before, between, and after each digital filter in the filter bank. The new 'internal' gains have to have an overall product of unity to retain the originally designed linear control performance. This permits better exploitation of the computational range of the digital filters,

which are configured to have a specific fixed point representation.

Hence, the TDFM scan system, including the electronics and the FPGA programmes, is designed as shown in Figure 3.17. In this paper, the $bit\text{-}shift(x, b)$ represents the bit-shift operation that shift an arbitrary input x by b integer-bits in zero-fill manner. In detail, $bit\text{-}shift(x, b_{BPF1})$ for the bandpass filter and $bit\text{-}shift(x, b_{LPF1})$ for the lowpass filter are introduced in the relative height sensing component. Here b_{LPF1}, b_{LPF2}, b_{BPF1}, and b_{BPF2} are signed integer parameters in each bit-shift operations for the low-pass filter and the bandpass filter in Figure 3.17a. The bit-shifts ($bit\text{-}shift(x, b_{BPF1})$, $bit\text{-}shift(x, b_{LPF1})$) at the inputs of each filters are paired with the bit-shifts ($bit\text{-}shift(x, b_{BPF2})$, $bit\text{-}shift(x, b_{LPF2})$) at the relevant filter outputs to set the combined gain of each pair, ($bit\text{-}shift(x, b_{BPF1})$, $bit\text{-}shift(x, b_{BPF2})$) and ($bit\text{-}shift(x, b_{LPF1})$, $bit\text{-}shift(x, b_{LPF2})$), to one. For the feedback control, FPGA boards take a long time to execute A/D conversion and D/A conversion. Thus, the data importation and exportation functions are designed to run as separate parallel programs. The bit-shift operations ($bit\text{-}shift(x, b_{E2C})$, $bit\text{-}shift(x, b_{Inter})$) are used to adjust the input range of the two digital filters respectively to avoid overflows. Here b_{E2C}, $b_{b_{Inter}}$, and b_{C2O} are signed integer parameters in each bit-shift operations for the control filter-bank (including Digital filter 1 and Digital filter 2 functional blocks) in Figure 3.17b. In order to retain the designed control magnitudes, another bit-shift $bit\text{-}shift(x, b_{C2O})$ is designed to compensate for the gain shift from the other two bit-shifts. At the output of the filter bank, a tunable gain *Gain* is introduced, to be adjusted for the change of the measurement sensitivity of the evanescent field sensing system. The configuration of (b_{E2C}∈[-32,32], b_{Inter}∈[-32,32]) determines the numerical working range of the digital feedback control loop. The functional range is bounded when the filter bank and *Gain* are confirmed.

Remark 3 Note that the poles and zeros of $H(z)$ are sensitive to the quantisation error of the fixed-point arithmetic configurations, especially for high order implementations. Hence, with respect to particular digital filter designs, the zeros and poles of a complex transfer function has to be carefully distributed into two digital filter blocks to avoid overflows and achieve high numerical accuracy. Thus, complex controllers, e.g. using robust control design, are implementable at fast clock frequency with some design flexibility. This is one other important reason for deploying two digital filters to implement the controller in this work. ∘

3.4.4 An optimisation Tool and Examples to Enhance the Implementation Robustness

The fixed-point based signal processing programs work only within a limited fixed-point numerical range. Practically, the range is dynamically configurable by manipulating the bit-shift operations in each specific filter. It is vital to avoid any computational failure, which can be caused by overflows or the lack of computational accuracy.

The digital feedback control program has to be designed robust to disturbances and the change of environmental conditions. In detail, a rapid disturbance change may cause overflows in the fixed-point-arithmetic based digital filters. The strength of the evanescent field influences the measurement sensitivity and determines the range and the precision of the signals. Hence, the methodology will be to design at first a continuous-time controller which is then discretised at the required sampling frequency. Subsequently, a simulation based optimisation of the FPGA-implementation parameters is practically carried out. Hence, the fixed-point based control programmes need to be optimised before being deployed on FPGA boards.

Although FPGAs have been widely used in industry for control purposes (Monmasson & Cirstea 2007), there are few research results presenting the design methodology and the relevant programming optimisation method. For instance, in the AFM control area, Soltani Bozchalooi (2015) proposed an evaluation method to optimise high-order digital controller implementations. However, this method only fits the controller that are made up by second order filters programmed in a particular programming structure, i.e. the method is not applicable to the high-speed filter design considering both execution speed and minimal memory-usage in Figure 3.15b. Alternatively, a method was developed by Fang et al. (2005) for optimising closed-loop controllers that are implemented on FPGA boards in fixed-point arithmetic. This method optimises each fixed-point arithmetic in the digital filtering implementation, specifically for a second-order controller in the paper, without considering the hardware resource limitation.

All the mentioned optimisation methods (Fang et al. 2005, Soltani Bozchalooi 2015) for the fixed-point arithmetic based digital control programmes are developed for a pre-designed filter/controller with fixed FPGA implementations. When a different controller is required for tests or an alternative closed-loop system, the FPGA board has to be stopped and reloaded with a different pre-configured fixed-point implementation. Differently, in the developed TDFM system, a consistent implementation is used for deploying different controllers. Only bit-shift operations are optimised offline to guarantee a robust digital filtering performance. As a result, it is possible to test different control algorithms under the same experimental condition. This also allows to online switch the absolute/relative height control algorithms that can be implemented by one single FPGA implementation, i.e. hardware cost for controller implementation is minimised.

Therefore, a universal optimisation tool is suggested to offline assess the digital signal processing programme designs prior to practical FPGA deployment. Within this work, a Simulink-based (The

MathWorks, Inc. 2018) simulation tool has been developed to verify the FPGA control performance before NI-FPGA on-board implementation in the NI-LabVIEW real-time control environment. The arithmetic operations are simulated using the fixed-point toolbox and introducing the practical time delays of the circuit to achieve an accurate replica of the practical implementation.

Case a: Optimisation of the FPGA programme in the sensing component

The sensing FPGA programme optimisation procedure is shown with an example of using the cantilever type B. In the design, the bandpass (with 330 - 370 kHz bandpass range) and low-pass filters (at 100 kHz cut-off frequency) are both 2nd order Butterworth filters directly implemented in the TDF-II form running at a 4 MHz clock frequency on the NI-7962R. Hence, the bandpass filter and lowpass filter (in discrete time) are given as

$$\begin{aligned} T_{BP}(z) &= \frac{0.005543z^2 + 0.01109z + 0.005543}{z^2 - 1.779z + 0.8008} \\ T_{LP}(z) &= \frac{0.03047z^2 - 0.03047}{z^2 - 1.654z + 0.9391} \end{aligned} \tag{3.5}$$

The criterion for testing the appropriateness of the fixed-point arithmetic sensing mechanism is to compare the sensing mechanism to the continuous-time simulation (as simulated for the NI-7962R). Thus, for comparison, the bandpass, the absolute value computation and the lowpass components are also simulated as continuous-time operators, while the output of these combined operations are sampled at 4 MHz to give $s_{cnt}(k)$. The averaged absolute error E_S between the fixed-point-arithmetic simulation output, s_{fpga}, and the continuous-time simulation output, $s_{cnt}(k)$, gives the comparative measure:

$$|\bar{E_S}|_{(b_{BP1},b_{LPF1})} = \frac{\sum_{k=0}^{k=m} |s_{fpga(b_{BP1},b_{LPF1})}(k) - s_{cnt}(k)|}{m} \tag{3.6}$$

where $s_{fpga(b_{BP1},b_{LPF1})}(k)$ indicates the relative height from the fixed-point-arithmetic simulation at the *k-th* sample time with a given pair of (b_{BP1},b_{LPF1}) . The test simulation, for each parameter set, is run for 0.1 s of simulation time, changing the amplitude of the input oscillation 0 - 2 V. The averaged absolute error $|\bar{E_S}|_{(b_{BP1},b_{LPF1})}$ as a function of the bit-shift values b_{BP1} and b_{LPF1} is shown in Figure 3.18. The bit-shift operations clearly influence the performance of the proposed sensing mechanism.

Case b: Optimisation of the FPGA feedback-control programme

The demonstration for feedback control programme optimisation is given for a relative height controller using the cantilever type B in water environment on a grade 0 glass sample-holder (0.085 - 0.13 mm thick). The cantilever is excited at 350 kHz with an oscillation amplitude about 2 nm. Here a linear controller (see (3.7)) is presented using a lag control concept (of which the design concept will be presented in Section 4.3.3 for the type A cantilevers working in water environment). The controller starts with a constant gain at low frequency and ends with a descending gain at high frequency. Two lags dropping their gain after 10 Hz are designed to have sufficient low frequency gain and to avoid any significant

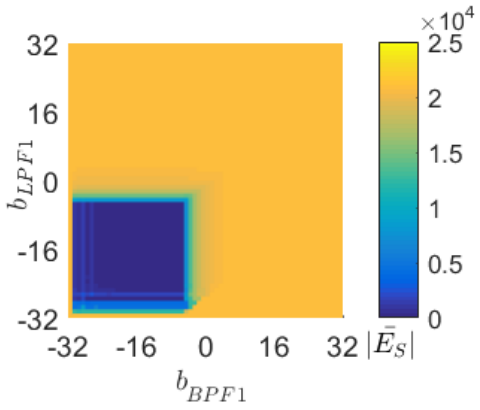

FIGURE 3.18: Evaluation ($|\bar{E}_s|$) of possible fixed-point-based FPGA programming configurations for a sensing mechanism configuration on NI-7962R.

control windup at low frequency. Importantly, a notch filter is introduced to cancel a resonant peak at high frequency (e.g. 35 kHz here). Hence, a continuous time control is designed

$$C_{CantB,L\&N}(s) = \frac{4.446 \times 10^4 s^3 + 9.593 \times 10^8 s^2 + 2.679 \times 10^{15} s + 5.045 \times 10^{19}}{s^4 + 2.525 \times 10^5 s^3 + 5.492 \times 10^{10} s^2 + 1.238 \times 10^{15} s + 3.885 \times 10^{16}}. \tag{3.7}$$

The open loop response of the controlled plant has a phase margin of 74.1° at the crossover frequency of 2.04 kHz with a gain margin of over 25 dB.

Subsequently, the design of the two filters, $F_{1,CantB,L\&N}$ and $F_{2,CantB,L\&N}$, result from the Tustin discretisation at a 500 kHz sampling frequency based on $C_{CantB,L\&N}(s)$ also including an extra gain :

$$\begin{aligned} F_{1,CantB,L\&N}(z) &= \frac{0.02703z - 0.02603}{z^2 - 1.951z + 0.9509} \\ F_{2,CantB,L\&N}(z) &= \frac{0.8173z^2 - 1.479z + 0.8173}{z^2 - 1.479z + 0.6346} \\ k_{Gain,CantB,L\&N} &= 4 \end{aligned} \tag{3.8}$$

It is evident that the design of the bit-shift operators has to be systematically done off-line, as a change of the bit-shift operator characteristics can easily affect closed-loop stability (see fixed-point arithmetic simulation examples in Figure 3.19c).

For the feedback control program on the NI-7854R, the parametric configurations are tested for different bit-shift triples of (b_{E2C}, b_{Inter}, b_{C2O}) from -32 to 32 bits. In fact, in this case, there is only freedom to optimise for $bit\text{-}shift(x, b_{E2C})$ and $bit\text{-}shift(x, b_{Inter})$, because $bit\text{-}shift(x, b_{C2O})$ has to realise the inverse of the other two operations to guarantee the overall gain of 1. For each bit-shift configuration pair (b_{E2C}, b_{Inter}) of different configurations, the control reference (on-board) is given as a square wave at 10 Hz with different amplitude levels for verifying the maximum controllable range. Specifically the amplitudes, r_{amp}, are configured as positive integers of 16 bits from 250 to 12500 which are kept constant during each simulation assessment. However, several tests are created, increasing at each simulation run the amplitude by 250. This creates a physical testing range of 0.76 - 3.815 V for

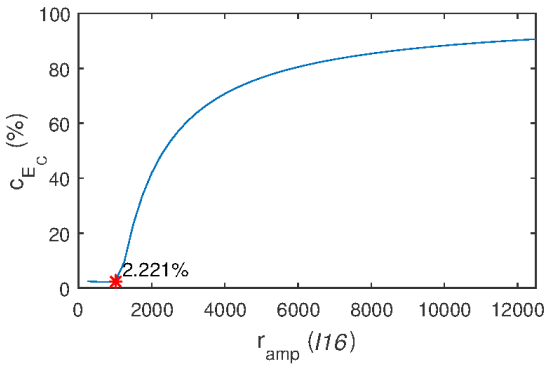

(a) Evaluation of feedback control configuration given $10Hz$ square wave reference with different amplitude on NI-7854R

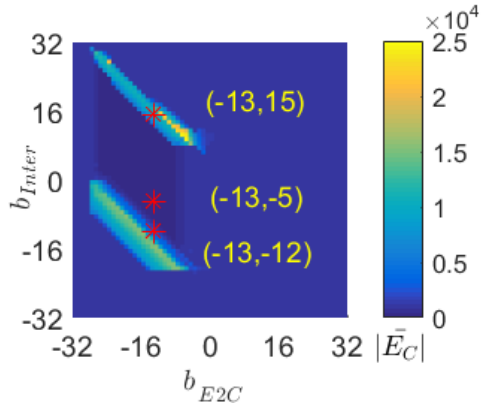

(b) Evaluation ($|\bar{E}_c|$) for feedback control configuration given $10Hz$ square wave reference amplitude as 1000 on NI-7854R

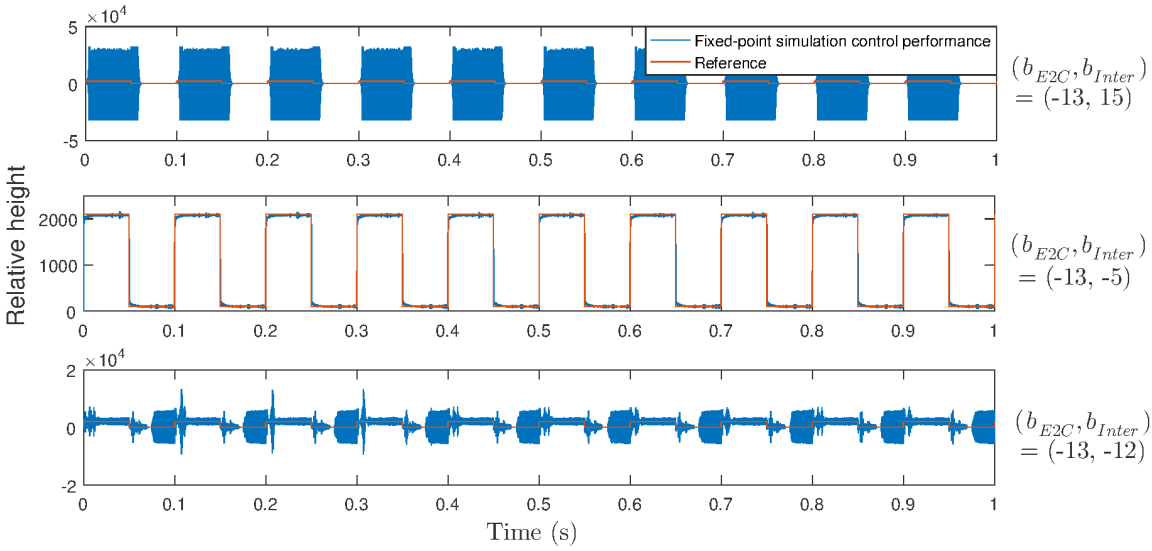

(c) Three fixed-point-arithmetic feedback control simulations for $10Hz$ square wave reference with different bit-shift operation configurations as marked in subfigure (b). Only $(b_{E2c}, b_{Inter}) = (-13, -12)$ permits a stable controller.

FIGURE 3.19: Evaluation of possible fixed-point-based FPGA programming configurations for a feedback control design in on NI-7854R.

this simulation. It will be seen that not every demand is feasible for this implementation, even after optimisation of bit-shifts b_{E2C} and b_{Inter}.

As a measure of assessment, the absolute value of the closed-loop control error, in a 16-bit integer representation, is exploited. Given a reference, $r(k)$, with an amplitude of r_{amp}, the evaluation $|\bar{E_C}|$ for a given bit-shift configuration of b_{E2C} and b_{Inter} is calculated as:

$$|\bar{E_C}|_{(b_{E2C},b_{Inter}),r_{amp}} = \frac{\sum_{k=0}^{k=n} |r(k) - y_{(b_{E2C},b_{Inter})}(k)|}{n} \tag{3.9}$$

Here $r(k)$ is an integer number representing the reference in closed-loop at the k-th simulated sampled-time. And $y_{(b_{E2C},b_{Inter})}(k)$ denotes the integer representation of the closed-loop control output at the

k-th simulated sampled-time. n is the maximum sampled simulation step run at 500 kHz during the simulation time of 1 s. With the specific reference amplitude configuration of r_{amp}, the minimal $|\bar{E_C}|$ among all possible pairs of (b_{E2C}, b_{Inter}) setups is divided by r_{amp} to create the following ratio:

$$c_{E_C, r_{amp}} = \frac{\min_{(b_{E2C}, b_{Inter})} |\bar{E_C}|(r_{amp})}{r_{amp}} \tag{3.10}$$

The c_{E_C} for increasing r_{amp} in each optimisation run is presented in Figure 3.19a. (Note the ordinate is scaled in % rather than within the range 0...1.). It is clear that the control error increases significantly when the reference amplitude is over 1000. With r_{amp} as 1000, the minimal c_{E_C} is less than 3% which indicates good feedback control performance of the fixed-point-arithmetic simulations. Moreover, $|\bar{E_C}|$ is shown in Figure 3.19b while the feedback control reference amplitude is 1000. Three example configurations are picked and their simulations are shown in Figure 3.19c. Two of them are not feasible and unstable, i.e. $(b_{E2c}, b_{Inter}) = (-13, 15)$ and $(b_{E2c}, b_{Inter}) = (-13, -5)$. Hence, the evaluation figure indicates that the overflows happen in the two bright regions, which have to be avoided in any practical feedback control implementation. This is also to protect the practical equipment, such as the cantilever, from damage.

3.5 Summary

This chapter presents the instrument and control (I&C) design of the TDFM system. The proposed design, particularly electronics design, is the first integrated TDFM control system that allows developing vertical positioning system control (see Chapter 4) for specimen morphology analysis in Chapter 6 at nanometre resolution. It can be seen that the developed sensing component has an improved sensing range of about 6 nm in an experimental condition in Chapter 4. This allows an improved TDFM scanning performance as discussed in Chapter 6. The sensing system can be further developed for real-time reconstruction of the interaction shear-force (see Chapter 5).

The I&C design for the TDFM system includes the digital control programme that allows online switching between two control systems, i.e. absolute height or relative height control (developed in Chapter 4). The FPGA hardware resource is significantly saved by the implementation of online reconfigurable digital filters in Section 3.4.3. Additionally, this results in the ease of control algorithm tests in the development procedure. The I&C design also integrates the TDFM with various functional features, including data-stream logging, trajectory planner, graphic user interface design, and so on.

In addition, an intuitive optimisation methodology is presented to enhance the FPGA programme robustness for the developed customisable digital filtering programmes. The proposed offline optimisation method permits optimising the fixed-point arithmetic configuration that enables dynamic specimen-scans in Chapter 6.

Importantly, the remarks on system preparation give an important guideline to minimise the laborious system adjustment effort. The provided systematic procedure will help with developing an automated AFM/TDFM system that is easy to use and requires least operational proficiency (see discussions in Chapter 7).

Chapter 4

Absolute & Relative Height Control

4.1 Introduction

The chapter presents the cantilever height control designs, including system identification and the closed-loop control implementation, in order to realise nano-precision scans in the TDFM. The design starts from measuring the nonlinear sensing curve of the absolute/relative height measurements. Based on the plant response in the time and the frequency domains, the controllers for the absolute/relative height control are designed for different control requirements. Particularly, the relative height positioning system is highly nonlinear and is only available in a limited ($\sim 6nm$) sensing range. Thus, the control development follows a step-wise manner, improving successively the system identification of the system dynamics (e.g. nonlinearity).

In this chapter, all related work is conducted in a wet environment created by ultra-pure water on a grade 0 glass slide (as the sample-holder). The optical path is carefully adjusted to generate the evanescent field above the glass slide, on which the system is optimised with sufficient sensitivity for nano-precision measurement. The cantilever type A is selected to be oscillated in the y-axis direction by a sine wave for an amplitude of approximately 2 nm at 200 kHz, which is around its first resonance in water. Hence, the cantilever oscillates with an amplitude of about 2 nm outside the shear-force interaction range in water medium. The temperature and humidity is controlled to be around $20°C$ and 50% by an air conditioning unit. This is used as the default experimental condition in most of the experimental scans and the shear force estimator development and tests in the next two chapters. Note that the positive direction of the fine piezo-actuator is opposite to the distance of the cantilever towards the sample-substrate/sample-holder slide in this chapter, because the fine piezo-actuator is mounted in the direction towards the x-y horizontal stage.

Supporting publications:

- *"A Multi-mode Transverse Dynamic Force Microscope - Design, Identification and Control"*, Zhang, K., G. Herrmann, M. Antognozzi, et al., Under journal peer-review.

- *"Enhancing fixed-point control robustness for experimental non-contact scans with the Transverse Dynamic Force Microscope"*, Zhang, K., T. Hatano, G. Herrmann, et al., *American Control Conference (ACC) 2018, IEEE.*

4.2 Absolute Height Control

The absolute height control requires to retain a constant distance from the cantilever to the sample-holder slide, the grade 0 glass slide, in scans. This requires that the closed-loop positioning system to track the surface profile of the sample-holder slide, which is flat and has low surface roughness. Hence, the main control design objective is to have a quick response to small surface bumpiness of the glass slide when the cantilever is moving along scan trajectories. Additionally, the absolute height measurement sensitivity varies with the experimental conditions, e.g. the optical path adjustment as discussed before. The absolute height positioning system has inherent uncertainties, including the cantilever tip geometry, the optical path adjustment, the scan medium, and so on. Hence, one other control design requirement is the robustness to some change of experimental conditions: particularly the system drift, the replacement of the cantilever, the adjustment of the optical path, and the change of the sample solution using the same buffer. Also, it will be seen that it is beneficial for the controller to be robust against the measurement noise due to electro-magnetic interference. It is vital that one robust controller is able to tackle the closed-loop control problem under varying experimental conditions, i.e. the control system is well integrated without the need of adjusting controllers under different conditions. This is a significant advancement and makes the system-operation easy and efficient, in contrast to an ad-hoc tuned PID controller used in previous work.

4.2.1 Sensing Curve

The sensing curve that represents the height in relation to the sample slide (the absolute height measure) is obtained from the total light strength measured with the photo detector as described in Chapter 3. The sensing curve of the absolute height measurement versus the cantilever position (away from the sample-holder slide) is measured 20 times as shown in Figure 4.1. To obtain the sensing curve, the cantilever is practically driven by the fine piezo-actuator in open-loop. The distance between the cantilever and the glass slide is computed from the actuation signal of the piezo-actuator.

It is known that the evanescent field wave strength decays exponentially with distance (Antognozzi et al. 2008) as confirmed here. Note that the absolute height measurement sensitivity depends on the optical path, which is specifically adjusted at the beginning of each experiment. Thus, the sensing curve has to be calibrated every time after the optical sensing mechanism is prepared for each experiment.

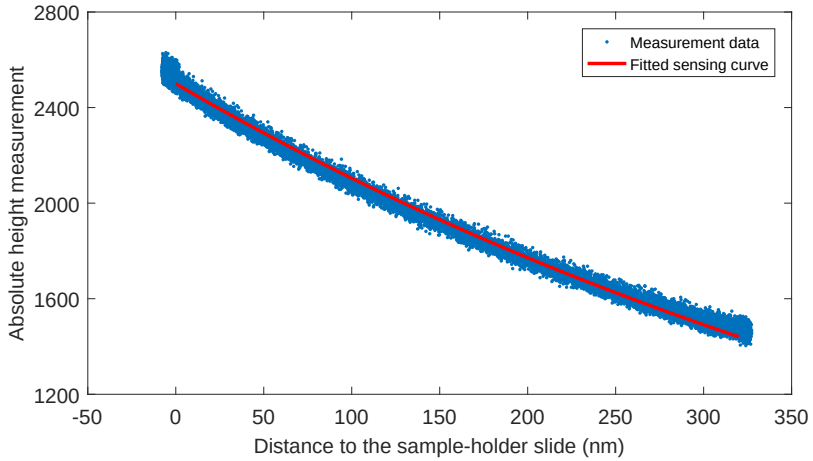

FIGURE 4.1: An absolute height sensing curve in the TDFM.

4.2.2 Open-loop System Identification

For system identification, the plant frequency response is measured in an open-loop manner. Before the system identification, the cantilever is positioned by the coarse piezo-actuator at 50 nm above the glass slide. The plant frequency response is identified by the swept-sine method with an excitation amplitude of 0.5 V (equating 11 nm actuation of the fine piezo-actuator) as shown in Figure 4.2. The measured plant response includes the computational and other hardware delays of overall $\sim$8 μs.

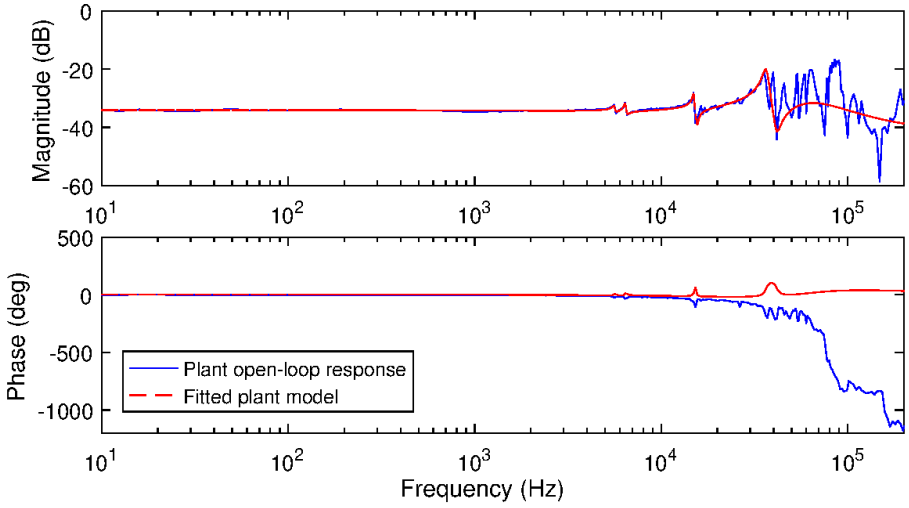

FIGURE 4.2: Absolute height plant frequency response using open-loop system identification.

The plant has a constant magnitude and little phase delay in the low frequency region. There are resonances appearing at 5 kHz, 6 kHz, 10.5 kHz, 30.5 kHz, and at various higher frequencies. It has been decided for the plant model $Plant_{AH}(s)$ to fit only the first four resonances, while any dynamics above 40 kHz are regarded as uncertainty. Hence, the plant model is given in continuous time as

$$Plant_{AH}(s) = \frac{Num_{Plant_{AH}}(s)}{Den_{Plant_{AH}}(s)} \tag{4.1}$$

where

$Num_{Plant_{AH}}(s) = 8.363 \times 10^{-3}s^{11} + 1.1091 \times 10^{3}s^{10} + 3.057 \times 10^{9}s^{9} + 9.553 \times 10^{14}s^{8} + 1.843 \times 10^{20}s^{7} + 1.260 \times 10^{25}s^{6} + 1.887 \times 10^{30}s^{5} + 4.897 \times 10^{34}s^{4} + 4.347 \times 10^{39}s^{3} + 6.999 \times 10^{43}s^{2} + 2.839 \times 10^{48}s + 3.260 \times 10^{52}$

and

$Den_{Plant_{AH}}(s) = s^{11} + 3.891 \times 10^{5}s^{10} + 2.215 \times 10^{11}s^{9} + 2.911 \times 10^{1}6s^{8} + 1.051 \times 10^{22}s^{7} + 4.221 \times 10^{26}s^{6} + 1.007 \times 10^{32}s^{5} + 1.967 \times 10^{36}s^{4} + 2.272 \times 10^{41}s^{3} + 3.206 \times 10^{45}s^{2} + 1.465 \times 10^{50}s + 1.657 \times 10^{54}$.

4.2.3 Robust Control Design

Robust H_∞ control is selected since the plant has a varying gain at low frequency and high-level uncertainty in the high frequency region. Here notch filters are not feasible because of the high computational cost for multiple high-performance notch-filter implementations. An H_∞ mixed-sensitivity synthesis is used to design a robust controller using the Robust Control Toolbox in Matlab (The MathWorks, Inc. 2018).

In the design, the mixed-sensitivity synthesis is applied to designing the sensitivity $S(s)$, complementary sensitivity $T(s)$, and the control effort $R(s)$:

$$\begin{aligned} S(s) &= \frac{1}{1 + G(s)C(s)} \\ R(s) &= \frac{C(s)}{1 + G(s)C(s)} \\ T(s) &= \frac{G(s)C(s)}{1 + G(s)C(s)} \end{aligned} \tag{4.2}$$

where $G(s)$ indicates a plant's frequency response and $C(s)$ is the controller frequency response in generic representation as shown in Figure 4.3. The designed controller $C(s)$ is computed to minimise the H_∞ norm γ of the augmented closed loop system $T_{augment}(s) = \begin{bmatrix} W_1(s)S(s) \\ W_2(s)R(s) \\ W_3(s)T(s) \end{bmatrix}$. As a result, the computed $C(s)$ satisfies the loop-shaping inequalities of

$$\begin{aligned} \overline{\sigma}(S(s)) &\leq \gamma \, \underline{\sigma}(\frac{1}{W_1(s)}) \\ \overline{\sigma}(R(s)) &\leq \gamma \, \underline{\sigma}(\frac{1}{W_2(s)}) \\ \overline{\sigma}(T(s)) &\leq \gamma \, \underline{\sigma}(\frac{1}{W_3(s)}) \end{aligned} \tag{4.3}$$

where $\overline{\sigma}$ and $\underline{\sigma}$ indicates the maximum the minimum singular values of the matrices. This means that the design of $W_1(s)$, $W_2(s)$, and $W_3(s)$ determines the shape of $S(s)$, $T(s)$, and $R(s)$. Hence, $W_1(s)$

needs to be large at the frequencies below the designed control bandwidth to achieve good disturbance attenuation. $W_2(s)$ is designed to guarantee the control signal responds to rapid change of the reference signal at low frequencies and is negligibly small within the high frequency region. $W_3(s)$ often requires to be large outside the desired control bandwidth for robustness.

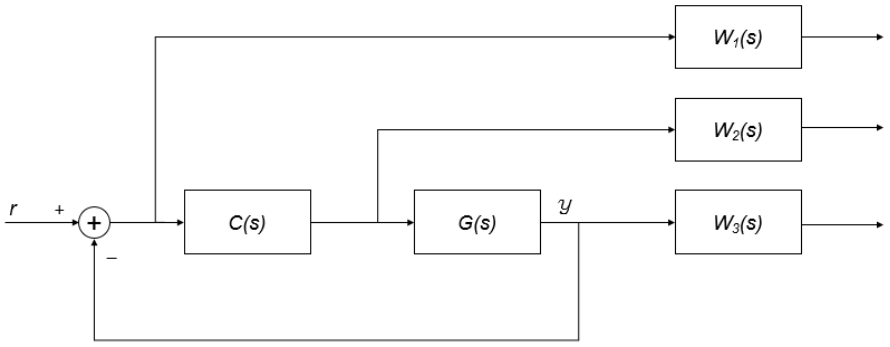

FIGURE 4.3: A schematic of the mixed-sensitivity design in this thesis. The controller $C(s)$ is designed to control the plant $G(s)$ following the reference signal r, where the control signal is u to control the ouput y. In the mixed-sensitivity design, the weights $W_1(s)$, $W_2(s)$, and $W_3(s)$ are designed to shape $S(s)$, $T(s)$, and $R(s)$ (see Equation (4.2)).

The absolute height H_∞ control design for the absolute height open-loop plant $Plant_{AH}(s)$ uses

$$\begin{aligned} W_{1,AH}(s) &= \frac{s^2 + 1.257 \times 10^5 s + 3.948 \times 10^9}{11.11 s^2 + 4.189 \times 10^4 s + 3.948 \times 10^7} \\ W_{2,AH}(s) &= \frac{s^2 + 1.257 \times 10^5 s + 3.948 \times 10^9}{0.01375 s^2 + 6.912 \times 10^4 s + 8.685 \times 10^{10}} \\ W_{3,AH}(s) &= \frac{s^2 + 5.027 \times 10^4 s + 6.317 \times 10^8}{1.088 \times 10^{-3} s^2 + 1367 s + 4.295 \times 10^8} \end{aligned} \tag{4.4}$$

where $W_{1,AH}(s)$, $W_{2,AH}(s)$, $W_{3,AH}(s)$ are the weights for sensitivity $S_{AH}(s)$, complementary sensitivity $T_{AH}(s)$, and the control effort $R_{AH}(s)$ of the absolute height control respectively (as shown in Figure 4.4). In detail, the complementary sensitivity $T_{AH}(s)$ is designed to remain between 0 dB and -3 dB until about 5 kHz below the first resonance. The transfer function for the control effort is designed to suppress the uncertainty over 40 kHz.

Here, the H_∞ norm γ_{AH} is 3.489 for the absolute height control design. The controller $C_{AH}(s)$ in continuous time is

$$C_{AH}(s) = \frac{Num_{C_{AH}}(s)}{Den_{C_{AH}}(s)} \tag{4.5}$$

where

$Num_{C_{AH}(s)} = 7.690 \times 10^4 s^{16} + 5.137 \times 10^{11} s^{15} + 1.211 \times 10^{18} s^{14} + 1.271 \times 10^{24} s^{13} + 7.344 \times 10^{29} s^{12} + 2.831 \times 10^{35} s^{11} + 7.742 \times 10^{40} s^{10} + 1.462 \times 10^{46} s^9 + 2.541 \times 10^{51} s^8 + 1.773 \times 10^{56} s^7 + 2.219 \times 10^{61} s^6 + 7.040 \times 10^{65} s^5 + 5.011 \times 10^{70} s^4 + 1.057 \times 10^{75} s^3 + 3.456 \times 10^{79} s^2 + 5.271 \times 10^{83} s + 2.266 \times 10^{87}$

and

$Den_{C_{AH}}(s) = s^{17} + 4.095 \times 10^{16} s^{16} + 6.758 \times 10^{12} s^{15} + 6.061 \times 10^{18} s^{14} + 3.121 \times 10^{24} s^{13} + 9.555 \times 10^{29} s^{12} +$

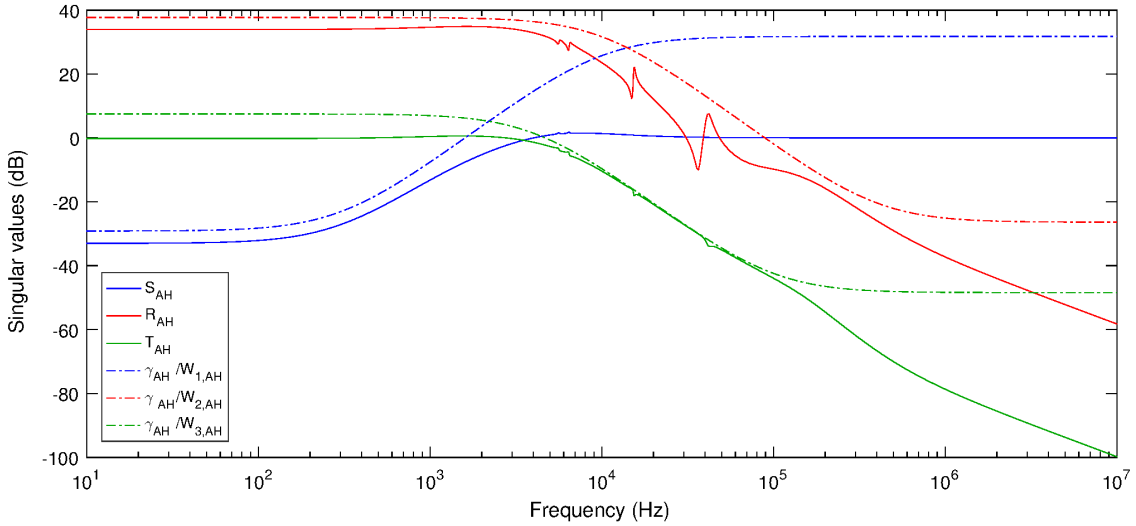

FIGURE 4.4: The mixed-sensitivity H_∞ design for the absolute height control.

$2.398 \times 10^{35}s^{11} + 4.207 \times 10^{40}s^{10} + 4.311 \times 10^{45}s^9 + 4.298 \times 10^{50}s^8 + 2.689 \times 10^{55}s^7 + 1.208 \times 10^{60}s^6 + 5.360 \times 10^{64}s^5 + 1.245 \times 10^{69}s^4 + 3.369 \times 10^{73}s^3 + 4.023 \times 10^{77}s^2 + 1.188 \times 10^{81}s + 1.020 \times 10^{84}$.

In order to implement $C_{AH}(s)$ on the FPGA, the controller is reduced to a 5th-order transfer function using a DC gain matching method (*modred* function in Matlab):

$$C_{AH,red}(s) = \frac{Num_{C_{AH,red}}(s)}{Den_{C_{AH,red}}(s)} \tag{4.6}$$

where

$Num_{C_{AH,red}(s)} = 1.360s^5 - 2.001 \times 10^5 s^4 + 1.085 \times 10^{11}s^3 - 9.708 \times 10^14s^2 + 8.646 \times 10^20s + 6.012 \times 10^{24}$

and

$Den_{C_{AH,red}}(s) = s^5 + 8.863 \times 10^4 s^4 + 9.788 \times 10^9 s^3 + 7.95 \times 10^{14}s^2 + 2.888 \times 10^{18}s + 2.687 \times 10^{21}$.

The open-loop system with the order reduced controller $C_{AH,red}(s)$ has a gain margin of 24 dB at 29.9 kHz and the phase margin is 67.2° at 3.53 kHz (Figure 4.5).

The controller in continuous time is discretised using Tustin's method at a sampling frequency of 500 kHz. In practice, the discrete controller is split into two discrete transfer functions:

$$\begin{aligned} C_{AH,1}(z) &= \frac{0.999z^2 - 1.959z + 0.995}{z^2 - 1.58z + 0.995} \\ C_{AH,2}(z) &= \frac{1.158z^3 - 3.480z^2 + 3.856z - 1.527}{z^3 - 2.840z^2 + 2.682z - 0.842}. \end{aligned} \tag{4.7}$$

The bit-shift operations have been optimised offline as (b_{E2C} , b_{Inter}, b_{C2O}) = (-13,5,8) via the optimisation method in Section 3.4.4.

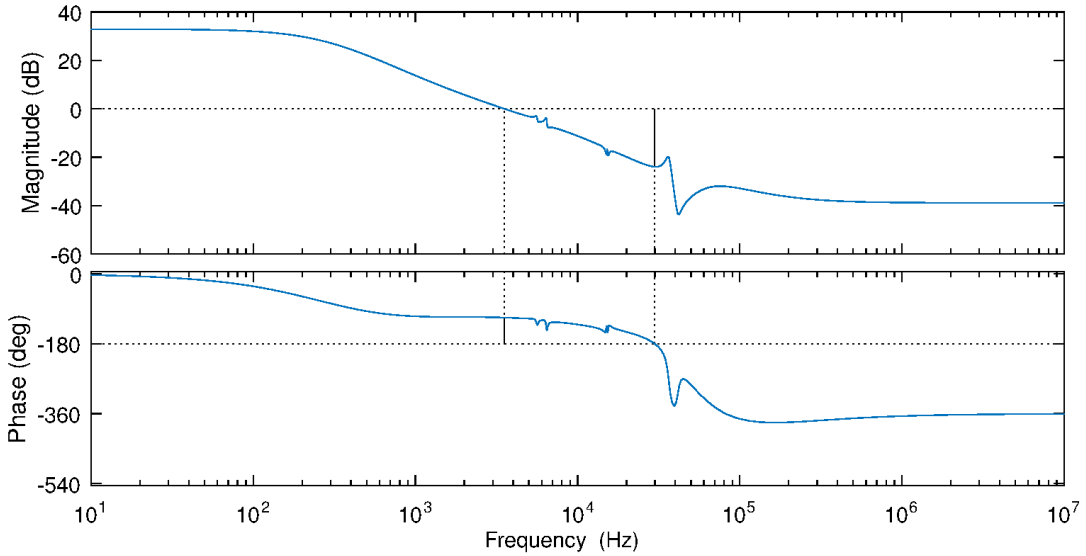

FIGURE 4.5: Absolute height open-loop response with the model reduced H_∞ controller in continuous time.

4.2.4 Control Performance

The control performance is tested to follow a sine wave reference at 1 kHz with a peak-to-peak value of 4 (absolute height measurement in $I16$) at 10 nm and 120 nm above the sample-holder slide. At an offset position of 10 nm above the glass slide, the cantilever is driven to move with a peak-to-peak displacement of 1 nm (see the control signal in Figure 4.6a). However, the control signal has a peak-to-peak displacement of approximate 1.5 nm, while the cantilever is controlled to track the same sine wave reference at an offset height of 120 nm above the sample-holder slide in Figure 4.6b. The control signals are the fine-piezo actuator displacements computed from the control signal assuming a linear voltage-distance relationship. Within the analysis for the peak-to-peak values, the absolute height measurement and the control signal (with the linear scale applied) are considered. The peak-to-peak values of the control signals are computed via a Fast Fourier Transformation algorithm using the fft function in Matlab (The MathWorks, Inc. 2018).

Compared with Figure 4.6, the absolute height sensing curve is slightly different from the measurement of Figure 4.1 due to the change of the glass slide. Additionally, the nonlinearity of the system can be observed from the change of the control signals tracking the same sinusoidal signal at different heights above the sample-holder slide. It is also worthy to note that the frequency range of the noise, found in the absolute height measurement signal, is well above the control bandwidth (see Figure 4.6). This is easily seen by applying a low pass filter with a bandwidth of 10 kHz to the absolute height measurement signal. The filtered absolute height measurement output follows the control reference well. Due to the hardware resource limitation, only a controller is applied to the positioning system without using an extra lowpass filter in the closed-loop design. The control performance shows that the designed controller tackles the noise predominant measurement well in practice.

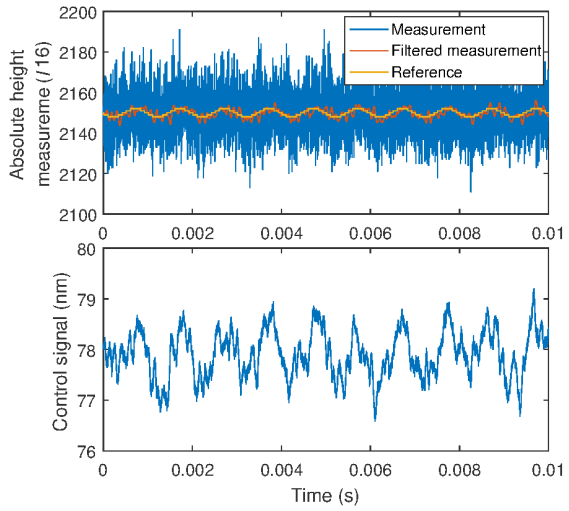

(a) Tracking a sine wave with a peak-to-peak size of 4 absolute height (≈ 1 nm) at 10 nm above sample-holder slide.

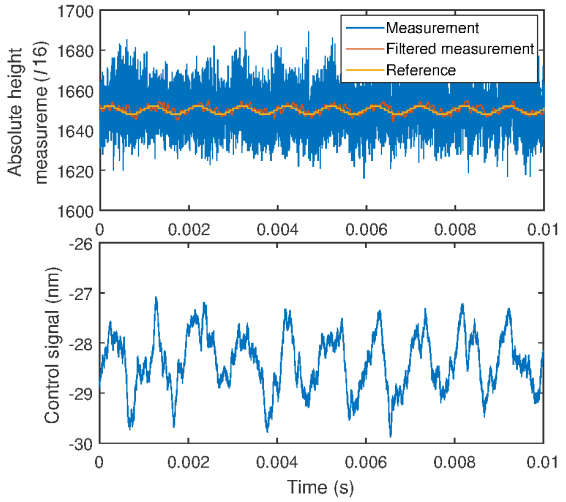

(b) Tracking a sine wave with a peak-to-peak size of 4 absolute height (≈ 1.5 nm) at 120 nm above sample-holder slide.

FIGURE 4.6: Absolute height tracking performance employing the H_∞ control for 1 kHz sine wave demands with 1 relative height amplitude at 10 nm and 120 nm above the sample-holder slide. Note that the filtered absolute height measurement output is obtained by applying a 3rd-order Butterworth lowpass filter (with 10 kHz cutoff frequency) to the control output signal, in order to demonstrate the performance clearly.

The control performance is then tested to track a sine wave reference at 100 Hz frequency. The sine reference has the same peak-to-peak value of 4 absolute height measurement at 10 nm and 120 nm away from the sample-holder slide (see Figure 4.7a and Figure 4.7b respectively). This pair of experiments are taken with a 2 hours time gap, which results in the drift of the coarse piezo-actuator working in open-loop. It can be seen that the absolute height feedback controller robustly compensates the creep effect of the open-loop coarse piezo-actuator.

To assess the tracking performance, the designed controller is used to track several square wave references at different time over a long period under the same experimental conditions. The controller is first assessed with a step size of 100 absolute height measurement in $I16$ (≈ 22 nm distance) at 1 kHz, controlling the absolute height starting at the position of 5 nm above the sample-holder slide (Figure 4.8). This test is purely to evaluate the tracking performance in an extreme scenario, e.g. significant change of disturbances. The absolute height controller has a settling time of less than 0.25 ms satisfying the H_∞ control design in this series of tests (see control performance in Figure 4.8 and Figure 4.9).

The closed-loop system is also tested to track the step references with a 4 (absolute height measurement in $I16$) (≈1 nm) step-size in three runs. The cantilever is initially positioned at 105 nm above the glass slide to follow a step reference at 1 kHz frequency (Figure 4.9a). In the second run, the cantilever is placed at 120 nm above the glass-slide to follow a step reference at 1 kHz frequency (the actual step displacement is about 1.5 nm in this case as shown in Figure 4.9b). The last run make the controller to follow a reference at 100 Hz frequency at where the cantilever is 10 nm above the glass slide (Figure 4.9c). The results demonstrates the controller is robust to achieve ∼1 nm tracking accuracy at different

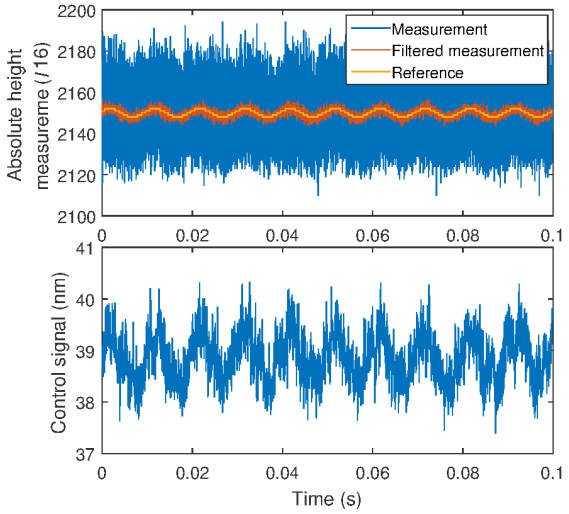

(a) Tracking a sine wave with a peak-to-peak size of 4 absolute height measurement in $I16$ (≈ 1 nm) at 10 nm above sample-holder slide.

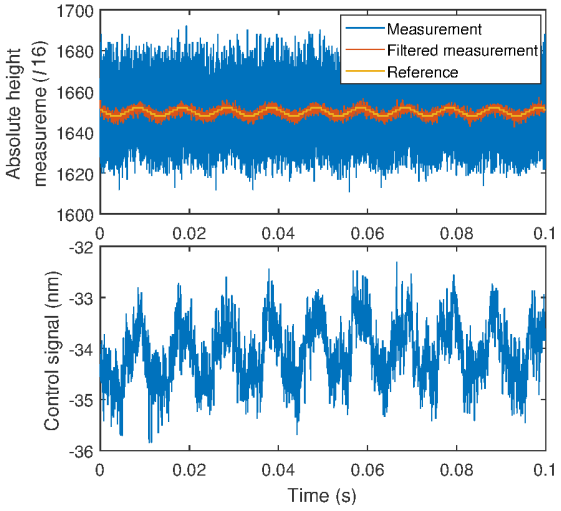

(b) Tracking a sine wave with a peak-to-peak size of 4 absolute height measurement in $I16$ (≈ 1.5 nm) at 120 nm above sample-holder slide.

FIGURE 4.7: Absolute height tracking performance employing the H_∞ control for 100 Hz sine wave demands with 2 absolute height amplitude at 10 nm and 120 nm above the sample-holder slide. Note that the filtered absolute height measurement output is obtained by applying a 3rd-order Butterworth lowpass filter (with 10 kHz cutoff frequency) to the control output signal, in order to demonstrate the performance clearly.

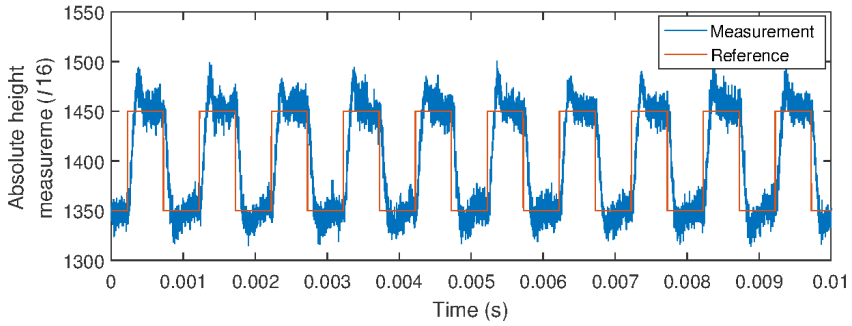

FIGURE 4.8: Absolute height tracking performance employing the H_∞ control for 1 kHz step demands with about 22 nm step size from 5 nm above the sample-holder slide.

heights over the sample-holder slides in the environment.

In control tests and scans, the controller has very similar control performance when specific experimental conditions change (e.g. replacing a new same-type cantilever, replacing the sample-holder slide to another of the same grade, changing the sample solution for one of the same medium, and adjusting the optical path). For instance, Figure 4.10 presents the absolute height control performance before and after a change of the (type A) cantilever. After the cantilever is changed, the sample-holder slide (a new glass-slide in the same grade 0) and the medium solution (purified water) are renewed. Therefore, the optical path has to be adjusted for an optimal sensitivity in each case. The cantilever is controlled to follow a step signal with 500 absolute height measurement (in $I16$) step-size from the same initial position at about 22 nm above the glass-slide. The reference step signals have a 500 Hz frequency and

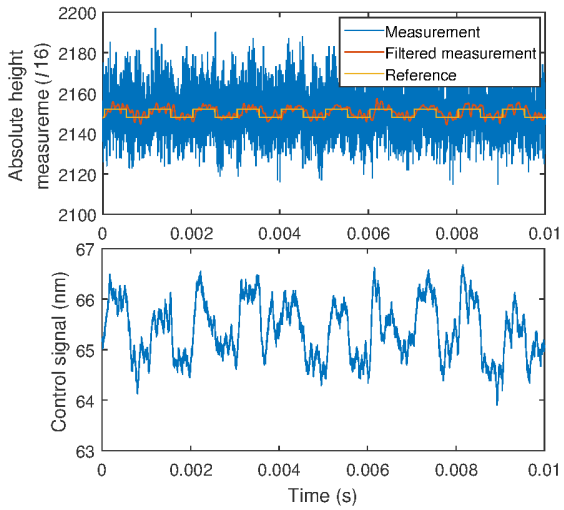

(a) Tracking a step signal at 1 kHz frequency with a step size of 4 absolute height (≈ 1 nm) at 10 nm above sample-holder slide.

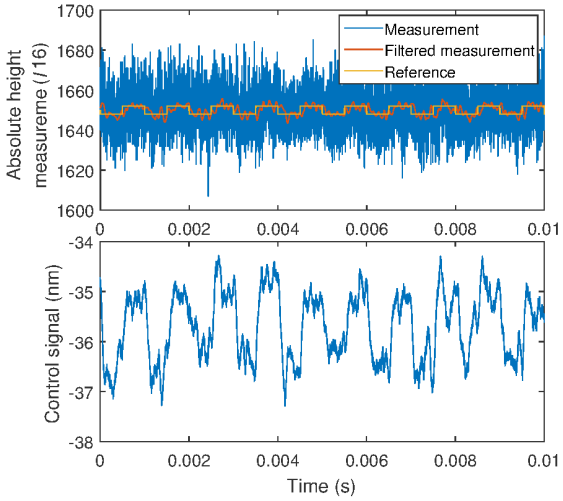

(b) Tracking a step signal at 1 kHz frequency with a step size of 4 absolute height (≈ 1.5 nm) at 120 nm above sample-holder slide.

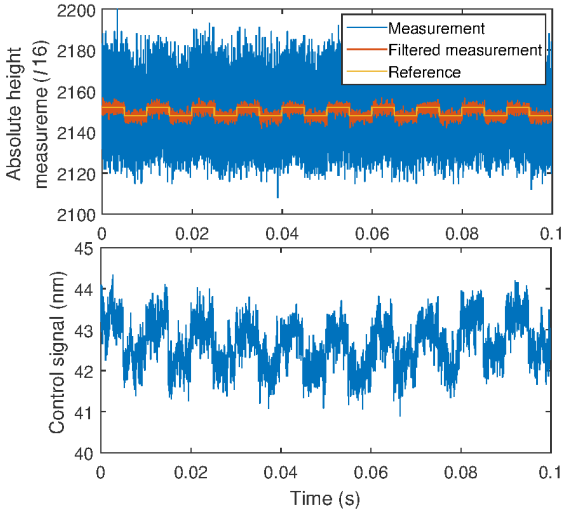

(c) Tracking a step signal at 100 Hz frequency with a step size of 4 absolute height (≈ 1 nm) at 10 nm above sample-holder slide.

FIGURE 4.9: Absolute height tracking performance employing the H_∞ control for step references with 4 absolute height measurement (∼1 nm) step-size. Note that the filtered absolute height measurement is obtained by applying a 3rd-order Butterworth low-pass filter (with 10 kHz cutoff frequency) to the control output signal, in order to demonstrate the performance clearly.

a 1 kHz frequency before and after renewing the cantilever respectively. In the two tests, the absolute height controller is robust to show similar performance of ∼0.1 ms rise time and ∼0.25 ms settling time. Note that the robustness relies on similar sensitivity of the adjusted evanescent field, and the mentioned similarity of the experimental conditions.

In brief, the H_∞ control is robust to some system uncertainties. Also, as shown in the presented control results, the closed-loop absolute height positioning system is capable to track the change of the vertical position well at a resolution of 1 nm in noise predominant conditions, i.e. the control design

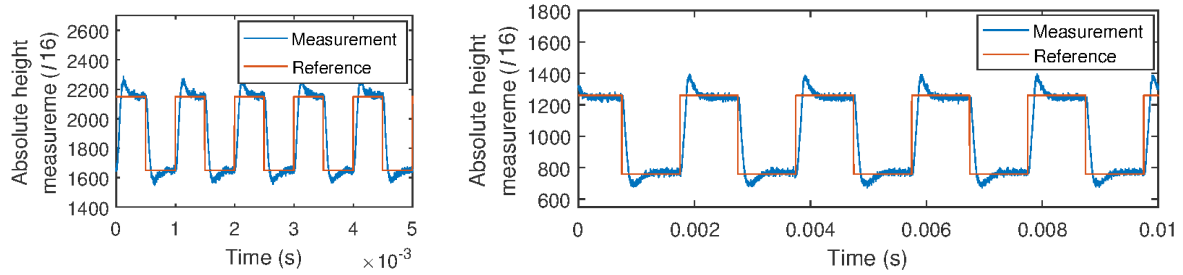

(a) Tracking a step signal at 500 Hz frequency with a step size of 500 absolute height (≈ 116 nm) at 22 nm above sample-holder slide before exchanging of cantilever.

(b) Tracking a step signal at 1 kHz frequency with a step size of 500 absolute height (≈ 116 nm) at 22 nm above sample-holder slide after exchanging of cantilever.

FIGURE 4.10: Absolute height tracking performance employing H_∞ control for step references with 500 absolute height measurement (in $I16$ ≈116 nm) step-size.

target is satisfied.

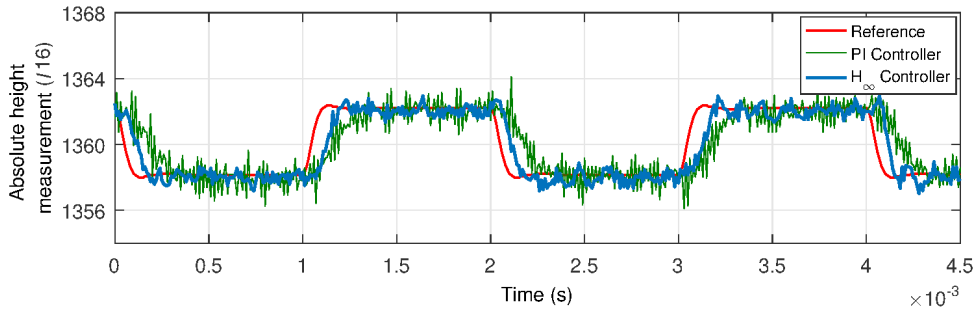

FIGURE 4.11: An example of an ad-hoc tuned PI controller tracking lowpass filtered step references with 4 absolute height measurement (in $I16$ ≈1 nm) step-size. Here, the absolute height measurement is lowpass-filtered with a 200 kHz cut-off frequency by the pre-amplifier. The digital controller has a sampling frequency of 100 kHz.

Remark 4 It is worthy to point out that the designed H_∞ control method has two significant advantages in comparison with an ad-hoc PID control method, such as the vertical positioning controllers in the previous TDFM (Harniman 2013). One advantage is that the control design is based on a good understanding of the vertical positioning system dynamics. Therefore, there is no need to tune the parameters of the control when the experimental conditions are not changed significantly as shown in this section. However, the user of an ad-hoc tuned PID controller has in general to tune the control gains every time carefully, in order to avoid damage to the fragile cantilever or the sample. The other important benefit is an improved control performance over the PID-controller with the H_∞ design. For instance, a PI controller was online tuned for the absolute height positioning system for the default experimental condition. After laborious PI gain adjustment, the proportional and integral gains were tuned to be 0.5 and 225×2^{10} at a sampling frequency of 100 kHz. Here, the absolute height measurement is lowpass filtered with a 200 kHz cut-off frequency before being acquired by the digital control board and used for control. The lowpass filter introduces an additional relatively significant phase-lag in the high frequency range

of the measurement, but it is a simple and efficient solution to help PI-controller retain control stability without control wind-up. In contrast, the developed H_∞ control algorithms have no requirements for an additional lowpass filter. For comparison, the PI controller and the H_∞ are implemented using the same set-up. Both controllers are tested to track a lowpass filtered square-wave signal with an amplitude of 4 absolute height measurement (in $I16$ approximating 1 nm) at 500 Hz in Figure 4.11. It can be seen that the H_∞ controller results in a 2-3 times faster response speed. Also, the PI controlled system has a poor control performance with more oscillations at high-frequencies. ◦

4.3 Relative Height Control

The relative height positioning system aims to maintain a constant distance between the oscillating cantilever and the sample-substrate. Thus, the primary objective is to control the cantilever oscillating amplitude (an indirect measurement of the shear force interaction) by driving the fine piezo-actuator along the vertical z-axis: i.e. the relative height is controlled to track the changing sample-substrate topography. It is critical for the closed-loop system to accurately track the topographic change in order to image the sample profile with sufficient details in nano-precision.

The relative height sensing range is highly limited. For the case of the experiments here, it is approximately a 6 nm range vertically above the sample-substrate. The feedback control will be unable to work properly as soon as the measurement range is exceeded. Moreover, the relative height positioning system plant dynamics are highly nonlinear. This is due to the nature of the complex atomic-force interaction and the lattice-like molecule structure of the confined water layer (as discussed in Section 2.2.2). The controller design requires a detailed frequency based model and the understanding of these nonlinearities.

In order to maintain the availability of the controller, a control requirement is a high closed-loop control bandwidth, i.e. the oscillating cantilever responds to rapid change of the sample-substrate topography without touching delicate samples at relatively fast scanning speeds. Certainly, the controller has to show robust performance to different uncertainties and the dynamic variation of the system. It is demonstrated in this section, that in relation to the absolute height controller, the relative height positioning system is subject to a very different set of sensing nonlinearities. The system dynamics are not only influenced by the change of experimental conditions but also by the highly constrained and nonlinear measurement range of ∼6nm in this case.

4.3.1 Sensing Curve

Precise relative height sensing curves are not measurable in open-loop due to the significant influence of Brownian motion, electrical noise, and disturbances. Hence, the relative height sensing curve, which is represented by the cantilever oscillation amplitude measurement as a function of the cantilever distance

to the sample-substrate (see the sensing electronic in Figure 3.17a), is measured 20 times as shown in Figure 4.12 employing the absolute height control. The optical sensitivity $S_{y,calib}$ (see Equation (3.2)) is adjusted to 6 mV/nm in a pre-experimental calibration. Again the actual separation distance is computed from the control signal, assuming a linear relationship for the fine piezo-actuator.

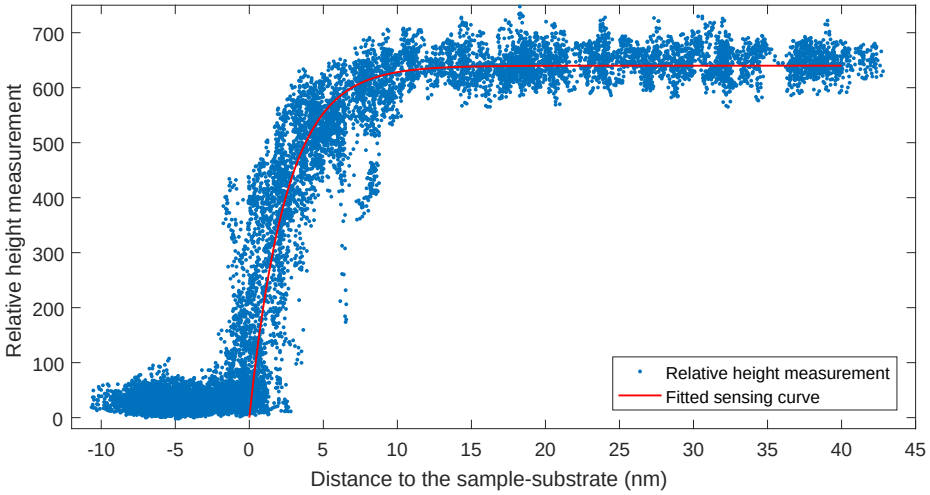

FIGURE 4.12: A relative height sensing curve in the TDFM.

The sensing curve, fitted by an exponential function in Figure 4.12, decreases as the cantilever approaches the sample-substrate. It is clear that the cantilever almost stops oscillating as soon as the extremely soft cantilever contacts the sample-substrate, i.e. the relative height measurements is therefore around 0. The relative height measurement reaches the maximum, when the shear-force interaction between the cantilever and the sample-substrate is negligible. The partial discontinuity and high uncertainty of this measurement curve has in particular two reasons: Brownian motion and the lattice-like structure of the confined water layer just above the specimen. The confined water layer creates molecule lattice structures through which the cantilever traverses. Passing through each lattice causes a discontinuity in the amplitude measurement, as observed here for a ∼6 nm range. Even though the relative height sensing curve is subject to Brownian motion and the lattice nonlinearities, the actual, fitted relative height sensing curve is almost consistent for various experimental conditions, when the same-type cantilever is excited by the same excitation amplitude with the similar optical sensitivity in the same scan medium. Hence, the calibration of the relative height sensing curve is not essential for every experiment. In contrast, the absolute height sensing curve always needs to be calibrated, because the measurement also varies with other factors, e.g. the glass slide thickness, the particle-density of the sample solution, and so on.

4.3.2 Open-loop System Identification

The plant frequency response is created by the swept-sine system identification. The cantilever is positioned by the coarse piezo-actuator in the vicinity of the range where the relative height sensing

mechanism works. The swept-sine signal is used to drive the fine piezo-actuatorwith with an excitation amplitude of 0.05 V (equating 1.1 nm) in the vertical direction. The identified model is measured as shown in Figure 4.13 with $S_{y,calib} = 6$ mV/nm and the default experimental conditions.

Similar to the frequency response using type B cantilevers in water/ambient condition (Hatano et al. 2016, Zhang et al. 2018), the plant response remains constant with a gain of about -0 dB until 1 kHz. In Figure 4.13, it is impossible to identify a clear resonance peak based on the magnitude response. The frequency response is considered uncertain starting from 4 kHz. The plant is fitted with a 5th order transfer function $Plant_{RH,OL}(s)$ in continuous time:

$$Plant_{RH,OL}(s) = \frac{Num_{Plant_{RH,OL}}(s)}{Den_{Plant_{RH,OL}}(s)} \tag{4.8}$$

where

$Num_{Plant_{RH,OL}}(s) = 7.815 \times 10^{-3}s^5 - 1.612 \times 10^4 s^4 + 1.791 \times 10^{10}s^3 + 3.389 \times 10^{15}s^2 + 1.463 \times 10^{20}s + 1.187 \times 10^{23}$

and

$Den_{Plant_{RH,OL}}(s) = s^5 + 9.881 \times 10^5 s^4 + 1.718 \times 10^{11}s^3 + 7.914 \times 10^{15}s^2 + 1.505 \times 10^{20}s + 1.106 \times 10^{23}$.

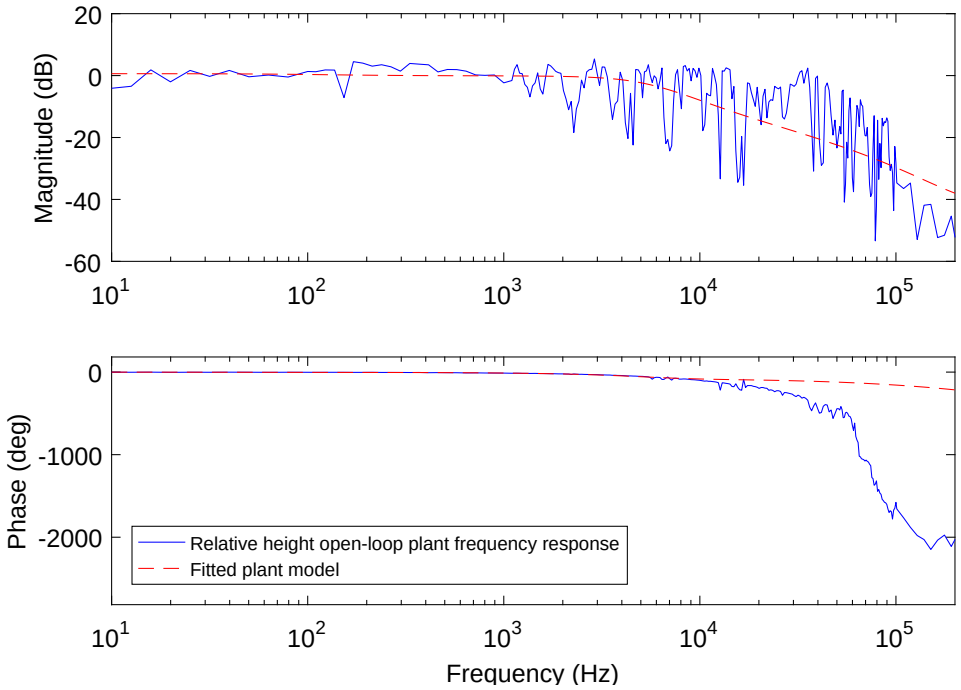

FIGURE 4.13: Relative height plant frequency response using open-loop system identification.

4.3.3 Lag-Control Design

Here a linear controller (see Equation (4.9)) is introduced using a lag control concept as the basis for further study. The controller starts with a constant gain at low frequency and ends with a descending gain

at high frequency. Two lags dropping their gains after 10 Hz and 1 kHz are designed to have sufficient low frequency gain and to avoid any significant control windup at low frequency. Hence, a continuous time controller is designed as

$$C_{RH,Lag}(s) = \frac{3819s + 1.2 \times 10^8}{s^2 + 1.893 \times 10^4 s + 1.541 \times 10^6}. \tag{4.9}$$

The open-loop response of the controlled plant has a phase margin of 72.6° at the crossover frequency of 971 Hz with a gain margin of over 28.9 dB at 8.68 kHz as shown in Figure 4.14. The zeros and poles of the controller $C_{RH,Lag}$ are distributed in two transfer functions and discretised using the Tustin method at 500 kHz sampling frequency as:

$$\begin{aligned} C_{RH,Lag1}(z) &= \frac{0.006364z + 0.006364}{z - 0.9998} \\ C_{RH,Lag2}(z) &= \frac{0.6074z - 0.5704}{z - 0.963}. \end{aligned} \tag{4.10}$$

The $C_{RH,Lag1(z)}$ and $C_{RH,Lag2}(z)$ are programmed in series on the NI-7854R with the offline optimised bit-shift operations (b_{E2C} , b_{Inter}, b_{C2O}) = (-14, 6, 8) (see Section 3.4.4).

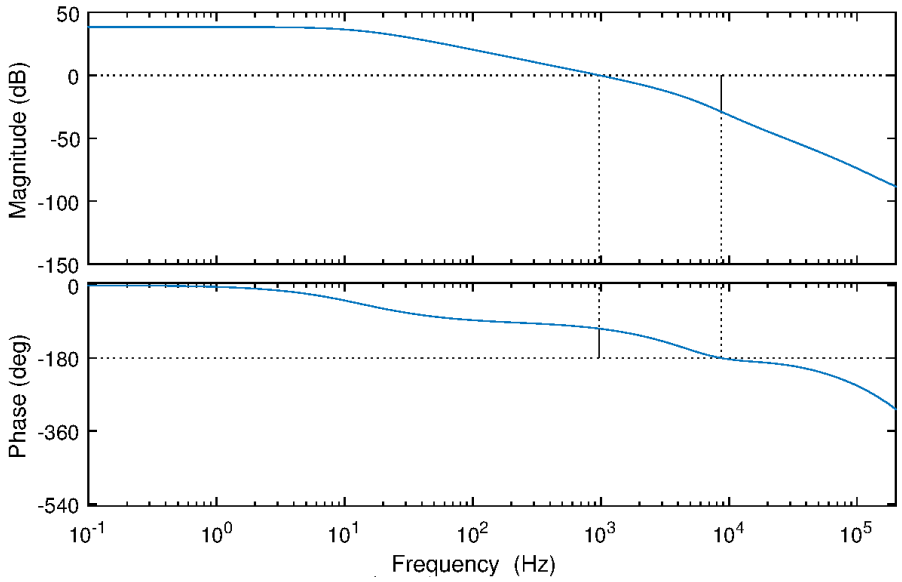

FIGURE 4.14: Relative height open-loop response with the lag-controller in continuous time.

According to the open-loop frequency response in different experimental conditions, it is necessary to design notch filters to decouple significant resonances of the relative height positioning system. For example, the relative frequency response has a significant resonance at 35 kHz in water, when a type B cantilever is used for the relative height measurement in (Zhang et al. 2018). The lag-control regime has to be designed with an additional notch-filter (see the controller designed by Zhang et al. (2018)) to guarantee a good control performance.

Remark 5 Before the lag-control implementation, a PID controller was tested and deemed unsuitable.

In related previous research, a phase locked loop (PLL) has been employed to measure the amplitude of the cantilever oscillation and a PI controller was applied and then ad-hoc tuned (Harniman et al. 2012). However, it was found here in this research that a PI control was not applicable to tackle feedback control in the 6 nm working range for the following reasons. The integral action of the PID-control is not suited to retain limited control action and a limited output range (considering that, for this piezo-actuated control loop, control signal and relative position are linearly related). The PID controlled relative height positioning system is easy to fail due to a rapid, even less than 2 nm change, of the reference signal (equating to a 2 nm change of the sample topographic profile). The simplified structure of a PID controller is not capable to compensate the low-frequency disturbances and the high frequency noise in a $\sim$6 nm working range. Hence, a PID control is not feasible for fragile specimens with steep topographic profiles. This situation is even more aggravated, when PID-controllers are ad-hoc tuned, similar to commercial AFMs, e.g. D3100 AFM (Veeco Instruments Inc. 2004). ◦

Remark 6 The significant input and output constraints of the control problem here create in principle an ideal opportunity to use input and output constraint compensation methods (e.g. the anti-wind-up controllers designed by Herrmann et al. (2004), Turner et al. (2009), etc.). However, much of the most significant problems were solved here through suitable frequency shaping control designs. For hardware resource and time reasons any of the above mentioned methods have not been rigorously investigated. ◦

4.3.4 Lag-Control Performance

A lag-control is tested by tracking a sine wave reference signal that has an amplitude of 100 (relative height measure in $I16$) at 100 Hz frequency. The reference sine wave is given at 200, 300, 400, and 500 relative height positions shown in Figure 4.15. The results show that the lag-controller can control the cantilever position following the reference signal at different heights. However, there is a significant phase delay when the system is controlled at 200 and 500 relative height positions. Also, at 200 and 500 relative height positions, the lag-controller cannot guarantee a good performance to track the 100 Hz sine wave reference. This indicates the lag-control only works in a specific relative height range due to its limited control capability, i.e. the lag-control is unable to tackle the nonlinearity of the system plant.

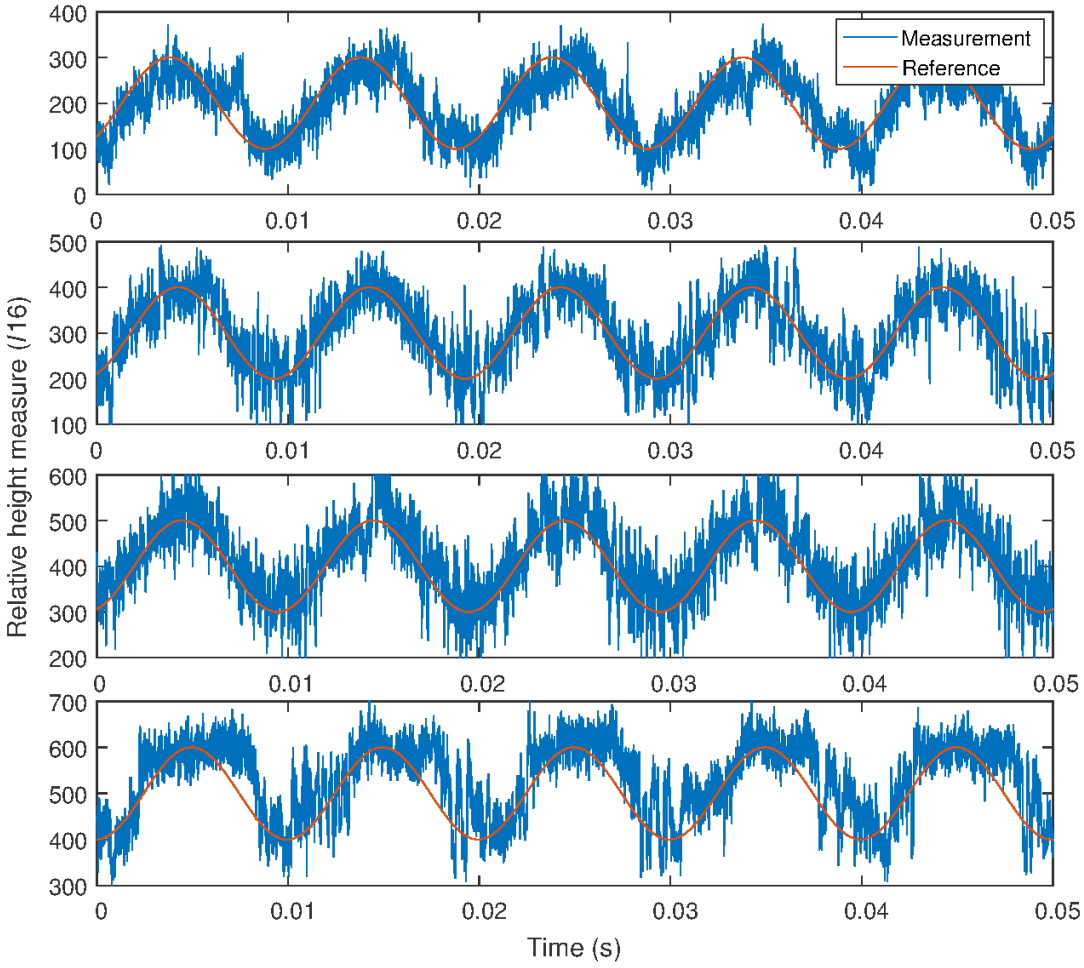

FIGURE 4.15: Relative height tracking performance employing the lag-control for a sine wave reference with 100 relative height amplitude at 100 Hz at different relative heights.

The lag-control performance is further assessed at different operation positions, i.e. at 200, 300, 400, and 500 relative height offsets again, while testing for a square wave reference signal (see Figure 4.16). The square wave reference has an amplitude of 100 (relative height measure in $I16$) at a frequency of 100 Hz. The control performance shows that the lag-control cannot track the reference accurately at 200 and 500 relative heights. The clear difference of the settling time at various relative height positions

demonstrates the variation of the plant dynamics at different demand reference offsets. Any disturbance, which forces a change of the cantilever position of 1 nm or more, may vitally result in inaccuracy or failure of the lag-controller.

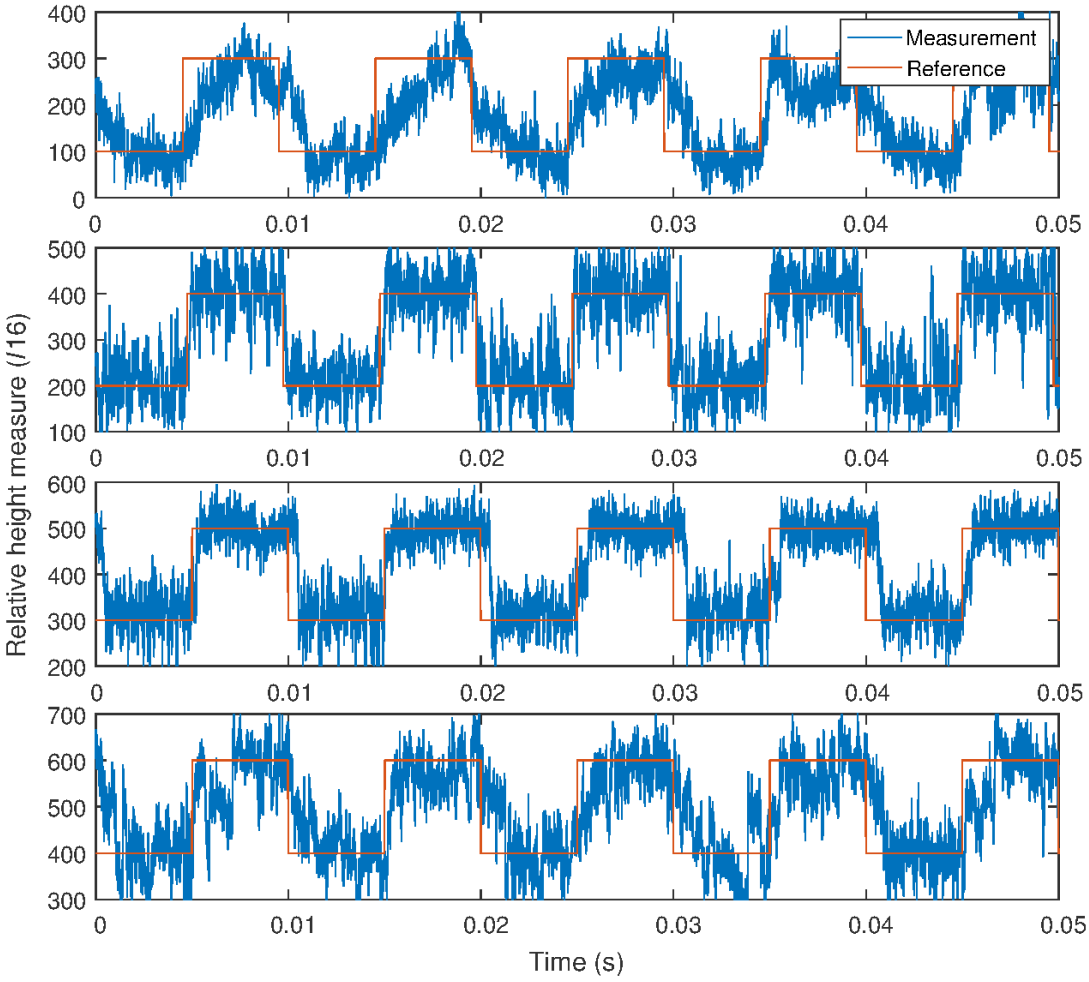

FIGURE 4.16: Relative height tracking performance employing the lag-control for a square wave reference with 100 relative height amplitude at 100 Hz at different relative heights.

4.3.5 System Nonlinearity Analysis using Improved System Identification in Closed-loop

Motivated to achieve advanced control performance, an improved system dynamics model has been identified in a closed-loop manner. The lag-controlled relative height positioning system allows to measure the plant response in closed-loop at different relative heights (from 150 to 550 relative height with a step size of 50). At each height, the closed-loop system response is measured by the swept-sine system identification method, giving the sine signals with 50 relative height amplitude. Hence, the plant response $G(j\omega)$ can be computed from the measured closed-loop sensitivity $T(j\omega)$ and the known control $C(j\omega)$

response by

$$G(j\omega) = \frac{T(j\omega)}{(1 - T(j\omega))C(j\omega)}. \tag{4.11}$$

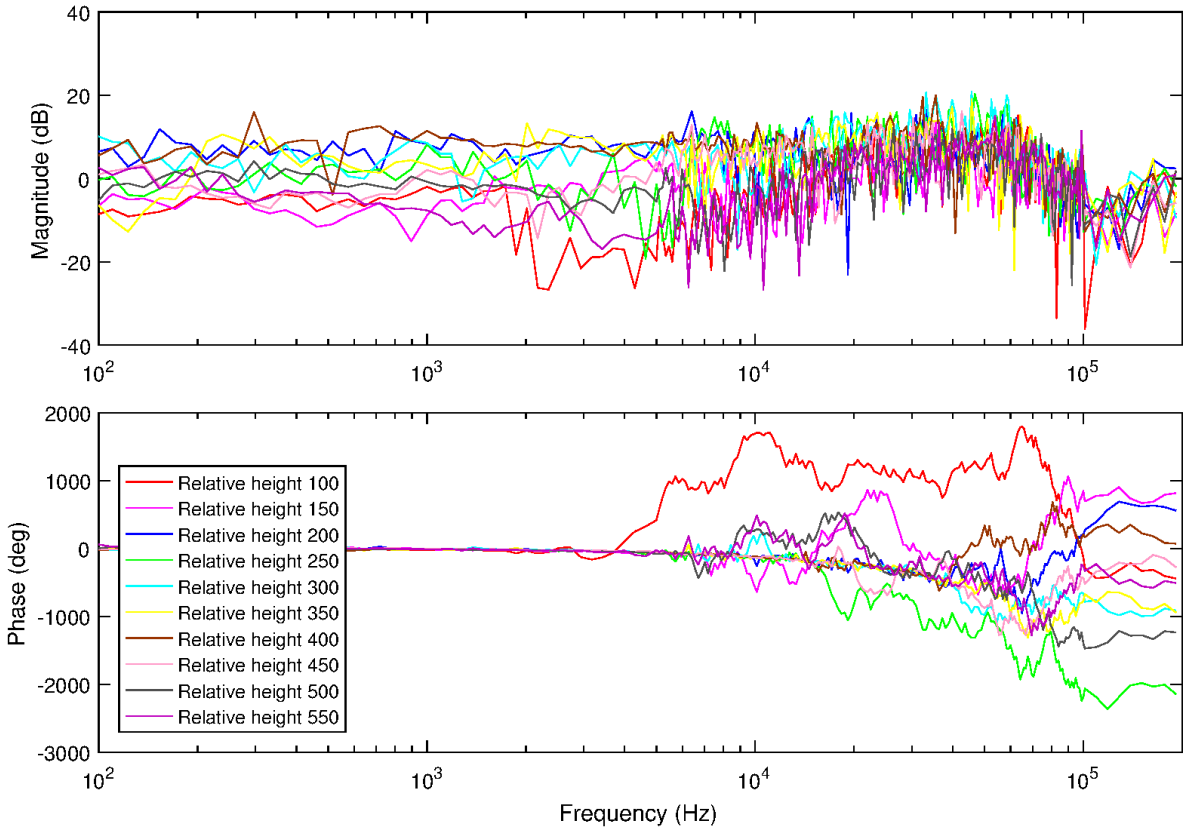

FIGURE 4.17: Relative height plant dynamics: frequency response using the closed-loop system identification at different relative heights.

The measured responses exhibit differences of the dynamics magnitude at low frequency range at each offsets as shown in Figure 4.17. Four representative examples in Figure 4.18 have been chosen among the results. Note that the measurements are affected by noise (as discussed earlier) which was also not easily suppressed by averaging the response. Despite this, it is visible that at each height the low frequency gain keeps constant until about 3 kHz. The magnitudes of the plant response at each operation heights gradually converges to a similar shape in the high frequency range from 11 kHz to 200 kHz. At different relative heights, the low frequency gain of the plant begins from -8 dB at 100 relative height, increases to 10 dB at 300 until 400 relative height, then drops to about -5 dB at 550 relative height. The plant response at high frequency has a magnitude of no more than 15 dB at all operational positions. Moreover, the phase of the plant dynamics starts from 0° at low frequency. At different relative height positions, the phase remains similar until 2 kHz and significantly varies after 10 kHz.

The strong plant nonlinearity significantly influences both the magnitude and the phase of the closed-loop control performance as the lag-control performance results shown. It can be seen from Section 4.3.3 and 4.3.4 that a control solution designed with simple frequency domain shaping methods hardly can

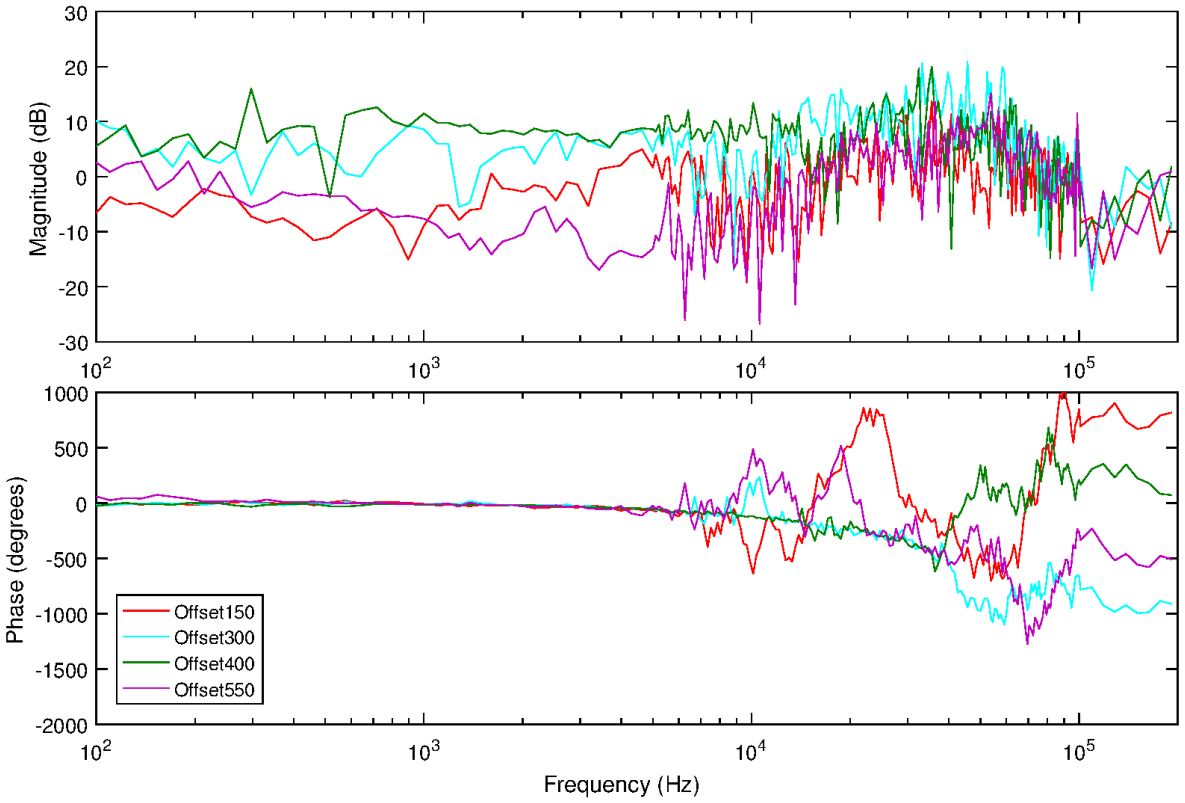

FIGURE 4.18: Representative relative height plant dynamics: frequency response measurement using the closed-loop system identification.

tackle dynamic scanning tasks in practice. Hence, the next section provides the design of a robust H_∞ control.

4.3.6 Robust Control Design

Due to the nonlinerity of the system plant, the mixed sensitivity H_∞ control design (using the same design concept in Section 4.2.3) is suggested for: a) an appropriate low-frequency sensitivity and sufficient bandwidth at various relative heights; and b) the suppression of uncertainty in the high frequency region.

The plant is modelled by the response at 400 relative height as shown in Figure 4.19. The position at 400 relative height equates about 3 nm over the sample-substrate in experimental scans. Based on the identified response, the plant is modelled as an 8th order transfer function with two resonances at 6.4 kHz and 33.9 kHz:

$$Plant_{RH}(s) = \frac{Num_{Plant_{RH}}(s)}{Den_{Plant_{RH}}(s)} \tag{4.12}$$

where

$Num_{Plant_{RH}}(s) = 0.5632s^8 + 5.069 \times 10^5 s^7 + 1.383 \times 10^{11} s^6 + 4.779 \times 10^{16} s^5 + 3.681 \times 10^{21} s^4 + 2.748 \times 10^{26} s^3 + 5.392 \times 10^{30} s^2 + 6.465 \times 10^{33} s + 5.485 \times 10^{37}$

and

$Den_{Plant_{RH}}(s) = s^8 + 5.4 \times 10^5 s^7 + 9.981 \times 10^{10} s^6 + 2.87 \times 10^{16} s^5 + 1.839 \times 10^{21} s^4 + 1.166 \times 10^{26} s^3 + 1.979 \times 10^{30} s^2 + 2.62 \times 10^{33} s + 2.326 \times 10^{37}$.

The mixed sensitivity design aims to shape the sensitivity $S_{RH}(s)$, the control effort $R_{RH}(s)$, and the closed-loop sensitivity $T_{RH}(s)$ using the weights $W_{1,RH}(s)$, $W_{2,RH}(s)$, and $W_{3,RH}(s)$ respectively. The weights are designed as

$$\begin{aligned} W_{1,RH}(s) &= \frac{s^2 + 8.168 \times 10^4 s + 1.579 \times 10^9}{6.4 s^2 + 6032 s + 1.263 \times 10^6} \\ W_{2,RH}(s) &= \frac{s^2 + 2.513 \times 10^4 s + 1.579 \times 10^9}{0.0048 s^2 + 3016 s + 4.737 \times 10^8} \\ W_{3,RH}(s) &= \frac{s^2 + 2.513 \times 10^4 s + 1.579 \times 10^9}{0.005 s^2 + 1257 s + 7.896 \times 10^7}. \end{aligned} \tag{4.13}$$

In detail, robustness to high frequency uncertainty is achieved considering the measured plant frequency response and by shaping sensitivity, co-sensitivity, and the product of controller and the co-sensitivity response to obtain a fast roll-off. Also, the conservative design (as shown in Figure 4.20) guarantees sufficient robustness to the varying plant response below 3 kHz. Therefore, the controller $C_{RH}(s)$ is obtained in continuous time as

$$C_{RH}(s) = \frac{Num_{C_{RH}}(s)}{Den_{C_{RH}}(s)} \tag{4.14}$$

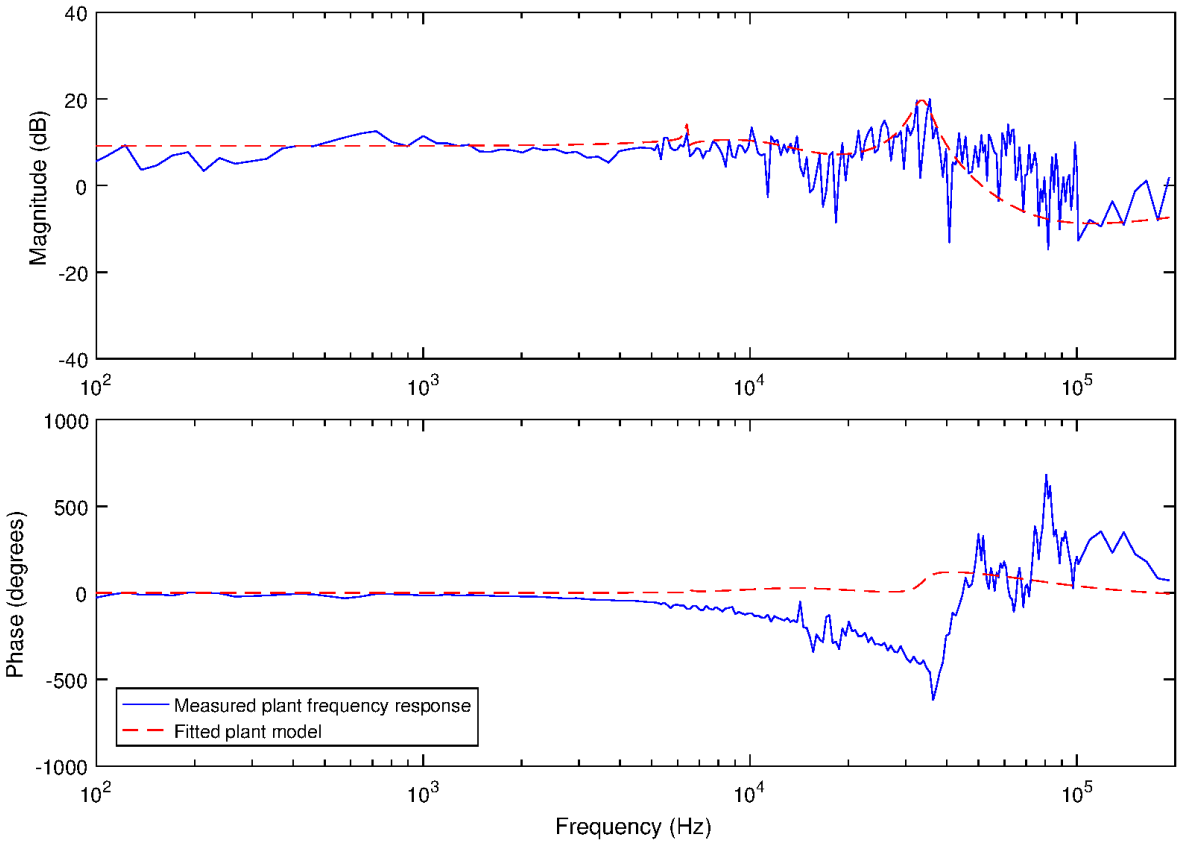

FIGURE 4.19: Relative height plant dynamics: frequency response and the fitted model at 400 relative height.

with

$Num_{C_{RH}}(s) = 2.908 \times 10^{-7}s^{13} + 5.318 \times 10^{4}s^{12} + 2.763 \times 10^{11}s^{11} + 2.421 \times 10^{17}s^{10} + 9.920 \times 10^{22}s^{9} + 2.665 \times 10^{28}s^{8} + 5.389 \times 10^{33}s^{7} + 7.570 \times 10^{38}s^{6} + 6.904 \times 10^{43}s^{5} + 4.288 \times 10^{48}s^{4} + 1.890 \times 10^{53}s^{3} + 5.465 \times 10^{57}s^{2} + 1.457 \times 10^{62}s + 6.185 \times 10^{65}$,

$Den_{C_{RH}}(s) = s^{13} + 7.521 \times 10^{6}s^{12} + 1.714 \times 10^{13}s^{11} + 1.222 \times 10^{19}s^{10} + 5.126 \times 10^{24}s^{9} + 1.363 \times 10^{30}s^{8} + 2.227 \times 10^{35}s^{7} + 2.195 \times 10^{40}s^{6} + 1.400 \times 10^{45}s^{5} + 5.112 \times 10^{49}s^{4} + 1.725 \times 10^{54}s^{3} + 2.985 \times 10^{58}s^{2} + 2.696 \times 10^{61}s + 5.577 \times 10^{63}$,

and the H_∞ norm $\gamma_{RH} = 4.39$.

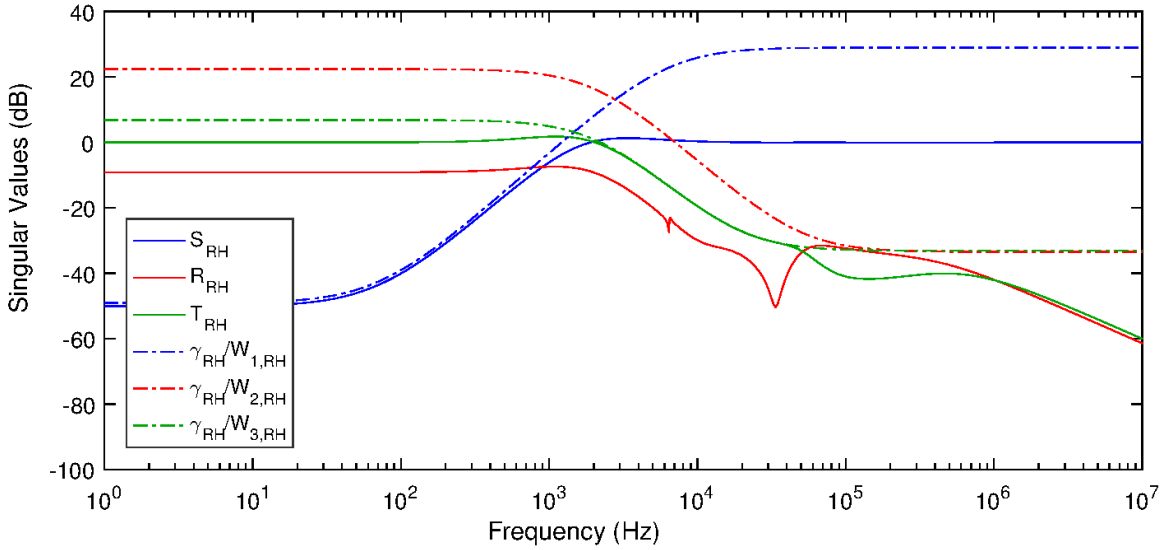

FIGURE 4.20: The mixed-sensitivity H_∞ design for the relative height control.

After using a DC gain matching model reduction method for controller order reduction, the controller is order-reduced to a 7th order transfer function

$$C_{RH,red}(s) = \frac{Num_{C_{RH,red}}(s)}{Den_{C_{RH,red}}(s)} \tag{4.15}$$

where $Num_{C_{RH,red}}(s) = -1.172 \times 10^{-3}s^{7} + 6.597 \times 10^{4}s^{6} + 8.807 \times 10^{10}s^{5} + 1.148 \times 10^{16}s^{4} + 4.373 \times 10^{21}s^{3} + 3.285 \times 10^{26}s^{2} + 1.758 \times 10^{31}s + 8.103 \times 10^{34}$ and $Den_{C_{RH,red}}(s) = s^{7} + 5.139 \times 10^{6}s^{6} + 3.517 \times 10^{12}s^{5} + 9.304 \times 10^{17}s^{4} + 1.503 \times 10^{23}s^{3} + 3.816 \times 10^{27}s^{2} + 3.493 \times 10^{30}s + 7.254 \times 10^{32}$. The open-loop response of the plant $Plant_{RH}(s)$ controlled by $C_{RH,red}(s)$ (Figure 4.21) has a phase margin of 58.7° at 1.99 kHz.

Here the 6th order H_∞ controller is discretised (using the Tustin's method) and split into two transfer functions for implementation on the NI-7854R:

$$\begin{aligned} C_{RH,1}(z) &= \frac{0.01954z^4 - 0.01382z^3 - 0.02197z^2 + 0.01534z + 0.001623}{z^4 - 1.678z^3 + 0.2012z^2 + 0.6936z - 0.2162} \\ C_{RH,2}(z) &= \frac{0.8054z^3 - 2.250z^2 + 2.220z - 0.7744}{z^3 - 2.420z^2 + 2.025z - 0.6056}. \end{aligned} \tag{4.16}$$

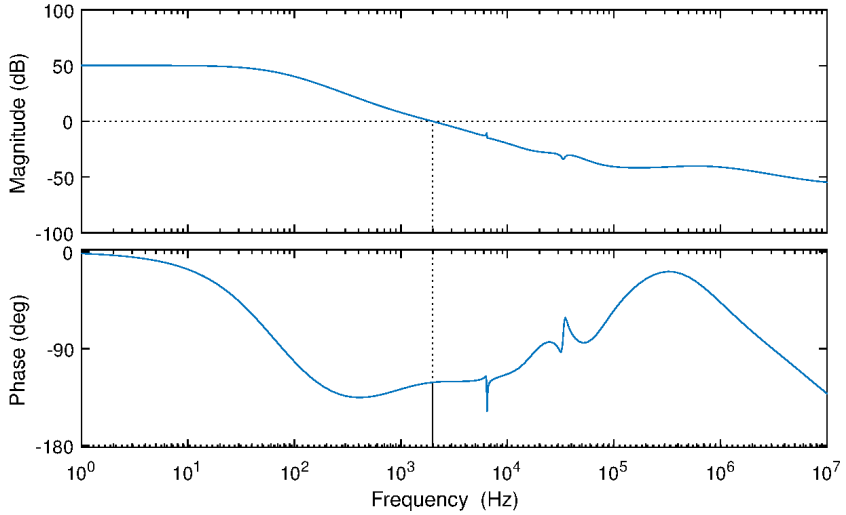

FIGURE 4.21: Relative height open-loop response with the model reduced H_∞ controller in continuous time.

The bit-shift operations are offline optimised as (b_{E2C} , b_{Inter}, b_{C2O}) = (-19, 8, 11) employing the proposed optimisation tool in Section 3.4.4.

4.3.7 Robust Control Performance

The H_∞ controller is used to track a sine wave reference at a frequency of 300 Hz with an amplitude of 50 (∼0.1 nm at the most sensitivity). For comparison, the sine-wave reference is given at 100, 200, 300, 400, and 500 relative height as shown in Figure 4.22a. It is clear that the H_∞ control has little phase delay and accurately tracks the 300 Hz sine wave. The results show that the H_∞ control has a good robustness to the plant nonlinearity over the whole operating range. However, the lag-controller fails to track 100 Hz frequency square wave references at relative height 200 and 500 (Figure 4.15)

The H_∞ controller is then assessed by tracking a square wave reference with an amplitude of 50 at a 300 Hz frequency at relative heights of 100, 200, 300, 400, 500 as shown in Figure 4.22b. The controller achieves a settling time of less than 0.5 ms satisfying the control design, whereas the lag-control has a settling time of about 2 ms at 200 relative height (Figure 4.16). The robust control design decoupled the noise signal well and achieved a vertical resolution of less than 1 nm (see results in Figure 4.22a and Figure 4.23).

The designed H_∞ controller is also applied to tracking a step reference signal from 150-450 (relative height in $I16$) at a frequency of 300 Hz. The consistent control performance is observed no matter the controller is tracking a rapid reference change (150 - 450 relative height, i.e. ∼ 2.5 nm) or small (100 relative height, i.e. ∼1 nm) reference change.

Note that the data in this section are taken at different times with the same optical sensing sensitivity. This shows that the relative height H_∞ controller is robust against the system drifting over time. Also,

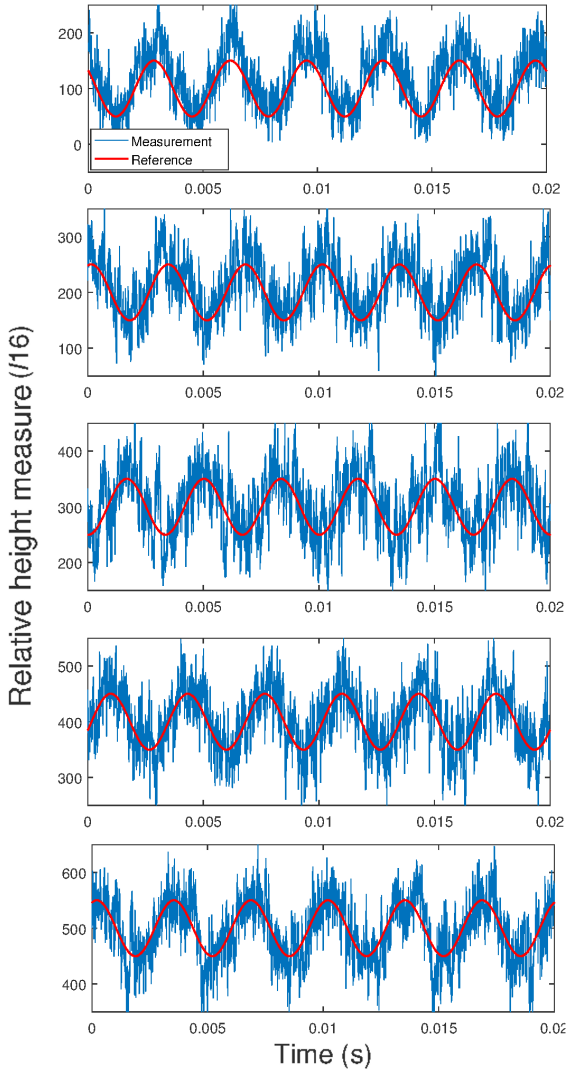

(a) Tracking a sine wave reference at 100, 200, 300, 400, 500 relative heights.

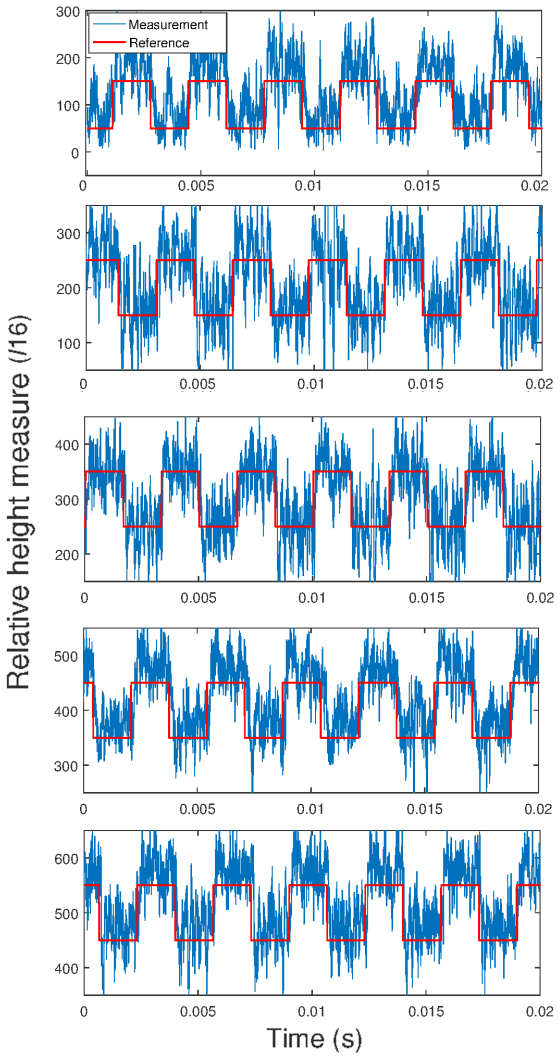

(b) Tracking a square wave reference at 100, 200, 300, 400, 500 relative heights.

FIGURE 4.22: Relative height tracking performance employing the H_∞ control for references with 50 relative height amplitude at 300 Hz frequency at different relative heights.

in experimental tests and scans, the H_∞ control design is proven to be robust against the change of experimental conditions, including the change of sample-solution in the same buffer, the adjustment of the optical path, the replacing of the cantilever, etc. The robustness of the controller is found to be significantly beneficial for facilitating sample-scans of the TDFM system.

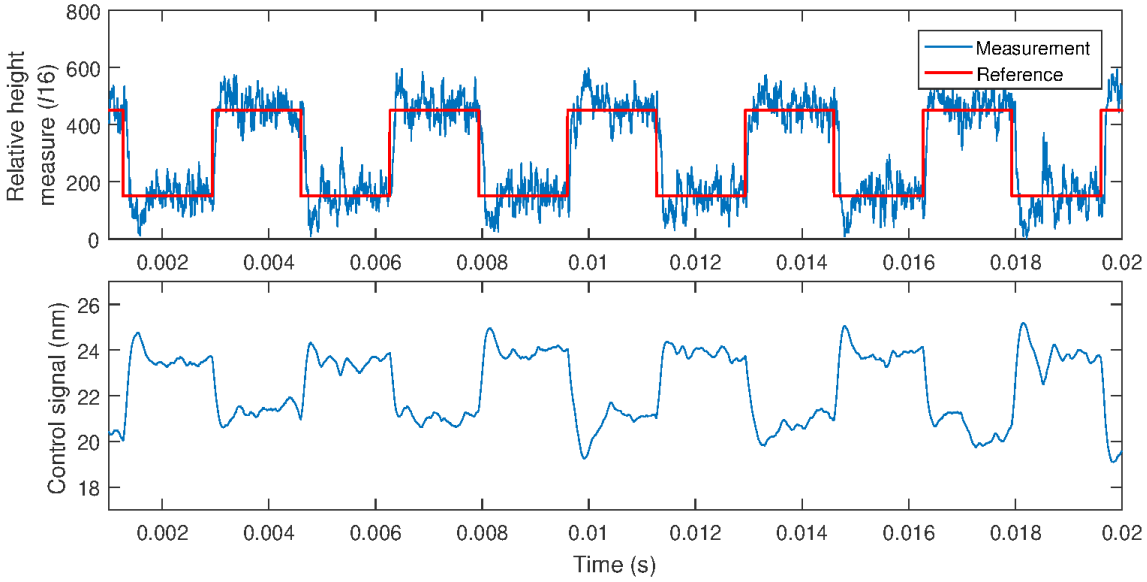

FIGURE 4.23: Relative height tracking performance employing the H_∞ control for a step reference from 150 to 450 relative height at 300 Hz frequency.

4.3.8 Output Relative Height Signal Distribution Assessment in Open and Closed loop

To address the contribution of the H_∞ and the lag control to the performance, the steady state performance characteristics of the lag controller and the H_∞ controller are compared with the open-loop measurement of the relative height sensor. In each case, the cantilever tip is placed at the relative heights of 100, 200, 300, 400, and 500 over the sample-substrate. 5000 samples are taken at each height for each of the three different cases.

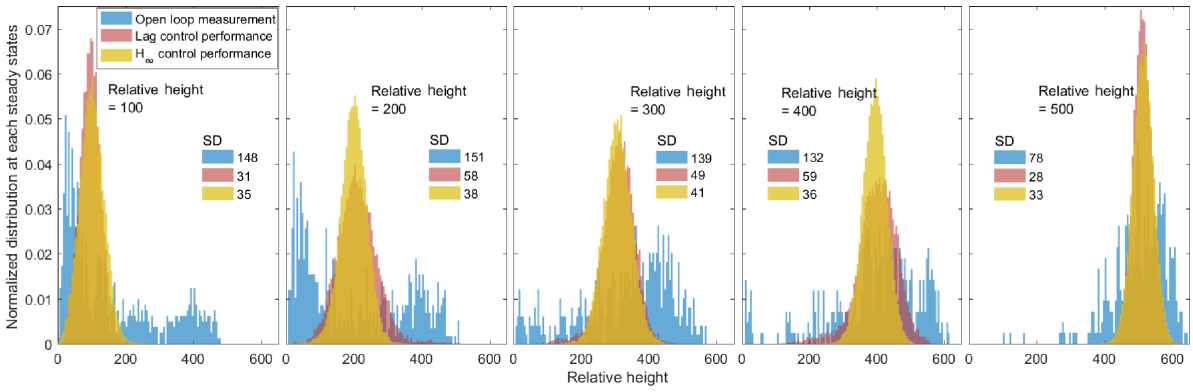

FIGURE 4.24: Steady state performance of the open-loop, lag-controlled, and H_∞-controlled relative height positioning system: The normalized histogram of relative height measurement at each relative height references (at 100, 200, 300, 400, and 500) in open-loop, the lag-controlled feedback loop, and the H_∞-controlled feedback loop. 'SD' indicates the standard deviation of the relative height measurements with respect to the expectation in each case.

In Figure 4.24, the normalized histogram shows that the open-loop regime cannot sufficiently guarantee

a constant value. Hence, it is impossible to maintain a stable shear-force interaction at the relatively high noise level in open-loop. In contrast, the lag control and the H_∞ control significantly improve the positioning accuracy. In detail, the lag control result has only at two relative height values of 100 and 500 the smallest standard deviation, while at all other heights, the H_∞ control has superior performance. The consistent performance of the H_∞ control addresses the robustness to the varying plant dynamics.

4.4 Summary

This chapter consists of the dynamics study and the control development for the absolute height control and the relative height control, of which concerned sensing mechanisms are presented in Chapter 3.

The absolute height measurement (in $I16$) is found to be an exponential function with respect to the actual cantilever-sample-holder distance (in nanometre) as discovered in previous work (Harniman 2013, Antognozzi et al. 2008). Therefore, the sensing curve is a continuous monotonic nonlinear function representing the property of the evanescent field. The absolute height positioning system (including the piezo-electric component) dynamics are identified in open-loop in the frequency domain. A robust H_∞ control is designed via a mixed-sensitivity method by shaping the weighting functions for sensitivity, co-sensitivity, and control effort. Then, the obtained H_∞ controller is order reduced, discretised, and applied to the TDFM digital control programmes. The proposed controller achieves a robust precise control performance at 1 nm resolution in practice. A comparison to PI control, which was previously applied to the TDFM absolute height control in (Harniman 2013, Harniman et al. 2012), shows that the H_∞ control has a better control performance and an enhanced robustness to measurement noises with improved operational convenience.

The relative height sensing curve is studied and investigated under various experimental conditions. Differently from the absolute height sensing curve, the relative height sensing curve is nonlinear and discontinuous following an overall monotonic trend. Beside the effects of Brownian motion, the discontinuity of the sensing curve is caused by the molecular structure of the confined water layer, which is lattice-like structured. The effect of the water molecular structure has been verified by Antognozzi et al. (2001) offline, computing the interaction shear-force alteration with respect to the probe-specimen distance. Similar phenomena have been observed in this thesis as a result (see Section 5.4.2) of the developed real-time shear-force reconstruction method later in Chapter 5.

The relative height positioning system is then identified in open-loop, in the frequency domain. Therefore, a lag-controller is applied to the system, whereas a PID control cannot work due to integration windup and the noise-predominant measurements. By using the lag-controller, it is found that the lag-controlled system cannot guarantee a consistent tracking performance within the whole relative height

sensing range. Therefore, a more precise investigation on the system dynamics is carried out in a closed-loop system identification method. The nonlinearity and the uncertainty of the system dynamics are measured and investigated. As a result, an H_∞ controller is proposed to the relative height positioning system for a robust control performance within the whole sensing range. In comparison to the lag-control design, experimental tests have shown that the proposed H_∞ control has an improved transient response and an advanced steady-state performance in the whole relative height sensing range.

The realisation of the two cantilever vertical positioning systems achieves 1 nm control performance in a noise predominant scenario. The robustness of both H_∞ control designs will provide an improved TDFM imaging quality, in contrary to the previous ad-hoc PI control strategy (Harniman 2013). Applying appropriate scanning principles, the developed two closed-loop positioning systems are integrated with the TDFM system design in Chapter 3 and result in the successful TDFM scans as shown in Chapter 6.

Chapter 5

Real-time Transverse Force Reconstruction

5.1 Introduction

This chapter presents a novel approach realising directly real-time reconstruction of the atomic interaction force in the TDFM. In contrast, previous relevant research has studied the interaction atomic-force from recorded cantilever deflection measurement using offline data-processing methods (e.g. the study (Payam et al. 2015, Labernadie et al. 2014, Ding et al. 2015) in typical AFMs and (Antognozzi et al. 2001, 2016) in TDFMs). Distinctive from the previous proof-of-concept work (Nguyen et al. 2016), this chapter presents a complete development procedure, including the modelling, the force estimation algorithm development, and the electronic implementation, to practically facilitate the real-time force sensing for specimen scans in practice. Our recent work (Nguyen et al. 2016) still required some processing of data within the attached experimental PC, focussing on the measurement and their instant presentation at individual x-y in-plane positions. In contrast, the algorithms presented here permit fast on-FPGA-system implementation with the capability to scan and safe whole images in real-time (The presentation follows in Chapter 6).

This chapter starts with the cantilever dynamics identification, analysis, and modelling. Based on the practical measurement, a two-inputs-single-output model is established to describe the cantilever dynamics, being excited by the external oscillation and driven by the shear-force of the confined water layer. In the second section, a sliding mode observer is developed, designed, and implemented to real-time estimate the interaction shear-force using FPGA. The viscosity and the elasticity over the sample-substrate is subsequently estimated by the host-PC according to the real-time force measurement. The results section presents the practical force measurement results demonstrating the effectiveness of the developed real-time interaction-force sensing component.

Supporting publications:

- *"A real-time transverse dynamic force estimator in fixed-point arithmetic"*, Zhang, K., G. Herrmann, M. Antognozzi, et al., Prepared for journal submission.

- *"Estimation of the shear force in transverse dynamic force microscopy using a sliding mode observer"*, Tien, TN., T. Hatano, S. Khan, K. Zhang, et al., *AIP Advances*, 2015, vol. 5(9), 097157.

5.2 Cantilever Dynamics

This section introduces the method to numerically model the cantilever oscillation to develop the shear force estimator. The theoretical state-space model is developed from a bending beam model using the method of lines. In order to apply the model to the estimation algorithm development, a specific procedure is employed to compute a low-order model, matching with the practical system response, which is experimentally measurable and presents partial dynamics of the system. Therefore, this low-order model is called a practical model to be used for the development of the shear force estimator.

5.2.1 Cantilever Dynamics Model

The cantilever oscillation dynamics can be assumed to be an Euler–Bernoulli bending beam as shown in Figure 5.1. The beam is excited at the upper end of the cantilever by a translation $u(t)$ in y direction at time t. Subsequently, the cantilever oscillates with the transverse displacement $y_c(\xi, t)$ in the scan medium freely. There is no specific shear-force created on the cantilever tip when the cantilever is outside the shear force interaction range. Here, ξ indicates the position value, along the natural beam (i.e. along the z-axis), starting from the upper end of the cantilever. As soon as the cantilever tip penetrates the confined water layer, the ordered water-molecule layer creates the shear force $f(t)$ in the opposite direction to the cantilever deflection along the y-axis.

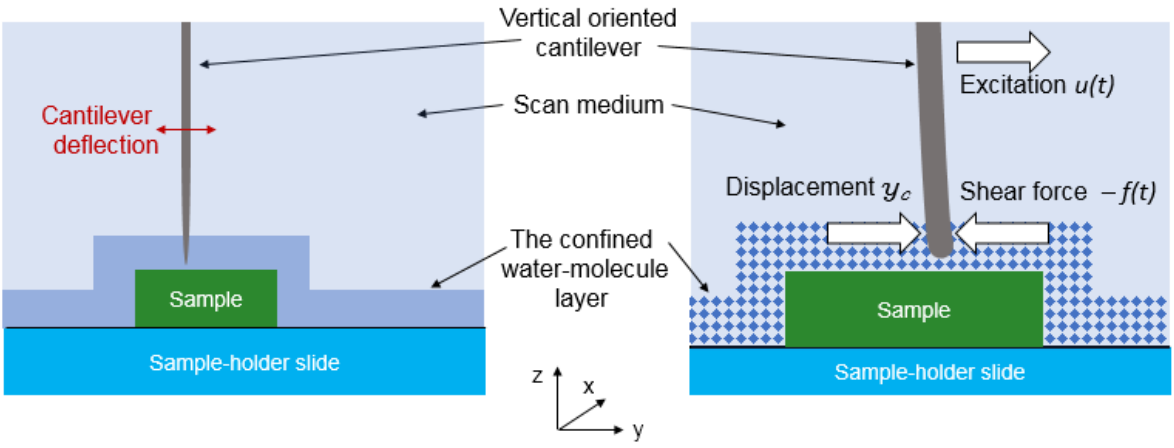

FIGURE 5.1: A schematic of the cantilever oscillation modelled as a bending beam oscillating in y direction. The beam is excited by $u(t)$ at the upper end the shear force $f(t)$ is created due to the interaction with the confined water layer. The beam displacement is the result of $u(t)$ and $f(t)$ together.

The well known Euler-Bernoulli equation from beam theory is used as the starting point to develop a model of the shear force interaction between the cantilever tip and the specimen (Antognozzi 2000).

Specifically, the partial differential equation is given as:

$$EI\frac{\partial^4}{\partial\xi^4}(y_c + \alpha\frac{\partial y_c}{\partial t}) + \rho A_s\frac{\partial^2 y_c}{\partial t^2} + \gamma d\frac{\partial y_c}{\partial t} = 0 \tag{5.1}$$

where the boundary conditions of the cantilever at time t are

$$y_c(\xi = 0) = u(t), \tag{5.2}$$

$$\frac{\partial y_c}{\partial \xi}(\xi = 0) = 0, \tag{5.3}$$

$$\frac{\partial^2 y_c}{\partial \xi^2}(\xi = L) = 0, \tag{5.4}$$

$$EI\frac{\partial^3 y_c}{\partial \xi^3}(\xi = L) = -f(t). \tag{5.5}$$

In Equations (5.1) to (5.5), α is the internal damping constant (s) added to present the dissipative internal damping force, E is Young's modulus of the cantilever material, I indicates the second moment of area, A_s is the cross-sectional area of the cantilever, ρ is its density, γ is the viscous coefficient (Nsm^{-3}) of damping in the term $\gamma d\frac{\partial y_c}{\partial t}$ presenting the dissipative force caused by the surrounding environment, w is the width of the cantilever, and L is the cantilever length.

Note that the length of the cantilever (18 μm) is assumed to be much greater than its thickness (200 nm). Therefore, Equation (5.1) can be written in the given format without the need to consider the rotatory inertia and the effect of the shear force of the cantilever. The cantilever deflection y_c depends on the position ξ and time t. The cantilever excitation $u(t)$ is a constant sine-wave oscillation provided by the dither piezo-actuator in the TDFM.

Specifically, the force $f(t)$ caused by the confined liquid layer can be separated into a viscous force and an elastic force:

$$f(t) = -\nu\frac{\partial y_c}{\partial t}|_{\xi=L} - \kappa y_c|_{\xi=L} \tag{5.6}$$

where ν is the constant of dissipative interaction and κ is the elastic interaction constant according to the Maxwell model (Antognozzi 2000).

The model in Equations (5.1) to (5.5) provides an understanding of the dynamic relationship of the cantilever excitation $u(t)$ and the shear force $f(t)$ influencing the cantilever tip position $y_t(t)$. The objective is to enable the estimation of the unknown shear-force signal $f(t)$ using an unknown input observer based only on knowledge of $y_t(t)$ and $u(t)$. As the $f(t)$ and $u(t)$ are not collocated, a cantilever model needs to be established to relate the system inputs $u(t)$ & $f(t)$ and the output $y_t(t)$.

Therefore, the method of lines is used to approximate the partial differential Equation (5.1) by a time-invariant ordinary differential equations as introduced in our previous work by Nguyen et al. (2016). This approach also retains some of the versatility of the partial differential equation, as forces and the scan-medium interferences can be modelled with good accuracy by choosing for instance the model parameter

γ and α. Most importantly, this approach will provide an accurate control engineering perspective on the influence of the unknown shear force, $f(t)$ (and also the excitation signal $u(t)$) on the output $y(t)$, and the chosen observed states of the system. The process for obtaining this model is to first conduct a method of lines analysis and then to use an established model reduction approach to obtain a good low order approximation of the dynamic relationship.

The main idea is to subdivide the cantilever into $n-1$ equal sections and to consider n nodes distributed along the probe. Therefore, the infinite dimensional partial differential equation can be approximated by a finite dimensional ordinary differential equation, when the measured top position $y_c|_{\xi=L}$, the shear force $f(t)$, and the excitation signal $u(t)$ are given. In this way, the spatial derivatives from Equation (5.1) are removed, retaining only the temporal derivative (see Equation (5.10)), resulting in a convenient model for observer design. The displacement y_c at node j is denoted by $y_{c,j}$ and let $\delta\xi$ represent the distance between two consecutive nodes. Using a finite difference formula, the boundary conditions Equations (5.3) to (5.5) approximate

$$y_{c,2} = y_{c,1}, \tag{5.7}$$

$$y_{c,n} - 2y_{c,n-1} + y_{c,n-2} = 0, \tag{5.8}$$

$$\begin{aligned} EI\frac{\partial^3 y_c}{\partial \xi^3}(\xi = L) &\approx EI\frac{y_{c,n}-3y_{c,n-1}+3y_{c,n-2}-y_{c,n-3}}{\partial \xi^3} \\ &= -f(t) \end{aligned} \tag{5.9}$$

respectively.

From Equations (5.2), (5.7), (5.8), and (5.9), it is clear that the values of $y_{c,1}$, $y_{c,2}$, $y_{c,n-1}$, and $y_{c,n}$ are "known", in the sense that they depend on the values of the remaining nodes. Hence, the evolution of the system depends on only $n-4$ nodes. Each of these nodes is described by a second-order ordinary differential equation. Therefore, the dynamics of the cantilever can be represented by a state space system of order of $2(n-4)$. Assuming each node is unified, the state variables are defined as

$$\begin{aligned} x_1 &= y_{c,3}, \\ x_2 &= \dot{y}_{c,3} - \tfrac{3EI\alpha}{\rho A_s \delta\xi^4}u, \\ x_3 &= y_{c,4}, \\ x_4 &= \dot{y}_{c,4} + \tfrac{EI\alpha}{\rho A_s \delta\xi^4}u, \\ &\dots \\ x_{2j-5} &= y_{c,j}, \\ x_{2j-4} &= \dot{y}_{c,j}, \\ &\dots \\ x_{2n-11} &= y_{c,n-3}, \\ x_{2n-10} &= \dot{y}_{c,n-3} + \tfrac{\alpha}{\rho A_s \delta\xi}f, \\ x_{2n-9} &= y_{c,n-2}, \\ x_{2n-8} &= \dot{y}_{c,n-2} - \tfrac{2\alpha}{\rho A_s \delta\xi}f \end{aligned} \tag{5.10}$$

for $j = 5, ..., n-4$, where $\dot{y}_{c,j}$ denotes the time derivative of y_c of the j node.

As a result, the linear time invariant system of the cantilever can be written in the state space as

$$\begin{aligned} \dot{x_l} &= A_l x_l + B_l u + D_l f \\ y_l &= C_l x_l \end{aligned} \tag{5.11}$$

where $x_l \in \mathbb{R}^{2(n-4)\times 1}$ denotes the state vector of the system. $A_l \in \mathbb{R}^{2(n-4)\times 2(n-4)}$, $B_l \in \mathbb{R}^{2(n-4)\times 1}$, and $D_l \in \mathbb{R}^{2(n-4)\times 1}$ are computed from the state variables defined in (5.10). Assuming n is sufficiently large (i.e. $\delta\xi \to 0$), the cantilever deflection y_l can be approximated by $y_{c,n-2}$. Hence, the $(2n-9)$th entry of $C_l \in \mathbb{R}^{2(n-4)\times 1}$ is 1 and the remaining entries are zero.

The dynamic model (5.11) is often expressed by a high order state-space model, as the amount of nodes n needs to be sufficiently large. This potentially results in a high order force estimator, that cannot be successfully implemented on digital hardware with limited hardware resource, particularly FPGA boards. In order to guarantee the implementability, a model reduction method needs to be applied to the high order state space model. Specifically, the standard balanced truncation method by Moore (1981) is used in Matlab. Practically, an 8th order state space mode can well approximate the high-order state-space model. The order reduced model is presented by

$$\begin{aligned} \dot{x}(t) &= Ax(t) + Bu(t) + Df(t) \\ y_t(t) &= Cx(t) \end{aligned} \tag{5.12}$$

which will be used to design the unknown input, force $f(t)$, estimator. Here, the cantilever tip displacement is presented by $y_t(t)$ $(= y_c(\xi, t)|_{\xi=L})$, representing a good approximation.

5.2.2 System Identification and Parametric Modelling

In order to facilitate the estimator, a practical model in the format of (5.12) has to be obtained considering various implementation factors, e.g. the amplifiers, the electronics, etc. Then, an estimator designed for the practical model is feasible to be implemented and used for the real-time force measurement.

Specifically, the excited cantilever oscillation dynamics of $u(t)$-to-$y_t(t)$ is measurable only when there is no shear force interaction involved in. Hence, the solution to obtain the precise cantilever numerical model is developed in the following procedure: a) identify the $u(t)$-to-$y_t(t)$ response of the cantilever oscillation outside the shear force interaction range; b) adjust the parameters of the theoretical state-space model (5.11) to match with the practically identified system dynamics (so that the fitted model is a practical model for the estimator design); c) reduce the fitted state-space model into a low-order format of (5.12) retaining the critical dynamics information around the cantilever oscillation frequency.

The cantilever dynamics are measured by using the swept-sine system identification method (see the set-up in Figure 5.2). During the identification, the dither piezo-actuator exciting the type A cantilever

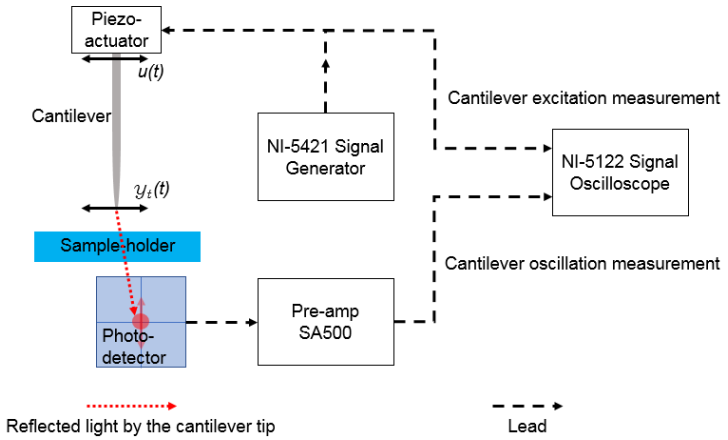

FIGURE 5.2: The practical set-up to identify the cantilever oscillation using the swept-sine system identification method. Since the force is unknown in the system identification, the cantilever has to be placed outside the shear-force interaction range to measure the system response from $u(t)$ to $y_t(t)$.

(as introduced in Section 3.2.1) is driven by sine waves with 0.1 V amplitude at 200 kHz. As a result, the cantilever is excited around its resonance in water medium with an oscillation amplitude of ∼2 nm without shear force interaction. Therefore, the maximal digital measurement (on the NI-7962R FPGA board) of the cantilever oscillation is in a pre-determined numerical range of 2^{10}, when the optical sensitivity $S_{y,calib}$ (see Equation (3.2) in Section 3.2.1) is optimised as 6 mV/nm. Hence, the investigated cantilever dynamics are very closed to the default experimental condition used in the practical force sensing tests and in real-time force scans when a 2 nm cantilever oscillation amplitude is typically used.

The frequency response $Y(s)/U(s)$ ($U(s) = \mathcal{L}\{u(t)\}$, $Y_t(s) = \mathcal{L}\{Y_t(t)\}$) of the $u(t)$-to-$y_t(t)$ plant is measured when the cantilever is placed at 20 nm above the sample-holder slide to avoid the influence of the shear force. As shown in the set-up, the identified frequency response has the input (excitation from the signal generator) and the output (optical data measurement from the photo-detector and then being amplified by the amplifier) in voltage. Hence, the practical model needs to fit the plant response computed from the input and output signals. This guarantees that the subsequently designed estimator can be deployed on the hardware without extra adjustment. Note that the measured frequency response is computed from the input and output signals that have different units in relation to the theoretical high-order state-space model. This measured frequency response also contains noise and the effects of amplifications. Therefore, a scaling factor needs to be applied to the theoretical model, in order to ensure that the magnitude of the model fits the measured response.

The $Y_t(s)/U(s)$ frequency response is measured for different type A cantilevers as the examples shown in Figure 5.3. The high similarity of different data sets demonstrates that the different type A cantilevers have very similar frequency response. The $Y_t(s)/U(s)$ plant has a first significant resonance around 200 kHz (confirmed as the first resonance in water). Other mechanical components, related to the cantilever fixture, cause resonances (at about 5 kHz, 15 kHz, etc.) at a much smaller magnitude. Note that each cantilever is found to be slightly different in terms of the mechanical properties. Specifically, the first

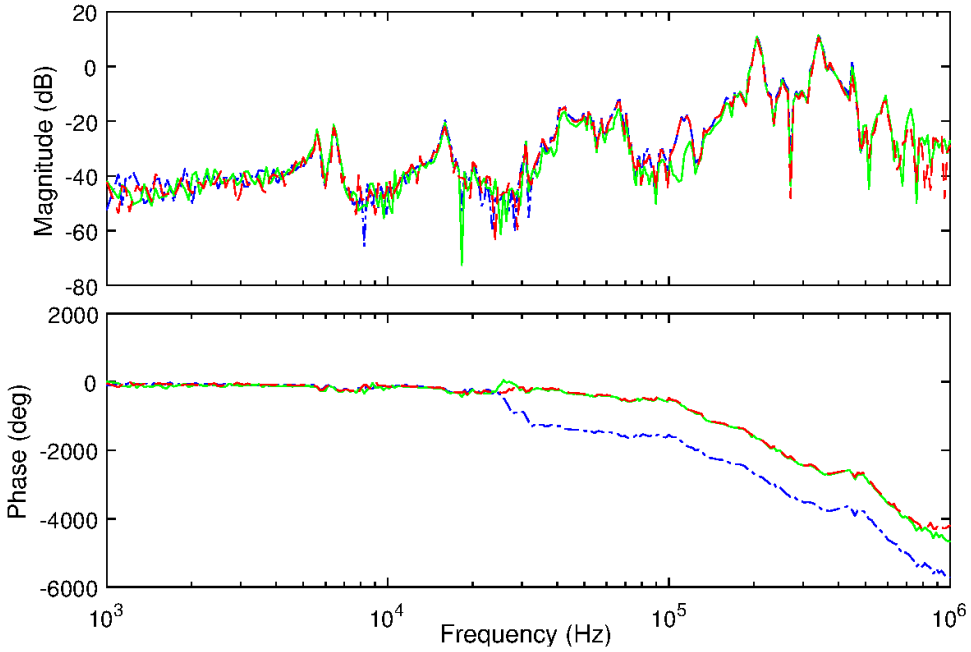

FIGURE 5.3: The measured frequency response in three different colours represents the dynamics of three different type A cantilevers via the swept sine system identification method. The system identifications for the three different cantilevers is carried out in the same water medium at different times. In each experiment, the cantilever oscillation is caused by only an excitation without any shear-force interaction.

resonances of different type A cantilever have slightly different magnitudes at the vicinity of 200 kHz. Hence, the $Y_t(s)/U(s)$ response needs to be measured for each cantilever to derive an accurate cantilever dynamics model.

After the $Y_t(s)/U(s)$ response is practically measured for a cantilever, the linear time-invariant model (in the state space form of Equation (5.11)) needs to be parametrically adjusted to fit the practical data. After deciding a sufficiently large n, the parameters α, γ, and the scaling factor are chosen to make sure the high-order state-space model fits the practically measured $Y_t(s)/U(s)$ response, while the other parameters are fixed specifications of the cantilever. The order reduced model (Equation (5.12)) precisely matches the high-order state-space model in Figure 5.4. Note that the cantilever only works at the excited resonance frequency in practice. Hence, the model needs to match the magnitude and the phase of the practical measurement around the excitation frequency. The frequency responses at other frequencies are not of interest for the force measurement objective. The state-space model of Equation (5.12) is determined having the frequency response as shown in Figure 5.5, which is the practical model to be used for developing the force estimator to be implemented on FPGA.

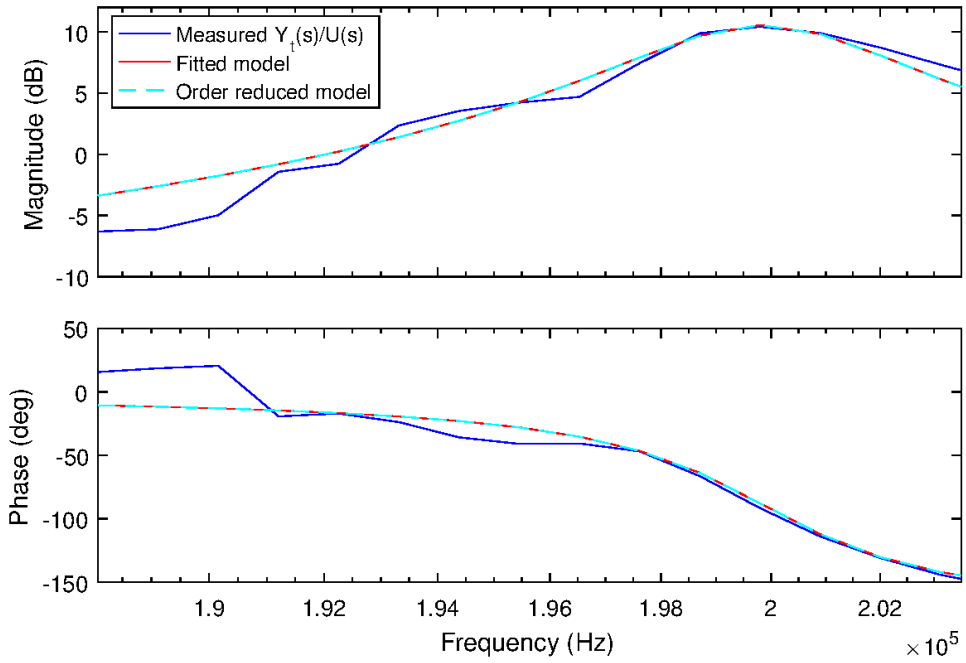

FIGURE 5.4: The fitted high-order and the order-reduced cantilever models are adjusted to match the measured $Y_t(s)/U(s)$ frequency response around the resonance frequency in detail.

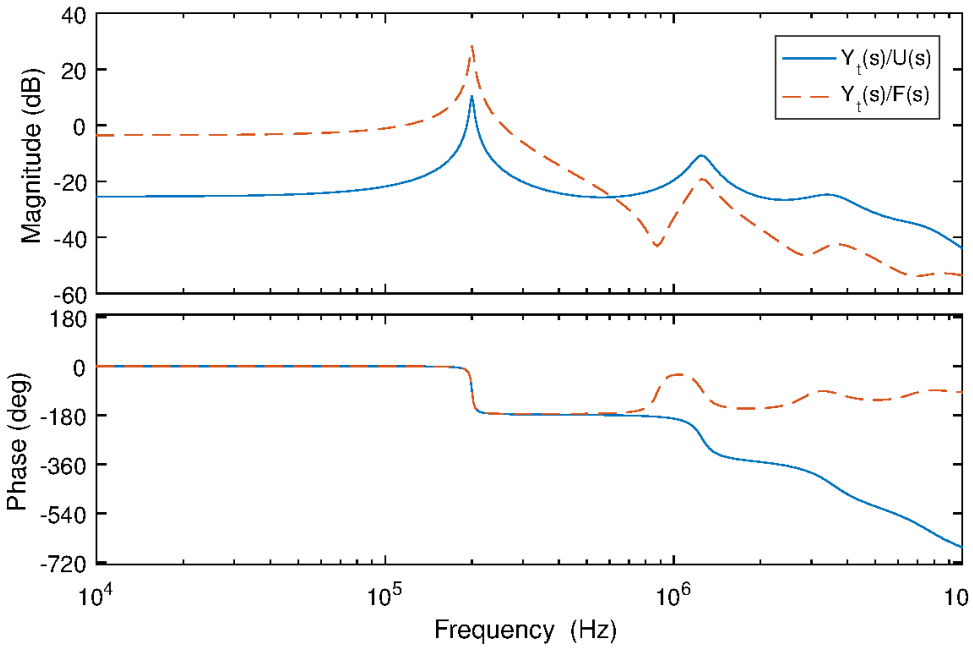

FIGURE 5.5: The order-reduced cantilever dynamics model: $Y_t(s)$, $U(s)$, and $F(s)$ indicate the cantilever tip displacement, excitation, and shear-force in the Laplace domain.

5.3 Shear Force Reconstruction

Based on the order reduced model, a sliding mode observer is developed to reconstruct the shear force in real-time. Motivated by estimating force signals at high frequency, the force estimator is designed as digital programme to be implemented on FPGA. The viscosity and the elasticity of the sample-substrate

surface can be estimated by an additional parameter estimation process at a slower speed to process the real-time force estimation on the host-PC. Importantly, the design of a high-frequency digital sliding mode observer is non-trivial considering several practical implementation issues.

5.3.1 Real-time Force Estimation

Here, a sliding mode observer based on previous research (Nguyen et al. 2015, 2016) is considered. Based on the system identification results, the practical model (written in the format of Equation (5.12)) is used to estimate the shear force $f(t)$ from the knowledge of only $y(t)$ and $u(t)$ in real-time. The sliding mode observer is designed as

$$\begin{aligned} \dot{\hat{x}}(t) &= A\hat{x}(t) + Bu(t) + D\phi + G(y_t(t) - \hat{y}_t(t)) \\ \hat{y}_t(t) &= C\hat{x}(t) \end{aligned} \tag{5.13}$$

where G is a gain matrix. $\hat{y}_t(t)$ denotes the estimated tip oscillation signal and ϕ is the nonlinear injection signal defined as

$$\phi = \begin{cases} -\Lambda sign(\hat{y}_t(t) - y_t(t)) & \text{if } |\hat{y}_t(t) - y_t(t)| \geqslant 1 \\ -\Lambda(\hat{y}_t(t) - y_t(t)) & \text{if } |\hat{y}_t(t) - y_t(t)| < 1 \end{cases} \tag{5.14}$$

and the $sign(\cdot)$ is the mathematical operation to take the sign of the input variable. This can be realised by multiplying the saturated $\hat{y}_t(t) - y_t(t)$ with a [-1,1] range by $-\Lambda$. Λ represents a positive scalar gain satisfying

$$\max(\|f(t)\|) < \Lambda. \tag{5.15}$$

The previous single-position results (Nguyen et al. 2015, 2016) show that, for an appropriate choice of G and the scalar Λ, the output estimation error $\hat{y}_t(t) - y_t(t)$ is driven to zero in finite time and a so-called sliding motion takes place (Edwards & Spurgeon 1997, 1998).

Here, a practical design chooses G as a zero matrix. Thus, we largely follow the design approach as suggested by Utkin (1981) and analysed by Edwards & Spurgeon (1998). Following Section 6.2 and Proposition 6.2 in the work (Edwards & Spurgeon 1998), the necessary and sufficient conditions for the existence of this observer are:

1. The matrix A is Hurwitz, i.e. stable, in the left half plane;
2. $CD \neq 0$, i.e. the model (A,D,C) is relative degree one;
3. The invariant zeros of (A,D,C) are stable, i.e. the zeros of the transfer function $C(sI - A)D$ are stable.

Practically, the first condition is always satisfied, considering that a mechanical beam subject to significant damping is modelled. The second and third condition is generally guaranteed through the practically guided model order reduction process, where stable zeros and a relative degree one transfer function of

$C(sI - A)D$ is enforced. It is also to mention that the original model (A_l,D_l,C_l) is also having stable zeros in the investigated cases here.

Hence, the force estimator is realised as

$$\begin{aligned} \dot{\hat{x}}(t) &= A\hat{x}(t) + Bu(t) + D\phi \\ \hat{y}_t(t) &= C\hat{x}(t) \end{aligned} \tag{5.16}$$

where ϕ is defined in (5.14).

Such an implementation has two significant advantages:

- The absence of the multiplication of two matrices saves significant digital design effort and hardware computational resource;
- G is not needed, otherwise the design of G would have to be robust for any change of the system (e.g. the cantilever), i.e. increases the difficulties to use the TDFM.

During the sliding motion, on average, the high frequency switching term ϕ must replicate $f(t)$ for sliding to be maintained. The average value of $-\phi$ necessary to maintain sliding is known as the equivalent injection (Edwards & Spurgeon 1998, Utkin 2013). Since the $\hat{y}_t(t) - y_t(t) \to 0$ as $t \to \infty$ due to the convergence (Utkin 2013), the negative value of the equivalent injection ϕ will be equal to $f(t)$.

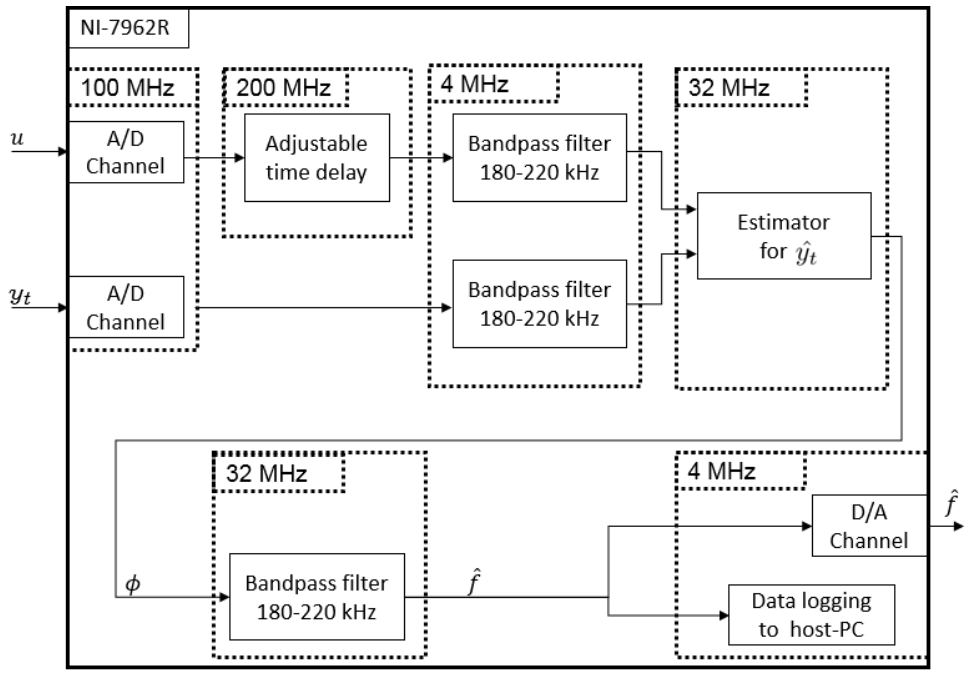

FIGURE 5.6: The digital design of the proposed shear-force reconstructor on the NI-7962R.

The previous single-position results of Nguyen et al. (2015, 2016) demonstrate that a simple first order low-pass filter applied to $-\phi$ can provide a good force estimation $\hat{f}(t)$. However, the hardware limitation,

e.g. the insufficient sampling rate of the injection, introduces quantisation errors/noise to $\hat{f}(t)$ over the whole frequency range. Practically, the $f(t)$ is caused by the tip oscillation determined by the excitation $u(t)$, i.e. the $f(t)$ mainly oscillates at the same frequency of $u(t)$. Hence, a bandpass filter is suggested to obtain the shear force information at the particular frequency, and additionally reduce the noise caused by the quantisation error. A 5th order bandpass filter is suggested in order to achieve good estimation performance at low computational resource cost. In experiments, the estimation error is mainly caused by inaccuracy due to the low sampling rate of 32 MHz and mechanical/electro-magnetic noise. The inaccuracy caused by the low sampling rate can be ignored when the interaction shear force significantly affects the cantilever . As a result, the shear force reconstructor is designed to be implemented on the NI-7962R as shown in Figure 5.6

5.3.2 Viscosity & Elasticity Estimation

The successful estimation of $f(t)$ enables to provide the real-time information of elasticity $\nu(t)$ and viscosity $\kappa(t)$ based on the dynamics (5.6). Here, the specimen surface mechanical properties, specifically ν and κ, vary during a dynamic scan. Hence, an unknown parameter estimation algorithm developed by Mahyuddin et al. (2014), Na et al. (2017) is selected due to a good adaptive parameter estimation performance via the following regime. Focusing on the model of (5.6), the output force is approximated by the real-time estimation $\hat{f}(t)$ that is a good approximation of the force f. The required variables are the measured oscillation signal $y_t(t)$ and the tip oscillation velocity $\dot{y}_t(t)$. Specifically, the tip oscillation velocity is the derivative of $y_t(y)$ that can be calculated by various methods. Hence, the estimation of $\nu(t)$ and $\kappa(t)$ is to estimate the unknown parameters according to the known states ($y_t(t)$ and $\dot{y}_t(t)$) and the known output $\hat{f}(t)$ in Equation (5.6).

Here, a parameter estimator developed by Mahyuddin et al. (2014), Na et al. (2017) is used. In detail, Equation (5.6) is rewritten into

$$\begin{aligned} f &= \begin{bmatrix} \dot{y}_t & y_t \end{bmatrix} \begin{bmatrix} -\nu \\ -\kappa \end{bmatrix} + \zeta \\ &= \Psi(t)\Theta + \zeta \end{aligned} \tag{5.17}$$

where $\Psi = \begin{bmatrix} \dot{y}_t & y_t \end{bmatrix}$ and $\Theta = \begin{bmatrix} -\nu \\ -\kappa \end{bmatrix}$, considering $\hat{f}(t) \to f(t)$ and a bounded disturbance/noise term ζ due to digital quantisation noise. A simple first order filter is introduced for each term of (5.17) in the form:

$$\begin{aligned} k\dot{f}_f(t) + f_f(t) &= f(t), \qquad f_f(0) = 0 \\ k\dot{\Psi}_f(t) + \Psi_f(t) &= \Psi(t), \qquad \Psi_f(0) = 0 \\ k\dot{\zeta}_f(t) + \zeta_f(t) &= \zeta(t), \qquad \zeta_f(0) = 0. \end{aligned} \tag{5.18}$$

Specifically, the computation of the $\Psi_f(t)$ filters $y_t(t)$ to calculate $y_{tf}(t)$, and consequently obtaining

$\dot{y}_{tf}(t)$ by

$$k\dot{y}_{tf}(t) + y_{tf}(t) = y_t(t), \qquad y_t(0) = 0. \tag{5.19}$$

This $\dot{y}_{tf}(t)$ is taken as $\dot{y}_t(t)$ instead of directly computing the derivative of $y_t(t)$ due to the digital nature of the signal. Therefore, the filtered (5.17) is written as

$$f_f = \Psi_f \Theta + \zeta_f, \tag{5.20}$$

assuming that the change in parameter value κ and ν in relation to the following regressor filter operation is slow and κ and ν can be regarded as (almost) constant.

Two filtered regressors $M(t)$ and $N(t)$ are formulated as

$$\begin{aligned} \dot{M}(t) &= -lM(t) + l\Psi_f^T(t)\Psi_f(t), \qquad M(0) = 0 \\ \dot{N}(t) &= -lN(t) + l\Psi_f^T(t)f_f(t), \qquad N(0) = 0 \end{aligned} \tag{5.21}$$

where l is a positive scalar, acting as a forgetting factor in this first order filtering process. Notice that $\dot{y}_t(t)$ and $f(t)$ are filtered and estimated from the measured $y_t(t)$. This results in $\zeta_f \to 0$ in Equation 5.20, when $t \to \infty$. As the output signal $y_t(t)$ is sinusoidal, the richness of the measurements (due to sinusoidal excitation) allows for estimating the two parameters, κ and ν, which implies that M is non-singular at all times (Nguyen et al. 2016). Therefore, the estimation of $\Theta = \begin{bmatrix} -\nu \\ -\kappa \end{bmatrix}$ is

$$\hat{\Theta} = M^{-1}N. \tag{5.22}$$

Given the presence of the forgetting factor, l, in the formulation of $M(t)$ and $N(t)$, this matrix-inversion formulation provides a lightweight and effective estimator for ν and κ.

5.3.3 Digital Implementation

The real-time force estimation is implemented on the NI-7962R FPGA as shown in Figure 5.6, considering the following practical issues.

The synchronisation of the system inputs $u(t)$ and $y_t(t)$ is critical for an accurate force estimation performance. Particularly, the measured y_t is always delayed by the electronics, mainly the optical sensor and the pre-amplifier. Hence, a delay programme is suggested to accurately synchronise u and y_t. The digital delay is manually adjustable for the u signal at the minimal delay step of 5 ns.

The presence of the measurement noise considerably influences the estimation precision in practice. The noise mainly consists of the high frequency electro-magnetic noise inherent from the electronics and the spiky noise caused by the A/D conversion (running at the maximum rate of 100 MHz). To reduce noise, two bandpass filters are applied to both u and y_t measurements. Then, the bandpass filtered signals

are used as the inputs of the shear force estimator. It is critical to guarantee the filtered u and y_t are changed by the same gain and phase. Hence, the identical filters are designed as 2nd order butter-worth filters with 180-220 kHz bandwidths at a running frequency of 4 MHz that is a sufficiently high sampling rate for the shear-force reconstruction.

The structure of the estimator has to be well designed to manage the complex digital filtering function running at a high sampling time. The result of Nguyen et al. (2015, 2016), focussing on a single point, used the collected data to process the algorithm in the associated PC within a continuous-time numerical process. As a result, the state space representation of (5.13) allowed for matrix-multiplication and continuous-time integration of $\dot{x}$. However, a direct, more complete, implementation on the FPGA is practically infeasible. To implement the observer with minimal hardware cost at high running speed, the estimator (5.16) is transformed into an observable canonical form and implemented by fixed-point arithmetic in a modified Transposed Direct Form II structure. This implementation structure allows the digital programme to execute the filtering by using one multiplication and two addition computations in series at one clock cycle time, practically, at 32 MHz sampling frequency. The complex digital filtering programme can be built up by careful execution of several computations in parallel.

Specifically, the estimator is discretised (using Tustin's method) and transformed into the observerable canonical form. The estimation of $y_t(t)$ in discrete time is given as

$$\hat{Y}_t(z) = \frac{\sum_{k=1}^{8} b_{u,k} z^{-k} U(z) + \sum_{k=1}^{8} b_{f,k} z^{-k} \Phi(z)}{1 + \sum_{k=1}^{8} a_{obs,k} z^{-k}} \tag{5.23}$$

where $\hat{Y}_t(z)$, $U(z)$, and $\Phi(z)$ are the discretised Laplace transformation of $y_t(t)$, $u(t)$, and $\phi(t)$. The coefficients are $b_{u,k=1,\ldots,8}$ = (-0.00037, 0.00333, -0.00871, 0.00615, 0.00728, -0.01413, 0.00801, -0.00156), $b_{u,k=1,\ldots,8}$ = (0.00200, -0.00829, 0.01550, -0.01743, 0.01306, -0.00655, 0.00193, -0.00022), and $a_{obs,k=1,\ldots,8}$ = (-5.39326, 12.96293, -18.487205, 17.60841, -11.90730, 5.79006, -1.88036, 0.30676). The estimation $\hat{y}_t(t)$ is implemented in the TDF-II format as shown in Figure 5.7.

For the implementation, the fixed-point arithmetic operations of the digital filters have to be carefully designed in order to guarantee sufficient computational accuracy. Practically, the estimator is formatted as a high-order two-inputs-single-output filter implemented by fixed-point arithmetic. The multiplication and addition operations have fixed numerical accuracy and range as soon as the fixed-point arithmetic is implemented on the FPGA. The zeros and poles of the high-order estimator are sensitive to the quantisation errors appearing at each fixed-point operation. Also, overflows have to be avoided by enlarging the numerical range of each arithmetic operation. However, both design requirements, reducing the quantisation error and increasing the numerical range, need to be designed considering the limited hardware resource of the FPGA board.

Before implementation, the computational accuracy can be assessed by replicating the fixed-point design in simulation. However, the actual impact on the hardware is only known after compilation of the

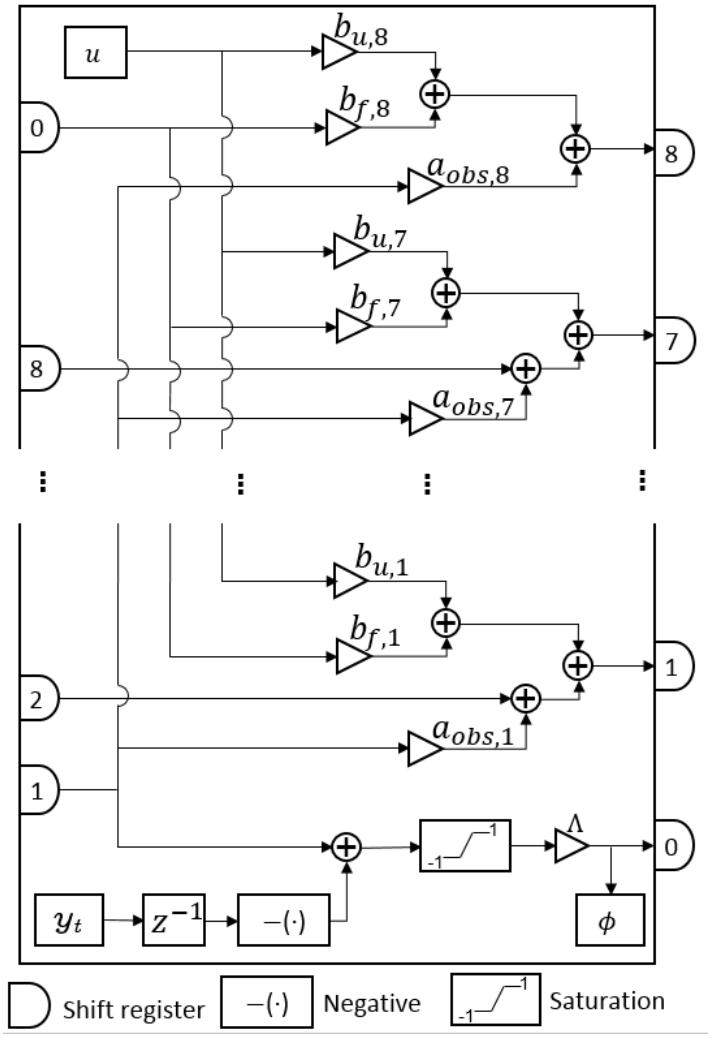

FIGURE 5.7: The digital design of the sliding mode observer to be implemented on FPGA. The estimator in Equation (5.23) is realised in Transposed Direct Form II. The injection ϕ is computed by the inputs u and y_t according to the sliding mode observer design of Equation (5.16). Specifically, a single clock cycle delay is applied to y_t as the $\hat{y}_t$ is delayed by one clock-cycle to calculate the estimation error.

designed programme. It needs a laborious trial-and-error design procedure for an optimised design. In detail, the replicated fixed-point based simulation is given a maximum feasible sampling rate, 32 MHz in practice. Then, mock $\tilde{u}$ and $\tilde{f}$ are given to a simulated cantilever dynamics model outputting a mock cantilever oscillation $\tilde{y}_t$ in continuous time. The mock $\tilde{y}_t$ and $\tilde{u}$ can be used by the digital estimator simulation in fixed-point arithmetic to get the estimated force $\tilde{f}_e$. In the process, different fixed-point configurations of multiplications and additions are tested in the simulation to guarantee $\tilde{f}_e \to \tilde{f}$. Then, the configured digital implementation is assessed by being compiled and deployed on the FPGA board, i.e. the off-line optimised programme is confirmed to be implementable considering practical hardware resource limitations. The optimised design meant to have the minimal difference between $\tilde{f}_e$ and $\tilde{f}$ when the digital implementation can be compiled and loaded on the NI-7062R.

In the optimised design shown as Figure 5.7, the fixed-point products are configured as signed

$fxp(41, 20)$. And the summing operations are optimised as signed $fxp(36, 20)$. As a result, the implemented force estimator provides the best convergence, i.e. the least magnitude of $|\tilde{f}_e - \tilde{f}|$, while the overall design consumes all hardware resource of the NI-7962R.

The injection signal ϕ has a constant high amplitude Λ which is practically hard-coded using a high value to satisfy Equation (5.15). Λ is configured to be 512 considering the A/D conversion range and the practical range of input signals. Also, the equivalent injection needs to be filtered by the suggested 5th order bandpass filter at a good computation precision. Hence, the fixed-point arithmetic operations of the filters, implemented as Butterworth filters in TDF-II form running at 32 MHz, are configured as signed $fxp(42, 16)$.

Therefore, the design of the real-time shear force estimator is shown as Figure 5.6. Each of the functional blocks are running in parallel to maximise the overall implementation rate of the estimation scheme. A 4 MHz data logging and D/A output rate is chosen, due to the speed limitation of the data streaming from the FPGA towards the host-PC.

Remark 7 The sampling rate of the sliding mode observer has to be high enough to guarantee a good estimation performance. Here, the estimator running at 32 MHz is found to be insufficient when the equivalent injection is filtered by a low-pass filter. In detail, a low-level quantisation error appears in the filtered injection ϕ at 32 MHz due to the limit imposed on the sampling rate. Practically, the low-sampled ϕ contains the necessary information of the estimated shear force at the cantilever oscillation frequency. Hence, a bandpass filter is a feasible solution to obtain $\hat{f}$ without the need of a hardware upgrade. Fixed-point simulations show that the sliding mode observer has to run at least 80 MHz to have a good approximation $\hat{f}$ averaged by a low-pass filter. ◦

Remark 8 It has been attempted to implement the sliding mode observer for the type B cantilever, which has a first resonance at ∼64 kHz in water medium. In this case, a good approximation of f can be obtained, in principle, by filtering the injection sampled at 32 MHz in fixed-point simulations. However, the estimated force $\hat{f}$ at 64 kHz is very small for the programming clock rate of 32 MHz. Therefore, the coefficients in the discretised estimator are numerically very small, i.e. exceeding the current hardware capacity. ◦

5.4 Real-time Force Estimation

The real-time force estimator is assessed in both simulation and practice. The simulation results show that the digital design provides a good shear-force estimation at a high convergence speed. The practical experiments presents the successful shear-force measurement at a 200kHz resonance frequency in real-time. This is the first time that shear-force measurement is completely real-time capable in practice so far and permits full specimen scans. The viscosity and elasticity of the sample-substrate surface is analysed

by the host-PC at a slower speed. The analysis of the real-time force measurement allows observation of the molecule-layers of the confined water-layer over the sample-holder slide.

5.4.1 Performance Assessment in Simulation

The real-time shear force estimator has to be assessed before FPGA implementation. Hence, a simulation assessment programme is developed in Simulink to optimise the digital fixed-point design and to assess the estimation performance. In the simulation, the cantilever oscillation is emulated by the state-space model fitted to the plant response measurement in continuous time. The digital observer design is replicated using the fixed-point tool and the digital latches are introduced as digital-delay units. Hence, the simulated digital force-estimator is exactly identical to the FPGA implementation.

The simulated type A cantilever is oscillated by a sine wave excitation to produce the tip-displacement amplitude of 2 nm at 200 kHz. A mock shear-force is given as a 200 kHz sine wave in the opposite direction of the cantilever excitation as in reality. For the simulation, the given shear force amplitude is configured to be 0.1 nN, dropping to 0 nN, increasing to 0.1 nN, and finally decreasing to 0.02 nN at random time as shown in Figure 5.8a.

The simulation shows that the digital design is able to estimate the shear force signal in real-time (Figure 5.8a). The estimation error (in Figure 5.8b) is easily computed by taking the difference between the given force and the estimated force. The root mean square (rms) of the real-time estimation error, caused by the quantisation error of the digital circuit design, is 0.01 nN at steady-state. The quantisation error results in a poor signal-to-noise ratio of the estimated force when the shear-force has little effect on the cantilever oscillation. The error can be further reduced to $\sim$1 pN rms when the sampling frequency of the $\hat{y}$ estimation increases to 100 MHz, which cannot be achieved by the current hardware. From the error signal, a good approximation of the shear-force signal is achieved at a high convergence speed within 0.02 ms.

The simulation results also demonstrate the implementation can reconstruct the shear force signal guaranteeing both amplitude and phase as shown in Figure 5.9. The design has a consistent convergence speed, no matter the shear-force increases or decreases.

5.4.2 Experimental Assessments

The shear-force estimator is then implemented on the NI-7962R FPGA and tested in the default experimental condition. A cantilever type A oscillates at 200 kHz with $\sim$2 nm amplitude when there is no shear-force interaction in water. There is no sample placed at the sample-holder slide which is a grade 0 glass slide. The cantilever is placed at 20 nm away from the sample-holder surface out of the interaction region. At this distance, without sinusoidal excitation, the estimator provides the real-time measurement

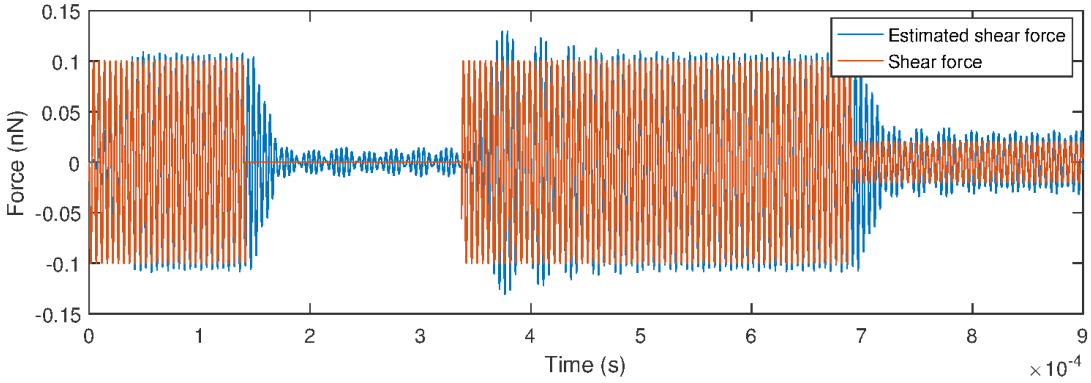

(a) The estimation performance of the designd shear-force observer in simulation.

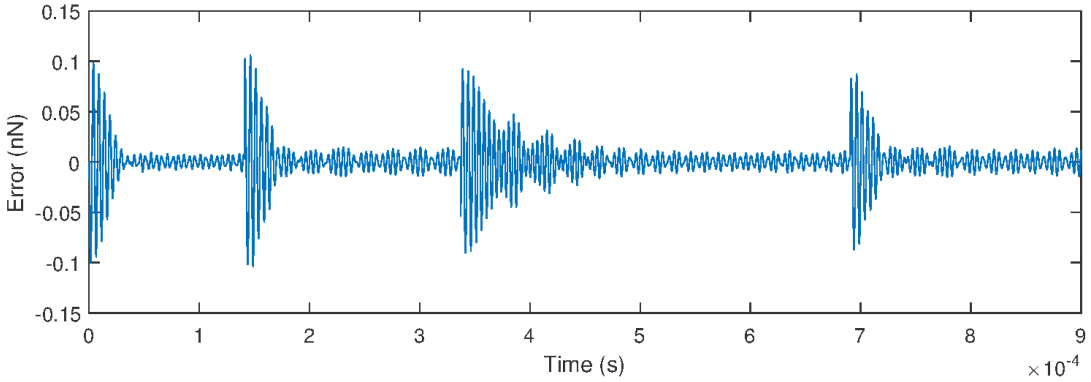

(b) The estimation error of the designd shear-force observer in simulation.

FIGURE 5.8: The designed real-time shear-force estimator is assessed in simulation. The cantilever oscillation is simulated in continuous-time based on the measured cantilever dynamics. The shear-force estimator is simulated to perform identically as the fixed-point implementation on FPGA. The estimation performance is tested to estimate a given varying shear-force signal.

caused by electro-magnetic noise and the Brownian motion as shown in Figure 5.10. It shows that the system has a noise amplitude at about 0.03 nN shear force amplitude and a 0.02 nN rms.

The shear force estimator is then tested by the following dynamic assessments. The cantilever is initialised to be at ∼6 nm above the sample-substrate at the boundary of the shear-force interaction range. The cantilever is then controlled to move towards the sample-substrate following a 100 Hz square wave with a step-size of 5 nm. The results in Figure 5.11 shows that the shear force estimator can measure a rapid shear-force amplitude ascending or descending change between 0.03-0.12 nN. As noise is a predominant factor in real-time measurement, the convergence time cannot be identified clearly. Because the closed-loop positioning system has a ∼0.25 ms settling time, an overall convergence time of the force reconstruction in less than 0.3 ms is achieved in practice.

At the initial position of ∼6 nm over the sample-substrate, the shear-force is measured when the cantilever continuously moves. The cantilever is controlled following a 100 Hz sine wave with a peak-to-peak value of 5 nm. The real-time shear-force is measured by the force estimator as presented in Figure 5.12.

The estimated force is streamed to and then processed by the host-PC for further analysis. Applying

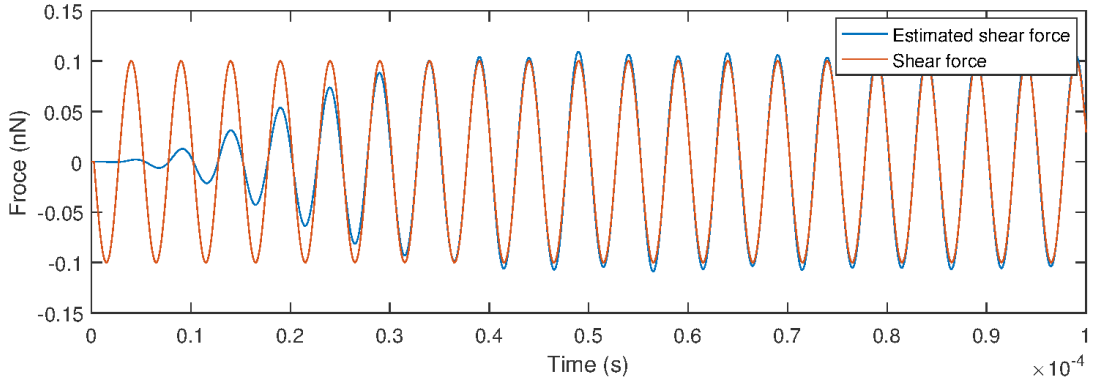

(a) The simulated shear-force estimation perfromance when the shear-force amplitude increase from 0 nN to 0.1 nN.

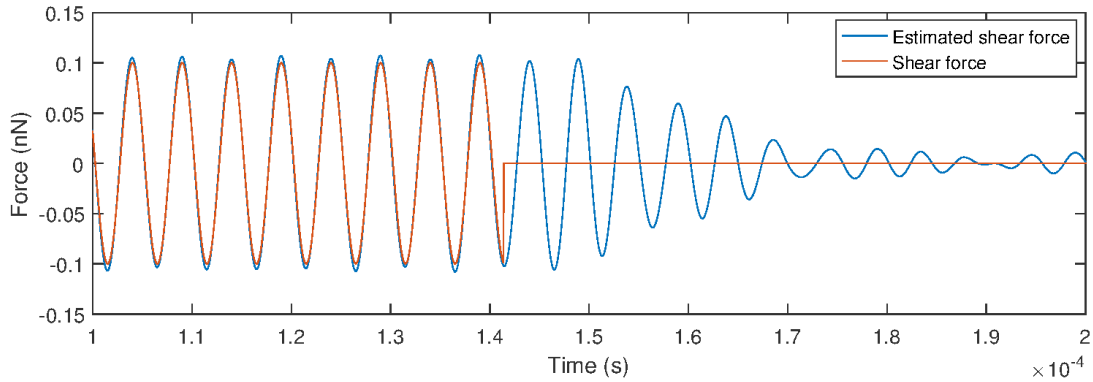

(b) The simulated shear-force estimation perfromance when the shear-force amplitude decrease from 0.1 nN to 0 nN.

FIGURE 5.9: The simulated shear-force estimation result is zoomed-in to investigate the convergence performance.

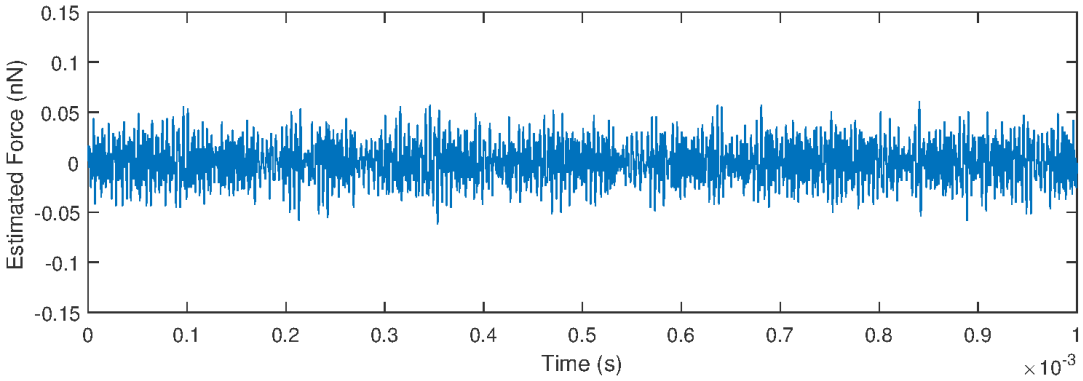

FIGURE 5.10: The real-time shear-force measurement when the cantilever is placed at about 20 nm above the sample-holder slide in water.

the proposed estimator, the viscosity ν and the elasticity κ constants can be online measured as shown in Figure 5.13a. Here, the filtering parameter k is chosen as 7.2343×10^{-7} to ensure a high filtering bandwidth for the $1/(ks+1)$ filters in Equation (5.18), i.e. richness of the data is guaranteed. The factor l is configured to be 6×10^3 to average the data in a relatively long period of about 0.3 ms time. Thus, considering the cantilever oscillation at 200 kHz, sufficient data is fed into the parameter estimator for an

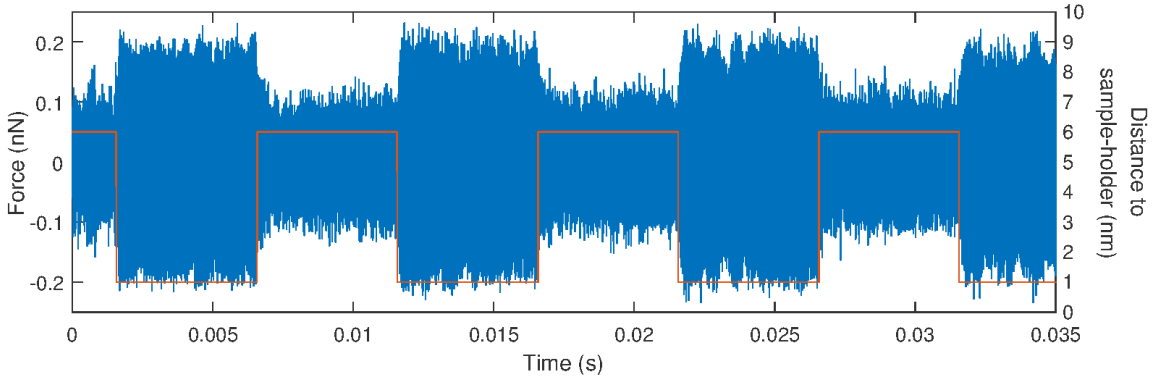

FIGURE 5.11: The real-time shear-force measurement (in blue) when the cantilever is controlled (following the trajectory in red) to jump between 1 nm and 6 nm above the sample-holder slide at 100 Hz frequency in water.

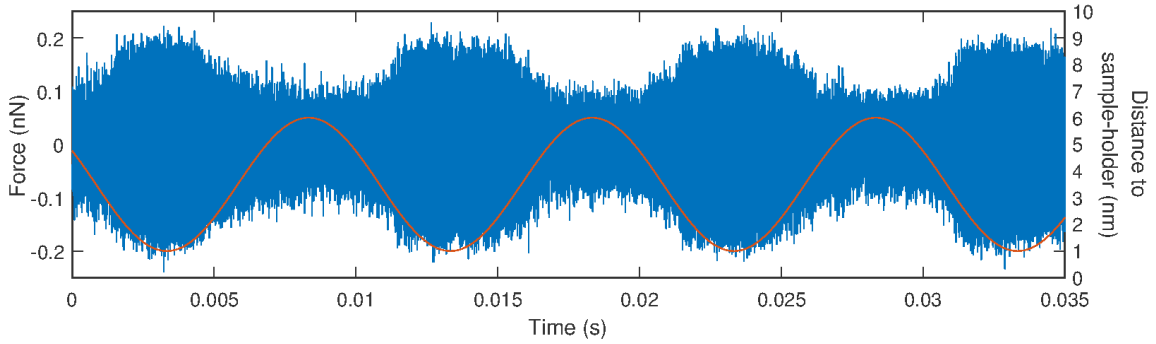

FIGURE 5.12: The real-time shear-force measurement (in blue) when the cantilever is controlled to continuously move between 1 nm and 6 nm above the sample-holder slide along a sine trajectory (in red) at 100 Hz frequency in water.

accurate estimation of viscosity ν and elasticity κ. Hence, in principle, dynamicly changing parameters of ν and κ can be measured within a settling time of 0.6 ms . The host-PC is not capable to run the ν and κ observer in real-time, so that these results are obtained offline at a slower speed in practice. The viscous and elastic forces are computed by the host-PC based on the real-time force measurement as shown in Figure 5.13b.

The effective values of the viscous and elastic forces, i.e. the standard deviation of the forces, with respect to the cantilever-sample distance can be obtained offline as shown in Figure 5.14. It can be seen that the elastic force and the viscous force both decreases as the cantilever-sample inter-distance increases as observed by Antognozzi (2000). Both the forces decay monotonically up to a range of ∼6 nm range agreeing within previous studies (Israelachvili & Pashley 1983) in water environment. Specifically, focusing on the predominant viscous force measurement, the force vs. distance behaves in a nonlinear manner. A discontinuity is repeatedly found in the interval range of 0.2-0.3 nm, roughly the diameter of the water molecule. This is caused by the lattice-like structure of the confined water layer covering the sample-substrate (see Figure 5.14). As the cantilever passes through each molecule lattice structures, the interaction force changes discontinuously as observed by previous force analysis results by Antognozzi

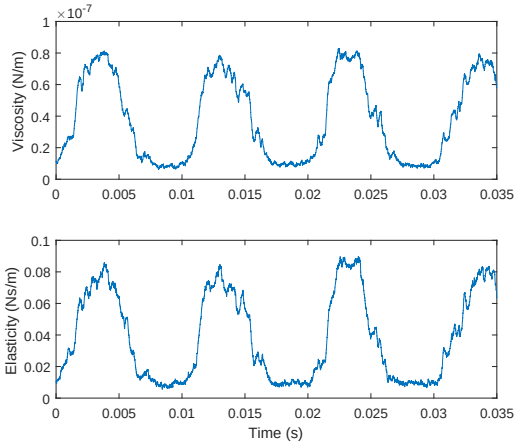

(a) Dynamic viscosity and elasticity estimation

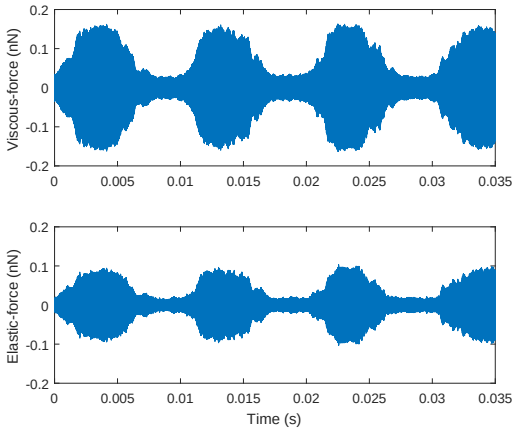

(b) Dynamic viscous and elastic forces estimation

FIGURE 5.13: Dynamic estimation of viscosity, elasticity, viscous force, and elastic force when the cantilever is controlled to continuously move between 1 nm and 6 nm above the sample-holder slide along a sine trajectory at 100 Hz frequency in water.

et al. (2001).

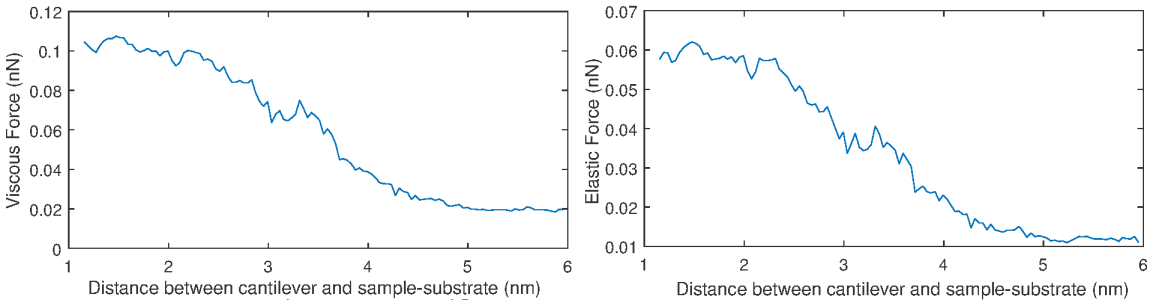

FIGURE 5.14: The viscous/elastic force vs. the distance to the sample-holder where the forces (rms) are computed from the real-time shear-force measurement at a single x-y in-plane position.

5.5 Summary

The section presents the first real-time interaction atomic-force reconstruction approach developed on the TDFM system in the AFM research area.

A practically oriented development procedure is introduced by starting with the cantilever oscillation modelling. After obtaining a practical cantilever model, a sliding mode observer is designed and then implemented in fixed-point arithmetic on FPGA. With the reconstructed shear-force, the viscosity and the elasticity over the specimen surface can be estimated via a proposed parameter estimation method.

Simulation assessments show the success of the developed shear-force reconstruction approach. After integrating all the functions with the TDFM system, the experimental results present the shear-force measurement has a convergence time of less than 0.1 ms in practice. The elasticity and the viscosity can be reconstructed within 0.6 ms. Experiments also show that the shear-force varied with the relative height distance, i.e. the discontinuity pattern of the shear-force vs. the relative distance matches with the size of the water molecules.

The developed novel features are integrated with the TDFM system. In Chapter 6, it can be seen that the developed force reconstruction approach achieves real-time force mapping. Additionally, the developed viscosity and elasticity reconstruction approach achieves the mechanical properties mapping over the specimen surface.

Chapter 6

Multi-mode Scans with the Transverse Dynamic Force Microscope

6.1 Introduction

This chapter presents three topography scanning modes, based on the sensing and control techniques developed and integrated in the TDFM system in previous chapters.

Two developed topography imaging methods, i.e. the constant absolute height scan mode (Section 6.2) and the constant relative height scan mode (Section 6.3), are introduced first. Significantly, the system has shown outstanding capability to resolve nano-structure of delicate samples in liquid environment in contrast to SEM and typical AFM methods. The new TDFM scanning modes, in particular the relative height modes, allow for a large depth of field and full dimensional information of the scanning specimen (see Section 6.3.4), whereas the previous TDFM mode only provides $\sim$2 nm imaging depth of field, i.e. the result only provides partial dimensional information of the specimens (Fletcher et al. 2013).

The novel feature of the TDFM is the realisation of dynamic shear-force/viscosity/elasticity measurement and scan over the top of specimens via a noncontact regime. The real-time interaction force and surface property measurement extends the information obtained from the specimens, i.e. this potentially helps with understanding the transient mechanism/surface-property of materials or bio-specimens.

Supporting publications:

- *"Design, system-identification, and digital control of a multimode Transverse Dynamic Force Microscope"*, Zhang, K., G. Herrmann, M. Antognozzi, et al., Under journal peer-review.
- *"A real-time transverse dynamic force estimation approach in fixed-point arithmetic"*, Zhang, K., G. Herrmann, M. Antognozzi, et al., In preparation.

- *"Real-Time sliding mode observer scheme for shear force estimation in a Transverse Dynamic Force Microscope"*, Tien, TN., S. Khan, T. Hatano, K. Zhang, et al., *Asian Journal of Control*, 2017, vol. 19, pp. 1-12

- *"Enhancing fixed-point control robustness for experimental non-contact scans with the Transverse Dynamic Force Microscope"*, Zhang, K., T. Hatano, G. Herrmann, et al., *American Control Conference (ACC) 2018, IEEE.*

6.2 Constant Absolute Height Scans - Contact Mode Scans

The constant absolute height scan mode retains a constant absolute height, i.e. the distance from the cantilever towards the sample-holder slide. The specimen top, that lays within the shear-force interaction sensing range under the cantilever, is imaged as scanning over the sample-substrate. In principle, this has similarity to the optical feedback mode in previous work (Harniman et al. 2012). In previous work, a PLL is used to obtain the indirect force measurement, e.g. amplitude/phase of the cantilever oscillation, of the interacting shear-force (Antognozzi et al. 2000, 2008, Harniman et al. 2012, Harniman 2013). The previous TDFM set-up consequently has a limited 2 nm morphology depth of field. This section suggests to use the proposed relative height sensing component and the relevant controller from Section 4.2.3 of Chapter 4. The developed novel TDFM set-up significantly improves the imaging depth up to ∼6 nm in liquid environment. This scan mode images the top bulges of the sample, which contact with the relative height sensing range. Therefore, it is named as the "contact mode" of the TDFM.

6.2.1 Scanning Methodology and Principle Verification

In contact mode scans, the absolute height is feedback controlled by the proposed controller and the relative height is simultaneously recorded as the topographic information (Figure 6.1a). After the sample is well-prepared, a scan can be carried out following the operation procedure: a) optimise the optical path to guarantee the sensitivity of absolute height and relative height (see Section 3.2.3 in Chapter 3); b) measure both the absolute height and the relative height sensing curves (see Section 4.2.1 and Section 4.3.1 in Chapter 4); c) initiate the absolute height control to control the distance between the cantilever and the sample-holder to be the demand scanning height (see Section 4.2.3 and Section 4.3.6 in Chapter 4); d) start the scanning programme after configuring the scanning specifications, including the scan speed, the scan resolution, and the scanned area size in the GUI (see Figure 3.14 in Chapter 3).

Therefore, in principle, the top of the specimen can be imaged as shown in Figure 6.1b. The topographic information within the relative height range is computed from the relative height sensing curve. The offset height is the absolute height for scanning and computed from the absolute height sensing curve.

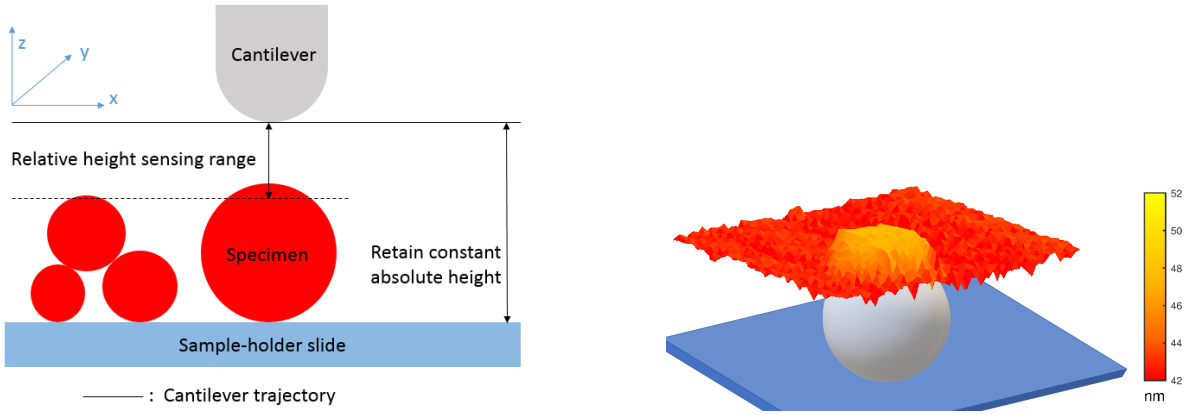

(a) Schematic of the contact mode

(b) Contact mode scanning principle in 3D

FIGURE 6.1: The scanning principle of the contact mode, i.e. the constant absolute height mode, of the TDFM. The schematic (a) shows that the cantilever keeps a constant distance above the sample-holder slide using the designed controller. The specimen top is imaged by the relative height sensing mechanism, as the cantilever enters the limited shear-force interaction range under the cantilever. Figure (b) demonstrates a scanned sphere imaged by the contact mode with limited depth of field in 3D.

The contact mode scan is initially verified in air (without an additional water-based solution) as shown in Figure 6.2. The sample is made of unknown gold particles attached to a grade 1 glass sample-holder slide. The glass slide is treated with acid to retain some $H+$ ions to fixate the gold particle to the glass surface. The sample solution is prepared to have a concentration of 4 μMol gold particles within 46 μl water buffer. The sample-substrate is ready to scan after drying out the water. In order to validate the relative height sensing, a cantilever type B is chosen as the force sensor to be excited at 350 kHz, the first resonant frequency, in air. This historically first successful scan with the contact mode is carried out in an ambient environment which has 53% humidity at a temperature of 21°C and for 1.1 bar pressure.

The scans are applied to an area of 800 nm × 800 nm size and the resolution is 2 nm/pixel with a scanning speed of 800 nm/s. The scan is taken from a position of about 100 nm above the sample-holder and brought down gradually. Nothing is imaged in Figure 6.2a until and including 525 absolute height, i.e. about 50 nm, where the specimen top is still not within the reach of the sensing range. (Here, the relative height measurement is used to indicate the distance directly without converting to the actual cantilever-slide distance in nanometre.) As the absolute height measurement increases, the distance from the cantilever to the sample-holder decreases (see Figures from 6.2a to 6.2l). It can be seen that the top part of a specimen appears at 528 absolute height measure (Figure 6.2b). As the cantilever approaches the glass slide, more topographic information is obtained from the scans. After the cantilever is brought down by more than 3 nm until about 540 absolute height (Figure 6.2j), the cantilever starts to contact with the specimen surface. Then, the cantilever begins to contact the specimen and the relevant topographic information is not correctly reflected in the scan. It can be seen that the topographic image at absolute height 540, 545, and 550 is horizontally extended in the (horizontal) x-axis direction (see Figure 6.2j - Figure 6.2l). This is because the cantilever cross-section is longer in the x direction (horizontal direction in the scanned image) than in the y direction (vertical direction in the scanned image), resulting in more

cantilever-specimen contact along the x-axis.

This scan mode images the specimen topography using the relative height measurement. Hence, there is no relative height measurement if the specimen does not enter the sensing depth, i.e. the relative height sensing range depended on the experimental conditions. The relative height sensing is disabled when the cantilever physically contacts with the specimens. In practice, the cantilever is often significantly larger than the specimen. In case, that the specimen is not firmly attached to the sample-holder, the specimen will be swept away by the oscillating cantilever or it will attach to the cantilever tip when the cantilever and the specimen physically contact each other. If the specimen is strongly attached to the sample-holder, the cantilever stops oscillation while a contact happens. Thus, this scan mode requires careful configuration of the cantilever-specimen distance. The cantilever-specimen separation has to be within a few nanometres allowing to pick up the structure of the specimen at the very top.

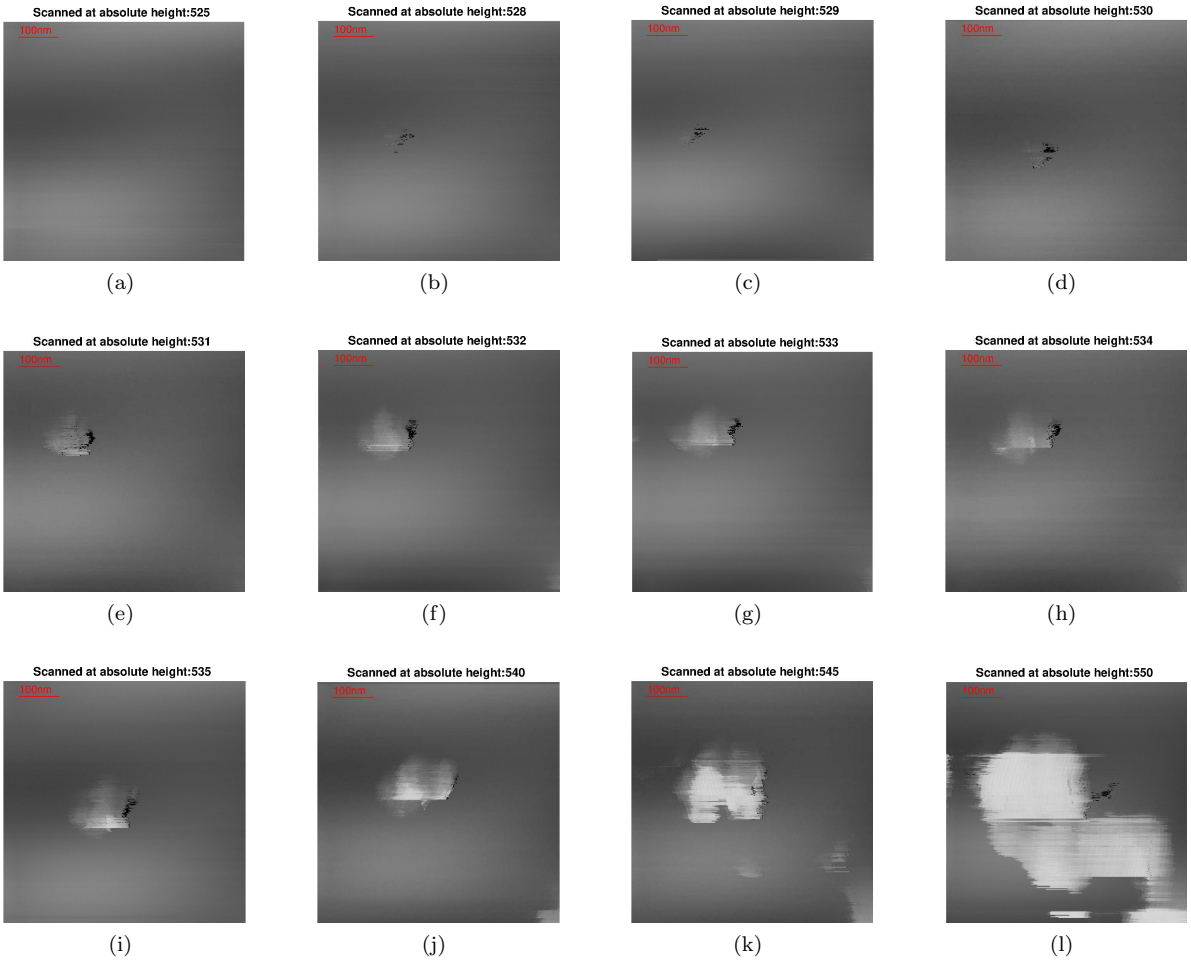

FIGURE 6.2: The contact mode is first tested by scanning unknown gold particles in air. The sample is attached to a grade 1 glass sample-holder slide. The TDFM employs a type B cantilever excited at 350 kHz. The scans are taken in an area of 800 nm × 800 nm size at 2 nm/pixel resolution at a scanning speed of 800 nm/s. With increasing absolute height measure, the cantilever gets closer to the sample-substrate. The specimens are not imaged at the beginning in (a), starts entering the sensing range from (b) until (i), and then contacts with the cantilever in (j)-(l).

Typically, the specimens are randomly distributed over the sample-holder slide. Hence, it is important to locate the positions of the target specimens avoiding physical cantilever-specimen contacts. One scenario is that the morphological information of the specimen is known a priori. In this case, the cantilever can be controlled to be at a known distance above the sample-holder slide avoiding physical contact between the cantilever and the specimen. The scan can be applied in a large scanning area to locate target specimens and then zoom into the area of interest for detailed scans.

The other circumstance is that there is no information about the specimens' size before scanning. The TDFM has to scan a large area at a sufficiently high distance. Then, the scans are applied to the area and the cantilever is carefully brought towards the sample-holder slide until the specimen top penetrates the sensing range, i.e. this confirms the height information and the horizontal location of the specimen. Otherwise, the whole cantilever approach procedure has to be repeated to other areas until the target specimen appears in a scanned area. By applying the latter method and zooming into the target area, the specimen-top can be consequently scanned as shown in Figure 6.2.

6.2.2 Scan Results

To assess the imaging performance, samples with standard shapes are selected: specifically polymer microspheres (R50, Fluoro-Max, Thermo Fisher Scientific Inc.) with a nominal diameter of 50 nm. The specimen solution is prepared in purified water buffer with a 10 mMol/L concentration of nano-sphere solution and 10 mMol/L concentration of $NiCl_2$, which creates salt bridges, bonding the nano-spheres to the glass slide. A 20 μl sample solution is applied to a grade 0 glass slide. Following that, about 5 mins time is needed to allow the nano particles to attach to the slide surface. More water buffer needs to be added ensuring a continuous scan medium. The following work will use this nano-sphere solution as the default sample solution for experimental scans in this chapter.

The sensing component employs a type A cantilever to be excited at 200 kHz in water medium. The cantilever oscillation amplitude is about 2 nm with optimised optical sensitivity, i.e. this allows 1 nm

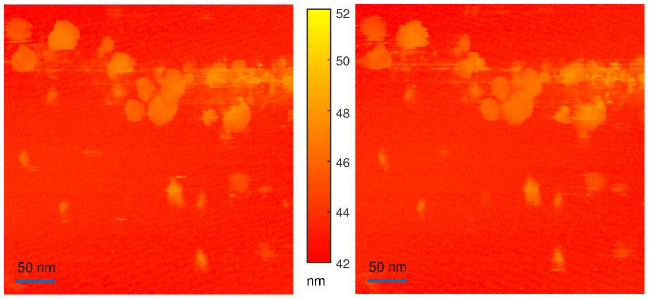

(a) Trace (left) and retrace (right) data of the experienmental scan

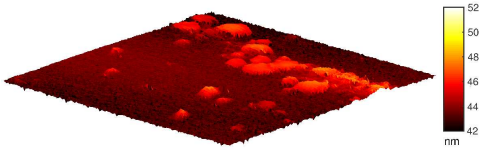

(b) 3D representation of the trace data

FIGURE 6.3: The contact mode scan is assessed by scanning nano-spheres with nominal 50 nm diameter in water medium. A 400 nm × 400 nm area is scanned at a resolution of 2 nm/pixel and at a scanning speed of 1.6 μm/s as shown in (a). The 3D image of the trace data is presented in (b).

imaging resolution in z direction. The cantilever is controlled to scan at 50 nm away from the glass slide. The depth of imaging is approximately 6 nm, as confirmed by the relative height sensing curve (see Section 4.3.1 in Chapter 4).

After the specimens are located, the experimental scan is applied to a 400 nm $\times$ 400 nm areas at a resolution of 2 nm/pixel and at a scanning speed of 1.6 μm/s. The topographic height measurement in nanometre is calibrated by the practical sensing curves (see sensing curve in Section 4.3.1 and the scan results in Figure 6.3a and 3D image in Figure 6.3b). It can be seen that only the very top part of each nano-sphere is imaged within the relative height sensing range ($\sim$6 nm) in the scans. In Figure 6.3a, both the trace (left) and retrace (right) images are generated by either the forth and back motion scans along the x-axis. The similarity between the trace and the retrace images indicates the success of the absolute height control and the contact mode scan regime. In the horizontal plane, the imaged particles have the shapes of circles with diameters less than 33 nm, which fits the dimension of the spherical cross sections at the scanning height. The vertical height of the imaged particles are also approximately 50 nm as expected at vertical resolution of 1 nm in z-direction.

6.3 Constant Relative Height Scans - Noncontact Mode Scans

The constant relative height scan mode retains a constant inter-distance between the cantilever and the sample-substrate. This is the shear-force feedback scan mode in typical SFMs (Betzig et al. 1992, Ruiter et al. 1997, Sikora et al. 2005, Mühlschlegel et al. 2006) or the previous TDFM (Antognozzi et al. 2008, Harniman et al. 2012). The vertical probe/cantilever oscillation is an indirect measurement of the interacting shear-force for feedback control. The measurements taken from the cantilever oscillation are either phase or amplitude. Specifically, the previous TDFM applications (Harniman et al. 2012) had about 2 nm imaging depth of field, i.e. the shear-force feedback scans are only applied to specimens less than 2 nm high, like DNA. In contrast, the proposed relative height sensing component improves the sensing range of the shear-force interaction, and the novel set-up consequently breaks the limitation of the specimens' size. Theoretically, the constant relative height allows imaging specimens of any size within the evanescent field. Practically, the dimension of the specimen is preferred to be smaller than the geometry of the cantilever tip, i.e. the scattered light caused by the specimen is weaker than the cantilever's reflection. As this scan mode always keeps the cantilever away from the specimens, this is a true noncontact scanning mode, named as the "noncontact mode", of the TDFM.

6.3.1 Scanning Methodology and Principle Verification

The noncontact mode controls the relative height maintaining a constant cantilever-oscillation amplitude, i.e. a constant shear-force interaction with the sample-substrate. At the same time, the absolute

height measurement is taken as the topographic data (Figure 6.4a). In principle, a nano-sphere will be 3D imaged as shown in Figure 6.4b.

The scanning procedure is suggested as the same as the contact mode procedure: a) optimise the optical sensitivity; b) measure absolute height and relative height sensing curves; c) initiate the relative height controller; d) start the scans with configured scanning specifications. Regardless the dimension of the specimens, the relative height is suggested to be 2-4 nm away from the sample-substrate. For smaller specimens, the relative height for scanning can be kept at 1-2 nm above the sample-substrate.

Different from the contact mode, the noncontact mode does not mandatorily need to measure the relative height sensing curve in practice, since the curve has been found robust and subject to little change in various applications. Because a constant relative height is applied to the whole sample-substrate for scans, the specimen's dimensional information and the topographic image in nanometre is directly obtained from the measured absolute height data and the absolute height sensing curve. The relative height sensing curve gives an exact measurement of the inter-distance between the cantilever and the sample-substrate in nanometre.

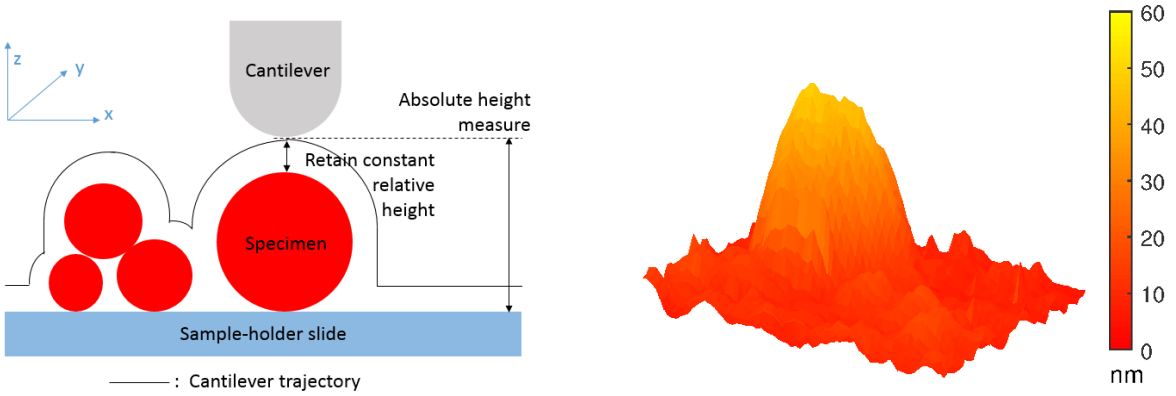

(a) Schematic of the noncontact mode

(b) Noncontact mode scanning principle in 3D

FIGURE 6.4: The scanning principle of the noncontact, constant relative height, mode in the TDFM. The cantilever is controlled to have a constant shear-force interaction level with the sample-substrate, and the absolute height measurement is recorded as the topographic data as shown in (a). A sphere-shaped particle will be imaged as (b) presents in 3D. The top sphere is completely imaged but the lower-half details cannot be obtained.

The proof of concept is carried out by scanning 20 μl default sample solution, i.e. the specimens are nano-spheres with 50 nm nominal diameter. The prepared sample solution is dropped on a grade 1 glass slide as the sample-holder. A type B cantilever is chosen to oscillate at 350 kHz, which is close to a resonance frequency of the cantilever in water. The cantilever excitation is adjusted to oscillate the cantilever with about 3 nm amplitude when outside the specimen interaction range.

The first non-contact scan has been carried out with a relative height lag-controller as shown in Figure 6.5. After locating the target specimens, the scanning speed is configured to be 800 nm/s in a range of 400nm $\times$ 400 nm at 150 $\times$ 150 pixels resolution. The scan is carried out by keeping $\sim$4 nm relative

height above the sample-substrate. The trace and retrace data both image the same nano-spheres with expected dimensional information, i.e. this indicates the success of the noncontact mode scan regime. The imaged dimension of nano-spheres matches with the expected topographic profile. However, this very first noncontact scan has a poor imaging quality. Also, the vertical dimension data calibrated by the absolute height sensing curve only has a field depth of about 20 nm. These are the result of poor control performance of the lag-controller and a poor cantilever quality factor at the excitation frequency.

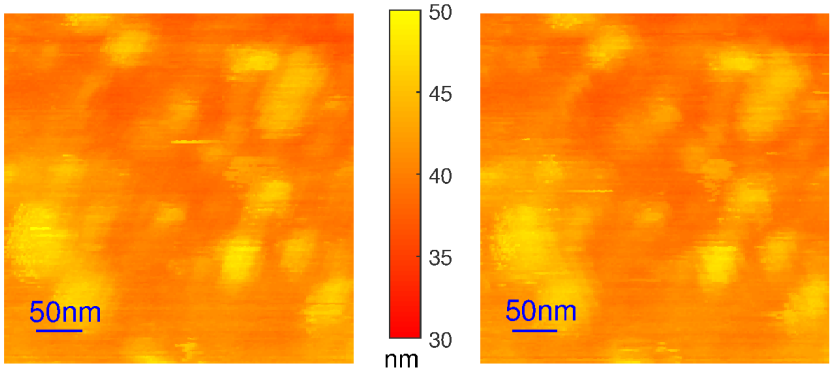

FIGURE 6.5: The first successful non-contact mode scan using the lag-control algorithm in water medium. The trace (left) and retrace (right) data are imaged at 800 nm/s speed in a range of 400nm × 400 nm at 150 × 150 pixels resolution.

6.3.2 Scan Results

The noncontact mode scan employs the developed H_∞ controller in the proposed TDFM system achieving an advanced imaging quality as shown in Figure 6.6a. The sample is 20 μl default nano-sphere solution dropped on a grade 0 glass slide in water medium. A cantilever type A is excited to oscillate with 2 nm amplitude at 200 kHz in the scan tests.

The noncontact mode scan is verified by scanning a 400 nm × 400 nm area at 2 nm/pixel resolution

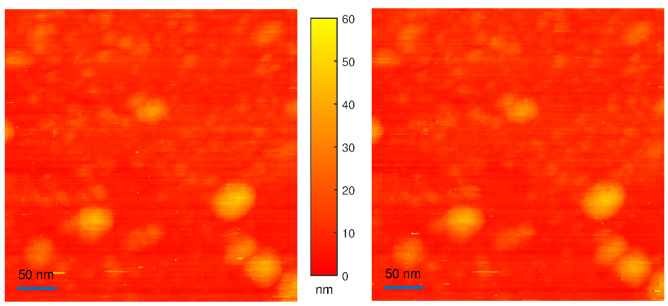

(a) Trace (left) and retrace (right) data of an experienmental scan

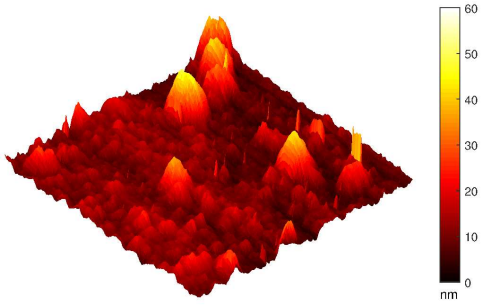

(b) 3D representation of the trace data

FIGURE 6.6: The noncontact mode scan is assessed by scanning nano-spheres with nominal 50 nm diameter in water medium. The TDFM applies the proposed H_∞ controller to a 400 nm × 400 nm area at a resolution of 2 nm/pixel and at a scanning speed of 1.6 μm/s as shown in (a). The 3D image of the trace data is presented in (b).

at a 1.6 μm/s scanning speed. The cantilever in these noncontact scans is kept at a 400 relative height (about 3 nm) over the sample-substrate practically. The topographical data is computed from the absolute height sensing signal. In Figure 6.6a, the similarity between the trace (left) and retrace (right) images shows that the relative height controller performs robustly providing good scan results in a non-contact manner. Good imaging quality is achieved enabling to observer small particles or rough surface of the glass slide at twice the scanning speed in comparison to the first lag-controlled scan in Figure 6.5. The particles are clearly visible with expected dimensional information in the 3D image of the race recording in Figure 6.6b. The specimen spheres have a diameter of about 50 nm along the vertical axis and in the horizontal plane in Figure 6.6. The noncontact mode scans have a robust and repeatable scanning performance in different tests (not shown here). It is evident that the developed noncontact scanning approach successfully provides precise topography measurements.

6.3.3 Test of Image Zooming

In the non-contact mode, it is easily possible to zoom into specimen detail as shown in Figure 6.7. A large scanning area of 800 nm $\times$ 800 nm size is scanned at a resolution of 2 nm at 3.2 μm/s speed in Figure 6.7a. It can be seen that some of the particles are not clearly visible due to the effect of disturbances at a high scanning speed. Hence, after the initial scan, the scanning system allows to zoom in to obtain more detail of the nano-sphere in the up-right of the large scanning area by translation in the x-y plane and adjusting the scanning specifications. The zoomed in figure has a resolution of 1 nm/pixel at the same scanning speed for a $\sim$200 nm$\times$200 nm area. The zoomed-in result shows that there are smaller particles lying beside the target 50 nm diameter nano-sphere. Also, some small particles are observed in the area (lower than the target sphere in Figure 6.7a) where they are invisible in the low-resolution image (in Figure 6.7b).

6.3.4 Resolving Nano-structure of a Delicate Specimen

The noncontact mode of the developed TDFM system shows an advanced performance to scan the morphology of delicate specimens. The advantage of this mode is the capability of imaging fragile specimens at nanometre resolution in liquid environment. In detail, the TDFM is suitable for topography imaging in liquid environment like other AFMs, e.g. the high-speed AFM (Ando et al. 2013) to scan biology specimens. However, the typical AFM will apply a force on the specimens' surface for imaging, i.e. fragile specimens can be damaged by the applied force. In contrast, the TDFM system obtains the topographic data in a noncontact manner without contacting the specimens. Hence, the TDFM system is capable to scan delicate specimens at nanometre resolution in liquid environment, i.e. this suits the study of live biological samples in tissues avoiding any damage.

An important result from previous work was to resolve the nanostructure of a complex self-assembled cage (Fletcher et al. 2013), automatically constructed by protein peptide modules, in a liquid environment.

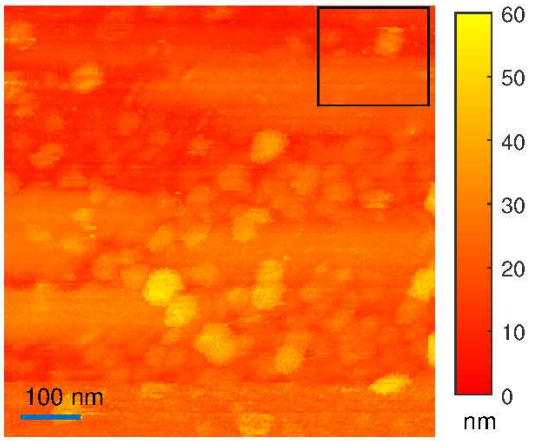

(a) A scanned topographic image of nano-particles at 2 nm/pixel resolution using the non-contact mode.

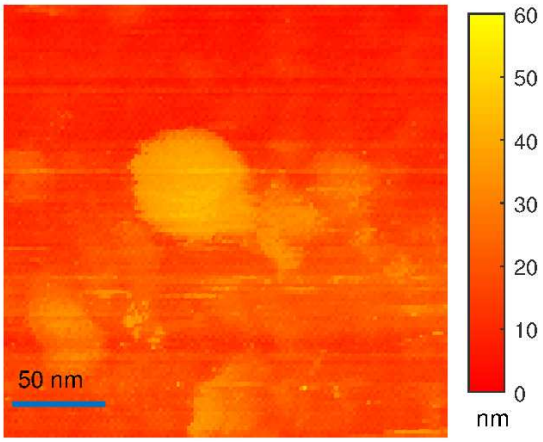

(b) A zoomed-in topographic image of the focused square-area in (a) at 1 nm/pixel resolution using the non-contact mode.

FIGURE 6.7: The zooming function of the TDFM is demonstrated for the noncontact mode scans. An 800 nm × 800 nm area is scanned at 3.2 μm/s speed at 2 nm/pixel resolution. The squared ∼200 nm × 200 nm area is zoomed-in at the same scanning speed at 1 nm/pixel resolution.

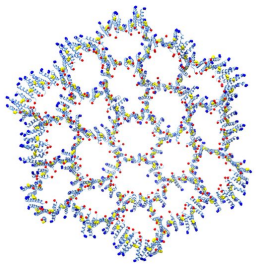

(a) Top view of the hexagons constructed by peptides after 5 ns assembly in atomistic molecular simulation

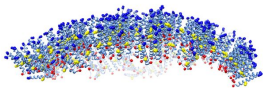

(b) Side view of the hexagons constructed by peptides after 5 ns assembly in atomistic molecular simulation

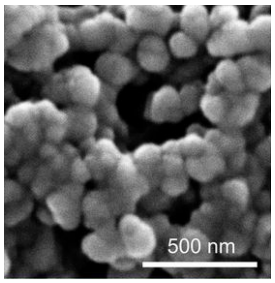

(c) Scanning electron micrographs of the SAGE particles after 1 hour assembly and being coated.

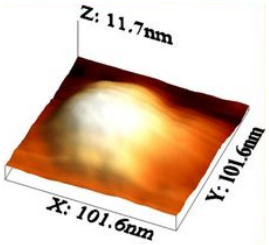

(d) 3D representation of a single SAGE scanned by a tapping mode AFM

FIGURE 6.8: SAGE particles simulated in atomistic molecular simulation and imaged by SEM and tapping-mode AFM (Fletcher et al. 2013).

It is vital to understand the biological compartments (Lodish et al. 2008, Tanaka et al. 2008) for studying the biomimetic assembly, developing new drugs/biological materials, and comprehending the protocells (Uchida et al. 2007, Hammer & Kamat 2012, Agapakis et al. 2012). The research of Fletcher et al. (2013) at the University of Bristol has shown that it is possible to produce self-assembled cage-like particles, named as SAGEs, which is made from a set of short peptides with about 2.3 nm width. One kind of SAGE particles can be constructed by nano-hexagonal patterns as a relevant simulation shows in Figure 6.8a. The SAGE surface is deformed into a curve shape after assembly (see the side view of a simulated SAGE surface in Figure 6.8b). Eventually, the SAGE is shaped as a hollow sphere-cage constructed by hexagonal patterns and is assembled in liquid. For SEM-imaging, it needs to be taken out of the buffer liquid, and to be coated by a complex procedure (After 1 hour of combining the material solutions, resuspended

material is transferred to a carbon-coated stub and sputter-coated with gold/palladium before imaging) (see Figure 6.8c). Although the particles appear as aggregates in particular micrographs in Figure 6.8c, they dispersed in solution and separated when deposited on porous membranes to be coated. Also, a typical AFM cannot image the hollow SAGE particles as shown in Figure 6.8d, because an AFM will easily crush the fragile structure by applying a force at the top of particles.

The previous TDFM set-up (Harniman et al. 2012, Harniman 2013) gives the possibility to image the delicate SAGE particles in liquid. In previous research, the TDFM retains a constant distance from the cantilever to the sample-holder slide and images the topography by recording the cantilever oscillation phase, i.e. Harniman et al.'s (2012) contact mode as shown in Figure 6.9a. The very top part of a SAGE is imaged as shown in Figure 6.9b and Figure 6.9c. The hexagonal structure made up by peptides are observed and confirmed without damage at the first time.

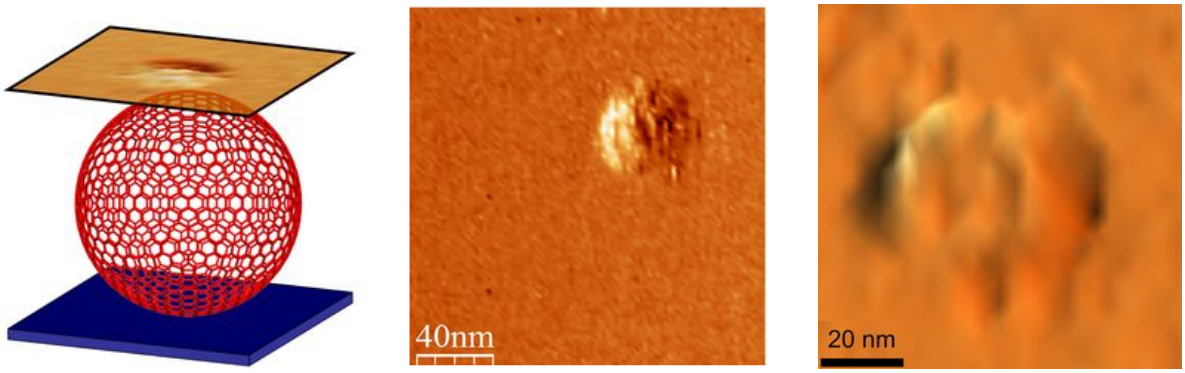

(a) (b) (c)

FIGURE 6.9: The topographic scanning results of SAGE particles in previous research by Fletcher et al. (2013) and Harniman (2013): (a) demonstrates the used scanning regime avoid damaging the particle, i.e. the contact mode is applied in the research; (b) and (c) is the scanned SAGE particle.

The TDFM in previous research successfully proves the nano-structure agreeing with the molecule level simulations at nano resolution. However, the previous result only provides limited information of the overall SAGE particles. Only the very top part of a SAGE is imaged with 2 nm depth of field in previous results, i.e. the shape of the SAGE below the imaged top surface cannot be confirmed. Due to the limited depth of field, only a few hexagonal structures are visible in the scanning result. Only the height (∼82 nm after 1 hour assembly) of the scanned top part can be confirmed by the previous contact mode scan, and there is no dimensional information measurement available in the x-y plane.

The developed TDFM noncontact mode is applied to SAGE scans resulting in full specimen topographic information as shown in Figure 6.10a. For scanning, the sample solution is produced with a SAGE concentration of 0.01 Mol/L, by mixing the material solutions with HEPES (a kind of organic chemical buffering agent of Good et al.'s (1966)) buffer to create pH 7.2 liquid environment. The SAGE solution is expected to be assembled after 1 hour of mixing the material solutions and will collapse after about 48 hours of existence in theory. The SAGE sample is dropped on a grade 0 glass slide after 24 hours

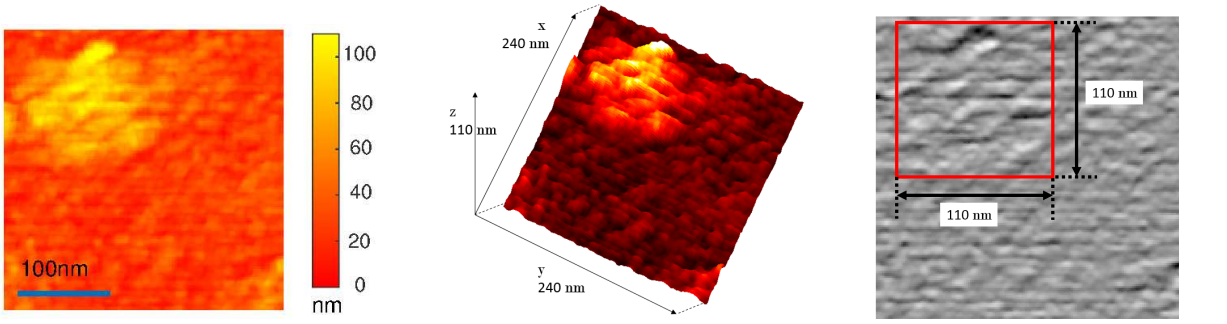

(a) A SAGE particle scan in the non-contact mode

(b) 3D morphology of a SAGE particle

(c) Gray image of a SAGE particle scan

FIGURE 6.10: A SAGE particle is scanned in the noncontact mode after 1 hour assembly: (a) shows the trace data of a SAGE using the proposed noncontact scanning mode; (b) is the 3D representation of the SAGE particle; (c) represents the topographic change of the retrace measurement in gray colour map, i.e. the topography contrast is enhanced.

of production. The TDFM system uses a type A cantilever excited at 200 kHz with an amplitude of 2 nm in the liquid environment. Applying the noncontact mode, the relative height for scans is configured to be 4 nm above the sample-substrate to scan a 250 nm $\times$ 250 nm area. The scan speed is 1.5 μm/s at a scanning resolution of 2 nm/pixel.

The noncontact scan results in Figure 6.10a shows that the top-half SAGE particle shapes similar to a half sphere with a diameter of about 110 nm. The success of scanning the 110 nm high SAGE particle additionally confirms that the non-contact mode can image delicate specimens without damage. As the SAGE theoretically is a sphere in 3D, as shown in Figure 6.10b, only the nano hex-structure at the top is clearly imaged similar to the previous contact mode scanning result. The 3D-image is converted into a gray image in Figure 6.10c. It is can be seen that more micro-structures are observed over the whole scanned SAGE particle. The hex-structures deform at the particle-edge from the top view, i.e. this proves that the shape of the SAGE particle is sphere-like (also see the view in 3D in Figure 6.10b). The edge length of the hexagonal structure is about 9$\pm$2 nm agreeing with the previous research by Fletcher et al. (2013). The micro hexagonal structure is observed in Figure 6.10b and 6.10c by taking the amplitude measurement of the cantilever oscillation. The result agrees that the SAGE particle has a sphere shape with about 110 nm diameter. Note that phase information of the cantilever oscillation is used in the previous result (Fletcher et al. 2013), so the edges are more obvious in Figure 6.9c than in the noncontact image Figure 6.10a measuring the amplitude.

The successful noncontact mode scan of SAGE particles demonstrates that the developed TDFM system has the following improved abilities:

- The TDFM can scan delicate specimens that the SEM and a typical AFM cannot image.
- The TDFM is able to resolve the nano-structure over the whole specimen top surface in a true non-contact manner.

- Almost the full dimensional knowledge is available at one single scan, breaking the previous limited imaging capability.
- The TDFM is able to scan large specimens at a standard commercial AFM (Veeco Instruments Inc. 2004) scanning speed, whereas the previous TDFM set-up (Harniman et al. 2012) is constrained by an imaging depth of about 2 nm.

6.4 Real-time Force Scan and Analysis

The TFDM allows a novel real-time shear-force-scan mode, which permits the online identification of viscous and elastic material constants scan across the specimens' top (see the developed method in Chapter 5). In the force-scan mode, the direct measurement of the interaction shear-force is provided in real-time at the first time, whilst other methods compute the interaction force or the elasticity/viscosity of the scanning surface offline (Payam et al. 2015, Labernadie et al. 2014, Ding et al. 2015, Rigato et al. 2015). The TDFM also allows online measuring the viscosity and elasticity property of the confined liquid layer covering the specimen surface. As a result, this feature gives an insight to understand the mechanical properties of the confined liquid layer, and physical mechanics/properties over specimen surfaces.

6.4.1 Real-time Force Scan

In principle, the force-scan mode enforces a constant distance from the cantilever away from the sample-holder slide. The real-time interaction shear-force is measured by the proposed shear-force estimator as the cantilever travels over the whole sample-substrate. The top bulges of specimens appear in the relative height sensing range and result in a lower relative height measurement caused by an increased shear-force. Hence, the shear-force scan mode can be verified by comparison with a contact mode scanning result in the same area.

The scans in the contact and force-scan modes are carried out under the same experimental conditions. A 20 μl default nano-sphere sample solution is prepared and dropped on a grade 0 glass slide. A type A cantilever is excited to oscillate with 2 nm amplitude at 200 kHz, the resonance frequency of the cantilever, in a water scan medium. An 800 nm $\times$ 800 nm area is scanned in the contact mode and then the force-scan mode, each at 50 nm above the glass slide at a resolution of 2 nm/pixel at a scanning speed of 1.6 μm/s. Hence, each pixel is measured in a period of 1.25 ms guaranteeing enough time for precise force/viscosity/elasticity measurement.

The contact mode scan presents the same trace and retrace images in Figure 6.11. The nano-spheres within the framed area is then targeted to be scanned in the real-time force scan mode. The resulting root mean square (rms) value of the force mesurement is real-time scanned for this area as shown in Figure 6.12a. The interaction shear-force image in Figure 6.12a exactly matches with the contact mode

scanning result in Figure 6.11. The interaction shear-force is stronger as the specimens' top-parts enters more into the relative height sensing range of the specimens. This interaction force strength image gives the understanding of dynamic interaction over a scanned area, i.e. this helps to analyse the dynamic mechanisms of biological specimen surfaces in real-time. Also, the detailed real-time shear force measurement as a function of time can be observed during dynamic scans. In detail, the shear-force measurement of a scanned raster-line can be monitored during a scan in real-time, e.g. the force measurement of the scanned (black) line in Figure 6.12a is presented in Figure 6.12b. This force reconstruction feature acts as a real-time shear-force sensor giving the time transient of the shear-force information.

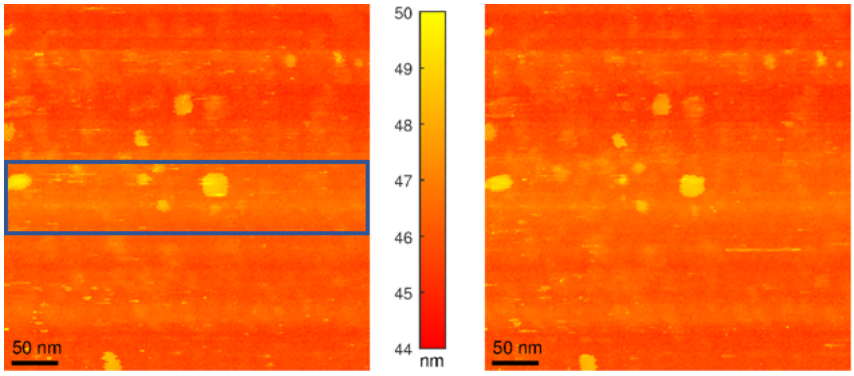

FIGURE 6.11: To assess the force-scan mode, a contact mode scan is carried out in an 800 nm × 800 nm area at 1.6 mum/s speed and 2 nm/pixel resolution in water. The specimens are ∼50 nm diameter nano-spheres. The squared area is scanned by the force-scan mode in comparison.

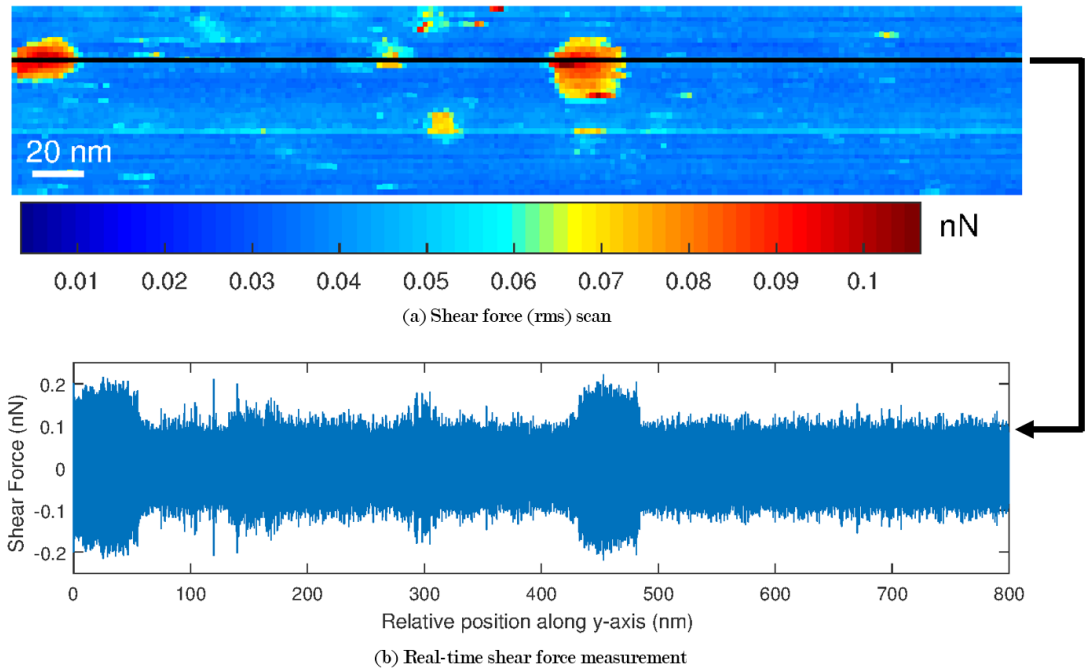

FIGURE 6.12: The force-scan result of scanning ∼50 nm diameter nano-spheres in real-time: (a) is the rms of the interaction shear-force over the target area; (b) presents the detailed shear-force measurement of a scanned raster (black) line during the scan.

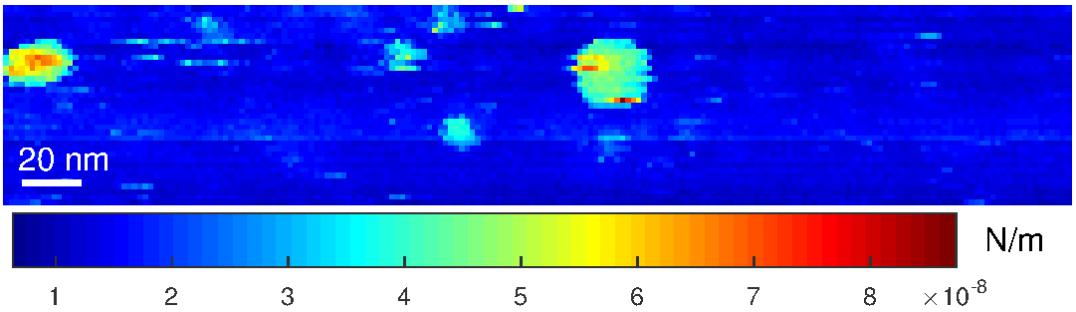

(a) Dynamic viscocity measurement over the scanned area

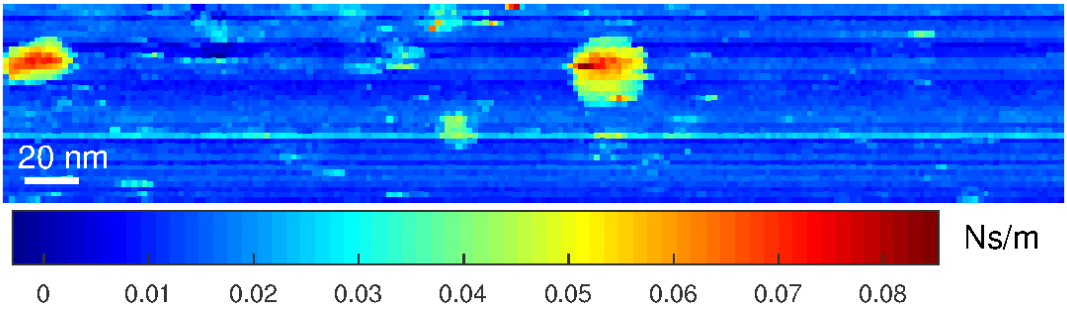

(b) Dynamic elasticity measurement over the scanned area

FIGURE 6.13: The viscosity and elasticity measurement over a scanned area. The viscosity and elasticity scanning results are computed in a process on the host-PC, online, at a slow speed.

The real-time force measurement is streamed to the host-PC to be processed for the elastic/viscous constant estimation (as discussed in Section 5.3.2 of Chapter 5). Therefore, the system additionally allows to measure the elasticity/viscosity of the scanned area. For example, the shear-force scan in Figure 6.12a is processed to analyse the elasticity in Figure 6.13a and the viscosity in Figure 6.13b over the nano-sphere top surface. The elasticity and the viscosity scanning results show high similarity over the whole scanned area with some obvious difference. Both the elasticity and viscosity increases with the increasing shear-force interaction agreeing with the fixed single position measurement in Figure 5.13a in Chapter 5. It can be seen that the elasticity varies with the topographic height in a gentle manner at the sphere top in Figure 6.13a. In contrast, the viscosity changes significantly over the nano-sphere surface, presenting a large high viscosity area at the top of the target sphere in Figure 6.13b.

The scanning results demonstrate that the force scan mode allows to online present four kinds of information: a) the shear-force interaction strength over a scan area in real-time; b) the real-time transient shear-force measurement over a period of time during a dynamic scan; c) online elasticity constant scan of the confined hybrid layer over a specimen top; d) the viscosity constant over a specimen top can be scanned online.

6.5 Discussion of Scanning Modes

Three developed scan modes of the TDFM system are presented and assessed in this chapter:

- **contact mode:** the cantilever is kept at a constant distance above the sample-holder slide to indirectly measure the shear-force interaction caused by the specimens' top in the interaction range.
- **noncontact mode:** the cantilever is controlled to retain a constant distance above the sample-substrate recording the distance from the cantilever to the sample-holder slide.
- **force-scan mode:** the cantilever scans at a constant height from the sample-holder providing real-time shear-force measurement from the specimen top in the shear-force interaction range; this mode presents the shear-force strength measurement of the scanned area in real-time, and the viscosity/elasticity measurement of the scanned area.

Particularly, the contact and noncontact modes are developed to obtain sample morphology in the TDFM system. The TDFM, in both scanning modes, can resolve nano-structure of delicate fragile specimens and avoid damage to specimens. In practice, both scan approaches achieve a resolution of 1 nm along the z-axis with the designed controllers. The TDFM system allows to image the specimens at 1 nm resolution with a commercial horizontal positioning stage.

In principle, both the imaging modes use the relative height measurement, which is an indirect measurement of the interaction force, for imaging or feedback control. The novel TDFM system employs the proposed relative height sensing mechanism. This results in a significant functional improvement in comparison to the previous set-up (Harniman et al. 2012). In detail, the contact mode improves the depth of field from 2 nm to 6 nm. The noncontact mode is able to scan large specimens up to about 100 nm high, which is limited to $\sim$2 nm high specimens in the previous set-up (Harniman 2013).

The contact and noncontact modes have different advantages due to their working principles. The contact mode requires a priori-knowledge about the height of the specimen so as to approach only the very top of the specimen and to carefully scan the cusps. A meticulous downward motion and repeated scans can then capture more detail with the contact-scan. However, physical contact between the cantilever and the specimen has to be avoided, i.e. the contact mode has a maximum imaging depth of 6 nm. The great advantage of the contact mode is that the cantilever is controlled to keep a constant distance from the sample-holder slide, which often has no rapid change over the surface. Hence, the contact mode scan can be driven at a relatively high speed. The imaging power is mainly limited by the relative height sensing bandwidth and the horizontal positioning stage performance.

The noncontact mode provides the topographic details of the sample-substrate from one single scan. In principle, the cantilever is always controlled away from the sample, while there is a danger of cantilever-specimen contact in the contact mode. Full dimensional information of an unknown particle is directly

obtained by the noncontact mode, whereas the contact mode needs a trial-and-error procedure to verify the top height of a particle. For instance, the contact and noncontact scan modes are applied to the same area for comparison. The trace images in the two scanning modes are shown in Figure 6.14. The scanned area is initially imaged in the noncontact mode providing the detailed topography of the scanned region. In contrast, the contact mode scan images only the top of the largest particle in the same frame. Hence, the non-contact mode suits the scan of dynamically changing specimens or complex sample solutions with dynamic changes, when the topographic information is not easily obtained a priori.

The force scan mode gives the direct measurement of the interaction force in real-time, whereas the contact mode only measures the interaction indirectly similar to typical AFMs. This is the first implementation of a real-time force measuring mechanism allowing full specimen scans. The four result-representations significantly enrich the capability of the TDFM in different respects. The force strength distribution directly measures the interaction force strength over the scanned surface, unlike in the previous research (e.g. in (Antognozzi et al. 2001)) where an offline data processing procedure is needed. The interaction shear-force sensing function enables the TDFM to be a real-time force sensor. In principle, the molecular mechanism of a specimen can be sensed by the developed TDFM in real-time, while the previous research (Scholz et al. 2011, Tang et al. 2013) has to process the recorded data after the measurement. The elasticity/viscosity measurement helps to comprehend the confined hybrid layer, constructed by the liquid and the specimen surface. Subsequently, it allows to understand the mechanical properties over the sample surface online. However, in previous AFM systems, the elasticity over a cell surface has to be computed from AFM scanning results using a complex computational method to study cell mechanics and their variations (Rigato et al. 2015).

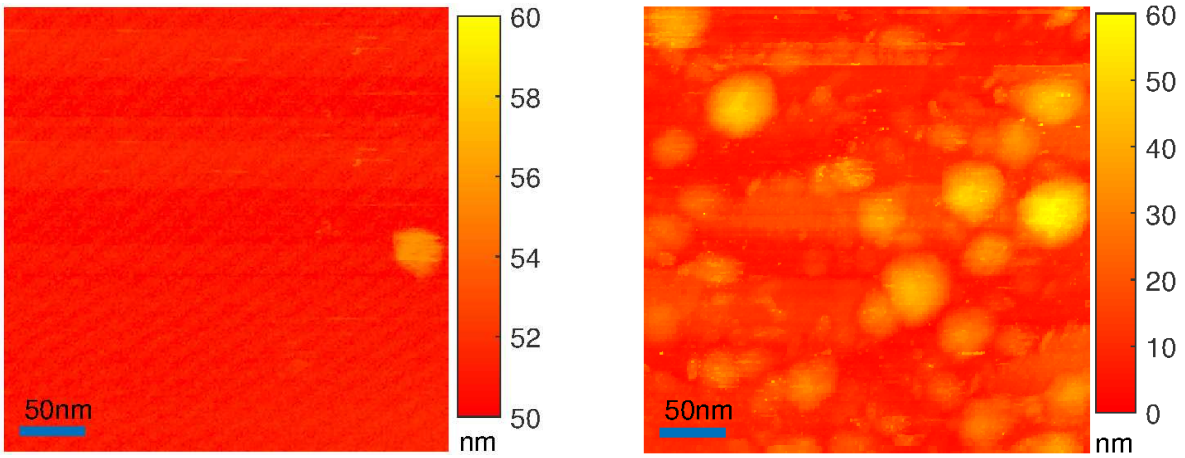

(a) Contact mode scan result

(b) Noncontact mode scan result

FIGURE 6.14: A comparison of the contact and noncontact mode scanning for the same area in the TDFM. The specimens are nano-spheres with 50 nm nominal diameter. The scans are carried out in water to scan a 400 nm × 400 nm size area at 1.6 μm/s speed and 2 nm/pixel resolution. The trace data of the contact mode scan (a) and the trace data of the noncontact mode scan (b) are presented for the same frame area.

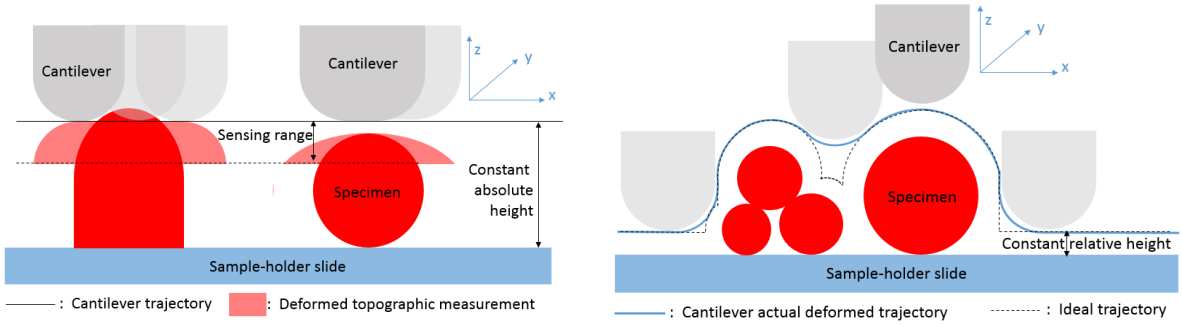

(a) Contact or force-scan mode

(b) Noncontact mode

FIGURE 6.15: The schematics present that TDFM measurement precision is affected by the cantilever tip geometry in practice. The cantilever tip with large radius, i.e. small curvature, results in a horizontal deformation of the measurement in the contact, noncontact, and force-scan modes.

Remark 9 The TDFM system always needs to consider the effects of the cantilever tip geometry. The cantilever tip has often sphere-like shape due to the manufacture method. The imaging resolution, or the sensitivity to atomic force interaction, is strongly related to the geometry of the tip. As the cross section of cantilevers are of rectangular shape wider in x than in y direction (see schematic in Figure 3.2b in Chapter 3 and Figure 6.15 here), the scan image may be deformed due to these characteristics. Specifically, the cantilever tip is curve-shaped with a diameter of about 200 nm, i.e. the thickness of the cantilever. Each cantilever tip has a different curvature due to the difference of manufacture. A very sharp tip with large curvature results in a small interaction area with the specimen top-surfaces, resulting in a high atomic-force interaction resolution. In contact or force scan modes, the tip with small curvature interacts with the specimen more along the x direction. This makes the scanned image horizontally extend (deform) in the x direction (Figure 6.15a). The same phenomenon happens when the cantilever physically contacts with a rigid specimen surface (see the left part of Figure 6.15a). In noncontact mode, the cantilever with larger tip results in a loss of specimen detail, i.e. a lower imaging resolution as shown in Figure 6.15b. Hence, a high quality scanned image with great details needs a sharp tip geometry, similar to typical AFMs (Giessibl 2003). ○

6.6 Summary

The development of three novel TDFM scanning methods are realised and experimentally tested in this chapter. Specifically, two morphology scanning methods significantly improve the depth of imaging in comparison with previous TDFM research. While guaranteeing an improved depth of imaging, the developed TDFM scanning system retains a high imaging resolution allowing to resolve nano-structure of delicate specimens in liquid environment. Moreover, the real-time shear-force reconstruction ability of the new TDFM system presents the capability to measure the transient interaction shear-force between the cantilever and the specimens. This also allows to measure the shear-force distribution and analyse

the mechanical properties (i.e. the elasticity and viscosity) over sample surfaces. This novel feature is an important basis for the TDFM to potentially create impact and to contribute to discoveries in the field of physics, biology, and medical research.

Chapter 7

Conclusions and Future Work

7.1 Conclusions and Discussions

The research work targets the I&C development of a high-precision system, TDFM system, that allows three shear-force scanning modes at nano-metre resolution. The developed new TDFM system is designed and facilitated to integrate with a digital control solution for real-time scans. Practical applications of the system demonstrate that the research objectives have been achieved by the research outcomes. Some physical phenomenons are observed within the development and experiments.

This section summarises the achievements and comments from four different horizons: the improvement of the TDFM system, the advanced techniques applied to the TDFM system, the investigations on the shear-force sensing mechanism, and the discoveries from the experimental results.

Improvements of the TDFM system

The developed TDFM system has significantly improved functionalities in each operation modes.

The contact mode has 6 nm depth of field that is tripled in comparison with the previous set-up. The noncontact mode images specimen topography as long as the evanescent field based sensing mechanism works. The experiments have shown that the noncontact mode can scan specimens up to 110 nm high. In contrast, the previous set-up is limited to imaging the specimens less than about 3 nm high in a so-called "force"-feedback mode (similar to the non-contact mode in this work) (Harniman 2013). The two morphology modes achieves 1 nm resolution without contact with specimens.

In addition to the two scanning modes, a completely novel scan mode, the force-scan mode, is facilitated in the TDFM. This force-scan mode allows to online map the force strength, elasticity, and viscosity over the scanned specimen's surface. The interaction force between the cantilever and the sample is reconstructed at fixed-positions or during dynamic scans in real-time. The TDFM reconstructed the interaction shear-force for a cantilever oscillating at 200 kHz frequency achieving $\sim$0.01 nN precision in about 0.3 ms; as well as the viscosity and elasticity parameters with a convergence time of 0.6 ms.

Advances in the system

There are several detailed technical improvements on the TDFM system from an engineering point of view.

One critical advance is the development of a simplified shear-force interaction, i.e. the relative height, sensing mechanism. The simplified electronic component permits triple sensing range of which the previous set-up allows. An additional benefit is simplifying the operation because of the reduction of the utilisation of a lock-in amplifier or a PLL device.

The other critical improvement is that the TDFM allows to give a direct measurement of the interaction shear-force signal at high precision. This is the first realisation of the real-time interaction force reconstruction, a fundamental function of AFM applications, for full frame scans. The function of online force and mechanical-properties mapping of specimens forecasts further discovery and impact in physics, chemistry, and biology fields.

The new TDFM system is developed as a well integrated AFM system, whereas the previous set-up only permits morphology functions. The novel TDFM system consists of system identification; online control performance assessment in x, y and z directions; real-time interaction shear-force reconstruction; and the three scanning modes.

The proposed control programme allows to apply advanced control algorithms to the vertical position control in z-direction. Specifically, the applied robust controllers are designed to be robust against noise, system drifts, and some variation of experimental conditions (like changing the same type cantilevers, sample solutions in the same buffer, sample-holders). In addition to enhanced control performance, the new system has no need for the operator to ad-hoc adjust the controllers during scans.

The novel TDFM system employs a robust control technique, specifically H_∞ control, achieving a robust and reliable control performance. Experimental tests demonstrated that the developed H_∞ control had an advanced control performance over the traditional PID control or lag-control scheme. Especially, for the relative height positioning system, the proposed H_∞-controller shows consistent performance tackling the nonlinear dynamics, which are difficult for traditional control algorithms to deal with. In addition, the robustness of the controller improves the ease of TDFM operation. It is found that there is little need to adjust the control parameters after slightly changing the experimental conditions.

Investigations on the TDFM

Essential investigations, focusing on the shear-force interaction sensing mechanism and appropriate configurations of scans, are carried out to enable the three scanning modes in practice.

The shear-force interaction sensing mechanism, the most critical technique to realise the morphology modes, has been investigated in the whole research. In order to study the sensing curve, the cantilever is controlled to move up and down vertically in the z-axis direction while remaining at different horizontally fixed positions. In case the cantilever oscillates at its resonance, the oscillation amplitude drops to zero as soon as the cantilever touches the sample-holder surface. This has been observed by Antognozzi (2000) and confirmed in this work.

When the cantilever moves downward to or upward from the sample-holder surface, the shear-force interaction are different in two directions at the same vertical height. This phenomenon was also observed by measuring the relative height measurement; and later reconstructing the viscous and elastic forces in Figure 5.13b, agreeing with previous related investigation (Antognozzi 2000). This is considered to be the result of the varying interaction when the cantilever enters or escapes from the confined water layer. Also, the reconstructed shear-force at a single horizontal position is slightly different when the cantilever moves in either direction (either down/up above the sample-holder slide) within the interaction range. This was not necessarily due to nonlinearity, e.g. hysteretic effects in the vertical direction. There are other possible factors, such as Brownian motion etc., which might have also an effect.

The possibility to realise multiple scanning modes was also investigated in ambient conditions. It was noted that the shear-force interaction range in ambient condition varies significantly with the humidity of the environment as observed by Antognozzi (2000). Hence, stable scanning performance in air is difficult to achieve in any TDFM scanning mode. In water medium, the imaging quality is affected by the tip geometry as discussed in section 6.5.

Successful scans still require significant experience with TDFM system operation. In the non-contact mode, a too small (relative height) scanning offset results in deformation of the measured topography, whereas a larger relative scanning height reduces the imaging quality. For contact mode scans, an insufficient absolute height easily causes cantilever-specimen collisions, i.e. the scan fails. However, the contact mode cannot image anything with a too high relative height (see Section 6.5).

Note that the cantilever excitation is always critical for the shear-force sensing mechanism. The excitation frequency has to be one of the cantilever's resonances in the scanning medium. The excitation amplitude determines the maximum amplitude of the cantilever tip oscillation, and subsequently the precision of the shear-force measurement accuracy. A large oscillation amplitude increases the output signal range, i.e. the accuracy and signal-to-noise ratio improve. However, this results in a poor lateral sensing precision due to an enlarged shear-force interaction area in the excitation direction (Antognozzi 2000). This trade-off has to be carefully considered to guarantee a sufficient topographic imaging quality.

Observations during the research

There are some interesting observations agreeing with some related research (Israelachvili & Pashley 1983, Antognozzi 2000, Antognozzi et al. 2001, Harniman 2013).

In a water environment, the relative height measurement range (i.e. the shear-force interaction range) of ∼6 nm, in principle, is caused by the confined water layer. The measured 6 nm separation distance matches with the research by Israelachvili & Pashley (1983). The forces caused by the confined water layer increase when the separation between the cantilever and specimens decreases within the 6 nm range. Similarly, a shear-force interaction range of about 8 nm is observed in the investigation on a TDFM by Antognozzi (2000).

The lattice structure of the water molecules results in the discontinuity of the interaction forces between the cantilever and the confined water layer in the TDFM. In this research, it was reconfirmed that the discontinuous change of the interaction forces, i.e. the reconstructed viscous and elastic forces (in Figure 5.13b). The forces vary with the cantilever-sample separation of about 0.2-0.3 nm in a nonlinear manner. Similar observation of the water molecule layers has been published (Antognozzi 2000, Antognozzi et al. 2001). These results in TDFM demonstrate that the lattice water molecule layers have a thickness of about 0.25 nm, as found by Israelachvili & Pashley (1983), agreeing with the size of water molecules.

At a fixed horizontal position, the elastic force varies with the cantilever-sample separation more rapidly than the viscous force changes as shown in Figure 5.13b. This phenomenon is more clearly observed while comparing the reconstructed elasticity and viscosity over the same nano-sphere specimens in Figure 6.13. This confirms the work by Antognozzi et al. (2001) demonstrating a steeper change of the elasticity than the viscosity when penetrating the confined water layer above the sample-holder slide.

Additionally, in an ambient environment, this work confirms that the humidity has a strong influence on the shear-force interaction, as a result of a varying water layer with humidity change. Experimental scans are carried out under 20-60% humidity at 19-21 °C in the same laboratory. Insufficient humidity, i.e. about 20-30% humidity, results in a too thin water layers to enable scans. Also, it takes some time for the confined water layer to grow for a freshly cleaned sample-holder (dried by nitrogen gas). This exactly matches with the quantity investigations by Antognozzi (2000).

7.2 Recommendations for Future Work

It is recommended to improve the TDFM at application and system levels.

The relative height sensing mechanism is developed from the concept of cantilever amplitude measurement. Taking the previous cantilever oscillation phase measurement.

The TDFM system relies on the evanescent field based sensing mechanism to achieve a high sensitivity to the shear force. This requires the use of transparent sample-holder slides and a complicated optical path design. Additionally, the size of the specimens has to be small enough to avoid significant influence on the evanescent field. One future work is suggested developing a novel cantilever design, which integrates a vertical cantilever probe with electro-based sensing mechanism permitting similar high shear-force sensitivity. As a result, the dependence on the complex optical path is avoided. Hence, the TDFM system hopefully can be used for the morphology analysis of relative large specimens.

At an application level, the cantilever vertical positioning system control is to be improved for a sub-nanometre imaging resolution. Importantly, the mechanical design of the vertical positioning system can be optimised in the cantilever excitation direction and the vertical direction for a high mechanical resonance, i.e. subsequently high control bandwidth. Additionally, it will be interesting to assess the control performance of other control algorithms, such as introducing feedforward compensation, gain-scheduling methods, or adaptive controllers.

The shear-force reconstruction algorithm is another potential research topic. In this research, the sliding mode observer introduces a nonlinear injection signal to reconstruct the shear-force signal. The nonlinear injection needs to be computed at a high sampling frequency for a good force approximation performance, i.e. this needs high performance digital hardware for practical realisation. Therefore, it is valuable to develop other force reconstruction algorithms with lower sampling frequency requirements to reduce the dependence on implementation hardware.

The TDFM can be developed as a high speed microscope to observe the transient status of the samples, for example, to observe the Brownian motion or chemical reactions. As introduced in the literature review, the design of a high-speed stage has gained great research interest in the AFM field. Specifically for the TDFM, an optimised dual-direction positioning stage (De Silva et al. 2017) is developed for further high-speed scanning applications. Also, the imaging speed can be improved by scanning along time-efficient trajectories, like following Lissajous patterns or a non-raster localised trajectory, instead of the typical raster trajectory.

Automation and design for an automated TDFM (or an AFM) system is the most recommended future work in the AFM field. One reason is that the operator has to learn and know the way to scan the specimens. The other reason is that it is difficult to verify the correctness of the scanned topography without sufficient understanding of the sample. The success of a scan cannot be ensured unless a known phenomenon or expected pattern is observed, when an AFM is applied to a complicated sample. Hence,

it is hard to use AFMs for quantity research or to discover unknown knowledge at nano-precision. Also, AFMs have to be well prepared by several adjustment procedures (e.g. cantilever localisation, optical system adjust, cantilever calibration, etc.). Successful scans strongly need the operator to have sufficient experience of both the specimens and the AFM itself, i.e. the AFM applications are restricted by experience of the operator. It is necessary for engineers to automate AFM systems in two aspects. The first step is to automate the preparation procedure to reduce the reliance on the operator's experience. Then, an automated scanning function can help with the imaging of complex samples for scientific exploration. A fully automated TDFM or AFM system is potentially useful in clinical diagnostics. This has been a subject of many discussions between the team of Herrmann's and affiliated colleagues.

Bibliography

Abramovitch, D. Y., Hoen, S. & Workman, R. (2009), 'Semi-automatic tuning of pid gains for atomic force microscopes', *Asian Journal of Control* **11**(2), 188–195.

Agapakis, C. M., Boyle, P. M. & Silver, P. A. (2012), 'Natural strategies for the spatial optimization of metabolism in synthetic biology', *Nature Chemical Biology* **8**(6), 527.

Agnew, C., Borodina, E., Zaccai, N. R., Conners, R., Burton, N. M., Vicary, J. A., Cole, D. K., Antognozzi, M., Virji, M. & Brady, R. L. (2011), 'Correlation of in situ mechanosensitive responses of the moraxella catarrhalis adhesin uspa1 with fibronectin and receptor CEACAM1 binding', *Proceedings of the National Academy of Sciences* **108**(37), 15174–15178.

Albrecht, T., Akamine, S., Carver, T. & Quate, C. (1990), 'Microfabrication of cantilever styli for the atomic force microscope', *Journal of Vacuum Science & Technology A: Vacuum, Surfaces, and Films* **8**(4), 3386–3396.

Albrecht, T., Grütter, P., Horne, D. & Rugar, D. (1991), 'Frequency modulation detection using high-q cantilevers for enhanced force microscope sensitivity', *Journal of Applied Physics* **69**(2), 668–673.

Amrute-Nayak, M., Antognozzi, M., Scholz, T., Kojima, H. & Brenner, B. (2008), 'Inorganic phosphate binds to the empty nucleotide binding pocket of conventional myosin ii', *Journal of Biological Chemistry* **283**(7), 3773–3781.

Andersson, S. B. (2007), 'Curve tracking for rapid imaging in afm', *IEEE Transactions on Nanobioscience* **6**(4), 354–361.

Ando, T. (2012), 'High-speed atomic force microscopy coming of age', *Nanotechnology* **23**(6), 062001.

Ando, T., Kodera, N., Maruyama, D., Takai, E., Saito, K. & Toda, A. (2002), 'A high-speed atomic force microscope for studying biological macromolecules in action', *Japanese Journal of Applied Physics* **41**(7S), 4851.

Ando, T., Kodera, N., Takai, E., Maruyama, D., Saito, K. & Toda, A. (2001), 'A high-speed atomic force microscope for studying biological macromolecules', *Proceedings of the National Academy of Sciences* **98**(22), 12468–12472.

Ando, T., Uchihashi, T. & Kodera, N. (2013), 'High-speed afm and applications to biomolecular systems', *Annual Review of Biophysics* **42**, 393–414.

Antognozzi, M. (2000), Investigation of the shear force contrast mechanism in transverse dynamic force microscopy., PhD thesis, University of Bristol.

Antognozzi, M. (2017), Micro-fabricated mechanical sensors for lateral molecular-force microscopy, *in* 'BristolBridge Annual Conference and Impact & Industry Day: Building Partnerships to Tackle the Global Challenge of AMR'. Attended on 2017 MAY 10.

Antognozzi, M., Bermingham, C., Harniman, R., Simpson, S., Senior, J., Hayward, R., Hoerber, H., Dennis, M., Bekshaev, A., Bliokh, K. et al. (2016), 'Direct measurements of the extraordinary optical momentum and transverse spin-dependent force using a nano-cantilever', *Nature Physics* **12**(8), 731.

Antognozzi, M., Haschke, H. & Miles, M. (2000), 'A new method to measure the oscillation of a cylindrical cantilever:"the laser reflection detection system"', *Review of Scientific Instruments* **71**(4), 1689–1694.

Antognozzi, M., Humphris, A. & Miles, M. (2001), 'Observation of molecular layering in a confined water film and study of the layers viscoelastic properties', *Applied Physics Letters* **78**(3), 300–302.

Antognozzi, M., Szczelkun, M. D., Round, A. N. & Miles, M. J. (2002), 'Comparison between shear force and tapping mode afm-high resolution imaging of dna', *Single Molecules* **3**(2-3), 105–110.

Antognozzi, M., Szczelkun, M., Humphris, A. & Miles, M. (2003), 'Increasing shear force microscopy scanning rate using active quality-factor control', *Applied Physics Letters* **82**(17), 2761–2763.

Antognozzi, M., Ulcinas, A., Picco, L., Simpson, S., Heard, P., Szczelkun, M., Brenner, B. & Miles, M. (2008), 'A new detection system for extremely small vertically mounted cantilevers', *Nanotechnology* **19**(38), 384002.

Antognozzi, M., Wotherspoon, A., Hayes, J. M., Miles, M. J., Szczelkun, M. D. & Valdrè, G. (2006), 'A chlorite mineral surface actively drives the deposition of dna molecules in stretched conformations', *Nanotechnology* **17**(15), 3897.

Arjmand, M. T., Sadeghian, H., Salarieh, H. & Alasty, A. (2008), 'Chaos control in afm systems using nonlinear delayed feedback via sliding mode control', *Nonlinear Analysis: Hybrid Systems* **2**(3), 993–1001.

Ashby, P. D. (2007), 'Gentle imaging of soft materials in solution with amplitude modulation atomic force microscopy: Q control and thermal noise', *Applied Physics Letters* **91**(25), 254102.

Ashby, P. D., Chen, L. & Lieber, C. M. (2000), 'Probing intermolecular forces and potentials with magnetic feedback chemical force microscopy', *Journal of the American Chemical Society* **122**(39), 9467–9472.

Atia, W. A. & Davis, C. C. (1997), 'A phase-locked shear-force microscope for distance regulation in near-field optical microscopy', *Applied Physics Letters* **70**(4), 405–407.

Balasubramanian, K. et al. (2014), 'Antibacterial application of polyvinylalcohol-nanogold composite membranes', *Colloids and Surfaces A: Physicochemical and Engineering Aspects* **455**, 174–178.

Baselt, D. R., Clark, S. M., Youngquist, M. G., Spence, C. F. & Baldeschwieler, J. D. (1993), 'Digital signal processor control of scanned probe microscopes', *Review of Scientific Instruments* **64**(7), 1874–1882.

Besançon, G., Voda, A. & Alma, M. (2008), On observer-based estimation enhancement by parametric amplification in a weak force measurement device, *in* 'Decision and Control, 2008. CDC 2008. 47th IEEE Conference on', IEEE, pp. 5200–5205.

Betzig, E., Finn, P. & Weiner, J. (1992), 'Combined shear force and near-field scanning optical microscopy', *Applied Physics Letters* **60**(20), 2484–2486.

Binnig, G., Quate, C. F. & Gerber, C. (1986), 'Atomic force microscope', *Physical Review Letters* **56**(9), 930.

Binnig, G. & Rohrer, H. (2000), 'Scanning tunneling microscopy', *IBM Journal of Research and Development* **44**(1/2), 279.

Binnig, G., Rohrer, H., Gerber, C. & Weibel, E. (1982), 'Surface studies by scanning tunneling microscopy', *Physical Review Letters* **49**(1), 57.

Brook, A., Bending, S., Pinto, J., Oral, A., Ritchie, D., Beere, H., Springthorpe, A. & Henini, M. (2002), 'Micromachined iii–v cantilevers for afm-tracking scanning hall probe microscopy', *Journal of Micromechanics and Microengineering* **13**(1), 124.

Butt, H.-J., Cappella, B. & Kappl, M. (2005), 'Force measurements with the atomic force microscope: Technique, interpretation and applications', *Surface Science Reports* **59**(1-6), 1–152.

Butt, H.-J. & Jaschke, M. (1995), 'Calculation of thermal noise in atomic force microscopy', *Nanotechnology* **6**(1), 1.

Caplan, J., Niethammer, M., Taylor II, R. M. & Czymmek, K. J. (2011), 'The power of correlative microscopy: multi-modal, multi-scale, multi-dimensional', *Current Opinion in Structural Biology* **21**(5), 686–693.

Carl Zeiss AG (2018), 'Zeiss microscopy', `https://www.zeiss.com/microscopy/int/home.html`. Online: Accessed on 2018 APR 09.

Carrasco, J., Hodgson, A. & Michaelides, A. (2012), 'A molecular perspective of water at metal interfaces', *Nature Materials* **11**(8), 667.

Carrasco, J., Klimeš, J. & Michaelides, A. (2013), 'The role of van der waals forces in water adsorption on metals', *The Journal of Chemical Physics* **138**(2), 024708.

Chang, C.-C., Banishev, A., Castillo-Garza, R., Klimchitskaya, G., Mostepanenko, V. & Mohideen, U. (2012), 'Gradient of the casimir force between au surfaces of a sphere and a plate measured using an atomic force microscope in a frequency-shift technique', *Physical Review B* **85**(16), 165443.

Chen, L., Cheung, C. L., Ashby, P. D. & Lieber, C. M. (2004), 'Single-walled carbon nanotube afm probes: optimal imaging resolution of nanoclusters and biomolecules in ambient and fluid environments', *Nano Letters* **4**(9), 1725–1731.

Coherent Inc. (2018), 'Cube', `https://www.coherent.com/lasers/laser/cw-solid-state-lasers/cube-lasers`. Online: Accessed on 2018 May 21.

Creemer, J., Helveg, S., Hoveling, G., Ullmann, S., Molenbroek, A., Sarro, P. & Zandbergen, H. (2008), 'Atomic-scale electron microscopy at ambient pressure', *Ultramicroscopy* **108**(9), 993–998.

Davila, J., Fridman, L. & Levant, A. (2005), 'Second-order sliding-mode observer for mechanical systems', *IEEE Transactions on Automatic Control* **50**(11), 1785–1789.

Davy, S., Spajer, M. & Courjon, D. (1998), 'Influence of the water layer on the shear force damping in near-field microscopy', *Applied Physics Letters* **73**(18), 2594–2596.

De Jonge, N. & Ross, F. M. (2011), 'Electron microscopy of specimens in liquid', *Nature Nanotechnology* **6**(11), 695.

De Lépinay, L. M., Pigeau, B., Besga, B., Vincent, P., Poncharal, P. & Arcizet, O. (2017), 'A universal and ultrasensitive vectorial nanomechanical sensor for imaging 2d force fields', *Nature Nanotechnology* **12**(2), 156.

De Silva, G., Burgess, S., Hatano, T., Khan, S., Zhang, K., Nguyen, T., Herrmann, G., Edwards, C. & Miles, M. (2017), 'Optimisation of a nano-positioning stage for a transverse dynamic force microscope', *Precision Engineering* **50**, 183–197.

De, T., Agarwal, P., Sahoo, D. R. & Salapaka, M. V. (2006), 'Real-time detection of probe loss in atomic force microscopy', *Applied Physics Letters* **89**(13), 133119.

Ding, Y.-x., Cheng, Y., Sun, Q.-m., Zhang, Y.-y., You, K., Guo, Y.-l., Han, D. & Geng, L. (2015), 'Mechanical characterization of cervical squamous carcinoma cells by atomic force microscopy at nanoscale', *Medical Oncology* **32**(3), 71.

Donald, A. M. (2003), 'The use of environmental scanning electron microscopy for imaging wet and insulating materials', *Nature Materials* **2**(8), 511.

Edwards, C. & Spurgeon, S. (1998), *Sliding mode control: theory and applications*, Crc Press.

Edwards, C. & Spurgeon, S. K. (1997), 'Sliding mode output tracking with application to a multivariable high temperature furnace problem', *International Journal of Robust and Nonlinear Control: IFAC-Affiliated Journal* **7**(4), 337–351.

El Rifai, O. M. & Youcef-Toumi, K. (2007), 'On automating atomic force microscopes: An adaptive control approach', *Control Engineering Practice* **15**(3), 349–361.

Eves, B. J. (2009), 'Design of a large measurement-volume metrological atomic force microscope (afm)', *Measurement Science and Technology* **20**(8), 084003.

Ewing, G. E. (2006), 'Ambient thin film water on insulator surfaces', *Chemical Reviews* **106**(4), 1511–1526.

Fang, Y., Feemster, M. G., Dawson, D. M. & Jalili, N. (2002), Nonlinear control techniques for the atomic force microscope system, *in* 'ASME 2002 International Mechanical Engineering Congress and Exposition', American Society of Mechanical Engineers, pp. 373–380.

Fang, Z., Carletta, J. E. & Veillette, R. J. (2005), 'A methodology for fpga-based control implementation', *IEEE Transactions on Control Systems Technology* **13**(6), 977–987.

Flegler, S. L., Heckman Jr, J. W. & Klomparens, K. L. (1993), 'Scanning and transmission electron microscopy: an introduction', *Oxford University Press(UK), 1993,* p. 225.

Fletcher, J. M., Harniman, R. L., Barnes, F. R., Boyle, A. L., Collins, A., Mantell, J., Sharp, T. H., Antognozzi, M., Booth, P. J., Linden, N. et al. (2013), 'Self-assembling cages from coiled-coil peptide modules', *Science* p. 1226558.

Fridman, L., Shtessel, Y., Edwards, C. & Yan, X.-G. (2008), 'Higher-order sliding-mode observer for state estimation and input reconstruction in nonlinear systems', *international Journal of Robust and Nonlinear Control* **18**(4-5), 399–412.

Fu, J. (1995), 'In situ testing and calibrating of z-piezo of an atomic force microscope', *Review of Scientific Instruments* **66**(7), 3785–3788.

Fujimoto, H. & Oshima, T. (2008), Contact-mode afm control with modified surface topography learning observer and ptc, *in* 'Industrial Electronics, 2008. IECON 2008. 34th Annual Conference of IEEE', IEEE, pp. 2515–2520.

Fukuma, T. & Jarvis, S. P. (2006), 'Development of liquid-environment frequency modulation atomic force microscope with low noise deflection sensor for cantilevers of various dimensions', *Review of Scientific Instruments* **77**(4), 043701.

Fukuma, T., Kimura, M., Kobayashi, K., Matsushige, K. & Yamada, H. (2005), 'Development of low noise cantilever deflection sensor for multienvironment frequency-modulation atomic force microscopy', *Review of Scientific Instruments* **76**(5), 053704.

Gebel Berg, E. (2015), 'Breaking the crystal ceiling'.

Giessibl, F. J. (2003), 'Advances in atomic force microscopy', *Reviews of Modern Physics* **75**(3), 949.

Gołek, F., Mazur, P., Ryszka, Z. & Zuber, S. (2014), 'Afm image artifacts', *Applied Surface Science* **304**, 11–19.

Good, N. E., Winget, G. D., Winter, W., Connolly, T. N., Izawa, S. & Singh, R. M. (1966), 'Hydrogen ion buffers for biological research', *Biochemistry* **5**(2), 467–477.

Grober, R. D., Harris, T. D., Trautman, J. K. & Betzig, E. (1994), 'Design and implementation of a low temperature near-field scanning optical microscope', *Review of Scientific Instruments* **65**(3), 626–631.

Guerra, P., Valbuena, A., Querol-Audí, J., Silva, C., Castellanos, M., Rodríguez-Huete, A., Garriga, D., Mateu, M. G. & Verdaguer, N. (2017), 'Structural basis for biologically relevant mechanical stiffening of a virus capsid by cavity-creating or spacefilling mutations', *Scientific Reports* **7**(1), 4101.

Guo, Z., Tian, Y., Liu, C., Wang, F., Liu, X., Shirinzadeh, B. & Zhang, D. (2015), 'Design and control methodology of a 3-dof flexure-based mechanism for micro/nano-positioning', *Robotics and Computer-Integrated Manufacturing* **32**, 93–105.

Hafner, J. H., Cheung, C. L. & Lieber, C. M. (1999), 'Growth of nanotubes for probe microscopy tips', *Nature* **398**(6730), 761.

Hamamatsu Photonics K.K. (2018), 'Psd modules', `http://www.hamamatsu.com/eu/en/product/category/3100/4012/4164/index.html`. Online: Accessed on 2018 May 21.

Hammer, D. A. & Kamat, N. P. (2012), 'Towards an artificial cell', *FEBS Letters* **586**(18), 2882–2890.

Hansen, O. & Boisen, A. (1999), 'Noise in piezoresistive atomic force microscopy', *Nanotechnology* **10**(1), 51.

Hao, H. W., Baro, A. & Saenz, J. (1991), 'Electrostatic and contact forces in force microscopy', *Journal of Vacuum Science & Technology B: Microelectronics and Nanometer Structures Processing, Measurement, and Phenomena* **9**(2), 1323–1328.

Harke, B., Chacko, J. V., Haschke, H., Canale, C. & Diaspro, A. (2012), 'A novel nanoscopic tool by combining afm with sted microscopy', *Optical Nanoscopy* **1**(1), 3.

Harniman, R. (2013), Harnessing a hybrid microscopy: vertically oriented probes in a scattered evanescent wave detection system, PhD thesis, University of Bristol.

Harniman, R. L., Plana, D., Carter, G. H., Bradley, K. A., Miles, M. J. & Fermín, D. J. (2017), 'Real-time tracking of metal nucleation via local perturbation of hydration layers', *Nature Communications* **8**(1), 971.

Harniman, R., Vicary, J., Hörber, J., Picco, L., Miles, M. & Antognozzi, M. (2012), 'Methods for imaging dna in liquid with lateral molecular-force microscopy', *Nanotechnology* **23**(8), 085703.

Hatano, T., Zhang, K., Khan, S., Nguyen, T., Herrmann, G., Edwards, C., Burgess, S. & Miles, M. (2016), A specimen-tracking controller for the transverse dynamic force microscope in non-contact mode, *in* 'American Control Conference (ACC), 2016', IEEE, pp. 7384–7389.

Herrmann, G., Turner, M. C., Postlethwaite, I. & Guo, G. (2004), 'Practical implementation of a novel anti-windup scheme in a hdd-dual-stage servo-system', *IEEE/ASME Transactions on Mechatronics* **9**(3), 580–592.

Heyde, M., Rademann, K., Cappella, B., Geuss, M., Sturm, H., Spangenberg, T. & Niehus, H. (2001), 'Dynamic plowing nanolithography on polymethylmethacrylate using an atomic force microscope', *Review of Scientific Instruments* **72**(1), 136–141.

Huang, P. (2013), Algorithmic approaches to high speed atomic force microscopy, PhD thesis, Boston University.

Humphris, A., Antognozzi, M., McMaster, T. & Miles, M. (2002), 'Transverse dynamic force spectroscopy: a novel approach to determining the complex stiffness of a single molecule', *Langmuir* **18**(5), 1729–1733.

Hutter, J. L. & Bechhoefer, J. (1993), 'Calibration of atomic-force microscope tips', *Review of Scientific Instruments* **64**(7), 1868–1873.

Israelachvili, J. N. & Pashley, R. M. (1983), 'Molecular layering of water at surfaces and origin of repulsive hydration forces', *Nature* **306**(5940), 249.

Ito, S., Unger, S. & Schitter, G. (2017), 'Vibration isolator carrying atomic force microscope's head', *Mechatronics* **44**, 32–41.

Itoh, T. & Suga, T. (1993), 'Development of a force sensor for atomic force microscopy using piezoelectric thin films', *Nanotechnology* **4**(4), 218.

Iwata, F., Sumiya, Y. & Sasaki, A. (2004), 'Nanometer-scale metal plating using a scanning shear-force microscope with an electrolyte-filled micropipette probe', *Japanese Journal of Applied Physics* **43**(7S), 4482.

James, P., Antognozzi, M., Tamayo, J., McMaster, T., Newton, J. & Miles, M. (2001), 'Interpretation of contrast in tapping mode afm and shear force microscopy. a study of nafion', *Langmuir* **17**(2), 349–360.

Jerez, J. L., Goulart, P. J., Richter, S., Constantinides, G. A., Kerrigan, E. C. & Morari, M. (2013), Embedded predictive control on an fpga using the fast gradient method, *in* 'Control Conference (ECC), 2013 European', IEEE, pp. 3614–3620.

Jerez, J. L., Goulart, P. J., Richter, S., Constantinides, G. A., Kerrigan, E. C. & Morari, M. (2014), 'Embedded online optimization for model predictive control at megahertz rates', *IEEE Transactions on Automatic Control* **59**(12), 3238–3251.

Joyce, S. A. & Houston, J. (1991), 'A new force sensor incorporating force-feedback control for interfacial force microscopy', *Review of Scientific Instruments* **62**(3), 710–715.

Karrai, K. & Grober, R. D. (1995), 'Piezoelectric tip-sample distance control for near field optical microscopes', *Applied Physics Letters* **66**(14), 1842–1844.

Karrai, K. & Tiemann, I. (2000), 'Interfacial shear force microscopy', *Physical Review B* **62**(19), 13174.

Khalil, H. K. & Praly, L. (2014), 'High-gain observers in nonlinear feedback control', *International Journal of Robust and Nonlinear Control* **24**(6), 993–1015.

Kim, H. & Gweon, D.-G. (2012), 'Development of a compact and long range xyθz nano-positioning stage', *Review of Scientific Instruments* **83**(8), 085102.

Kim, S. M., Hsu, A., Park, M. H., Chae, S. H., Yun, S. J., Lee, J. S., Cho, D.-H., Fang, W., Lee, C., Palacios, T. et al. (2015), 'Synthesis of large-area multilayer hexagonal boron nitride for high material performance', *Nature Communications* **6**, 8662.

Kiselyova, O. I., Yaminsky, I. V., Karpova, O. V., Rodionova, N. P., Kozlovsky, S. V., Arkhipenko, M. V. & Atabekov, J. G. (2003), 'Afm study of potato virus x disassembly induced by movement protein', *Journal of Molecular Biology* **332**(2), 321–325.

Knoll, M. & Ruska, E. (1932), 'Das elektronenmikroskop', *Zeitschrift für Physik* **78**(5-6), 318–339.

Kodera, N., Sakashita, M. & Ando, T. (2006), 'Dynamic proportional-integral-differential controller for high-speed atomic force microscopy', *Review of Scientific Instruments* **77**(8), 083704.

Kohl, D., Riel, T., Saathof, R., Steininger, J. & Schitter, G. (2016), Auto-tuning pi controller for surface tracking in atomic force microscopy-a practical approach, *in* 'American Control Conference (ACC), 2016', IEEE, pp. 7396–7401.

Kos, A. B. & Hurley, D. C. (2007), 'Nanomechanical mapping with resonance tracking scanned probe microscope', *Measurement Science and Technology* **19**(1), 015504.

Kuiper, S., Van den Hof, P. & Schitter, G. (2013), 'Integrated design of the feedback controller and topography estimator for atomic force microscopy', *Control Engineering Practice* **21**(8), 1110–1120.

Kuo, C.-C. & Chen, Y.-R. (2012), 'Rapid optical measurement of surface texturing result of crystalline silicon wafers for high efficiency solar cells application', *Optik-International Journal for Light and Electron Optics* **123**(4), 310–313.

La Rosa, A., Cui, X., McCollum, J., Li, N. & Nordstrom, R. (2005), 'The ultrasonic/shear-force microscope: Integrating ultrasonic sensing into a near-field scanning optical microscope', *Review of Scientific Instruments* **76**(9), 093707.

Labernadie, A., Bouissou, A., Delobelle, P., Balor, S., Voituriez, R., Proag, A., Fourquaux, I., Thibault, C., Vieu, C., Poincloux, R. et al. (2014), 'Protrusion force microscopy reveals oscillatory force generation and mechanosensing activity of human macrophage podosomes', *Nature Communications* **5**, 5343.

Lee, D.-w., Ono, T. & Esashi, M. (2000), 'High-speed imaging by electromagnetic alloy actuated probe with dual spring', *Journal of Microelectromechanical Systems* **9**(4), 419–424.

Lee, S., Howell, S., Raman, A. & Reifenberger, R. (2002), 'Nonlinear dynamics of microcantilevers in tapping mode atomic force microscopy: A comparison between theory and experiment', *Physical Review B* **66**(11), 115409.

Levy, R. & Maaloum, M. (2001), 'Measuring the spring constant of atomic force microscope cantilevers: thermal fluctuations and other methods', *Nanotechnology* **13**(1), 33.

Liang, S., Medich, D., Czajkowsky, D. M., Sheng, S., Yuan, J.-Y. & Shao, Z. (2000), 'Thermal noise reduction of mechanical oscillators by actively controlled external dissipative forces', *Ultramicroscopy* **84**(1-2), 119–125.

Lodish, H. F., Zhou, B., Liu, G. & Chen, C.-Z. (2008), 'Micromanagement of the immune system by micrornas', *Nature Reviews Immunology* **8**(2), 120.

Mahyuddin, M. N., Na, J., Herrmann, G., Ren, X. & Barber, P. (2014), 'Adaptive observer-based parameter estimation with application to road gradient and vehicle mass estimation', *IEEE Transactions on Industrial Electronics* **61**(6), 2851–2863.

Marcus, R., Ravi, T., Gmitter, T., Chin, K., Liu, D., Orvis, W., Ciarlo, D., Hunt, C. & Trujillo, J. (1990), 'Formation of silicon tips with¡ 1 nm radius', *Applied Physics Letters* **56**(3), 236–238.

Marinello, F., Savio, E., Bariani, P. & Carmignato, S. (2009), 'Coordinate metrology using scanning probe microscopes', *Measurement Science and Technology* **20**(8), 084002.

Martin, Y., Williams, C. & Wickramasinghe, H. K. (1987), 'Atomic force microscope–force mapping and profiling on a sub 100-å scale', *Journal of Applied Physics* **61**(10), 4723–4729.

Meyer, G. & Amer, N. M. (1988), 'Novel optical approach to atomic force microscopy', *Applied Physics Letters* **53**(12), 1045–1047.

Monmasson, E. & Cirstea, M. N. (2007), 'Fpga design methodology for industrial control systems—a review', *IEEE Transactions on Industrial Electronics* **54**(4), 1824–1842.

Moore, B. (1981), 'Principal component analysis in linear systems: Controllability, observability, and model reduction', *IEEE Transactions on Automatic Control* **26**(1), 17–32.

Mühlschlegel, P., Toquant, J., Pohl, D. & Hecht, B. (2006), 'Glue-free tuning fork shear-force microscope', *Review of Scientific Instruments* **77**(1), 016105.

Na, J., Herrmann, G. & Zhang, K. (2017), 'Improving transient performance of adaptive control via a modified reference model and novel adaptation', *International Journal of Robust and Nonlinear Control* **27**(8), 1351–1372.

National Instruments (NI) Co. (2015), 'A global leader in test, measurement, and control solutions', `http://www.ni.com/`. Online: Accessed on 2018 May 21.

Necipoglu, S., Cebeci, S. A., Has, Y. E., Guvenc, L. & Basdogan, C. (2011), 'Robust repetitive controller for fast afm imaging', *IEEE Transactions on Nanotechnology* **10**(5), 1074–1082.

Necipoğlu, S., Demirel, B. & Güvenc, L. (2010), Fast afm scanning with parameter space based robust repetitive control designed using the comes toolbox, *in* 'ASME 2010 10th Biennial Conference on Engineering Systems Design and Analysis', American Society of Mechanical Engineers, pp. 599–606.

Newport Co. (2015), 'Ajs high-precision adjustment screws', `https://www.newport.com/f/ajs-high-precision-adjustment-screws`. Online: Accessed on 2018 May 21.

Newport Co. (2018), 'Optical table guide', `https://www.newport.com/g/optical-tables`. Online: Accessed on 2018 APR 15.

Nguyen, T., Hatano, T., Khan, S. G., Zhang, K., Edwards, C., Harniman, R., Burgess, S. C., Antognozzi, M., Miles, M. & Herrmann, G. (2015), 'Estimation of the shear force in transverse dynamic force microscopy using a sliding mode observer', *AIP Advances* **5**(9), 097157.

Nguyen, T., Khan, S. G., Hatano, T., Zhang, K., Edwards, C., Herrmann, G., Harniman, R., Burgess, S. C., Antognozzi, M. & Miles, M. (2016), 'Real-time sliding mode observer scheme for shear force estimation in a transverse dynamic force microscope', *Asian Journal of Control* .

NIKON Co. (2015), 'The ultimate in optical performance and system flexibility', `https://www.nikoninstruments.com/images/stories/PDFs/cfi60_2ce-mssh-4.pdf`. Online: Accessed on 2018 May 21.

Nobel Media (2018), 'Nobel prizes and laureates', `https://www.nobelprize.org/`. Online: Accessed on 2018 APR 09.

NuNano Ltd. (2018), 'Ultra-soft probes: Unrivalled force sensitivity', `https://www.nunano.com/ultra-soft-probes/`. Online: Accessed on 2018 APR 12.

Ojima, M., Arimoto, A., Chinone, N., Gotoh, T. & Aiki, K. (1986), 'Diode laser noise at video frequencies in optical videodisc players', *Applied optics* **25**(9), 1404–1410.

Ortega-Esteban, A., Horcas, I., Hernando-Pérez, M., Ares, P., Perez-Berna, A., San Martín, C., Carrascosa, J., De Pablo, P. & Gómez-Herrero, J. (2012), 'Minimizing tip–sample forces in jumping mode atomic force microscopy in liquid', *Ultramicroscopy* **114**, 56–61.

Park, K.-D., Park, D. J., Lee, S. G., Choi, G., Kim, D.-S., Byeon, C. C., Choi, S. B. & Jeong, M. S. (2014), 'Operation of a wet near-field scanning optical microscope in stable zones by minimizing the resonance change of tuning forks', *Nanotechnology* **25**(7), 075704.

Payam, A. F., Martin-Jimenez, D. & Garcia, R. (2015), 'Force reconstruction from tapping mode force microscopy experiments', *Nanotechnology* **26**(18), 185706.

Payam, A. F., Rahman, E. M. A. & Fathipour, M. (2011), Control of atomic force microscope based on the fuzzy theory, *in* 'Fuzzy Controllers, Theory and Applications', InTech.

Pedrak, R., Ivanov, T., Ivanova, K., Gotszalk, T., Abedinov, N., Rangelow, I., Edinger, K., Tomerov, E., Schenkel, T. & Hudek, P. (2003), 'Micromachined atomic force microscopy sensor with integrated piezoresistive sensor and thermal bimorph actuator for high-speed tapping-mode atomic force microscopy phase-imaging in higher eigenmodes', *Journal of Vacuum Science & Technology B: Microelectronics and Nanometer Structures Processing, Measurement, and Phenomena* **21**(6), 3102–3107.

Phillips, D., Padgett, M., Hanna, S., Ho, Y.-L., Carberry, D., Miles, M. & Simpson, S. (2014), 'Shape-induced force fields in optical trapping', *Nature Photonics* **8**(5), 400.

Physik Instrumente (PI) GmbH & Co. (2008), 'Piezoelectrics in positioning', `http://www.www.pi-usa.us/pdf/2009_PI_Piezo_University_Designing_with_Piezo_Actuators_Tutorial.pdf`. Online: Accessed on 2018 May 09.

Physik Instrumente (PI) GmbH & Co. (2015), 'Pi (physik instrumente): Leading provider of precision motion and positioning systems', `http://www.physikinstrumente.com/`. Online: Accessed on 2018 May 21.

Putman, C. A., De Grooth, B. G., Van Hulst, N. F. & Greve, J. (1992), 'A detailed analysis of the optical beam deflection technique for use in atomic force microscopy', *Journal of Applied Physics* **72**(1), 6–12.

Rasmussen, P., Thaysen, J., Bouwstra, S. & Boisen, A. (2001), 'Modular design of afm probe with sputtered silicon tip', *Sensors and Actuators A: Physical* **92**(1-3), 96–101.

Ren, X. & Fang, Y. (2013), 'Frequency based combination control strategy for afms', *IFAC Proceedings Volumes* **46**(5), 600–605.

Requicha, A. A., Baur, C., Bugacov, A., Gazen, B., Koel, B., Madhukar, A., Ramachandran, T., Resch, R. & Will, P. (1998), Nanorobotic assembly of two-dimensional structures, *in* 'Robotics and Automation, 1998. Proceedings. 1998 IEEE International Conference on', Vol. 4, IEEE, pp. 3368–3374.

Rigato, A., Rico, F., Eghiaian, F., Piel, M. & Scheuring, S. (2015), 'Atomic force microscopy mechanical mapping of micropatterned cells shows adhesion geometry-dependent mechanical response on local and global scales', *ACS Nano* **9**(6), 5846–5856.

Roy, R., Chen, W., Cong, L., Goodell, L. A., Foran, D. J. & Desai, J. P. (2013), 'A semi-automated positioning system for contact-mode atomic force microscopy (afm)', *IEEE Transactions on Automation Science and Engineering* **10**(2), 462–465.

Rugar, D. & Hansma, P. (1990), 'Atomic force microscopy', *Physics Today* **43**(10), 23–30.

Ruiter, A., Van Der Werf, K., Veerman, J., Garcia-Parajo, M., Rensen, W. & Van Hulst, N. (1998), 'Tuning fork shear-force feedback', *Ultramicroscopy* **71**(1-4), 149–157.

Ruiter, A., Veerman, J., Van Der Werf, K. & Van Hulst, N. (1997), 'Dynamic behavior of tuning fork shear-force feedback', *Applied Physics Letters* **71**(1), 28–30.

Sader, J. E. (1998), 'Frequency response of cantilever beams immersed in viscous fluids with applications to the atomic force microscope', *Journal of Applied Physics* **84**(1), 64–76.

Sahin, O. & Erina, N. (2008), 'High-resolution and large dynamic range nanomechanical mapping in tapping-mode atomic force microscopy', *Nanotechnology* **19**(44), 445717.

Sahin, O., Magonov, S., Su, C., Quate, C. F. & Solgaard, O. (2007), 'An atomic force microscope tip designed to measure time-varying nanomechanical forces', *Nature Nanotechnology* **2**(8), 507.

Sandoz, P., Friedt, J.-M. & Carry, E. (2008), 'Vibration amplitude of a tip-loaded quartz tuning fork during shear force microscopy scanning', *Review of Scientific Instruments* **79**(8), 086102.

Savage, N. (2008), 'Vibration isolation', *Nature Photonics* **2**(2), 118.

Schäffer, T. E. (2005), 'Calculation of thermal noise in an atomic force microscope with a finite optical spot size', *Nanotechnology* **16**(6), 664.

Schitter, G., Allgöwer, F. & Stemmer, A. (2003), 'A new control strategy for high-speed atomic force microscopy', *Nanotechnology* **15**(1), 108.

Schitter, G., Astrom, K. J., DeMartini, B. E., Thurner, P. J., Turner, K. L. & Hansma, P. K. (2007), 'Design and modeling of a high-speed afm-scanner', *IEEE Transactions on Control Systems Technology* **15**(5), 906–915.

Schitter, G., Menold, P., Knapp, H., Allgöwer, F. & Stemmer, A. (2001), 'High performance feedback for fast scanning atomic force microscopes', *Review of Scientific Instruments* **72**(8), 3320–3327.

Schitter, G. & Phan, N. (2008), Field programmable analog array (fpaa) based control of an atomic force microscope, *in* 'American Control Conference, 2008', IEEE, pp. 2690–2695.

Schitter, G., Stark, R. & Stemmer, A. (2004), 'Fast contact-mode atomic force microscopy on biological specimen by model-based control', *Ultramicroscopy* **100**(3-4), 253–257.

Schitter, G. & Stemmer, A. (2002), 'Eliminating mechanical perturbations in scanning probe microscopy', *Nanotechnology* **13**(5), 663.

Schitter, G., Stemmer, A. & Allgöwer, F. (2004), 'Robust two-degree-of-freedom control of an atomic force microscope', *Asian Journal of Control* **6**(2), 156–163.

Scholz, T., Altmann, S. M., Antognozzi, M., Tischer, C., Hörber, J.-K. H. & Brenner, B. (2005), 'Mechanical properties of single myosin molecules probed with the photonic force microscope', *Biophysical Journal* **88**(1), 360–371.

Scholz, T., Vicary, J., Jeppesen, G., Ulcinas, A., Hörber, J. & Antognozzi, M. (2011), 'Processive behaviour of kinesin observed using micro-fabricated cantilevers', *Nanotechnology* **22**(9), 095707.

Schönenberger, C. & Alvarado, S. (1989), 'A differential interferometer for force microscopy', *Review of Scientific Instruments* **60**(10), 3131–3134.

Sebastian, A., Sahoo, D. R. & Salapaka, M. V. (2003), An observer based sample detection scheme for atomic force microscopy, *in* 'Decision and Control, 2003. Proceedings. 42nd IEEE Conference on', Vol. 3, IEEE, pp. 2132–2137.

Sebastian, A. & Salapaka, S. M. (2005), 'Design methodologies for robust nano-positioning', *IEEE Transactions on Control Systems Technology* **13**(6), 868–876.

Shibata, T., Unno, K., Makino, E. & Shimada, S. (2004), 'Fabrication and characterization of diamond afm probe integrated with pzt thin film sensor and actuator', *Sensors and Actuators A: Physical* **114**(2-3), 398–405.

Shiraishi, T. & Fujimoto, H. (2012), 'High-speed atomic force microscope by surface topography observer', *Japanese Journal of Applied Physics* **51**(2R), 026602.

Sikora, A., Gotszalk, T., Sankowska, A. & Rangelow, I. W. (2005), 'Application of scanning shear-force microscope for fabrication of nanostructures', *Journal of telecommunications and information technology* pp. 81–84.

Simpson, S. H., Phillips, D. B., Brzobohaty, O., Antognozzi, M., Hanna, S. & Zemánek, P. (2015), Shape adapted optical forces and interactions, *in* 'Optical Trapping Applications', Optical Society of America, OtM4E.3.

Soltani Bozchalooi, I. (2015), Design and control of high-speed and large-range atomic force microscope, PhD thesis, Massachusetts Institute of Technology.

Sparks, A. & Manalis, S. (2006), 'Atomic force microscopy with inherent disturbance suppression for nanostructure imaging', *Nanotechnology* **17**(6), 1574.

Stark, R. W., Drobek, T. & Heckl, W. M. (1999), 'Tapping-mode atomic force microscopy and phase-imaging in higher eigenmodes', *Applied Physics Letters* **74**(22), 3296–3298.

Steffens, C., Manzoli, A., Oliveira, J. E., Leite, F. L., Correa, D. S. & Herrmann, P. S. P. (2014), 'Bio-inspired sensor for insect pheromone analysis based on polyaniline functionalized afm cantilever sensor', *Sensors and Actuators B: Chemical* **191**, 643–649.

Stoustrup, J. & H Niemann, H. (2002), 'Fault estimation—a standard problem approach', *International Journal of Robust and Nonlinear Control* **12**(8), 649–673.

Sulchek, T., Hsieh, R., Adams, J., Yaralioglu, G., Minne, S., Quate, C., Cleveland, J., Atalar, A. & Adderton, D. (2000), 'High-speed tapping mode imaging with active q control for atomic force microscopy', *Applied Physics Letters* **76**(11), 1473–1475.

Sun, L., Wang, J., Rong, W., Li, X. & Bao, H. (2008), 'A silicon integrated micro nano-positioning xy-stage for nano-manipulation', *Journal of Micromechanics and Microengineering* **18**(12), 125004.

Suzuki, Y., Higuchi, Y., Hizume, K., Yokokawa, M., Yoshimura, S. H., Yoshikawa, K. & Takeyasu, K. (2010), 'Molecular dynamics of dna and nucleosomes in solution studied by fast-scanning atomic force microscopy', *Ultramicroscopy* **110**(6), 682–688.

Tan, C. P. & Edwards, C. (2010), 'Robust fault reconstruction in uncertain linear systems using multiple sliding mode observers in cascade', *IEEE Transactions on Automatic Control* **55**(4), 855–867.

Tanaka, S., Kerfeld, C. A., Sawaya, M. R., Cai, F., Heinhorst, S., Cannon, G. C. & Yeates, T. O. (2008), 'Atomic-level models of the bacterial carboxysome shell', *Science* **319**(5866), 1083–1086.

Tang, T.-Y. D., Antognozzi, M., Vicary, J. A., Perriman, A. W. & Mann, S. (2013), 'Small-molecule uptake in membrane-free peptide/nucleotide protocells', *Soft Matter* **9**(31), 7647–7656.

Thaysen, J., Boisen, A., Hansen, O. & Bouwstra, S. (2000), 'Atomic force microscopy probe with piezoresistive read-out and a highly symmetrical wheatstone bridge arrangement', *Sensors and Actuators A: Physical* **83**(1-3), 47–53.

The MathWorks, Inc. (2018), 'Matlab', `https://uk.mathworks.com/products/matlab.html`. Online: Accessed on 2018 May 21.

Thormann, E., Pettersson, T., Kettle, J. & Claesson, P. M. (2010), 'Probing material properties of polymeric surface layers with tapping mode afm: Which cantilever spring constant, tapping amplitude

and amplitude set point gives good image contrast and minimal surface damage?', *Ultramicroscopy* **110**(4), 313–319.

Tien, S., Zou, Q. & Devasia, S. (2005), 'Iterative control of dynamics-coupling-caused errors in piezoscanners during high-speed afm operation', *IEEE Transactions on Control Systems Technology* **13**(6), 921–931.

Trache, A. & Lim, S.-M. (2010), 'Live cell response to mechanical stimulation studied by integrated optical and atomic force microscopy', *Journal of Visualized Experiments: JoVE* (44).

Tuma, T., Haeberle, W., Rothuizen, H., Lygeros, J., Pantazi, A. & Sebastian, A. (2014), 'Dual-stage nanopositioning for high-speed scanning probe microscopy', *IEEE/ASME Transactions on Mechatronics* **19**(3), 1035–1045.

Tuma, T., Lygeros, J., Kartik, V., Sebastian, A. & Pantazi, A. (2012), 'High-speed multiresolution scanning probe microscopy based on lissajous scan trajectories', *Nanotechnology* **23**(18), 185501.

Turner, M. C., Herrmann, G. & Postlethwaite, I. (2009), 'Improving sector-based results for systems with dead-zone nonlinearities and constrained control applications', *Automatica* **45**(1), 155–160.

Uchida, M., Klem, M. T., Allen, M., Suci, P., Flenniken, M., Gillitzer, E., Varpness, Z., Liepold, L. O., Young, M. & Douglas, T. (2007), 'Biological containers: protein cages as multifunctional nanoplatforms', *Advanced Materials* **19**(8), 1025–1042.

Ulcinas, A., Valdre, G., Snitka, V., Miles, M. J., Claesson, P. M. & Antognozzi, M. (2011), 'Shear response of nanoconfined water on muscovite mica: role of cations', *Langmuir* **27**(17), 10351–10355.

Uluç, K., Kujoth, G. C. & Başkaya, M. K. (2009), 'Operating microscopes: past, present, and future', *Neurosurgical focus* **27**(3), E4.

Utkin, V. (1981), Principles of identification using sliding regimes, *in* 'Soviet Physics Doklady', Vol. 26, p. 271.

Utkin, V. I. (2013), *Sliding modes in control and optimization*, Springer Science & Business Media.

Vahdat, V. & Carpick, R. W. (2013), 'Practical method to limit tip–sample contact stress and prevent wear in amplitude modulation atomic force microscopy', *ACS Nano* **7**(11), 9836–9850.

Valdrè*, G., Antognozzi, M., Wotherspoon, A. & Miles, M. J. (2004), 'Influence of properties of layered silicate minerals on adsorbed dna surface affinity, self-assembly and nanopatterning', *Philosophical Magazine Letters* **84**(9), 539–545.

Valdrè, G., Moro, D., Hounsome, C. & Antognozzi, M. (2012), 'Spm nanolithography of hydroxy-silicates', *Nanotechnology* **23**(38), 385301.

Veeco Instruments Inc. (2004), 'Dimension 3100 manual', `https://www.scu.edu/media/school-of-engineering/photos/cns/Dimension3100D-Manual.pdf`. Online: Accessed on 2018 May 21.

Vicary, J., Ulcinas, A., Hörber, J. & Antognozzi, M. (2011), 'Micro-fabricated mechanical sensors for lateral molecular-force microscopy', *Ultramicroscopy* **111**(11), 1547–1552.

Von Ardenne, M. (1938), 'The scanning electron microscope: Theoretical fundamentals', *Z. Phys* **109**, 553–572.

Wallace, J. (2015), 'Photonics products: Vibration-isolation tables: Isolation tables support stable optical setups', *Laser Focus World* .

Wong, T. & Welland, M. (1993), 'A digital control system for scanning tunnelling microscopy and atomic force microscopy', *Measurement Science and Technology* **4**(3), 270.

Wu, Y., Zou, Q. & Su, C. (2009), 'A current cycle feedback iterative learning control approach for afm imaging', *IEEE Transactions on Nanotechnology* **8**(4), 515–527.

Yamashita, H., Kodera, N., Miyagi, A., Uchihashi, T., Yamamoto, D. & Ando, T. (2007), 'Tip-sample distance control using photothermal actuation of a small cantilever for high-speed atomic force microscopy', *Review of Scientific Instruments* **78**(8), 083702.

Yong, Y. K., Bhikkaji, B. & Moheimani, S. R. R. (2013), 'Design, modeling, and fpaa-based control of a high-speed atomic force microscope nanopositioner', *IEEE/ASME Transactions on Mechatronics* **18**(3), 1060–1071.

Zahl, P., Bierkandt, M., Schröder, S. & Klust, A. (2003), 'The flexible and modern open source scanning probe microscopy software package gxsm', *Review of Scientific Instruments* **74**(3), 1222–1227.

Zhang, K., Hatano, T., Herrmann, G., Antognozzi, M., Edwards, C., Burgess, S., Nguyen, T. & Miles, M. (2018), Enhancing fixed-point control robustness for experimental non-contact scans with the transverse-dynamic force microscope, *in* 'American Control Conference (ACC), 2018', IEEE.

Zhang, K., Hatano, T., Tien, T., Herrmann, G., Edwards, C., Burgess, S. C. & Miles, M. (2015), 'An adaptive non-raster scanning method in atomic force microscopy for simple sample shapes', *Measurement Science and Technology* **26**(3), 035401.

Zhang, Y., Fang, Y. & Dong, X. (2010), Output feedback robust adaptive controller design for dynamic atomic force microscopy, *in* 'Control Applications (CCA), 2010 IEEE International Conference on', IEEE, pp. 1666–1671.

Zhao, B., Brittain, W. J., Zhou, W. & Cheng, S. Z. (2000), 'Afm study of tethered polystyrene-b-poly (methyl methacrylate) and polystyrene-b-poly (methyl acrylate) brushes on flat silicate substrates', *Macromolecules* **33**(23), 8821–8827.

Ziegler, D., Naujoks, N. & Stemmer, A. (2008), 'Feed-forward compensation of surface potential in atomic force microscopy', *Review of Scientific Instruments* **79**(6), 063704.

Zou, Q., Leang, K. K., Sadoun, E., Reed, M. & Devasia, S. (2004), 'Control issues in high-speed afm for biological applications: Collagen imaging example', *Asian Journal of Control* **6**(2), 164–178.

Zygo Co. (2008), 'Error sources-zygo corporation', `https://www.zygo.com/library/papers/`. Online: Accessed on 2018 APR 16.